

ADDRESSING THE NEAR-FAULT DIRECTIVITY EFFECTS FOR THEIR  
IMPLEMENTATION TO DESIGN SPECTRUM

A THESIS SUBMITTED TO  
THE GRADUATE SCHOOL OF NATURAL AND APPLIED SCIENCES  
OF  
MIDDLE EAST TECHNICAL UNIVERSITY

BY

SAED MOGHIMI

IN PARTIAL FULFILLMENT OF THE REQUIREMENTS  
FOR  
THE DEGREE OF DOCTOR OF PHILOSOPHY  
IN  
CIVIL ENGINEERING

SEPTEMBER 2017



Approval of the thesis:

**ADDRESSING THE NEAR-FAULT DIRECTIVITY EFFECTS FOR THEIR  
IMPLEMENTATION TO DESIGN SPECTRUM**

submitted by **SAED MOGHIMI** in partial fulfillment of the requirements for the degree of **Doctor of Philosophy in Civil Engineering Department, Middle East Technical University** by,

Prof. Dr. Gülbin Dural Ünver  
Dean, Graduate School of **Natural and Applied Sciences** \_\_\_\_\_

Prof. Dr. İsmail Özgür Yaman  
Head of Department, **Civil Engineering** \_\_\_\_\_

Assoc. Prof. Dr. Yalın Arıcı  
Supervisor, **Civil Engineering Dept., METU** \_\_\_\_\_

**Examining Committee Members:**

Prof. Dr. Murat Altuğ Erberik  
Civil Engineering Dept., METU \_\_\_\_\_

Assoc. Prof. Dr. Yalın Arıcı  
Civil Engineering Dept., METU \_\_\_\_\_

Assoc. Prof. Dr. Mustafa Tolga Yılmaz  
Engineering Science Dept., METU \_\_\_\_\_

Prof. Dr. Sinan Akkar  
Kandilli Observatory and Earthquake Research Institute.,  
Earthquake Engineering Department.,  
Bogazici University \_\_\_\_\_

Assist. Prof. Dr. Karin Şeşetyan  
Kandilli Observatory and Earthquake Research Institute.,  
Earthquake Engineering Department.,  
Bogazici University \_\_\_\_\_

Date: 8 September 2017

**I hereby declare that all information in this document has been obtained and presented in accordance with academic rules and ethical conduct. I also declare that, as required by these rules and conduct, I have fully cited and referenced all material and results that are not original to this work.**

Name, Last name: Saed Moghimi

Signature :

## **ABSTRACT**

### **ADDRESSING THE NEAR-FAULT DIRECTIVITY EFFECTS FOR THEIR IMPLEMENTATION TO DESIGN SPECTRUM**

Moghim, Saed

Ph.D., Department of Civil Engineering

Supervisor: Assoc. Prof. Dr. Yalın Arıcı

SEPTEMBER 2017, 213 pages

Near-Fault Forward-Directivity (NFFD) ground motions are highly polarized and they have the potential to impose larger seismic demands on the structures. This is due to the presence of impulsive signals in the beginning of their velocity waveforms, which amplifies the response spectrum in periods close to pulse period.

Different directivity models proposed recently can be used together with Ground Motion Prediction Equations (GMPEs) to estimate the response spectrum exposed to pulse-type ground motions. This study utilizes two directivity models to investigate the effect of different seismological and geometrical parameters on the amplification level that the directivity effect imposes on the response spectrum. It is shown that in Shahi and Baker (2011) (the first directivity model utilized in this study) slip rate, fault characteristic magnitude, hazard level and source-site geometric parameters play important role, on the response spectrum amplification. In Chiou and Spudich (2013) (the second directivity model), the characteristic magnitude and source-site geometry are the determining parameters. The observations from the case studies are used to set some simple rules for reflecting the forward-directivity effects on design spectra at the 475-year and 2475-year return periods.

The concept of ground motion polarization (directionality) is also utilized in the determination of maximum rotated component (RotD100) for NFFD ground motions.

For this purpose RotD100 is calculated for the near fault ground motions with and without forward-directivity effect and a conversion factor is proposed by taking the ratios of spectral demands of RotD100 horizontal component between pulselike and non-pulse recordings.

Keywords: Forward-directivity, Directionality, Ground motion prediction models, Probabilistic seismic hazard assessment, Pulse-type ground motion, Seismic design code

## ÖZ

### YAKIN FAY YÖNELİM ETKİLERİNİN TASARIM SPEKTRUMLARINA UYGULANMALARI İÇİN İRDELENMELERİ

Moghimi, Saed

Doktora, İnşaat Mühendisliği Bölümü

Tez Yöneticisi: Doç. Dr. Yalın Arıcı

Eylül 2017, 213 sayfa

Faya Yakın İleri Direktivite (FYİD) zemin hareketleri oldukça polarize olup yapılar üzerinde yüksek sismik talepler oluşturma potansiyeline sahiptir. Bu olay, hız dalgasının başında yer alan atım-tipi sinyallerin titreşim periyotlarına yakın periyotlarda tepki spektrumunu arttırmamasından dolayıdır.

Atım-tipi zemin hareketlerine maruz kalan tepki spektrumunun tahmini için, Zemin Hareketleri Tahmin Denklemleri (ZHTD) ile birlikte kullanılacak farklı direktivite modelleri son zamanlarda önerilmiştir. Bu çalışmada iki direktivite modeli kullanılarak farklı sismolojik ve geometrik parametrelerin, direktivite etkisinden dolayı tepki spektrumu üzerinde oluşturdukları amplifikasyon seviyesi incelenmiştir. Bu çalışmada kullanılan birinci direktivite modeli olan Shahi ve Baker (2011) 'de gösterildiği üzere kayma oranı, fayın karakteristik büyüklüğü, tehlike seviyesi ve kaynak-saha geometrik parametreleri, tepki spektrumunu arttırmada önemli roller oynamaktadır. İkinci model olarak kullanılan Chiou ve Spudich (2013) de ise, karakteristik büyüklük ve kaynak-saha geometrisi belirleyici parametrelerdir. Örnek çalışmalardan yapılan gözlemler, 475 yıl ve 2475 yıllık dönüşüm periyotları tasarım spektrumları üzerindeki ileri direktivite etkisini yansıtmak üzere bazı basit kurallar oluşturmak için kullanılmıştır.

Zemin hareketi kutuplaşması (yönlülük) konsepti aynı zamanda FYİD zemin hareketleri için maksimum dönük bileşen (RotD100) belirlenmesinde de kullanılmıştır. Bu amaçla, direktivite etkisi özelliğini taşıyan ve taşımayan faya yakın yer hareketleri için RotD100 bileşeni hesaplanmıştır. Ardından puls-tipi ve puls-tipi olmayan kayıtlar arasındaki RotD100 spektral taleplerinin oranı alınarak bir dönüşüm faktörü önerilmiştir.

Anahtar Kelimeler: İleri direktivite, Yönlülük, Yer hareketi tahmin modelleri, Olasılık sismik tehlike analizi, Atım-tipi yer hareketi, Deprem tasarım yönetmelikleri

Dedicated to My Parents

## ACKNOWLEDGMENTS

I would like to express my deepest gratitude to Prof. Dr. Sinan Akkar who had a great role in my thesis with his kind advice, support, guidance and encouragement as the co-advisor.

I would also like to express my respect and gratitude to my thesis advisor Assoc. Prof. Dr. Yalın Arıcı for his support and help whenever I needed. The study was financially supported by TUBITAK under “**1001 - Scientific and Technological Research Projects Funding Program**” with the 113M308 project number. I would like to thank TUBITAK for providing the required facilities for implementation of scientific projects.

I want to thank my thesis committee members Prof. Dr. Murat Altuğ Erberik, Assoc. Prof. Dr. Mustafa Tolga Yılmaz, Asst. Prof. Dr. Karin Şeşetyan, Prof. Dr. Ali Pınar and Assoc. Prof. Dr. Ayşegül Askan Gündoğan for their kind support and encouragement during this study.

Many thanks to Prof. Dr. Erdal Şafak, Prof. Dr. Eser Çaktı, , Prof. Dr. Nuray Aydınoglu, Prof. Dr. Ayşe Edinçliler, Assoc. Prof. Dr. Ümit Dikmen, Dr. Mine Demircioğlu, Assoc. Prof. Dr. Ufuk Hancılar, Assoc. Prof. Dr. Eren Uçkan and Assoc. Prof. Dr. Gülüm Tanırcan because of their valuable support, help, and comments whenever I needed. Their sincere and friendly attitude during my stay in Kandilli Observatory and Earthquake Research Institute made memorable moments in my mind. It was a great honor for me to have the chance to know Prof. Dr. Mustafa Erdik and to benefit from his experience and research in the field of near-fault earthquakes in my work. I express my thanks to Prof. Dr. Mustafa Erdik.

During my stay in Kandilli Observatory and Earthquake Research Institute I also had the chance to meet Asst. Prof. Dr. Yin Cheng, one of my best friends in my life. I particularly thank Asst. Prof. Dr. Yin Cheng for our fruitful discussions, and his comments, encouragement and friendship during my study. I would like to express

my deepest gratitude to my good friends Asst. Prof. Dr. Özden Saygılı and PhD candidates Mr. Emrullah Dar and Mehran Ghasabe for their very kind support and help during my study.

I was also lucky to know Mr. Osman Bal, PhD candidates Ms. Zeynep Coşkun, Mr. Yasin Toksoy, Ms. Gülen Uncu, Ms. Bahar Fareghi and Dr. Cem Yenidoğan. I would like to thank them for their kind support and help during my work in Kandilli Observatory and Earthquake Research Institute.

Many thanks to my best friends Mr. Said Valizadeh, Mr. Shahab Moghimi, Mr. Reza Daghestani and PhD candidate Mr. Edris Ghaderi.

Finally, I would like to thank all my family members, my parents, my brothers and sisters who have always supported, encouraged and helped me to move towards my goals in life.

## TABLE OF CONTENTS

ABSTRACT .....	v
ÖZ.....	vii
ACKNOWLEDGMENTS.....	x
TABLE OF CONTENTS .....	xii
LIST OF TABLES .....	xv
LIST OF FIGURES.....	xvii
CHAPTERS	
1. INTRODUCTION.....	1
1.1 Problem Statement.....	1
1.2 Objective and Scope of the Research .....	3
1.3 Outline of the Thesis.....	3
2. METHODOLOGY, LITERATURE SURVEY AND THEORITICAL PRINCIPLES.....	5
2.1 Introduction.....	5
2.2 Directivity Models.....	12
2.2.1 Somerville et. al (1997) and Abrahamson (2000) Directivity Models.....	14
2.2.2 Bayless and Somerville (2013) Directivity Model (NGA-WEST2) ..	16
2.2.3 Rowshandel (2013) Directivity Model (NGA-WEST2) .....	18
2.2.4 Shahi and Baker (2013) Directivity Model (NGA-WEST2).....	19
2.2.5 Spudich and Chiou (2013) Directivity Model (NGA-WEST2) .....	19
2.3 Consideration of Near-Fault Effects in Earthquake Design Codes .....	20
2.4 Directionality (Maximum Direction Component) .....	27
3. A STUDY ON MAJOR SEISMOLOGICAL AND FAULT-SITE PARAMETERS AFFECTING NEAR-FAULT DIRECTIVITY GROUND-	

MOTION DEMANDS DUE TO STRIKE-SLIP FAULTING FOR THEIR POSSIBLE INCLUSION IN SEISMIC DESIGN CODES .....	29
3.1 Introduction .....	29
3.2 Narrow-Band Forward-directivity Models .....	34
3.2.1 Shahi and Baker (2011) Model (SHB11).....	34
3.2.2 Chiou and Young-2014 (CHY-14) and Chiou and Spudich-2013 (CHS13) Directivity Model.....	39
3.2.3 Specific Comparisons Between SHB11, CHS13 .....	42
3.3 Significance of Major Seismological Parameters in NFFD Spectral Amplitudes .....	49
3.4 Spatial Extension of Directivity Dominated Sites (Regions) in the Fault Vicinity.....	57
3.5 Summary and Conclusion.....	61
4. A PROPOSED RELATIONSHIP BETWEEN DIRECTIVITY AND NONDIRECTIVITY SPECTRAL AMPLITUDES FOR MAXIMUM DIRECTION 65	
4.1 Introduction .....	65
4.2 Horizontal Component Definitions .....	67
4.3 Ground-motion Data Set.....	71
4.4 Conceptual Discussions on $RotD_{100_{directivity}}$ .....	77
4.5 Proposed Model for Calculation of $RotD_{100_{directivity}}$ .....	80
4.6 Summary and Conclusion.....	87
5. AMPLIFICATION MODELS FOR FORWARD-DIRECTIVITY .....	93
5.1 Introduction .....	93
5.2 Complex Nature of Forward-directivity Spectral Amplification .....	94
5.2.1 A Comprehensive 475-year Return Period Spectral Amplification Expression from the SHB11 Narrow-band Model.....	95
5.2.2 Estimating the 2475-year Return Period Spectral Amplifications from the Complicated Formulations Developed from SHB11 Narrow-band Directivity Model.....	102
5.3 Simplified Directivity Amplification Equations for SHB11 and CHS13	109
5.3.1 Relationship between the Characteristic Magnitude and Amplification Period Range .....	111

5.3.2	Simplified Amplification Equation for SHB11 Model .....	115
5.3.3	Simplified Directivity Amplification Equations for CHS13 Narrow-Band Model .....	129
5.3.4	Taper function for the distance.....	134
5.3.5	Residual Analyses .....	138
5.4	Consideration of Proposed Directivity Amplification Models for Directivity Dominant Maximum Direction Spectrum .....	143
6.	CONCLUSION AND DISCUSSIONS.....	147
6.1	Summary and Conclusions .....	147
6.2	Recommendations for further research.....	150
	REFERENCES .....	153
	APPENDICES.....	159
	A. GEOMETRICAL CALCULATIONS FOR SEISMIC HAZARD ANALYSIS WITH THE DIRECTIVITY MODELS .....	159
	A.1 Geometrical Calculations for Chiou and Spudich (2013) model .....	159
	A.2 Geometrical Calculations for Shahi and Baker (2011) Model (r and s).....	164
	B. THE MATHEMATICAL MODEL AND THE ALGORITHM USED IN THE PSHA CALCULATIONS FOR THE SHB11 MODEL.....	167
	B.1 Algorithm used in SHB11 PSHA .....	167
	B.2 The Numerical eEvaluation of Integral in PSHA .....	170
	B.3 The Matlab Code developed for PSHA .....	175
	C. LIST OF PULSE-TYPE AND NON-PULSE-TYPE NEAR-FAULT GROUND MOTIONS.....	205
	CIRCULUM VITAE.....	211

## LIST OF TABLES

### TABLES

Table 2.1 Coefficients used in the modified Somerville et al. (1997) directivity model by Abrahamson (2000) for average horizontal spectral component .....	16
Table 2.2 Seismic source type (from Table 16-U of UBC-97).....	21
Table 2.3 Near source factor $N_a$ (from Table 16-S from UBC-97).....	22
Table 2.4 Near source factor $N_v$ (from Table 16-T from UBC-97) .....	22
Table 2.5 Near-Fault factor $N_A$ for the sites near the Chelungpu Fault in Taiwanese seismic design code (Chai et al. 2000).....	23
Table 2.6 Near-Fault factor $N_v$ for the sites near the Chelungpu Fault in Taiwanese seismic design code (Chai et al. 2000).....	23
Table 2.7 Proposed near-fault factors for Chinese Seismic Design Code in stiff soil site (Li et al. 2007) .....	23
Table 2.8 Near-fault factors for Iranian seismic design code, $M_w < 6.5$ (Yaghmaei-Sabegh and Mohammad-Alizadeh 2012).....	24
Table 2.9 Near-fault factors for Iranian seismic design code, $6.5 \leq M_w \leq 7.0$ (Yaghmaei-Sabegh and Mohammad-Alizadeh 2012).....	25
Table 2.10 Maximum near fault factor $N_{max}(T)$ (New Zealand Standard, NZS 2004) .....	25
Table 3.1 Decomposition of average slip rates for the exponential and characteristic earthquakes represented by the stochastic earthquake recurrence model used in the fictitious fault segments .....	51
Table 3.2 Proposed rules for (a) SHB11 and (b) CHS13 to define the spatial distribution of directivity affected spectral amplifications within the fault.....	60
Table 4.1 Definitions of horizontal component metrics.....	70
Table 4.2 Classification of the records for different magnitude, distance and site class ranges and the related subgroups.....	81
Table 4.3 Period-dependent variation of $Sa_{RotD100directivity}$ to $Sa_{RotD100nodirectivity}$ ratios presented in Figure 4.14.....	89
Table 4.4 Period-dependent variation of $Sa_{RotD100}$ to $Sa_{RotD50}$ ratios presented in Figure 4.17 .....	91
Table 5.1 Coefficients of the directivity dominant spectral amplifications of Equation (5.1) for sites located along $R_x/L = 0$ .....	99
Table 5.2 Coefficients of the directivity dominant spectral amplifications of Equation (5.1) for sites located along $R_x/L = 0.5$ .....	100
Table 5.3 Geometric parameters for determination of four region boundaries defined for the calculation of amplifications .....	106

Table 5.4 Coefficient for fitted median and standard deviation curves of NRM <sub>amp</sub> (T) .....	108
Table 5.5 $\alpha_{T_{max}}$ and $\beta_{T_{max}}$ coefficients for AMP <sub>T<sub>max</sub>,base</sub> – SHB11 .....	120
Table 5.6 $\alpha_{T_{10}}$ and $\beta_{T_{10}}$ coefficients for AMP <sub>T<sub>10</sub>,base</sub> – SHB11 .....	120
Table 5.7 $\alpha_{T_{10}}$ , $\beta_{T_{10}}$ , $\gamma_{T_{10}}$ and $\zeta_{T_{10}}$ coefficients for AMP <sub>T<sub>10</sub>,base</sub> – SHB11 .....	120
Table 5.8 Scale factor values for T <sub>max</sub> and T = 10s for the computation of geometric scale factors at different R <sub>x</sub> /L values (SHB11 model) .....	121
Table 5.9 $\alpha_{T_{corner}}$ and $\beta_{T_{corner}}$ coefficients for linearly fitted AMP(T <sub>corner</sub> ) function - CHS13 .....	130
Table 5.10 Geometric scale factor for different R <sub>x</sub> /L values -CHS13 .....	131
Table C. 1 List of near-fault pulse type ground motions (Last access 20/09/2016) .....	205
Table C. 2 List of near-fault nonpulse ground motions (Last access 20/09/2016)	208

## LIST OF FIGURES

### FIGURES

Figure 2.1 Strike normal forward-directivity and backward-directivity ground velocities from the 1992 Landers earthquake (Somerville et al. 1997) .....	6
Figure 2.2 Illustration of orientations of motion from fling step and directivity effects in strike slip and dip-slip ruptures (Somerville 2002).....	7
Figure 2.3 Response spectrum of pulse-type records with a) $0.6 \leq T_p < 1.5$ (mean $T_p = 1.0$ s) and b) $1.5 \leq T_p < 2.5$ (mean $T_p = 1.9$ s). The plots also show the response spectrum computed from conventional Abrahamson and Silva (1997) GMPE and the broad-band model by Somerville et al. (1997) (Tothong et al. 2007).....	9
Figure 2.4 Fault normal velocity time histories of moderate and large magnitude earthquakes and corresponding acceleration response spectra together with the UBC 94 spectrum shown as reference (Somerville 2003) .....	11
Figure 2.5 Geometric parameters used in Somerville (1997) directivity model.....	15
Figure 2.6 UBC 97 design spectrum calculated for seismic zone 4, soil type $S_D$ and seismic source type A for closest distances 2, 5, 10 and 15km. ....	22
Figure 2.7 Near-Fault adjustment factor as a function of distance and spectral period (CALTRANS 2013). ....	26
Figure 2.8 Response spectrum of Gebze station-1999 Kocaeli earthquake calculated for different rotated orientations of two horizontal components, together with geometric mean, RotD50 and RotD100 components illustrated for different spectral periods .....	28
Figure 3.1 (a) the parameters defining fault-site geometry in SHB11 for a strike-slip fault (b) contours of pulse occurrence probability for a rupture nucleating at the center of the fault .....	37
Figure 3.2 Algorithm implemented to run PSHA with SHB11 directivity model... 39	
Figure 3.3 a) Illustration of Direct Point Parameter ( $DPP$ ) from a fictitious source-site geometry: $PHPD$ is the E-path with length $E$ and $P_D$ is the direct point, b) Sites along the same racetrack and the computed $DPP_i$ ( $i = 1$ to $n$ ) .....	41
Figure 3.4 Algorithm implemented to run PSHA with SHB11 directivity model... 42	
Figure 3.5 Plan view of fault-site configuration used in this study. (The red rectangle encloses the sites 8, 9 and 10 that are used in the deterministic scenario).....	42
Figure 3.6 Comparison of the SHB11 and CHS13 directivity models at the sites 8, 9 and 10 (Figure 3.5) for 2475-year return period $S_a$ for a fault of $L = 150$ km and a slip rate of $s = 1$ cm/year. ....	44
Figure 3.7 The Youngs and Coppersmith (1985) stochastic model to describe the earthquake recurrence in PSHA runs. The minimum magnitude, $M_{\min}$ , is always	

considered as $M_w$ 5 in the probabilistic earthquake scenarios. The characteristic magnitude, $M_{ch}$ , is determined from the mean $M_w$ estimated from the empirical $M_w$ vs. RA relationship in (Wells and Coppersmith 1994). .....	45
Figure 3.8 Variation of forward-directivity spectral amplifications as a function of $\alpha$ (alpha) at Site 9 for the fictitious PSHA scenario considered in Figure 3.6. ....	46
Figure 3.9 475-year probabilistic spectral amplifications for forward-directivity computed by (a) SHB11 and (b) CHS13 (via CY14) for a fault length of $L = 100\text{km}$ and $s = 2\text{cm/year}$ .....	49
Figure 3.10 Non-exceedance probabilities (cumulative density functions) of directivity spectral amplifications according to Shahi and Baker (2011) directivity model given a range of $R_x/L$ , $T/T_{max}$ and average slip rate. First three rows show the probabilities for the 475-year return period. The last three rows pertain to the 2475-year return period probabilities .....	52
Figure 3.11 Same as Figure 3.10 but the forward-directivity model is Chiou and Spudich (2013; Chapter 6 in Spudich et al., 2013) implemented in Chiou and Youngs (2014) GMPM .....	54
Figure 3.12 Period-dependent 2475-year forward-directivity spectral amplifications estimated by SHB11 and CHS13 for PSHA scenarios of fault lengths $L = 100\text{km}$ (top row), $L = 150\text{km}$ (middle row) and $L = 300\text{km}$ (bottom row) having $s_{total} = 2.0\text{cm/year}$ . The first two columns show mean spectral amplifications of SHB11 (first column) and CHS13 (second column) for sites located at a constant $R_y$ and the last two columns show mean spectral amplifications of SHB11 (third column) and CHS13 (fourth column) for sites located at a constant $R_x/L$ .....	55
Figure 3.13 The spatial distribution of the forward-directivity spectral amplifications by SHB11 in terms of the return period, slip rate and the fault length (thus the characteristic earthquake magnitude) .....	58
Figure 3.14 The spatial distribution of the forward-directivity spectral amplifications by CHS13 in terms of the return period, slip rate and the fault length (thus the characteristic earthquake magnitude) .....	59
Figure 3.15 Simplified geometries to highlight the directivity affected regions in the ruptured fault vicinity for directivity spectral amplitudes greater than 1.1. Left panel: SHB11, Right panel: CHS13 .....	60
Figure 4.1 (a) Illustration of polarization by plotting the displacement response of horizontal components at $T = 2\text{s}$ for at the Rolleston station from the 24 September 2010 $M_w 7.1$ Darfield earthquake), (b) $S_a$ values at $T = 2.0\text{s}$ obtained by rotating the horizontal ground-motion components at $0^\circ \leq \theta \leq 179^\circ$ (Bradley and Baker 2015) ...	68
Figure 4.2 Magnitude versus distance distribution of (a) pulselike and (b) non-pulse ground motions for different styles of faults (dip-slip and strike-slip) .....	72
Figure 4.3 Comparisons of SN/SP spectral ratios at $T = 2\text{s}$ , $3\text{s}$ , $4\text{s}$ and $5\text{s}$ by considering the $\theta = 45^\circ$ criterion as the boundary between pulselike and non-pulse strike-slip recordings. The red solid lines show the average of pulselike and non-pulse SN/SP ratios. ....	74

Figure 4.4 Comparisons of SN/SP spectral ratios at $T = 2s, 3s, 4s$ and $5s$ by considering the $\phi = 45^\circ$ criterion as the boundary between pulseline and non-pulse dip-slip recordings. The red solid lines show the average of pulseline and non-pulse SN/SP ratios. ....	75
Figure 4.5 Comparisons of SN/SP spectral ratios at $T = 2s, 3s, 4s$ and $5s$ by considering the $X\cos(\theta) = 0.5$ criterion as the boundary between pulseline and non-pulse strike-slip recordings. The red solid lines show the average of pulseline and non-pulse SN/SP ratios. ....	76
Figure 4.6 Comparisons of SN/SP spectral ratios at $T = 2s, 3s, 4s$ and $5s$ by considering the $Y\cos(\phi) = 0.5$ criterion as the boundary between pulseline and non-pulse dip-slip recordings. The red solid lines show the average of pulseline and non-pulse SN/SP ratios. ....	77
Figure 4.7 Comparison of different scaling (conversion) models proposed for $Sa_{RotD100}/Sa_{GMRotI50}$ ratio.....	78
Figure 4.8 $Sa_{RotD100directivity}$ (from pulseline records) spectral amplitudes of individual ground motions of the bins given in Table 4.2.....	82
Figure 4.9 $Sa_{RotD100nodirectivity}$ (from non-pulse records) spectral amplitudes of individual ground motions of the bins given in Table 4.2 .....	83
Figure 4.10 $AF_{directivity}$ curves computed from median $Sa_{RotD100directivity}$ to $Sa_{RotD100nodirectivity}$ ratios of the ground-motion bins presented in Table 4.2 .....	84
Figure 4.11 $Sa_{RotD50directivity}$ (from pulseline records) spectral amplitudes of individual ground motions of the bins given in Table 4.2. The solid black lines are the log-mean (median) spectral curves of each bin.....	85
Figure 4.12 $Sa_{RotD50nodirectivity}$ (from non-pulse records) spectral amplitudes of individual ground motions of the bins given in Table 4.2. The solid black lines are the log-mean (median) spectral curves of each bin.....	86
Figure 4.13 Median $Sa_{RotD50directivity}$ to $Sa_{RotD50nodirectivity}$ ratios computed by normalizing the median $Sa_{RotD50directivity}$ spectrum of each pulse-like ground-motion bin in Table 4.2 with the corresponding median $Sa_{RotD50nodirectivity}$ spectrum of non-pulse ground-motion bin .....	87
Figure 4.14 Median of $Sa_{RotD100directivity}$ to $Sa_{RotD100nodirectivity}$ ratios presented in Figure 4.10.....	88
Figure 4.15 RotD100 to RotD50 spectral amplitude ratios for the pulseline bins in Table 4.2.....	90
Figure 4.16 RotD100 to RotD50 spectral amplitude ratios for the nonpulse bins in Table 4.2.....	90
Figure 4.17 Medians of RotD100 to RotD50 spectral ratio curves computed from pulseline (Figure 4.15) and non-pulse (Figure 4.16) bins.....	92
Figure 5.1 Spatial distribution of sites around the fictitious fault and the sites located in the boundary region enclosed by red rectangles .....	95

Figure 5.2 Bilinear trend for directivity-dominated spectral amplifications along fault strike, $R_x/L$ , direction for a suit of spectral periods (FL = 100km, $s = 1.0\text{cm/year}$ , $R_y=15\text{km}$ ) .....	96
Figure 5.3 Maximum amplification values and location of the sites which experience the maximum value .....	97
Figure 5.4 Residuals between PSHA (observed) and the estimated directivity amplifications for 475-year return period .....	101
Figure 5.5 Normalization of 2475-year return period narrow-band spectrum to conventional spectrum.....	102
Figure 5.6 Normalized period-dependent 2475-year to 475-year directivity dominant spectral amplification ratios of 42 sites (grey curves) and corresponding logarithmic mean, $\pm\sigma$ as well as $2\sigma$ over logarithmic mean a) fictitious fault with 50km length and $s = 1\text{cm/year}$ b) fictitious fault with 100km length and $s = 1\text{cm/year}$	104
Figure 5.7 Comparison of $\text{NRM}_{\text{amp}}$ and the related contour maps for classification of the sites a) $\text{NRM}_{\text{amp}}$ vs $T(\text{sec})$ for FL=20km, $S=1\text{cm/year}$ b) contour map of $\text{NRM}_{\text{amp}}$ for $T=2.0\text{sec}$ FL=20km, $S = 1\text{cm/year}$ c) $\text{NRM}_{\text{amp}}$ vs $T(\text{sec})$ for FL=100km, $S=1\text{cm/year}$ d) contour map of $\text{NRM}_{\text{amp}}$ for $T=4.0\text{sec}$ FL=100km, $S=1\text{cm/year}$ .	105
Figure 5.8 Classification of the area around the fault into four regions with respect to $\text{NRM}_{\text{amp}}(T)$ intensities.....	107
Figure 5.9 Spatial distribution of the sites around the fault and the sites located in the boundary region.....	111
Figure 5.10 $T_{\text{max}}$ and $T_{\text{corner}}$ values for directivity amplifications. The earthquake scenario is FL=150km ( $M_{\text{ch}}=7.25$ ), $s = 0.5\text{cm/year}$ , $1\text{cm/year}$ , $2\text{ cm/year}$ a) SHB11 model b) CHS13 model.....	113
Figure 5.11 Median SHB11 and CHS13 directivity amplifications in terms of $M_{\text{ch}}$ and the variation of $T_{\text{max}}$ and $T_{\text{corner}}$ with the characteristic magnitudes.....	114
Figure 5.12 Relationship between characteristic magnitude and the spectral period ( $T_{\text{mc}}$ ) at which the maximum directivity amplification occur. Dashed red line is the fit to the actual trend given in black .....	115
Figure 5.13 SHB11-based directivity amplification vs $M_{\text{ch}}$ relationship together with linear fits calculated for the sites 3, 9, 15 and 21 at spectral period $T_{\text{max}}$ a) 475-year return period b) 2475-year return period .....	117
Figure 5.14 SHB11-based directivity amplification vs $M_{\text{ch}}$ relationship together with linear fits calculated for the sites 3, 9, 15 and 21 at $T = 10\text{s}$ a) 475-year return period b) 2475-year return period.....	118
Figure 5.15 SHB11-based directivity amplification vs $M_{\text{ch}}$ relationship together with cubic fits calculated for the sites 3, 9, 15 and 21 at $T = 10\text{s}$ a) 475-year return period b) 2475-year return period.....	119
Figure 5.16 Observed geometric scale factors for $\text{AMP}_{T_{\text{max}}}$ - 475-year return period and $s = 0.5\text{cm/year}$ , $s = 1.0\text{cm/year}$ and $s = 2.0\text{cm/year}$ (SHB11).....	123
Figure 5.17 Observed geometric scale factors for $\text{AMP}_{T_{\text{max}}}$ - 2475-year return period and $s = 0.5\text{cm/year}$ , $s = 1.0\text{cm/year}$ and $s = 2.0\text{cm/year}$ (SHB11).....	124

Figure 5.18 Observed geometric scale factors for $AMP_{T_{10}}$ - 475-year return period and $s = 0.5\text{cm/year}$ , $s = 1.0\text{cm/year}$ and $s = 2.0\text{cm/year}$ (SHB11).....	125
Figure 5.19 Observed geometric scale factors for $AMP_{T_{10}}$ - 2475-year return period and $s = 0.5\text{cm/year}$ , $s = 1.0\text{cm/year}$ and $s = 2.0\text{cm/year}$ (SHB11).....	126
Figure 5.20 Effect of characteristic magnitude and slip rate on the directivity amplifications for SHB11 model computed from proposed simplified expressions a) 475-year return period b) 2475-year return period .....	127
Figure 5.21 Effect of fault-site geometry ( $R_x/L$ ) on the directivity amplifications of SHB11 narrow-band model computed from the proposed simplified formulations a) 475-year return period b) 2475-year return period .....	128
Figure 5.22 Base amplification factors and magnitude relationships together with linear line fits calculated for sites 4, 10, 16 and 22 at spectral period $T_{\text{corner}}$ - CHS13 model, 475- and 2475-year return period.....	130
Figure 5.23 Calculation of Geometric Scale Factor for $AMP_{T_{\text{corner}}}$ - 475-year CHS13 .....	132
Figure 5.24 Amplification Model for RotD50 Component of CHS13 a) 475-year Return Period b) 2475-year return period .....	133
Figure 5.25 Distance Tapering of Directivity Amplification Factor.....	135
Figure 5.26 Observed ad estimated directivity amplifications as a function of $R_y$ for simplified SHB11 model.....	136
Figure 5.27 Observed ad estimated directivity amplifications as a function of $R_y$ for CHS13 model.....	137
Figure 5.28 Residuals computed from PSHA (observed) and estimated directivity amplifications for SHB11 narrow-band directivity model, for the 475-year return period.....	139
Figure 5.29 Residuals computed from PSHA (observed) and estimated directivity amplifications for SHB11 narrow-band directivity model for the 2475-year return period.....	140
Figure 5.30 Residuals of PSHA and estimated amplification factors for CHS13 model, for the 475-year return period .....	141
Figure 5.31 Residuals of PSHA and estimated amplification factors for CHS13 model, for the 475-year return period .....	142
Figure 5.32 Return periods related to the spectral amplitudes of pulse-like and nonpulse recordings .....	143
Figure A.1 Fault normal vector .....	159
Figure A.2 Closest point of the site to the fault plane.....	160
Figure A.3 Calculation of direct point for the case that closest point is located inside the rupture area.....	161
Figure A.4 Calculation of direct point for the case that closest point is located outside the rupture area.....	162
Figure A.5 Geometrical information for the calculation of average scalar radiation pattern ( <b>FS</b> ) parameter (Spudich et al. 2013) .....	163

Figure A.6 Geometrical calculations for Shahi and Baker (2011) model .....	164
Figure B.1 Algorithm for SHB11 PSHA narrow-band model .....	169
Figure B.2 Illustration of lognormal distribution for magnitude-pulse period and related probability of pulse period.....	171
Figure B.3 Relation between magnitude and pulse period with maximum probability .....	172
Figure B.4 Relation between magnitude and pulse period with maximum probability .....	172
Figure B.5 a) Site definition b) Discretized values applied in EZ-FRISK.....	173
Figure B.6 Response spectrum calculated for FL=20km, S=1.0com/year for site 15 with EZ-FRISK and the Matlab code (2475-year return period) .....	174
Figure B.7 Input file format for PSHA.....	175

# CHAPTER 1

## INTRODUCTION

### 1.1 Problem Statement

The near-fault ground motions have been the subject of studies in both seismology and earthquake engineering fields in the last two decades. The developments in strong ground-motion instrumentation as well as strong-ground motion databases led to rich and high-quality near-fault ground motions that provided valuable opportunities to study the different aspects of near-fault ground motions. In particular, with the increased number of near-fault records, the ground-motion prediction equations (GMPEs) have started to update their models to reflect the eminent features of near-fault recordings on the estimated spectral ordinates.

Estimation of seismic demands on structures is a challenging step in Performance Based Seismic Engineering (PBSE). The specific features of near-fault ground motions should be considered properly by seismic design spectrum at different hazard levels (represented by return periods in the seismic design codes) in order to provide solid information on the proper performance assessment of buildings against such ground motions. For example, some near-fault ground motions impose large amplitude and impulsive waveforms due to directivity effects that result in significant deformation demands on structures. Hence, defining these effects via simple rules for their incorporation in seismic design codes is important.

In recent years, the researchers modeled the directivity amplifications on the response spectrum either by increasing the spectral ordinates monotonically over a range of periods (e.g., Somerville et al., 1997; Abrahamson, 2000) or by amplifying the response spectra in a narrow period range close to the period of impulsive waveforms (pulse period,  $T_p$ ) (e.g., Tothong et al., 2007; Shahi and Baker, 2011). Both of these

approaches cause significant changes on the spectral amplitudes, which should be studied carefully to devise proper rules for near-fault directivity effects for seismic design codes. These rules would also be useful for quick assessment of structural damage against directivity-dominated seismic demand via different approaches in PBEE (e.g., probabilistic structural damage assessment).

While some seismic codes like the 1997 edition of the Uniform Building Code (UBC, 1997) incorporate the near-fault effects in design spectrum, a robust methodology to include directivity effects in design spectrum is still unavailable. Depending on the seismological features of directivity-dominated ground motions as well as source-site geometry the design spectrum can change considerably. For example, the pulse period of pulselike ground motions (one of the salient features of directivity dominated records) change the spectral period band where directivity related spectral amplification is prominent. Because pulse period to fundamental building period ratio is important to understand the maximum demand on structures subjected to directivity dominated ground motions, addressing the pulse-period effect on design spectrum is important.

Apart from directivity effects, the horizontal component orientation that gives the maximum spectral demands is important for sites located in the vicinity of active faults. The maximum horizontal component is simply referred to as directionality in the literature and its effects are different than the directivity effects. For sites close to the active faults the inclusion of these two effects would amplify the spectral ordinates significantly. The currently GMPEs consider the directionality effects on the response spectrum estimates because this spectral demand is assumed to be more critical in some codes (e.g., ASCE, 2010; BSSC, 2009; 2015) for design, in particular for structures having symmetric stiffness in all directions (azimuth-independent structures). However, the directionality effects are considered as generic cases by current GMPEs and there are currently no ground-motion predictive models that explicitly consider the directivity and directionality effects at the same time. To this end, updating seismic design codes based on incorporation of forward-directivity effect and ground motion polarization seems to be an urgent need. To this end the seismic design spectrum in the near future should consider directivity and directionality effects at the same time.

## 1.2 Objective and Scope of the Research

The main goal of this study is to determine the seismic load levels for near-fault directivity-dominant ground motions. For this purpose, two directivity models (Shahi and Baker, 2011; Chiou and Spudich, 2013) are used in the context of probabilistic seismic hazard assessment (PSHA) methodology to extract the directivity amplification factors for response spectrum by considering a suit of earthquake scenarios. The earthquake scenarios account for seismological parameters and source-site geometry that can be important in the spectral amplitude variation when directivity is prominent. In essence, the thesis proposes models to account for directivity effects on design response spectra at two return periods: 475-year and 2475-year.

The ground-motion polarization (or directionality effect) is the second important topic investigated by this study to demonstrate the level of amplification in response spectrum for sites close to the fault when both directivity and directionality are effective. To this end, pulselike (directivity dominant) ground motions are utilized and their spectra for maximum direction are compared (ratios are computed) with those of near-fault records where directivity is insignificant.

## 1.3 Outline of the Thesis

The overall structure of the study takes the form of six chapters, including this introductory chapter. In **Chapter two** the most important characteristics of near-fault directivity-dominated ground motions are introduced. Theoretical backgrounds, fundamental concepts of the renown directivity models are presented. The functional forms of proposed directivity models are also introduced in this chapter. The concept of ground-motion polarization “known as directionality” is discussed briefly. (This topic is further studied in Chapter four). Finally, the incorporation of near-fault effects in seismic design codes are discussed in the last part of this chapter.

In the **third chapter** the fundamental features of two directivity models utilized in this study (SHB11 and CHS13) are presented. The mathematical and conceptual differences between these models are discussed using probabilistic earthquake scenarios. The selected seismological and geometrical input parameters utilized in the PSHA are introduced and the effect of these parameters on the level of

amplification are discussed. The interrelation between these parameters in the amplification models are also investigated.

In **Chapter four** different horizontal component definitions of ground motions together with related important conversion models are presented. The importance of ground-motion polarization is discussed for near-fault directivity-dominated ground motions. Finally, a conversion model is proposed for estimation of the maximum rotated component for forward-directivity near fault ground motions.

The results and discussions of chapter three are utilized in **Chapter five** to propose directivity induced spectral amplification models for use in design spectrum. The proposed amplification equations consider the source-site geometry in its functional form. The effects of fault-site configuration for the estimation of directivity-dominated spectral ordinates are discussed through complicated and simplified models proposed in this study. Finally, comparisons are done in terms of amplification models proposed in this chapter and the conversion model proposed in Chapter four.

**Chapter six** summarizes the work and highlights the main conclusions. In addition, recommendations are provided for the future studies. There are three appendices at the end of this dissertation showing the PSHA and maximum direction codes as well as the ground-motion database used in chapter four.

## CHAPTER 2

### METHODOLOGY, LITERATURE SURVEY AND THEORITICAL PRINCIPLES

#### 2.1 Introduction

One of the significant features of near-fault directivity-dominant ground motions is the presence of impulsive signals in their waveforms. In principle, when an earthquake fault ruptures and propagates towards a site at a speed close to the shear-wave velocity, the generated waves arrive at the site, generating a “distinct” velocity pulse in the ground-motion time history, which is dominantly observed in the strike-normal direction. This velocity pulse usually occurs at the beginning of the velocity waveform of the directivity-dominated record. Such ground motions are known for their severe damage potential on structures, which is known for several decades. In contrast, for sites opposite to the direction of rupture propagation, the seismic energy arrives during a longer time interval, generating lower-frequency motions with smaller amplitudes. This phenomenon is known as backward directivity. Records of backward directivity are potentially less damaging.

Directivity affects the amplitude, duration and frequency content of the near-fault ground motions for medium-to-large magnitude earthquakes due to magnitude-sensitive velocity pulses. Forward-directivity also causes azimuthal variations in ground-motion amplitudes between strike-normal and strike-parallel components, which also change as a function of ruptured fault-site geometry (i.e., spatial variation around the fault). These azimuth-dependent changes in the amplitude, duration and frequency content of the directivity-dominated incident seismic waveforms make the description of this phenomenon for engineering use (its effects on response spectrum or structural behavior) quite complicated.

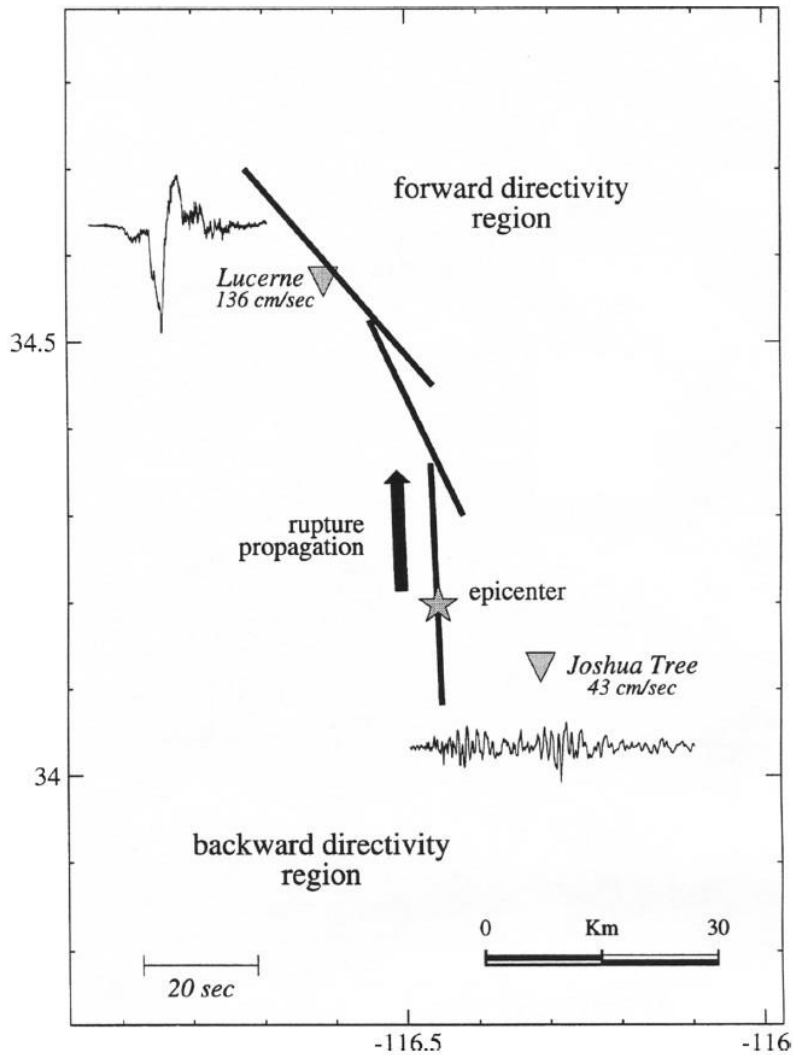


Figure 2.1 Strike normal forward-directivity and backward-directivity ground velocities from the 1992 Landers earthquake (Somerville et al. 1997)

Housner and Trifunac (1967) were the first researchers who observed ground motions with long-period, strong velocity and displacement pulses in the 1966 Parkfield earthquake. The second earthquake with impulsive signals in some of the fault-normal components is the 1971 San Fernando earthquake (Boore and Zoback 1974; Niazy 1975). Since then, several near-fault pulslike ground motions carrying directivity features are recorded (e.g., 1992 Landers earthquake, 1994 Northridge earthquake, 1995 Kobe earthquake, 1999 Kocaeli earthquake; 1999 Düzce earthquake, 1999 ChiChi earthquake, etc.). However, pulse-type records with forward-directivity effect are not observed in all near-fault ground motions.

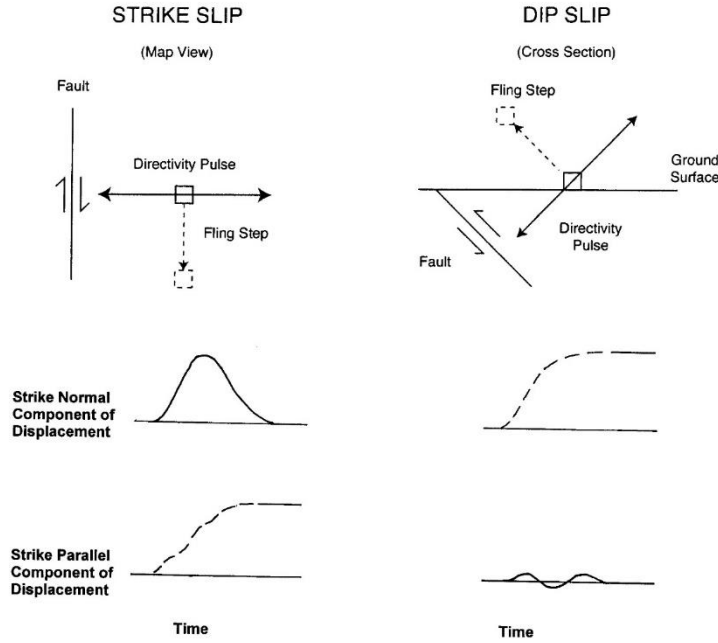


Figure 2.2 Illustration of orientations of motion from fling step and directivity effects in strike slip and dip-slip ruptures (Somerville 2002)

Figure 2.1 shows the velocity time histories of the 1992 Landers earthquake for two sites, which experienced both forward- and backward-directivity. Studies show that impulsive ground motions having long-period pulses impose severe inelastic demands on medium-to-high rise buildings due to their large amplitudes (Hall et al. 1995; Alavi and Krawinkler 2004). Strike-normal components of ground motions with forward-directivity effects usually impose larger demands than the other horizontal components on buildings hence the structures are more vulnerable for structural damage against this component. Bertero et al. (1978) studied the destructive effect of pulse-type ground motions on medium-to-high rise buildings but the observed structural damage in the 1994 Northridge earthquake also revealed the vulnerability of high-rise buildings against pulse-type ground motions (Gupta and Krawinkler 1999). The earthquakes following the Northridge earthquake with directivity dominated recordings (1995 Kobe, 1999 Kocaeli and 2009 L'Aquila earthquakes) reconfirmed the destructive potential of near-fault ground motions as well as their socio-economic impact (Alavi and Krawinkler 2001; Chioccarelli and Iervolino 2010).

The other important characteristic of near-fault records is known as “fling-step”. Unlike the pulselike effect, which is a dynamic action of the fault movement during the earthquake, fling step is the static feature of the fault movement. In the near-fault directivity-dominated records the fling-step effect (or residual displacement) is observed in the displacement waveforms.

Figure 2.2 illustrates and compares the most important features of pulselike and fling-step waveforms for near-fault directivity-dominated ground motions. As it can be seen from this figure the residual displacements (fling-step) are observed in the strike-parallel direction in strike-slip faults as in the case of the 1999 Kocaeli and Duzce earthquakes (Kalkan et al. 2004; Akkar and Gülkan, 2001). On the other hand, the residual displacement is observed in the strike-normal direction for dip-slips faults as in the case of the 1999 Chi-Chi (reverse) earthquake (Mavroeidis and Papageorgiou 2003). As fling-step occurs in the fault slip direction (unlike the pulselike signal) some researchers (Kalkan and Kunnath 2006) assumed that it is independent of forward-directivity.

Conventional GMPEs (ground-motion prediction equations) do not consider the effect of directivity in the estimation of response spectrum ordinates for near-fault ground motions. Therefore they may under-predict the seismic demand for the sites, which experience forward-directivity and over-predict it for sites with backward directivity effects. Individual forward-directivity models were developed for their use together with conventional GMPEs to estimate the response spectrum exposed to pulse-type ground motions (e.g., Somerville et al. 1997, later modified by Abrahamson 2000; Tothong et al. 2007; Shahi and Baker 2011). However, since the databases used to develop most of the conventional GMPEs include pulselike directivity-dominated ground motions the blind usage of such directivity models may double count the directivity effects in the estimated spectral ordinates. In fact, the directivity models developed under NGA-WEST1 (Power et al. 2008) could not be used practically for this reason. The conventional GMPEs developed in this project could not provide reference ground-motion estimates near the faults so that a specific directivity model (developed from the same project) could not correct the reference estimations for forward directivity. In order to prevail this problem, NGA-WEST2 (Bozorgnia et al. 2014) directivity group (Spudich et al. 2013) developed directivity

functions for reference estimations of conventional GMPEs or they proposed directivity models that can be embedded into the original predictive model.

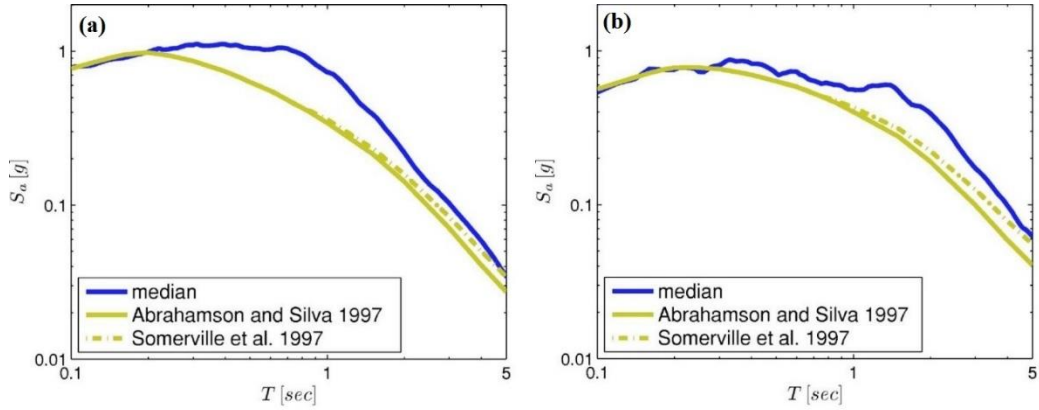


Figure 2.3 Response spectrum of pulse-type records with a)  $0.6 \leq T_p < 1.5$  (mean  $T_p = 1.0$ s) and b)  $1.5 \leq T_p < 2.5$  (mean  $T_p = 1.9$ s). The plots also show the response spectrum computed from conventional Abrahamson and Silva (1997) GMPE and the broad-band model by Somerville et al. (1997) (Tothong et al. 2007)

The directivity models proposed up to now can be classified in two groups that are known as broad-band and narrow-band models. Broad-band models amplify the response spectrum uniformly in medium-to-long period range while the narrow-band models amplify the response spectrum in a narrow range of periods close in the vicinity of pulse period ( $T_p$ ). The narrow-band effect of pulse-type records are given in Figure 2.3 (Tothong et al., 2007) that shows the median response spectra of fault normal pulse-type ground motions for two different  $T_p$  bins. The mean pulse period of first group is  $\overline{T_p} = 1.0$ s and the mean pulse period of second type group is equal to  $\overline{T_p} = 1.9$ s. The response spectrum estimated from conventional Abrahamson and Silva (1997) GMPE as well as the broad-band model of Somerville et al. (1997) are also plotted in Figure 2.3. The pulse-type spectrum (representative of narrow-band model) shows a peak amplification close to the pulse period. The peak amplification flattens down and approaches to the conventional GMPE as the periods shift away from  $T_p$ . The broad-band model of Somerville et al. (1997) estimates larger response spectrum values with respect to conventional Abrahamson and Silva (1997) GMPE starting from  $T = 0.6$ s. The broad-band spectral amplification monotonically continues towards longer periods. The amplifications imposed by the broad-band model are smaller with respect to those of spectra representing narrow-band model.

As depicted in Figure 2.3 the narrow-band nature of pulse-type records results in peaked response spectrum shapes close to  $T_p$ . The pulse period is a function of earthquake magnitude (Mavroeidis and Papageorgiou 2003; Somerville 2003; Baker 2007): larger the magnitude of an earthquake, the greater is the pulse period. Thus, the earthquakes with impulsive signals and smaller magnitudes will have shorter pulse periods, which results in amplified spectral ordinates from small-to-medium period range. On the other hand, large magnitude earthquakes possess larger pulse periods and the response spectrum peaks at a larger period range.

Figure 2.4 illustrates the velocity time histories and corresponding response spectra of fault normal, fault parallel and vertical component of pulselike ground motions having magnitudes in two intervals:  $6.7 < M_w < 7.0$  and  $7.2 < M_w < 7.6$  (Somerville 2003). Besides this figure shows the design spectrum of the 1994 edition of Uniform Building Code (UBC 1994) as reference. The fault normal components (shown as solid lines) of  $6.7 < M_w < 7.0$  records show peak spectral values in the period range between  $0.5s < T < 2.5s$  that are considerably larger than those proposed by UBC (abbreviated as UBC 94). The fault normal response spectra of  $6.7 < M_w < 7.0$  records are also greater than the response spectrum of  $7.2 < M_w < 7.6$  records in the intermediate period range. The larger magnitude records ( $7.2 < M_w < 7.6$ ) exhibit a clear bump in the period interval close to  $T = 4s$  in their fault normal components, which are (in some cases) larger than the UBC 94 response spectrum. The fault parallel components of these records (shown by long dashed lines) are also illustrated in this figure. This component exhibits smaller response spectrum amplitudes with respect to their fault normal counterparts for both moderate and large magnitudes.

Baker (2007) proposed a quantitative model for identification of pulselike waveform in a ground-motion time history using wavelet analysis. He uses the pulse indicator parameter in order to classify the ground motion as pulse-type or non-pulse-type in which the ground motions having pulse indicators greater than 0.85 are considered to contain dominant pulse signals. Baker (2007) applies two additional criteria for identifying the pulselike ground motions, which are most likely caused by directivity effects. These additional criteria are (1) the pulse waveforms should arrive early in the time history and (2) the corresponding peak ground velocity (PGV) should be greater than 30cm/s.

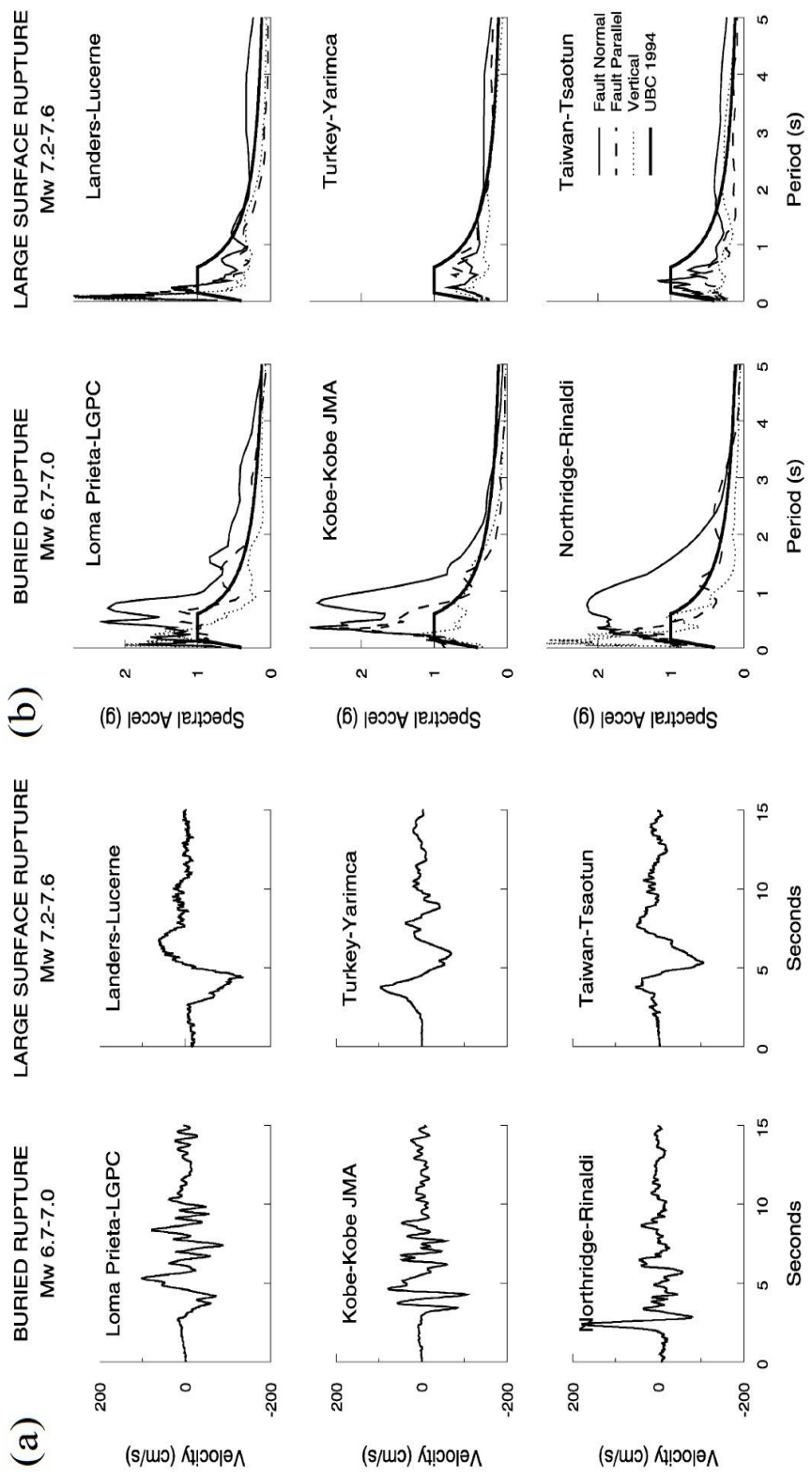


Figure 2.4 Fault normal velocity time histories of moderate and large magnitude earthquakes and corresponding acceleration response spectra together with the UBC 94 spectrum shown as reference (Somerville 2003)

Determination of pulse period is another important parameter in pulselike ground motions. Several methods are proposed for the determination of pulse period. The pulse period is the period related to the peak of velocity response spectrum of pulse-type ground motion in one of these methods. Baker (2007) used the wavelet analysis method for the measurement of pulse period. He defined the period of maximum Fourier amplitude of wavelet as the pulse period. He also showed that the pulse period determined from these two approaches (Fourier spectrum vs. velocity response spectrum) are close to each other in most cases. The pulse period obtained from the Fourier amplitude of wavelet is slightly larger than the pulse period from the spectral velocity method.

The excessive structural damage induced by near-fault ground motions made a number of codes revise their provisions to reduce the risk against similar future excitations (e.g., UBC, 1997). For example, the 1997 version of UBC (UBC 97) considers the effects of near-fault ground motions in terms of elastic acceleration response spectrum. However, the information about the displacement demand on structures exposed to directivity-dominant ground motions is not still firmly available (Alavi and Krawinkler 2001; Alavi and Krawinkler 2004; Gupta and Krawinkler 1999). Depending on the pulse period occurring due to directivity, characteristics of design spectrum can change considerably and UBC 97 was criticized to fail capturing the critical changes (Akkar and Gulkan 2001).

This chapter summarizes the background theory for important and recently proposed directivity models. In addition, the consideration of near-fault effects in some seismic design codes are discussed. The concept of directionality is introduced briefly here because it is discussed together with directivity in detail in Chapter 4.

## **2.2 Directivity Models**

Since directivity effect is identified as one of the most important features of near-fault ground motions, several research groups proposed models in order to incorporate the directivity effect in GMPEs. These models were developed from databases containing ground-motion recordings of active crustal region (ACR) earthquakes. In general, the models follow a similar approach to improve the spectral acceleration estimations due to directivity: the model developers use an existing GMPE as base ground-motion

predictor and modify the median estimations and log standard deviations of GMPEs through additional functions for directivity effects. The directivity functions need some detailed information about finite fault rupture, hypocenter location and slip direction. They generally consider fault rupture location and source-site geometry. As indicated previously, directivity models are categorized in two major groups: broad-band and narrow-band models. The response spectrum is increased monotonically in broad-band models for medium-to-long period range when directivity is of concern. However, as discussed in the above paragraphs, the recent studies showed that the response spectrum ordinates of pulselike (directivity-dominated) ground motions are amplified in a narrow period range, which is close to pulse period (Alavi and Krawinkler 2001; Mavroeidis and Papageorgiou 2003; Somerville 2003; Tothong et al. 2007; Tothog and Cornell 2007). Thus, the more recent directivity models focus on this specific feature of directivity dominant ground motions to reflect it on the spectral acceleration estimates.

The next subsection covers the important directivity models. Somerville et. al (1997) directivity model, which is modified by Abrahamson (2000) is considered first because it is the most well-known and earliest directivity model in the literature. NGA-WEST2 (Bozorgnia et al., 2014) directivity models (Spudich et al. 2013) follow this review because they are the most recent and comprehensive directivity models. Note that the NGA-WEST1 (Power et al., 2008) directivity models (Spudich and Chiou 2008; Rowshandel 2010) are excluded in the review because they are updated by the successor NGAWEST2 directivity models.

In the NGA-WEST2 project, the directivity models were included in GMPEs *ab initio* with the coefficients determined simultaneously with all other estimator coefficients of GMPE. The directivity predictors were centered on their average value. In addition, the NGA-WEST2 directivity models use distance metrics (rupture distance;  $R_{rup}$  and Joyner-Boore distances  $R_{jb}$ ) instead of normalized distance parameters, like the parameters used in Somerville et al. (1997). Rowshandel, Shahi and Baker, Spudich and Chiou and Chiou and Spudich directivity models of NGAWEST2 are explicitly “narrow-band” while the Bayless and Somerville model is classified as “broad-band”. The closest point concept (point on the fault plane closest to the site of interest) is used in all NGA-WEST2 directivity models except Shahi and Baker. However, the

main disadvantage of the closest point concept is that it results in large shifts in the location of closest point for small shifts in the site location. This is referred to as “discontinuity” by the model developers. The model proposed by Chiou and Spudich also uses a linear integration for the definition of “so-called” DPP parameter, which results in smoother maps of directivity compared to the IDP parameter of the Spudich and Chiou model. (These parameters are discussed in detail in the next section). It should be noted that the Shahi and Baker (2011) and Chiou and Spudich (2013) models, which have been used as the directivity predictor models in this study will be discussed in more detail in the next chapters.

### 2.2.1 *Somerville et. al (1997) and Abrahamson (2000) Directivity Models*

The model proposed by Somerville et al. (1997) is known as the first directivity model established under a physical model. This model uses two geometric parameters to incorporate directivity effects on the ground-motion equations. First, the angle between the direction of rupture propagation and the direction of waves traveling from the fault to the site, and second, the fraction of the fault rupture surface that lies between the hypocenter and the site (Figure 2.5). Somerville et al. (1997) modify the average horizontal acceleration response spectrum and the duration of acceleration time history to incorporate the directivity effect in ground motions. The model also proposes a spectral ratio of strike-normal to strike-parallel components for ground motions with directivity effect. Equation 2.1 shows the functional form of the directivity model for the average horizontal component used in Somerville et al. (1997) model.

$$\ln(y) = C_1(T) + C_2(T) \cdot X \cdot \cos(\theta) \quad \text{for strike slip faults} \quad 2.1a$$

$$\ln(y) = C_1(T) + C_2(T) \cdot Y \cdot \cos(\varphi) \quad \text{for dip slip faults} \quad 2.1b$$

This model was modified by Abrahamson (2000) in order to incorporate the effect magnitude and distance saturation in directivity model. Abrahamson (2000) has used Equation 2.2 as the functional form of base directivity model.

$$\ln(y) = C_1(T) + 1.88C_2(T) \cdot X \cdot \cos(\theta) \quad \text{for } \cos(\theta) \leq 0.4 \quad 2.2a$$

$$\ln(y) = C_1(T) + 1.88C_2(T) \cdot 0.4 \quad \text{for } \cos(\theta) > 0.4 \quad 2.2b$$

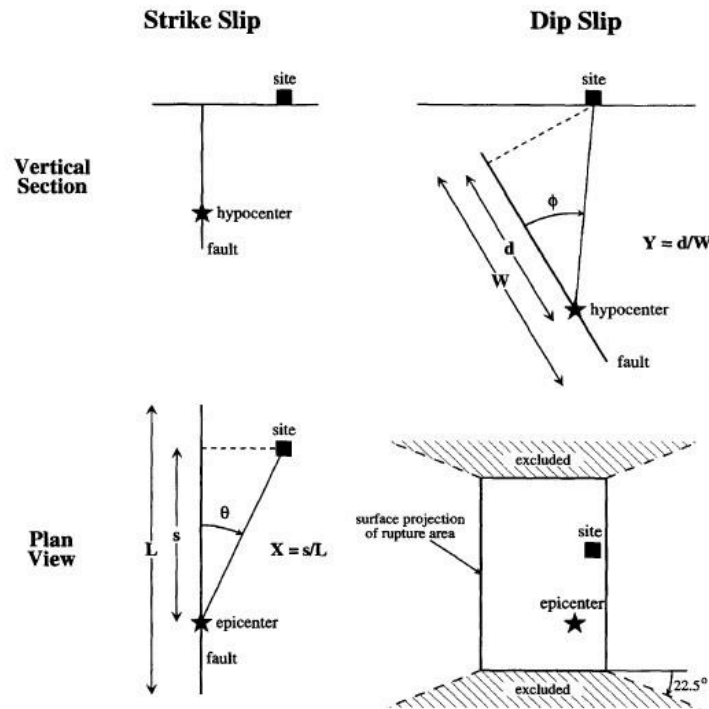


Figure 2.5 Geometric parameters used in Somerville (1997) directivity model.

Abrahamson (2000) used a cap of 0.4 for  $X\cos(\theta)$  for the model because his evaluations of empirical data did not show any evidence that  $X\cos(\theta)$  exceeds 0.4 for directivity-dominated ground motions. Abrahamson (2000) also used the distance and magnitude taper functions to reduce the directivity effect to zero for distances greater than 60km and magnitudes smaller than 6. The distance and magnitude taper functions are shown in Equations 2.3 and 2.4. The  $C_1(T)$  and  $C_2(T)$  coefficients used in this model are listed in Table 2.1.  $R_{rup}$  and  $M$  denote to rupture distance and moment magnitude respectively in Equations 2.3 and 2.4. Abrahamson (2000) showed that the implementation of this directivity model in GMPEs reduces the logarithmic standard deviation up to 0.05 at  $T=3\text{sec}$ .

$$\begin{aligned}
T_d(R_{rup}) &= 1 && \text{for } R_{rup} < 30\text{km} \\
T_d(R_{rup}) &= \frac{1-(r-30)}{30} && \text{for } 30\text{km} < R_{rup} < 60\text{km} \\
T_d(R_{rup}) &= 1 && \text{for } R_{rup} > 60\text{km}
\end{aligned} \tag{2.3}$$
  

$$\begin{aligned}
T_m(M) &= 1 && \text{for } M \geq 6.5 \\
T_m(M) &= \frac{1-(m-6.5)}{0.5} && \text{for } 6 < M \leq 6.5 \\
T_m(M) &= 0 && \text{for } M < 6.5
\end{aligned} \tag{2.4}$$

Table 2.1 Coefficients used in the modified Somerville et al. (1997) directivity model by Abrahamson (2000) for average horizontal spectral component

Period (sec)	C <sub>1</sub>	C <sub>2</sub>
<b>0.6</b>	0	0
<b>0.75</b>	-0.084	0.185
<b>1</b>	-0.192	0.423
<b>1.5</b>	-0.344	0.759
<b>2</b>	-0.452	0.998
<b>3</b>	-0.605	1.333
<b>4</b>	-0.713	1.571
<b>5</b>	-0.797	1.757

### 2.2.2 Bayless and Somerville (2013) Directivity Model (NGA-WEST2)

This model (explained in detail in Chapter 2 of Spudich et al., 2013) is basically an updated form of Somerville et al. (1997) directivity model. The functional form of the model for predicting the median spectral acceleration for directivity effect is shown in Equation 2.5:

$$\ln(Sa_{dir}) = \ln(Sa) + f_D \tag{2.5}$$

where  $f_D$  is the directivity parameter. The directivity parameter is a function of geometric directivity predictor, the distance, magnitude, and azimuth tapers, which are shown in Equation 2.6.

$$f_D = (C_0 + C_1 \cdot f_{geom}) \cdot T_{CD} \cdot T_{Mw} \cdot T_{AZ} \quad 2.6$$

where  $C_0$  and  $C_1$  are period, fault type and horizontal component dependent coefficients. Geometric directivity predictor ( $f_{geom}$ ) for strike-slip and dip-slip faults is shown in Equation 2.7.

$$f_{geom} = \ln(s) \cdot (0.5 \times \cos(2\theta) + 0.5) \quad \text{for strike slip faults} \quad 2.7a$$

$$f_{geom} = \ln(d) \cdot \cos\left(\frac{R_x}{W}\right) \quad \text{for dip slip faults} \quad 2.7b$$

where:

$s$  is the length of striking fault rupturing towards site,

$\theta$  is the angle between the direction of rupture propagation and the direction of waves traveling from fault to site,

$d$  is the length of dipping fault rupturing toward site,

$R_x$  is the horizontal distance from top edge of the rupture,

$W$  is the fault width (km),

$T_{CD}$  is distance taper function,

$T_{Mw}$  is magnitude taper function, and

$T_{AZ}$  is azimuth taper function.

The distance taper functions reduce the directivity effect from maximum to zero for  $0.5 < R_{rup}/L < 1.0$  and  $1.5 < R_{rup}/W < 2.0$  for strike-slip and dip-slip faulting mechanisms, respectively. The magnitude taper function also reduces the directivity effect from maximum to zero for  $6.5 > M_w > 5.0$  for both strike-slip and dip-slip faulting mechanisms. Azimuth taper function is only applied to dip-slip faulting mechanisms and it is in Equation 2.8.

$$T_{az}(Az) = 1 \quad \text{for strike slip faults} \quad 2.8a$$

$$T_{az}(Az) = \sin(|Az^2|) \quad \text{for dip slip faults} \quad 2.8b$$

where  $Az$  is the NGA source to site azimuth.

### 2.2.3 Rowshandel (2013) Directivity Model (NGA-WEST2)

This model (explained in detail in Chapter 3 of Spudich et al., 2013) keeps the directivity parameter  $\xi'$  developed in the previous directivity models of Rowshandel (2006) and Rowshandel (2010). Some modifications were applied to the previous predecessor models so that directivity parameter  $\xi'$  can be computed based on the direction of rupture or the direction of slip, or the combination. Also the centered value of directivity parameter ( $\xi$ ) is used in this model instead of  $\xi'$  as can be seen in Equation 2.9.

$$\xi = (\xi' - \xi'_c) \cdot LD \cdot DT \cdot WP \quad 2.9$$

where

$\xi'$  is the traditional wide-band directivity parameter before applying any corrections,

$LD$  is the rupture length de-normalization factor,

$\xi'_c$  is the directivity-centering parameter,

$DT$  is the distance-taper, and

$WP$  is the narrow-band multiplier.

Rowshandel (2013) defines the “rupture unit vector” (p) (along the vector connecting hypocenter and sub-fault i), “rupture-to-site unit vector” (q) (along the vector connecting the sub-fault i and site) and “unit slip vector” (s) (unit vector along the slip direction) geometric parameters in order to calculate the slip-based ( $\xi'_s$ ) and rupture-based ( $\xi'_p$ ) directivity parameters. The slip-based directivity parameter ( $\xi'_s$ ) is the scalar product of “unit slip vector” (s) and “rupture-to-site unit vector” (q) while the rupture-based directivity parameter ( $\xi'_p$ ) is the scalar product of “rupture unit vector” (p) and “rupture-to-site unit vector” (q). The directivity parameter ( $\xi'$ ) is taken as the weighted average of these two parameters as shown in Equation 2.10.

$$\xi' = a \cdot \xi'_s + (1 - a) \cdot \xi'_p \quad 2.10$$

where  $a$  and  $(1-a)$  are the relative weights contributing to the slip-based ( $\xi'_s$ ) and rupture-based ( $\xi'_p$ ) directivity parameters. Rupture length de-normalization factor is used in this model to ensure that the same directivity effect is obtained for the same

length of rupture. Rowshandel (2013) proposes a distance taper function for his model, which is dependent on the period of ground motion. A narrow-band multiplier is used in this model, which amplifies the directivity effect in the vicinity of pulse period with a normal distribution centered at  $T_p$ .

#### 2.2.4 *Shahi and Baker (2013) Directivity Model (NGA-WEST2)*

Shahi and Baker (2013) as a follow up of their research published in 2011 (i.e., Shahi and Baker, 2011), propose another narrow-band directivity model (Chapter 4 in Spudich et al., 2013) by refitting the Campbell and Bozorgnia (2008) functional form for with and without directivity effects. The model is represented in Equations 2.11 and 2.12.

$$\ln Sa_{i,j} = f(M_i, R_j, T, V_{S30}, \theta) + I_{directivity} \cdot \ln Amp(T, T_p) + \eta_i + \varepsilon_{i,j} \quad 2.11$$

$$\ln Amp(T, T_p) = b_0 \exp(b_1 \left( \ln \left( \frac{T}{T_p} \right) - b_2 \right)^2) \quad 2.12$$

The  $f(M_i, R_j, T, V_{S30}, \theta)$  is the base ground-motion model (functional form is inherited from CB08) fitted to NGA-West2 database for predicting the intensity of records without any pulse effect (designated as CBR by Shahi and Baker, 2013). The indices  $i$  and  $j$  refer to  $i^{\text{th}}$  earthquake and  $j^{\text{th}}$  station in Equation 2.11.  $\ln Amp(T, T_p)$  computes the amplification of  $\ln Sa$  at periods close to  $T_p$  due to presence of directivity pulse. Shahi (2013) computed  $b_0$ ,  $b_1$  and  $b_2$  by fitting CB08 functional form with this directivity model to NGA-West2 data (designated as CBSB by the proponents).  $I_{directivity}$  takes a value of unity upon the existence of pulslike waveforms. Otherwise, its value is zero.  $T_p$  and  $I_{directivity}$  are treated as random variables in SHB13 for use within a probabilistic framework.

#### 2.2.5 *Spudich and Chiou (2013) Directivity Model (NGA-WEST2)*

This model (explained in detail in Chapter 5 of Spudich et al., 2013) is an updated form of Spudich and Chiou (2008) which uses “*Isochrone Theory*” in order to characterize the directivity effect in GMPEs. The functional form of the directivity parameter is given in Equation 2.13.

$$\hat{f}_D(x) = f_r(R, R_1, R_2) \cdot b(M, T) \cdot (IDP(x) - \overline{IDP}(R)) \quad 2.13$$

where  $IDP$  is the isochrone directivity parameter and  $b(M, T)$  and  $q(M, T)$  are given in Equations 2.14 and 2.15 respectively.

$$b(M, T) = c_2 + c_3 \cdot \max(M - c_1, 0) \cdot \exp(q(M, T)) \quad 2.14$$

$$q(M, T) = -\frac{[\log_{10}(T) - (c_4 + c_5 \cdot M)]^2}{2g^2} \quad 2.15$$

$C_1, C_2, C_3, C_4, C_5$  and  $g$  are period-independent coefficients.  $f_r$  is the distance taper function which reduces the directivity effect from maximum to zero for  $40 < R_{rup} < 70$  km and  $x$  is the site location of interest. The model is narrow-band and the period that maximum amplification occurs is a function of earthquake magnitude. The centered value of Isochrone Directivity Parameter ( $IDP$ ) is used in the model in which  $\overline{IDP}(R)$  is the average value of the  $IDP$  over the footprint of constant  $R$ .

### 2.3 Consideration of Near-Fault Effects in Earthquake Design Codes

The discussions in the previous sections indicate that the seismic design spectrum needs to be updated to reflect the directivity effects. One important point that should be noted here is that the higher intensity of near-fault ground motions and consequently larger response spectrum amplitudes due to the close distance to the ruptured fault is different from the spectral amplifications that are imposed by directivity effects. Therefore, the effect of near-fault ground motions and forward-directivity effects should not be treated in the same way in design spectrum. In this section, a brief review about the approaches that are utilized to address the directivity effects on seismic design codes will be discussed.

UBC 97 is the first earthquake code that applies the distance and seismic activity dependent near-fault factors on the design response spectrum. The near-fault related provisions in UBC 97, in a way, aimed to minimize the near-fault originated damage risk experienced after the 1994 Northridge earthquake.

Design response spectrum of UBC 97 is represented by the seismic coefficients  $C_a$  and  $C_v$  together with spectral periods  $T_0$  and  $T_s$ . The code has four seismic zones that are represented by seismic zone factor  $Z$ . In addition, the code has defined three

seismic source types addressing high, medium and low seismicity. Seismic source types and their definitions are illustrated in Table 2.2.

Table 2.2 Seismic source type (from Table 16-U of UBC-97)

Seismic Source Type	Seismic Source Description	Seismic Source Definition	
		Maximum $M_w$	Slip Rate, SR (mm/year)
<b>A</b>	Faults that are capable of producing large magnitude events and that have a high rate of seismic activity	$M \geq 7.0$	$SR \geq 5$
<b>B</b>	All faults other than Types A and C	$M \geq 7.0$ $M < 7.0$ $M \geq 6.5$	$SR < 5$ $SR > 2$ $SR < 2$
<b>C</b>	Faults that are not capable of producing large magnitude earthquakes and that have a relatively low rate of seismic activity	$M \geq 7.0$	$SR \leq 2$

Near-fault effects are represented by the near source factors  $N_a$  and  $N_v$ .  $N_a$  represents the near-source effects for short period range (or acceleration controlled spectral region) and  $N_v$  represents the near-source effects for medium-to-long period range (or velocity controlled spectral region) of response spectrum. These factors are defined in terms of closest distance to the seismic sources as well as the seismic source type (depending on maximum moment magnitude,  $M_w$  and slip rate in mm/year). The factors are applied on the seismic coefficients  $C_a$  and  $C_v$  for the sites located in high seismicity regions (seismic zone 4). Near source coefficients,  $N_a$  and  $N_v$  are shown in Table 2.3 and Table 2.4. Figure 2.6 shows the design spectrum of UBC 97 calculated for seismic zone 4, soil type  $S_D$  and seismic source type A for closest distances 2, 5, 10 and 15km. The UBC97 equations that are used to calculate the response spectrum are also shown in Figure 2.6.

Table 2.3 Near source factor  $N_a$  (from Table 16-S from UBC-97)

Seismic source type	Closest distance to known seismic source		
	$\leq 2\text{km}$	5km	10km
A	1.5	1.2	1.0
B	1.3	1.0	1.0
C	1.0	1.0	1.0

Table 2.4 Near source factor  $N_v$  (from Table 16-T from UBC-97)

Seismic source type	Closest distance to known seismic source			
	$\leq 2\text{km}$	5km	10km	$\geq 15\text{km}$
A	2.0	1.6	1.2	1.0
B	1.6	1.2	1.0	1.0
C	1.0	1.0	1.0	1.0

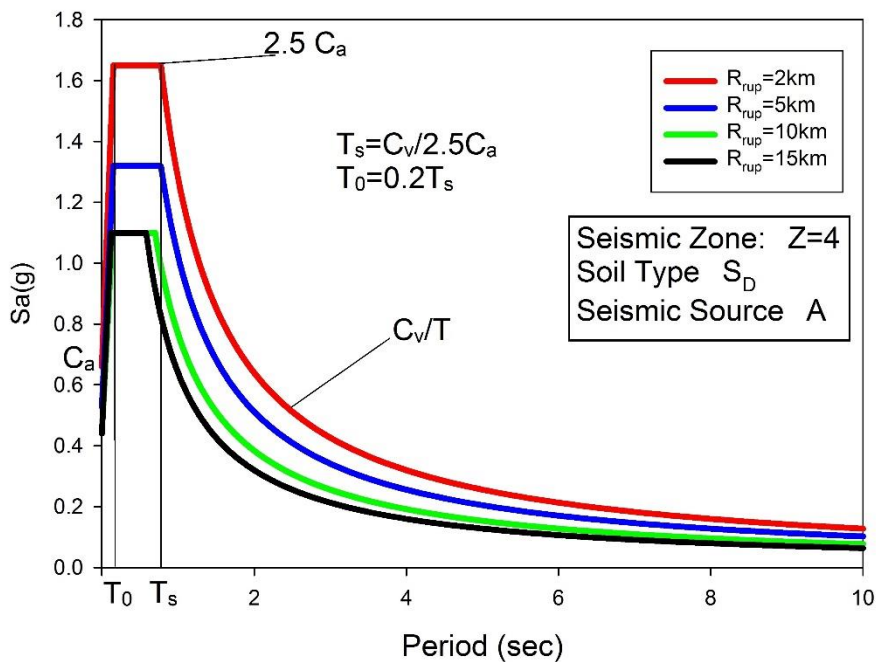


Figure 2.6 UBC 97 design spectrum calculated for seismic zone 4, soil type  $S_D$  and seismic source type A for closest distances 2, 5, 10 and 15km.

Chai et al. (2000) followed the same approach in UBC 97 to incorporate the near-fault effects in Taiwanese seismic design code. They used the data recorded from the Chi-Chi earthquake in CWB stations with source-to-site distances less than 15km from the Chelungpu Fault in order to update the near-fault factors proposed in UBC 97 for Taiwanese seismic design code. These coefficients are updated for rock site conditions (Type 1 soil profile) and the seismic zone A with zone factor  $Z=0.33$  according to Taiwanese seismic design code. The updated near-source factor  $N_A$  and  $N_v$  for Taiwanese seismic design code at rock sites near the Chelungpu Fault are given in Table 2.5 and Table 2.6.

Table 2.5 Near-Fault factor  $N_A$  for the sites near the Chelungpu Fault in Taiwanese seismic design code (Chai et al. 2000)

<b>Distance</b>	<b><math>\leq 2\text{km}</math></b>	<b>4km</b>	<b><math>\geq 6\text{km}</math></b>
<b><math>N_A</math></b>	1.34	1.16	1.0

Table 2.6 Near-Fault factor  $N_v$  for the sites near the Chelungpu Fault in Taiwanese seismic design code (Chai et al. 2000)

<b>Distance</b>	<b><math>\leq 2\text{km}</math></b>	<b>6km</b>	<b><math>\geq 10\text{km}</math></b>
<b><math>N_v</math></b>	1.7	1.3	1.0

Table 2.7 Proposed near-fault factors for Chinese Seismic Design Code in stiff soil site (Li et al. 2007)

<b>Intensity (Mercalli)</b>	<b>Distance (km)</b>	<b><math>N_a</math></b>	<b><math>N_v</math></b>
<b>VII</b>	<b>2</b>	1.0	1.7
	<b>15</b>	1.0	1.0
<b>VIII</b>	<b>2</b>	1.8	1.9
	<b>8</b>	-	1.0
	<b>15</b>	1.2	1.0
<b>IX</b>	<b>2</b>	1.2	1.8
	<b>6</b>	1.2	-
	<b>9</b>	-	1.6
	<b>15</b>	1.0	1.5

Li et al. (2007) used the data from 137 earthquakes from United States, Turkey, Japan, Taiwan and China that are recorded at distances less than 15km from the ruptured fault to update a ground-motion attenuation relationship. Subsequently they used this equation to calculate the near-fault factors for Chinese seismic design code. They also use the same concept of UBC 97 for the consideration of near-fault effects. The proposed coefficients for Chinese seismic design code at spectral periods of  $T=0.3s$  (short period) and  $T=1.0s$  (long period) are given in Table 2.7. These coefficients are given for stiff soil condition type.

Yaghmaei-Sabegh and Mohammad-Alizadeh (2012) used 143 near-fault records from 26 earthquakes from different parts of the world including United States, Iran, Japan, Turkey and Taiwan in order to update their ground-motion attenuation relationship for near-fault earthquakes. The near-fault factors in short and long periods ( $N_a$  and  $N_v$ ) are proposed for the highest seismicity zone in Iran (with an effective peak ground acceleration of 0.35g) and spectral periods  $T=0.3$  and 1.0sec respectively. These factors are given in Tables 2.9 and 2.10 for different soil types and magnitude ranges.

Table 2.8 Near-fault factors for Iranian seismic design code,  $M_w < 6.5$  (Yaghmaei-Sabegh and Mohammad-Alizadeh 2012)

Distance (km)		R<2			R=6		
Soil Type/ $M_w$		6.0	6.2	6.4	6.0	6.2	6.4
Na	I	1.0	1.0	1.0	1.0	1.0	1.0
	II	1.0	1.0	1.0	1.0	1.0	1.0
	III	1.0	1.0	1.05	1.0	1.0	1.0
	IV	1.0	1.0	1.0	1.0	1.0	1.0
Nv	I	1.0	1.0	1.1	1.0	1.0	1.0
	II	1.0	1.0	1.05	1.0	1.0	1.0
	III	1.0	1.05	1.1	1.0	1.0	1.0
	IV	1.0	1.1	1.1	1.0	1.0	1.0

Table 2.9 Near-fault factors for Iranian seismic design code,  $6.5 \leq M_w \leq 7.0$   
(Yaghmaei-Sabegh and Mohammad-Alizadeh 2012)

Distance (km)		R<2			R=6			R=12		
Soil Type/ $M_w$		6.6	6.8	7.0	6.6	6.8	7.0	6.6	6.8	7.0
Na	I	1.0	1.0	1.1	1.0	1.0	1.0	1.0	1.0	1.0
	II	1.0	1.1	1.15	1.0	1.0	1.0	1.0	1.0	1.0
	III	1.0	1.1	1.1	1.0	1.0	1.0	1.0	1.0	1.0
	IV	1.0	1.1	1.1	1.0	1.0	1.0	1.0	1.0	1.0
Nv	I	1.2	1.4	1.5	1.0	1.1	1.1	1.0	1.0	1.0
	II	1.25	1.35	1.5	1.0	1.15	1.2	1.0	1.0	1.0
	III	1.3	1.35	1.45	1.1	1.15	1.2	1.0	1.0	1.0
	IV	1.35	1.4	1.4	1.1	1.2	1.2	1.0	1.0	1.0

Table 2.10 Maximum near fault factor  $N_{max}(T)$  (New Zealand Standard, NZS 2004)

Period (sec)	$N_{max}(T)$
$\leq 1.5$	1.0
2.0	1.12
3.0	1.36
4.0	1.60
$\geq 5.0$	1.72

The New Zealand seismic design code (New Zealand Standard, NZS 2004) considers a uniform amplification of response spectrum for near-fault effects. The amplification factor,  $N(T,D)$  is function of spectral period, hazard level and distance. The amplification factor is calculated from Equations 2.16 and 2.17. The period dependent maximum near fault factor,  $N_{max}$  is given in Table 2.10.

- for annual probability of exceedance  $\geq 1/250$ :

$$N(T, D) = 1 \quad 2.16$$

- for annual probability of exceedance  $< 1/250$ :

$$N(T, D) = N_{max}(T) \quad D < 2\text{km} \quad 2.17a$$

$$N(T, D) = 1 + (N_{max}(T) - 1) \times \frac{20-D}{18} \quad 2\text{km} < D \leq 20\text{km} \quad 2.17b$$

$$N(T, D) = 1.0 \quad D > 20\text{km} \quad 2.17c$$

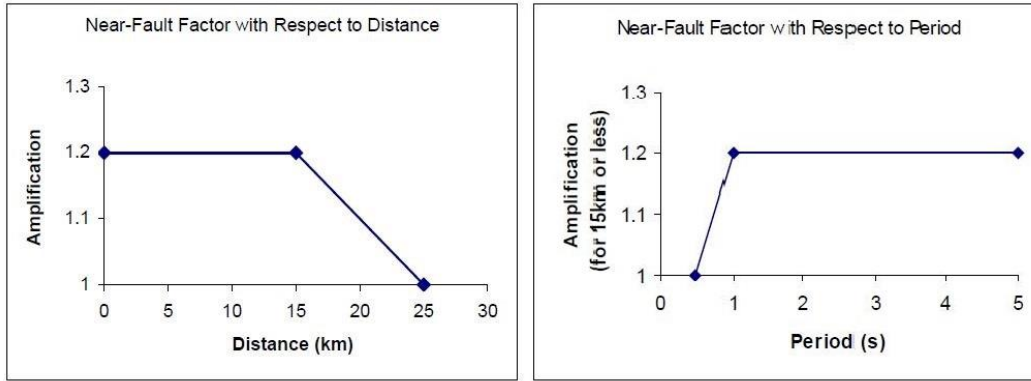


Figure 2.7 Near-Fault adjustment factor as a function of distance and spectral period (CALTRANS 2013).

The Caltrans seismic design criteria (CALTRANS, 2013) proposed by California Department of Transportation offers near-fault adjustment factors as a function of distance and spectral period. This seismic design code considers a maximum amplification factor equal to 1.2 for sites located within 15km around the fault. The amplification factor is applied for spectral ranges larger than 0.5s increasing from 1.0 for spectral period  $T=0.5\text{s}$  to 1.2 for spectral period  $T=1.0\text{sec}$ . The amplification factor given in CALTRANS (2013) is shown in Figure 2.7. The distance measure in this proposed factor is based on the closest distance to any point on the fault plane.

The most recent building and non-building seismic design codes in the U.S: ASCE 7-10 (ASCE, 2010) and FEMA P-750 (BSSC, 2009) as well as FEMA P-1090 (BSSC, 2015) use maximum direction of spectral acceleration (referred to as directionality – see following subsection) however they do not include near-fault effects explicitly. For the sake of completeness it should be noted that current version of Turkish Seismic Design Code (TEC 2007) does not apply any amplification on design response spectrum due to near fault effects.

As discussed in this section the near-fault effects are incorporated in seismic design codes via either a uniform scaling of a fixed spectral shape (UBC 1997; Taiwanese

seismic design code Chai et al. 2000) or a monotonic increase of amplitudes with magnitude (New Zealand Standard, NZS 2004). Both approaches are not entirely the correct way to consider the near-fault effects and they are not able to resolve the problem consistently, because design procedures should pay attention to the special distribution characteristics of near-fault ground motions around the seismic source (Alavi and Krawinkler 2004). In the following chapters, this study will provide some useful rules to surmount the current inconsistencies about the inclusion of directivity effects in seismic design codes.

#### **2.4 Directionality (Maximum Direction Component)**

In addition to directivity, another parameter of potential interest is ground motion directionality. When using a GMPE to predict a response spectrum parameter associated with horizontal shaking, the two-directions of horizontal components must be considered. The predicted ground motion parameters (e.g., spectral acceleration at a specified period, peak ground acceleration, or peak ground velocity) can be defined in a variety of ways with regard to multi-component horizontal shaking. Common methods that are used to quantify spectral acceleration from two horizontal components take the geometric mean of the spectral accelerations of the two as-recorded ground motion components. Different definitions of horizontal components of ground motions are proposed recently to take the maximum or the median spectral acceleration observed when looking over all horizontal orientations. Figure 2.8 shows the response spectrum of Gebze station-1999 Kocaeli earthquake. The response spectrum is calculated for different orientations of rotated ground motion ( $0 \leq \theta < 180$ ). For this purpose two horizontal components of the ground motion time series are combined into a single component which is  $\theta$  degree rotated from  $H_1$  component. The response spectrum is then computed for the rotated component and this calculation is repeated for all orientations ( $0 \leq \theta < 180$ ). The median value of all rotated response spectrum amplitudes at a specific spectral period is called as RotD50 and the maximum value is known as RotD100 component (Boore, 2010). These components are also shown in this figure together with geometric mean value of two horizontal as recorded components. This figure shows very clearly the effect of ground motion

orientation in variation of spectral amplitude. The issue of directionality is discussed with more detail in Chapter four.

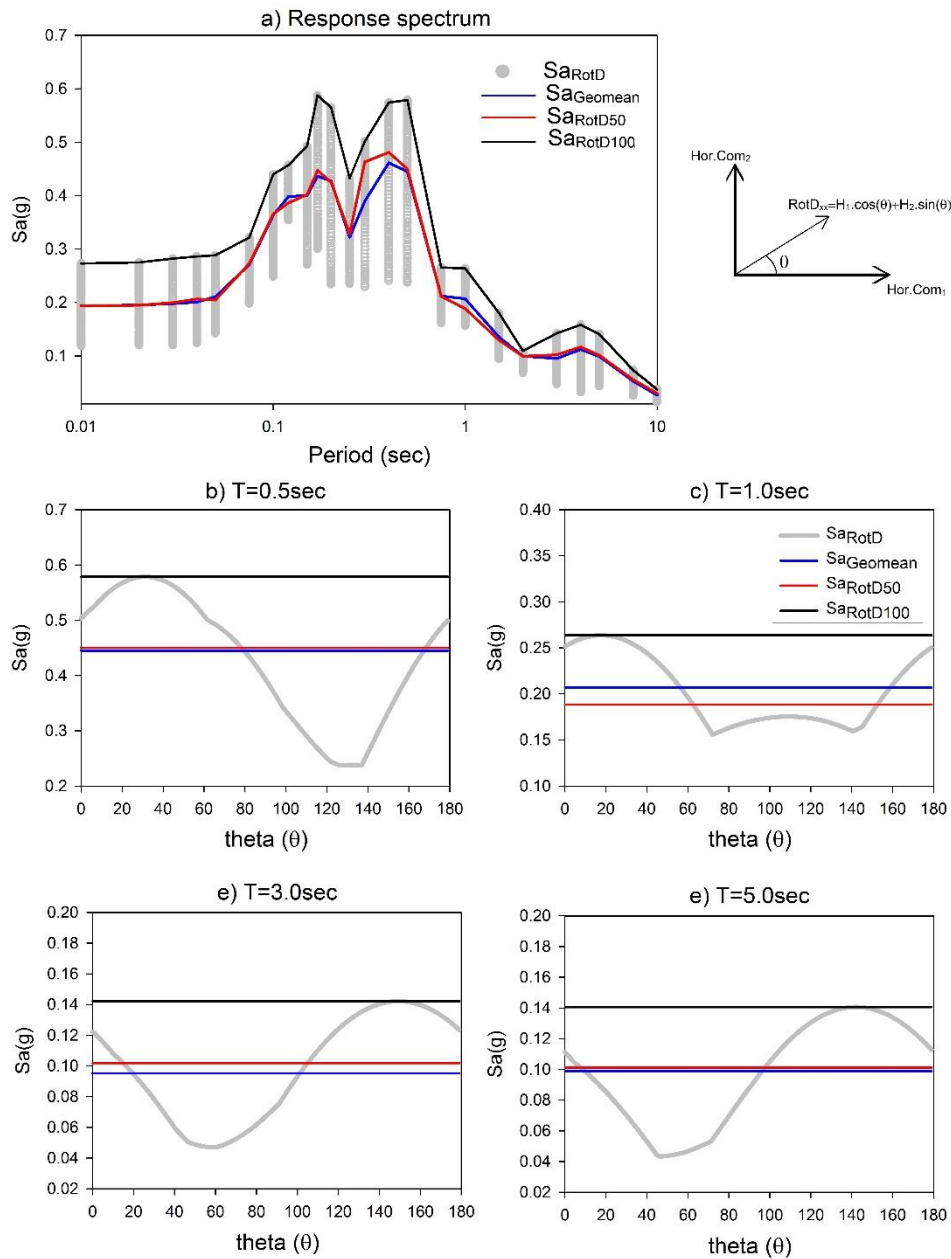


Figure 2.8 Response spectrum of Gebze station-1999 Kocaeli earthquake calculated for different rotated orientations of two horizontal components, together with geometric mean, RotD50 and RotD100 components illustrated for different spectral periods

## CHAPTER 3

### **A STUDY ON MAJOR SEISMOLOGICAL AND FAULT-SITE PARAMETERS AFFECTING NEAR-FAULT DIRECTIVITY GROUND- MOTION DEMANDS DUE TO STRIKE-SLIP FAULTING FOR THEIR POSSIBLE INCLUSION IN SEISMIC DESIGN CODES**

This chapter is submitted to the journal of Soil Dynamics and Earthquake Engineering with the title of  
A study on major seismological and fault-site parameters affecting near-fault directivity ground-motion demands due to strike-slip faulting for their possible inclusion in seismic design codes

Sinan Akkar, Saed Moghimi and Yalın Arıcı

Soil Dynamics and Earthquake Engineering, Ref: SOILDYN\_2017\_192

#### **3.1 Introduction**

When the horizontally polarized S-wave (SH-wave) radiation pattern aligns with the direction of rupture propagation and direction to the site, the ground motions are largest. This phenomenon is the major principle behind forward-directivity according to Somerville et al. (1997). The forward-directivity is more prominent within the ends of the strike-slip fault that suggests directivity being more significant when rupture travels longer distances (Spudich and Chiou 2008). The coincidence of the maximum SH-wave radiation pattern and the rupture propagation toward the site produces a large displacement pulse normal to the fault strike. The minimum in the radiation pattern of vertically polarized S-wave (SV-wave) that is in the direction of seismic wave propagation produces small dynamic displacements superimposed on a larger static displacement (fling step) parallel to the fault. Instead of large pulses, the waveforms are dominated by low-amplitude and long-duration motions when the

rupture propagates away from the site. This phenomenon is called as backward directivity and it is not within the scope of this chapter.

The near-fault forward-directivity (NFFD) ground motions have been recorded in many earthquakes during the past 50 years [e.g., Port Hueneme earthquake in 1957 (Housner and Hudson 1958); Parkfield earthquake in 1966 (Housner and Trifunac 1967); San Fernando earthquake in 1971 (Boore and Zoback 1974; Niazy 1975); Landers earthquake in 1992 (Campbell and Bozorgnia 1994); Northridge earthquake in 1994 (Somerville et al. 1996); Kobe earthquake in 1995 (Fukushima et al. 2000); Marmara earthquakes in 1999 (Akkar and Gulkan 2001); Chi-Chi earthquake in 1999 (Chen et al. 2001); L'Aquila earthquake in 2009 (Chioccarelli and Iervolino 2010); Christchurch earthquake in 2011 (Bradley and Cubrinovski 2011)]. Their distinct features in terms of dynamic source characteristics as well as the large-amplitude impulsive horizontal and vertical waveforms that increase the damage potential on structures have led to many seismological and engineering studies. Modelling of high-slip zones and directivity (e.g., Somerville et al. 1999; Mai et al. 2005; Seekins and Boatwright 2010; Spudich et al. 2004; Schmedes and Archuleta 2008), influence of fault mechanisms on directivity (e.g., Oglesby et al. 2000) and dynamic rupture modeling to characterize super shear zones (e.g., Dalguer and Day 2007; Dunham and Archuleta 2005) are among the topics investigated by the seismological community to explain the physics behind the directivity-dominant ground motions. Inherently, the engineering community is interested in the damaging effects of such ground motions on different structural systems (e.g., Bertero et al. 1978; Anderson and Naeim 1984; Anderson and Bertero 1987; Heaton et al. 1995; Sasani and Bertero 2000; Anderson et al. 2003; Alavi and Krawinkler 2004; Champion and Liel 2012). The variations in the elastic and inelastic horizontal spectral quantities under NFFD ground motions were investigated thoroughly (e.g., Malhotra 1999; Ambraseys and Douglas 2003; Mavroeidis et al. 2004; Menun and Fu 2002; Akkar et al. 2004; Bray and Rodriguez-Marek 2004; Tothong and Cornell 2006; Chioccarelli and Iervolino 2010; Rupakhety et al. 2011; Iervolino et al. 2012; Chiou and Youngs 2014). The engineering studies on the definition of the response spectrum for NFFD ground motions consider the pulse period ( $T_p$ ), the peak ground velocity to peak ground acceleration (PGV/PGA) and the peak ground displacement to peak ground velocity

(PGD/PGV) ratios as well as the pseudo-velocity spectrum (PSV) to account for the dominant impulsive signal effect on the spectral shape. Recently, there is an increasing effort to incorporate the directivity effects within the probabilistic seismic hazard and damage assessment procedures using linear and nonlinear structural response quantities (Tothong and Cornell 2006; Tothong and Cornell 2008; Tothong et al. 2007; Iervolino and Cornell 2008; Shahi and Baker 2011; Shahi 2013; Chioccarelli and Iervolino 2013; Chiou and Youngs 2014; Baltzopoulos et al. 2015; Baltzopoulos et al. 2016; Almufti et al. 2015).

One of the most important contributions on the modelling of forward-directivity is developed by Somerville et al. (1997). This model estimates the spectral amplifications along the strike-normal and strike-parallel components as well as their geometric average due to rupture directivity to modify the spectral ordinates predicted by conventional (no-directivity) ground-motion predictive models (GMPMs). The model estimations are valid for moment magnitudes  $M_w > 6.5$  with a dependence on normalized rupture to fault length and the angle between the rupture propagation direction and the site. The spectral amplifications by Somerville et al. (1997) increase monotonically after  $T = 0.6$ s. This type of forward-directivity model is referred to as the broad-band model in the literature. Later, Abrahamson (2000) proposed some modifications to the Somerville et al. (1997) directivity model for improving the limitations in directivity scaling of large magnitude events due to the use of normalized distance. The response spectrum amplifications due to directivity are investigated more systematically in the NGA-West1 (Power et al. 2008) and NGA-West2 (Bozorgnia et al. 2014) projects. The forward-directivity modelers in NGA-West1 (Spudich and Chiou 2008; Rowshandel 2010) propose corrections to the median predictions of the NGA-West1 no-directivity GMPMs. The implementation of these directivity models to the NGA-West1 GMPMs experienced conceptual difficulties because the median predictions of the no-directivity NGA-West1 GMPMs already include the NFFD ground motions in their datasets. Thus, the identification of reference directivity conditions corresponding to the median estimations of NGA-West1 GMPMs are unclear while implementing the corrections of the forward-directivity models. As a surrogate to this shortcoming, the NGA-West2 forward-directivity modelers (Bayless and Somerville, Rowshandel, Shahi and

Baker, Spudich and Chiou, and Chiou and Spudich – see Spudich et al. 2013) developed their models for their direct inclusion to the functional forms of the NGA-West2 GMPMs. Besides, the NGA-West2 directivity models utilize either the Joyner-Boore (RJB) or rupture (Rrup) distance in order to provide consistent scaling of forward-directivity for the entire magnitude range of interest (Spudich et al. 2014). The NGA-West2 directivity models by Rowshandel, Shahi and Baker, Spudich and Chiou, and Chiou and Spudich are defined as narrow-band models because the spectral ordinates are amplified only within a specific period interval that is sensitive to the magnitude. The Chiou and Spudich directivity model is adopted by the NGA-West2 Chiou and Youngs (2014) GMPM. The Shahi and Baker model is based on an older version of the directivity model proposed by the same authors (Shahi and Baker, 2011) that makes use of the Boore and Atkinson (2008) functional form from NGA-West1. The other directivity modelers published their functional forms and regression coefficients for their implementation to either the NGA-West1 or NGA-West2 GMPMs. Most of the NGA-West2 forward-directivity models suggest a maximum distance of 70km to 80km from the ruptured fault surface for the directivity effect. Although the NGA-West2 directivity models account for the sophisticated features of directivity phenomenon, there is still some room for their further improvement. For example, except for Rowshandel, no other model can clearly distinguish the directivity effects between the reverse and normal faults. However, Oglesby et al. (2000) have already shown the rupture-dynamic reasons for expecting larger amplitude near-fault motions from the reverse events rather than the normal ruptures. The wide range of studies on the NFFD ground motions are yet to show their full implications on the seismic design codes. To the best knowledge of the authors, the 1997 version of the Uniform Building Code (UBC, 1997) is the first seismic design code with a design spectrum explicitly accounting for the near-source effects. This code introduces two near-fault factors  $N_a$  and  $N_v$  to amplify the short-period and the long-period range in the design spectrum. Both  $N_a$  and  $N_v$  depend on the seismic activity of the fault and amplify the design spectrum for directivity effects for  $R_{rup} \leq 15\text{km}$ . The Taiwanese (Chai and Teng 2012; Chai et al. 2001), Chinese and Iranian (Yaghmaei-Sabegh and Mohammad-Alizadeh 2012) seismic design codes use the UBC-97 approach to include the forward-directivity effects on the definition

of design spectrum ordinates. The current seismic design code in China incorporates the near-source effects for base isolated structures with distance-dependent amplification factors. The New Zealand seismic code (New Zealand Standard, NZS 2004) includes the forward-directivity effects for distances up to 20km to the ruptured fault and spectral periods  $T \geq 1.5$ s provided that the spectrum's return period is 250-year or more. The Caltrans seismic design guidelines (CALTRANS 2013) amplify the design spectrum for  $T > 0.5$ s by a distance and period dependent near-fault adjustment factor. The adjustment factor increases spectral ordinates by 20% for  $R_{rup} \leq 15$ km and it linearly tapers to zero between rupture distances  $15\text{km} < R_{rup} \leq 25\text{km}$ . Caltrans (2013) states the validity of above amplifications for horizontal spectral ordinates having equal probability in all orientations [e.g., GMRotI50 or RotD501 horizontal component definitions as proposed in Boore et al. (2006) and Boore (2010) that are used by NGA-West1 and NGA-West2 GMPMs, respectively]. Upon the use of maximum direction (RotD100) horizontal spectral ordinates (Boore 2010) in which their occurrences are not equally probable in all orientations, Caltrans (2013) suggests an additional 15% to 25% spectral amplification over the previously suggested amplifications for a full coverage of NFFD effects. The suggested additional spectral amplifications are in line with the findings of Huang et al. (2008), Watson-Lamprey and Boore (2007) and Beyer and Bommer (2006) for  $R_{rup} \leq 5$ km. It should be noted that the 2009 edition of the NEHRP provisions (BSSC. 2009) as well as the 2010 edition of the ASCE 7-10 standards (ASCE7-10) have started to use the maximum direction component in the definition of horizontal design spectrum since the collapse probability would be reduced for structures designed against maximum direction spectral demands (BSSC, 2009). This horizontal component definition can also capture the strong polarization of directivity-dominant recordings (Boore 2006; Boore 2010).

This chapter investigates the influence of the magnitude, pulse period (or magnitude-dependent period band where the elastic response spectrum is amplified due to directivity), fault length, seismic activity, fault-site geometry, orientation of incident seismic wave with respect to fault-strike as well as the annual exceedance rate on the NFFD spectral amplitudes. A suite of strike-slip earthquake scenarios are generated via probabilistic seismic hazard assessment (PSHA) and implemented the narrow-

band directivity models of Shahi and Baker (SHB11; Shahi and Baker 2011) and Chiou and Spudich (CHS13; Chapter 6 in Spudich et al., 2013) that is adopted by the Chiou and Youngs (2014) GMPM to study the effects of the above mentioned parameters on NFFD. The use of multiple directivity models provided us an opportunity to understand the influence of different methodologies in estimating the directivity response spectral amplifications. The important features of the considered directivity models are explained at first. The discussion continues by presenting the spectral amplitude distributions conditioned on the investigated seismological and geometrical parameters to assess their significance in directivity-based spectral amplifications. The chapter is finalized by mapping the spatial influence of directivity for different probabilistic earthquake scenarios that could be of interest to the modern seismic design codes. The outcomes highlighted in the chapter provide a good ground for the robust implementation of directivity effects on the code-based design spectra.

## **3.2 Narrow-Band Forward-directivity Models**

The following subsections discuss the main features of SHB11 and CHS13 directivity models to highlight their underlying conceptual differences. The reader can refer to the relevant literature cited in this study to understand the details of each model.

### **3.2.1 *Shahi and Baker (2011) Model (SHB11)***

SHB11 establishes a probabilistic seismic hazard assessment model to consider the spectral amplitude modifications at sites subjected to pulselike waveforms due to directivity. The premise in SHB11 is that the directivity is the primary source for pulse dominated ground motions recorded at locations close to the ruptured fault. This probabilistic model follows the approach used in Tothong et al. (2007) and includes the probability of pulse occurrence for a given fault-site geometry as well as the probability of observing a pulse in a particular orientation given a pulse is observed at the site and the distribution of magnitude-dependent pulse period,  $T_p$ .

The proponents of SHB11 use the quantitative pulse classification algorithm by Baker (2007) that employs wavelet theory to extract the impulsive signal features from the ground velocity of near-fault recordings. Shahi and Baker (2011) rotated such ground motions in all possible directions and classified them as pulselike whenever any one

of the rotated components is dominated by an impulsive waveform according to the pulse indicator index<sup>1</sup> (Baker 2007). The period associated with the maximum Fourier amplitude of the extracted pulse was used as a measure of pulse-period,  $T_p$  in SHB11.

SHB11 estimates the amplification (and deamplification) of response spectrum ordinates for the existence (and absence) of pulse in near-source region. Equation 3.1 shows the conceptual approach behind SHB11 while calibrating ground-motion spectral amplitudes for directivity. Here,  $P^*(S_a > x | m, r, z)$  is the probability of spectral ordinate,  $S_a$ , exceeding  $x$  ( $S_a > x$ ) given the occurrence of an earthquake of magnitude  $m$  at distance  $r$  under modified GMPM.  $z$  represents fault-to-site geometry information that has an important impact on marking the directivity effects. It is comprised of the parameters  $s$  and  $\alpha$  where  $s$  is the distance along the rupture plane from the epicenter toward the site and  $\alpha$  is the smallest angle between incident S-wave and the fault strike. (See the illustrations in **Error! Reference source not found.**a as well as further discussions in the paragraph below for the parameters described here).

$$\begin{aligned}
 P^*(S_a > x | m, r, z) = & \\
 & P(\text{pulse} | m, r, z) \cdot P(S_a > x | m, r, z, \text{pulse}) + \\
 & [1 - P(\text{pulse} | m, r, z)] \cdot P(S_a > x | m, r, \text{no pulse})
 \end{aligned} \tag{3.1}$$

Equation 3.1 splits the probability of  $S_a > x$  into two cases depending on whether or not the pulselike ground motion is observed: the first two probabilities on the right hand side are probabilities of observing a pulse and  $S_a > x$  upon the occurrence of pulse. The last two probabilities consider observing no pulse and  $S_a > x$  when no pulse is observed. Thus, the modification of spectral intensities,  $S_a$ , depend on the pulse occurrence or non-occurrence cases.

The pulse occurrence is taken as the probability of observing a pulselike ground motion at a site in the direction  $\alpha$  degrees from the strike of the fault. The pulse occurrence, at any orientation with respect to fault strike, is a function of source-site

---

<sup>1</sup> Baker (2007) requires (a) pulse indicator index to be greater than 0.85, (b) impulsive signal occurring at the beginning of the ground-velocity waveform and (c) peak ground velocity being greater than 30 cm/s for a ground motion to be classified as directivity dominated.

geometry and SHB11 uses a logistic regression to model this probability (Equation 2). **Error! Reference source not found.** shows the contour map of the estimated pulse occurrence probabilities by Equation 3.2 for a rupture originating at the middle of fault segment. Note that the occurrence probability of the pulse increases towards the edges of the fault that is consistent with the basics of forward-directivity discussed in (Shahi and Baker 2011). SHB11 uses Equation 3.2 to estimate the probability of pulse at a given orientation  $\alpha$  with respect to fault strike. In essence, the product of Equations 3.2 and 3.3 gives the pulse occurrence probability for a given source-site geometry and orientation with respect to fault strike:  $P(\text{pulse} | m, r, z)$ . Inherently, the no-pulse occurrence case is  $1 - P(\text{pulse} | m, r, z)$  that is given in the last term on the right hand side of Equation 3.1.

$$P(\text{pulse}|r, s) = 1/[1 + e^{(0.642+0.167r-0.075s)}] \quad 3.2$$

$$P(\text{pulse at } \alpha|\text{pulse}) = \min[0.67, 0.67 - 0.0041(77.5 - \alpha)] \quad 3.3$$

The exceedance probability of  $S_a$  for *pulse observed* case (i.e.,  $P(S_a > x | m, r, z, \text{pulse})$ ) as well as its counterpart ( $S_a$  exceedance for “*no pulse observed*” case;  $P(S_a > x | m, r, \text{no pulse})$ ) are lognormal as given in Equations 3.4 and 3.5, which require the computation of  $\mu_{\ln S_a, \text{pulse}}$ ,  $\sigma_{\ln S_a, \text{pulse}}$ ,  $\mu_{\ln S_a, \text{no pulse}}$  and  $\sigma_{\ln S_a, \text{no pulse}}$ .

$$P(S_a > x | m, r, z, \text{pulse}) = 1 - \Phi\left(\frac{\ln(x) - \mu_{\ln S_a, \text{pulse}}}{\sigma_{\ln S_a, \text{pulse}}}\right) \quad 3.4$$

$$P(S_a > x | m, r, \text{no pulse}) = 1 - \Phi\left(\frac{\ln(x) - \mu_{\ln S_a, \text{no pulse}}}{\sigma_{\ln S_a, \text{no pulse}}}\right) \quad 3.5$$

Here,  $\mu$  and  $\sigma$  represent the mean and standard deviation of the logarithmic  $S_a$  values, respectively that are obtained from GMPMs. The “*pulse observed*” case represents the amplification of the spectral ordinates in the vicinity of  $T_p$  whereas the “*no pulse observed*” case accounts for the inherent reduction in the spectral ordinates for non-pulselike ground motions. These two phenomena cannot be mimicked properly by traditional (conventional) GMPMs because they do not model the distinctive effects of pulselike and non-pulselike ground motions separately. (They rather combine these two effects with tradeoffs depending on the distributions of their ground-motion datasets). The following lines summarize the rationale behind the development of these parameters for the “*pulse observed*” and “*no pulse observed*” cases.

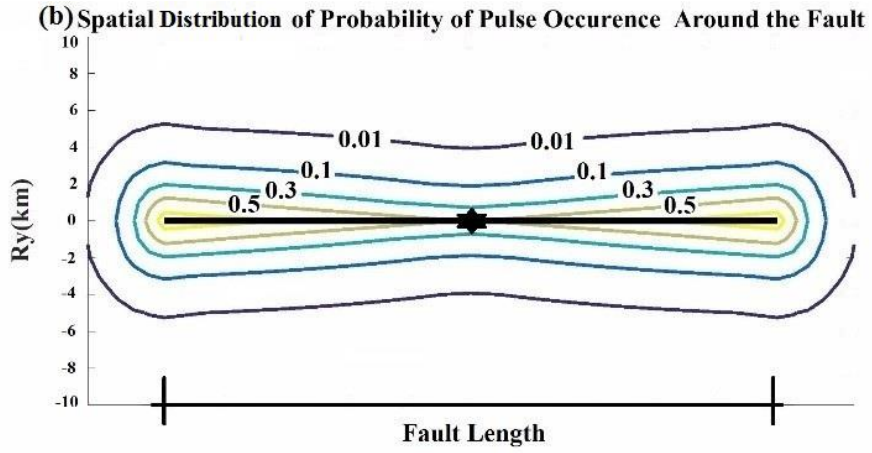
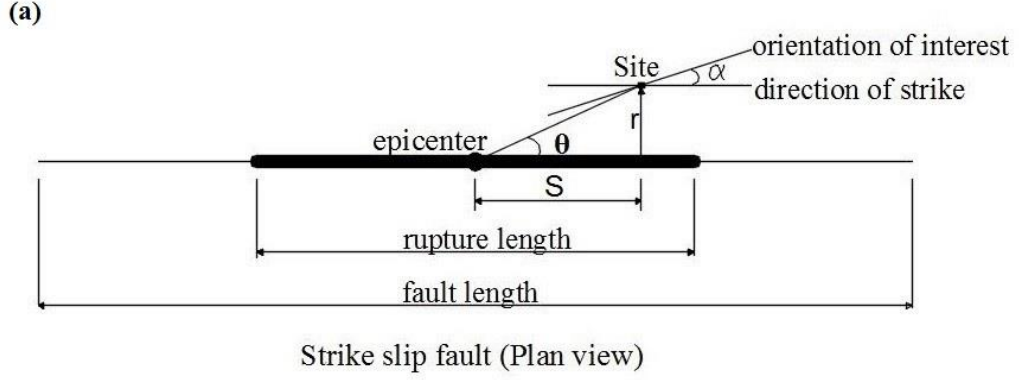


Figure 3.1 (a) the parameters defining fault-site geometry in SHB11 for a strike-slip fault (b) contours of pulse occurrence probability for a rupture nucleating at the center of the fault

According to SHB11,  $S_a$  only for pulselike motions ( $S_{a,pulse}$ ) can be represented by modifying their pulse-removed spectral ordinates ( $S_a'$ ) with an amplification factor ( $A_f$ ). Thus, the average of logarithmic spectral amplitudes only for pulselike motions ( $\mu_{lnS_{a,pulse}}$ ) is

$$\mu_{lnS_{a,pulse}} = \mu_{lnA_f} + \mu_{lnS_a'} \quad 3.6$$

The logarithmic average estimated from a conventional GMPM ( $\mu_{lnS_{a,gmm}}$ ) is assumed to approximate  $\mu_{lnS_a'}$  in Shahi and Baker (2011). Thus, Equation 3.6 simplifies to

$$\mu_{lnS_{a,pulse}} = \mu_{lnA_f} + \mu_{lnS_{a,gmm}} \quad 3.7$$

SHB11 reduces the standard deviation of the traditional GMPM ( $\sigma_{lnS_{a,gmm}}$ ) by a factor  $R_f$  to represent  $\sigma_{lnS_{a,pulse}}$  (Equation 3.8). This is because the modified ground-motion model in SHB11 only accounts for pulse-like ground motions that, presumably, yields lower aleatory variability than that of the traditional GMPM.

$$\sigma_{\ln S_{a,pulse}} = R_f \cdot \sigma_{\ln S_{a,gmm}} \quad 3.8$$

Following a similar approach as in the case of pulse-like ground motions, SHB11 applies a correction (deamplification,  $D_f$ ) factor to the logarithmic average of a traditional GMPM ( $\mu_{\ln S_{a,gmm}}$ ) to approximate the logarithmic average spectral ordinates ( $\mu_{\ln S_{a,nopulse}}$ ) of non-pulse-like ground motions (Equation 3.9).

$$\mu_{\ln S_{a,nopulse}} = \mu_{\ln D_f} + \mu_{\ln S_{a,gmm}} \quad 3.9$$

SHB11 does not foresee any modification for the standard deviation of the non-pulse-like ground motions ( $\sigma_{\ln S_{a,nopulse}}$ ) and uses the standard deviations reported by conventional GMPMs ( $\sigma_{\ln S_{a,gmm}}$ ). The empirical relationships for  $\mu_{\ln S_{a,pulse}}$ ,  $\sigma_{\ln S_{a,pulse}}$ ,  $\mu_{\ln S_{a,nopulse}}$  and  $\sigma_{\ln S_{a,nopulse}}$  as well as an algorithm for their implementation to PSHA are given in Shahi and Baker (2011). The authors calibrated their narrow-band model by using the conventional GMPM proposed by Boore and Atkinson (2008) indicating, however, that it can be equally applicable to other conventional GMPMs. Under the light of above discussions, the mean annual frequency by which  $S_a$  at the site subjected to directivity exceeds a value  $x$  is.

$$\begin{aligned} v_{S_a}(x) = & v \int_m \int_r \int_z P(pulse|m, r, z) \\ & \cdot \int_{t_p} P(S_a > x|m, r, z, t_p) \cdot f_{T_p|Z,M,R} \cdot f_{Z|M,R} \cdot f_{M,R} \cdot dm \\ & \cdot dr \cdot dz \cdot dt_p \\ & - \int_m \int_r \int_z P(S_a > x|m, r, no pulse) \\ & \cdot (1 - P(pulse|m, r, z)) \cdot f_{Z|M,R} \cdot f_{M,R} \cdot dm \cdot dr \cdot dz \end{aligned} \quad 3.10$$

In Equation 3.10  $v$  is the mean rate of occurrence of earthquakes on the fault above a minimum threshold. The capital letters denote random variables whereas the lowercase letters indicate realizations of these random variables.  $f_{T_p|Z,M,R}$ ,  $f_{Z|M,R}$  are joint probability density functions (PDFs) but the research showed that the pulse period  $T_p$  only depends on magnitude and the first PDF reduces to  $f_{T_p|M}$ . Upon the existence of multiple faults, Equation 3.10 should be calculated separately for each one and the summation of the resulting mean annual exceedance frequencies should

be used to obtain the total directivity induced seismic hazard. Figure 3.2 shows the algorithm used in the computation of  $v_{Sa}(x)$  by SHB11.

```

For a given period
Set  $\alpha$  ( $\alpha=90^\circ$  to represent strike normal component)
Set P=0
Compute minimum rate of occurrence ( $v_{min}$ ) from Equation 4.6 (McGuire 2004) [52]
for All magnitudes  $i$  ( $m_i$ )
  Compute P ( $M=m_i$ ) from characteristic recurrence model in [81]
  Compute mean rupture area (RA) from RA vs.  $M_w$  relationship in [79] ( $\log(ra_i)=-3.42+0.9 \times m_i$ )
  for all positions of rupture  $j$  ( $ra_{ij}$ )
    Compute geometric parameters ( $r_{ij}$  and  $z_{ij}$ ) -  $z_{ij}$  is source-to-site geometric parameters ( $r$  and  $s$ ) shown in Figure 1.a
    Compute P( $R=r_{ij}$ )
    Compute P( $Z=z_{ij}$ )
    Compute P(pulse |  $r_{ij}, z_{ij}$ ) from Equation (2)
    Compute P(pulse at  $\alpha=90^\circ$  | pulse) from Equation (3)
    P(pulse |  $m_i, r_{ij}, z_{ij}$ )=P(pulse |  $r_{ij}, z_{ij}$ ) $\times$ P(pulse at  $\alpha=90^\circ$  | pulse)
    Compute P ( $S_a > x$  |  $m_i, r_{ij}, z_{ij}$  no pulse) from Equation (5)
    Compute  $\mu_{lnTp,i}$  and  $\sigma_{lnTp,i}$  from:  $\mu_{lnTp}=-5.73+0.99 \times m$  and  $\sigma_{lnTp}=0.56$ 
    for all pulse period values  $k$  ( $T_{p,ik}$ )
      Compute P( $T_p=T_{p,ik}$ ) - given  $\mu_{lnTp,i}$  and  $\sigma_{lnTp,i}$  and considering lognormal distribution for pulse period
      Compute P ( $S_a > x$  |  $m_i, r_{ij}, z_{ij}$  pulse) from Equation (4)
      Compute P' ( $S_a > x$  |  $m_i, r_{ij}, z_{ij}$ ) from Equation (1)
      P=P+P( $M=m_i$ ) $\times$ P ( $r=r_{ij}$ ) $\times$  P ( $z=z_{ij}$ ) $\times$  P( $T_p=T_{p,ik}$ ) $\times$ P' ( $S_a > x$  |  $m_i, r_{ij}, z_{ij}$ )
    end
  end
end
 $v_{total}=v_{min} \times P$ 

```

Figure 3.2 Algorithm implemented to run PSHA with SHB11 directivity model  
Geometrical calculations and the algorithm utilized in PSHA are explained in Appendices A and B in more detail.

### 3.2.2 Chiou and Young-2014 (CHY-14) and Chiou and Spudich-2013 (CHS13) Directivity Model

Chiou and Spudich (Chapter 6 in Spudich et al., 2013) define Direct Point Parameter (*DPP*) as an alternative to Isochrone Directivity Parameter (*IDP*) (Spudich and Chiou, 2008; Chapter 5 of Spudich and Chiou in Spudich et al., 2013) to model directivity by considering the effects of the slip distribution and radiation pattern of a finite source as well as the isochrone velocity (a quantity closely related to rupture velocity – high isochrone velocity is an indication of strong directivity effects). Besides its stronger theoretical foundation, DPP is also advantageous from a calculation standpoint with respect to IDP (Chapter 6 in Spudich et al., 2013).

Figure 3.3 illustrates *DPP* on a simplified fault-site geometry. It is the intersecting point of the fault projected direct ray  $\overline{P_H P_P}$  with the slipped area boundary,  $\Gamma$ . Chiou and Spudich formulate *DPP* as given in Equation 3.11:

$$DPP = \ln(\hat{c}' \cdot \max(E, 0.1f) \cdot \max(\overline{FS}, 0.2)) \quad 3.11a$$

$$\hat{c}' = \frac{1}{\left(\frac{1}{0.8} - \frac{R_{HYP} - R_D}{E}\right)} \quad \text{for } E > 0 \quad 3.11b$$

$$\hat{c}' = 0.8 \quad \text{for } E = 0 \quad 3.11c$$

As one can infer from Equation 3.11a,  $DPP$  is the convolution of isochrone velocity ratio ( $\hat{c}'$ ), length of  $E$ -path ( $E$  or the larger of fault length or width,  $f$  see Figure 3.3a) that is closely associated with the highest isochrone velocity, hence an indicator of pulse dominance, and the average  $S$ -wave radiation pattern over  $E$ -path ( $\overline{FS}$ ). Equation 3.11b indicates that the isochrone velocity ratio is proportional to the difference between hypocentral distance,  $R_{Hyp}$  ( $\overline{P_H P_S}$ ) and the distance to the Direct Point,  $R_D$  ( $\overline{P_D P_S}$ ). The same expression also suggests an inverse relation between  $\hat{c}'$  and  $E$ . The physical interpretations of these observations advocate maximized directivity effects towards the edges of the faults where  $E$  is large and  $R_{Hyp} - R_D$  difference is small.

The GMPM by Chiou and Youngs (2014) (CY14) uses  $DPP$  as the predictor of forward-directivity effect. Equation 3.12 shows the directivity function used in CY14. Given an earthquake scenario, CY14 centers  $DPP$  on its mean ( $DPP_{mean}$ ) over a suite of sites located at the same distance (Figure 3.3b). The particular influence of forward-directivity at a specific site  $i$  along the same racetrack is determined by subtracting the  $DPP_{mean}$  from  $DPP_i$  ( $\Delta DPP$ ; Equation 3.12a). For a given site  $i$ , a large difference between the  $DPP_i$  and  $DPP_{mean}$  (i.e., large  $\Delta DPP$ ) indicates stronger forward-directivity effects in CY14. However, when  $\Delta DPP$  is zero, one can infer that the directivity does not dominate the spectral amplitudes at the site of interest for CY14.

$$f_{DPP} = c_8 \cdot f_R \cdot f_M \cdot e^{-c_{8a}(M - c_{8b})^2} \cdot \Delta DPP; \Delta DPP = DPP_i - \overline{DPP} \quad 3.12a$$

$$f_R = \max\left[0, 1 - \frac{\max(R_{rup} - 40)}{30}\right] \quad 3.12b$$

$$f_M = \max\left[1, \frac{\max(M - 5.5, 0)}{0.8}\right] \quad 3.12c$$

In the above expressions,  $f_R$  and  $f_M$  are the taper functions for the distance and magnitude, respectively.  $f_M$  reduces  $f_{DPP}$  to zero over the magnitude range from  $M_w$

6.3 to 5.5. The distance taper function  $f_R$  does not reduce  $f_{DPP}$  for  $R_{rup} \leq 40\text{km}$  but  $f_{DPP}$  is linearly tapered down to zero starting from 40km to 70km. In Equation 3.12a  $c_8$ ,  $c_{8a}$  and  $c_{8b}$  are the regression coefficients computed by CY14. CHS13 is used via CY14 in this study but continue to refer this compound model as CHS13 in this chapter. Figure 3.4 presents the simplified algorithm used for the implementation of CHS13 in PSHA.

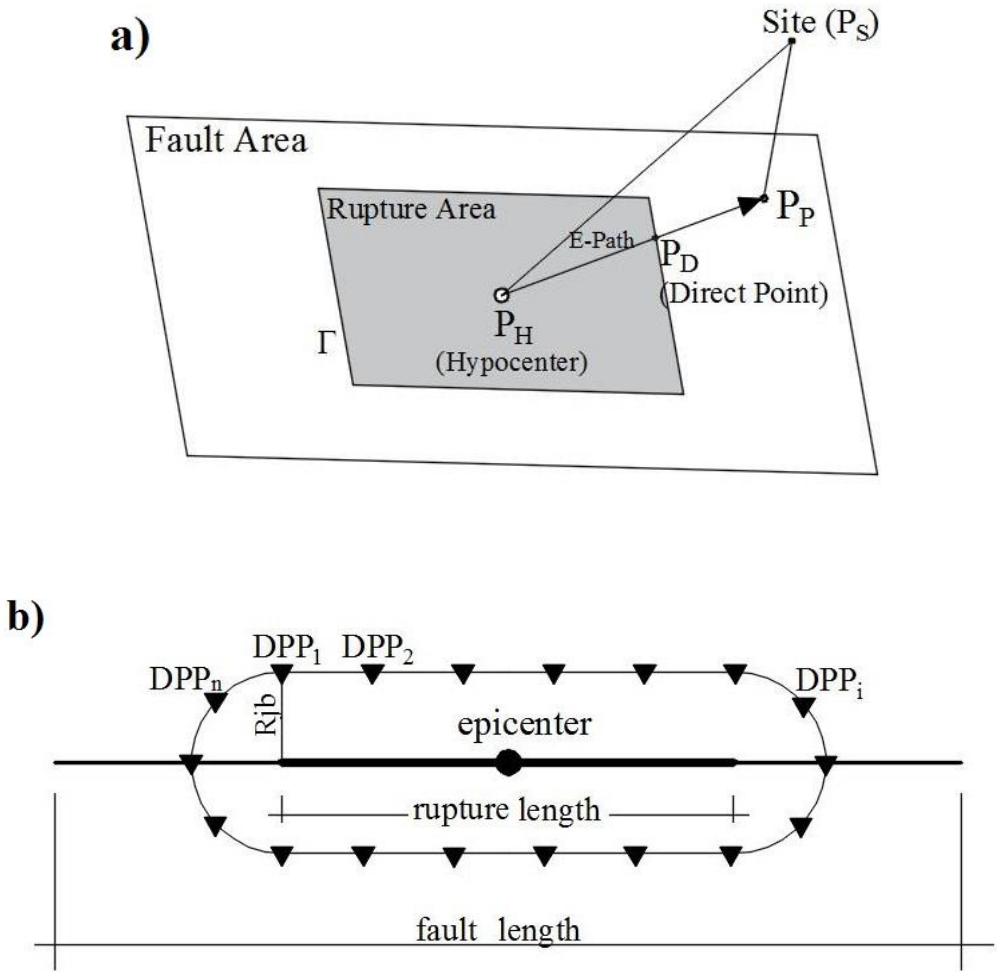


Figure 3.3 a) Illustration of Direct Point Parameter ( $DPP$ ) from a fictitious source-site geometry:  $\overline{P_H P_D}$  is the E-path with length  $E$  and  $P_D$  is the direct point, b) Sites along the same racetrack and the computed  $DPP_i$  ( $i = 1$  to  $n$ )

```

T=Period of interest
Set P=0
Compute minimum rate of occurrence ( $v_{min}$ ) from Equation 4.6 (McGuire 2004) [52]
for All magnitudes  $i$  ( $m_i$ )
  Compute  $P(M=m_i)$  from characteristic recurrence model in [81]
  Compute mean rupture area (RA) from RA vs.  $M_w$  relationship in [79] ( $\log(ra_i)=-3.42 + 0.9 \times m_i$ )
  for all positions of rupture  $j$  ( $ra_{ij}$ )
    Compute geometric parameters ( $r_{i,j}$ )
    Compute  $P(R=r_{i,j})$ 
    Compute  $f_{DPP}$  from Equations (11) and (12)
    Compute  $P(S_a > x | m_i, r_{i,j}, f_{DPP})$ 
   $P = P + P(M=m_i) \times P(R=r_{i,j}) \times P(S_a > x | m_i, r_{i,j}, f_{DPP})$ 
end
end
 $v_{total} = v_{min} \times P$ 

```

Figure 3.4 Algorithm implemented to run PSHA with SHB11 directivity model

### 3.2.3 Specific Comparisons Between SHB11, CHS13

This section compares the two directivity models introduced in the previous section using some PSHA case studies to have insight about their prominent features. The comparisons would help the reader to follow the discussions in the next section that examines the sensitivity of response spectrum amplifications against the chosen seismological parameters under directivity dominant hazard scenarios.

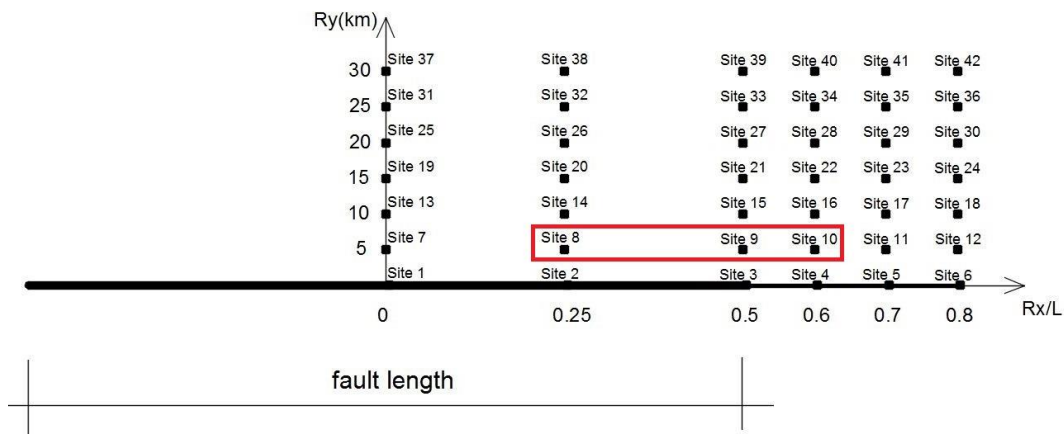


Figure 3.5 Plan view of fault-site configuration used in this study. (The red rectangle encloses the sites 8, 9 and 10 that are used in the deterministic scenario)

The discussions in this section as well as the subsequent sections make use of the fault-site geometry layout given in Figure 3.5. The site distributions are symmetric with respect to vertical axis ( $R_y$ ) that crosses at the mid-length of the fault. Thus, there is a mirror image distribution of the sites on the left-hand side with respect to the fault

center (designated by  $R_x/L = 0$  in Figure 3.5). The fault length normalized horizontal axis ( $R_x/L$ ) runs parallel to the fault strike. The sites are located at every 5km in the strike-normal direction whereas their distribution is extended beyond the fault edges by  $0.3L$  in the strike parallel direction to capture the spatial variation in forward-directivity along the horizontal plane. Strike-slip fault mechanism is considered in earthquake scenarios because directivity models cannot fully capture the directivity effects for dip-slip faulting mechanisms (Spudich et al. 2013). The site condition is also represented by a generic rock site of  $V_{S30} = 760\text{m/s}$  throughout the study.

Figure 3.6 compares the 2475-year return period<sup>2</sup> spectral estimates by SHB11 and CHS13 (top row) and corresponding spectral amplifications (bottom row) at sites 8, 9 and 10 (enclosed by a red rectangle in Figure 3.5) for a vertically dipping strike-slip fault segment of length  $L = 150\text{km}$  and width  $w = 10\text{km}$ . The slip rate of the fictitious fault is chosen as  $\dot{s} = 1\text{cm/yr}$  and the mean magnitude vs. ruptured area (RA) relationship by Wells and Coppersmith (1994) yields characteristic magnitude of  $M_{ch} 7.2$  for this fault when the entire segment is ruptured. (Side note: The mean moment magnitude,  $M_w$ , that is estimated from the empirical  $M_w$  vs. RA relationship of Wells and Coppersmith is used in the  $M_{ch}$  computations of fault segments considered in the probabilistic earthquake scenarios in this study). The Youngs and Coppersmith (1985) characteristic earthquake recurrence model is used in this case study as well as in all PSHA runs to define the temporal distribution of earthquakes. The characteristic model is illustrated in Figure 3.7 for convenience. The exponential part of the model considers earthquake activities between  $5.0 \leq M_w \leq M_{ch} - 0.25$ . The uncertainty in characteristic earthquake magnitudes is represented as a uniform distribution within  $M_{ch} \pm 0.25$  in the earthquake recurrence model. These specific features of the stochastic earthquake recurrence model are the same in all probabilistic earthquake scenarios. The discrete magnitudes varying from  $M_w 5$  to  $M_{ch} + 0.25$  (dependent of fault length) and the corresponding mean rupture areas obtained from RA vs.  $M_w$  relationships of Wells and Coppersmith (1994) are used in the PSHA runs presented in this section as well as those discussed in the other sections (See Figure 3.2 and Figure 3.4 for the PSHA algorithms).

---

<sup>2</sup> Return period is the reciprocal of mean annual exceedance rate of a spectral ordinate exceeding a specific threshold.

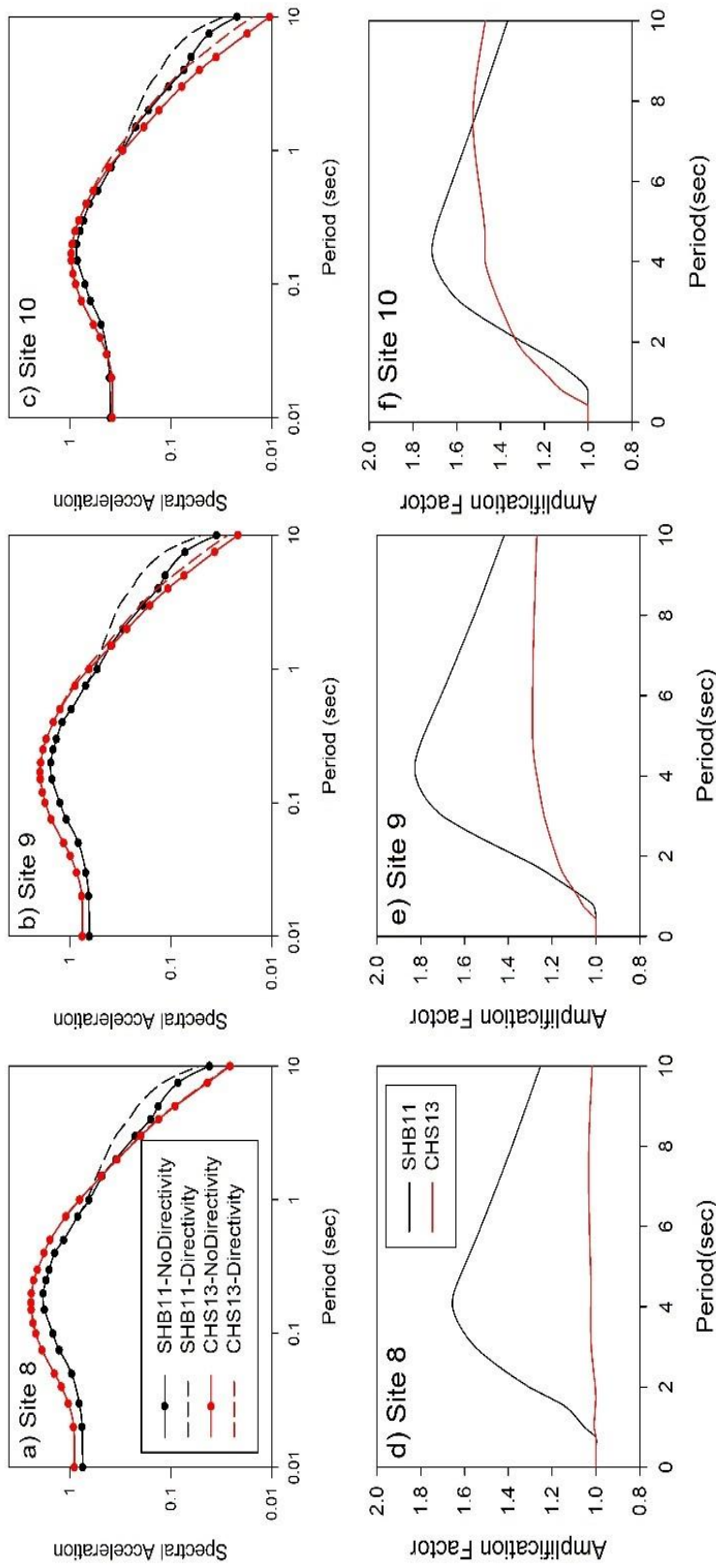


Figure 3.6 Comparison of the SHB11 and CHS13 directivity models at the sites 8, 9 and 10 (Figure 3.5) for 2475-year return period  $S_a$  for a fault of  $L = 150\text{km}$  and a slip rate of  $\dot{s} = 1\text{ cm/year}$ .

Rupture lengths of discrete scenarios in PSHA are determined by dividing the mean rupture areas with the constant fault width ( $w=10\text{km}$ ) whenever  $\sqrt{RA} > w$ . For  $\sqrt{RA} < w$ , rupture length is computed as  $\sqrt{RA}$  in this study. The hypocenter of the rupture is taken at the center of the ruptured area. This information is necessary in the computation of  $\Delta PP$  at the sites of interest. For completeness, the “*directivity*” and “*no directivity*” spectra are both plotted. The latter case is represented by the conventional GMPM counterpart of each directivity model (i.e., BA08 for SHB11 and CY14 with  $\Delta PP = 0$  for CHS13). The spectral amplifications are the normalized plots of “*directivity*” and “*no directivity*” cases. The magnitude-dependent pulse period for SHB11 is estimated from the  $T_p$ - $M_w$  expression in Shahi (2013). SHB11 estimates strike-normal (fault-normal; FN  $\alpha = 90^\circ$ ) horizontal spectrum for the “*directivity*” case because the model first fits to strike-normal case and then modifies the amplitudes for different  $\alpha$  according to pulse occurrence conditioned on  $\alpha$ . Thus, the spectral amplifications of SHB11 represent strike-normal to GMRotI50 (Boore et al. 2006) horizontal component ratios; the latter component definition is used by BA08. The other model uses RotD50 (Boore 2010) horizontal component definition for both the “*directivity*” and “*no directivity*” cases.

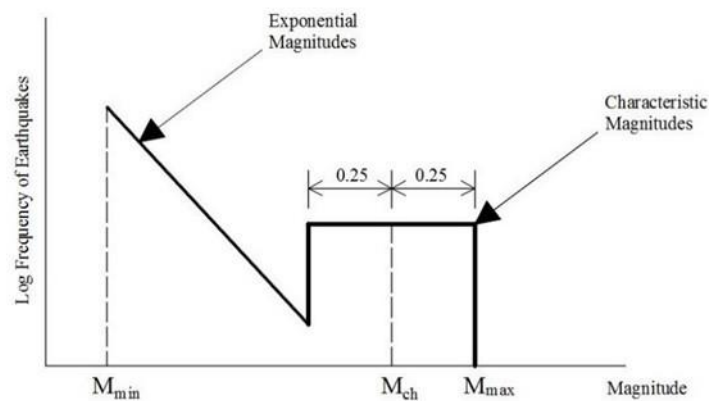


Figure 3.7 The Youngs and Coppersmith (1985) stochastic model to describe the earthquake recurrence in PSHA runs. The minimum magnitude,  $M_{\min}$ , is always considered as  $M_w$  5 in the probabilistic earthquake scenarios. The characteristic magnitude,  $M_{\text{ch}}$ , is determined from the mean  $M_w$  estimated from the empirical  $M_w$  vs. RA relationship in (Wells and Coppersmith 1994).

The comparative plots in Figure 3.6 indicate similar spectra for the “*no directivity*” case. The observed discrepancies are within tolerable ranges and can be the attributes

of different modeling perspectives. The observed similarity in the spectral estimates of “no directivity” can be explained by previous research (e.g., Abrahamson et al. 2008; Gregor et al. 2014) that advocate similar trends in conventional GMPMs provided that the hazard is dominated by large magnitudes. The negligible difference between GMRotI50 and RotD50 horizontal component definitions (Boore 2010) is the other supporting factor for the similar spectra in the “no directivity” case. The spectral amplitudes as well as the spectral amplifications by SHB11 is larger with respect to CHS13, which can be attributed to the fault-normal spectral amplitude estimations of this model. In fact, Figure 3.8 shows the variation of forward-directivity spectral amplifications for different pulse orientation angles ( $0^\circ \leq \alpha \leq 90^\circ$ ; see **Error! Reference source not found.**) at Site 9 by SHB11. Figure 3.8 indicates that the difference in forward-directivity spectral amplitudes can reach up to 50% to 60% between the strike-parallel ( $\alpha = 0^\circ$ ) and strike-normal ( $\alpha = 90^\circ$ ) pulse orientation. This observation brings forward the importance of horizontal component definition while addressing the directivity effects on the spectral amplitudes. This issue is partially addressed by Huang et al. (2008).

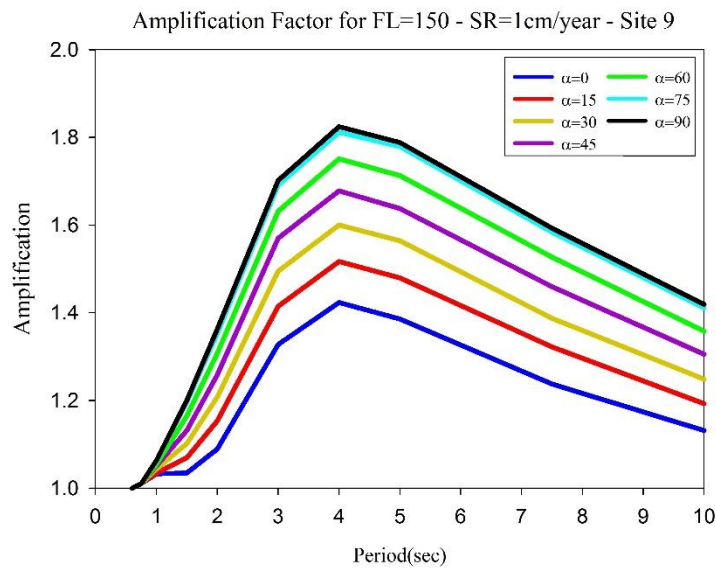


Figure 3.8 Variation of forward-directivity spectral amplifications as a function of  $\alpha$  (alpha) at Site 9 for the fictitious PSHA scenario considered in Figure 3.6.

Figure 3.6 also indicates that SHB11 reaches its maximum at  $T \sim 4.0$ s that is close to the median  $T_p$  for a characteristic earthquake of  $M_w$  7.2 (Shahi and Baker 2011; Shahi 2013). (This period is called as  $T_{max}$  throughout the text because  $T_p$  is a log-normally

distributed random variable in the PSHA runs that use SHB11 directivity model - Figure 3.2). The spectral amplification factors estimated by SHB11 are less sensitive to the fault-site geometry with respect to CHS13 because the variation of amplifications from one site to the other are not as significant as in the case of CHS13 (bottom row panels in Figure 3.6). CHS13 does not estimate any spectral amplification due to directivity at site 8 because  $\Delta PP = 0$ . The directivity amplifications by CHS13 are quite prominent at Site 10 that is slightly beyond the fault's right end whereas SHB11 estimates maximum directivity amplifications at Site 9 that is located at the right end of the subject fault. Previous studies (Schmedes and Archuleta 2008; Spudich and Chiou 2008) showed that the maximum directivity amplifications occur within the ends of the fault due to stronger directivity as the distance the rupture travels is longer. Thus, the observed spectral amplification estimates by CHS13 as well as SHB11 are consistent and they display physically justifiable patterns. Nevertheless the conceptual differences in the model development phase between SHB11 and CHS13 are reflected on to the observed discrepancies in the directivity amplification. It should be noted that the directivity model proposed by Shahi and Baker accounts for the fault-site geometry in the probabilistic framework by increasing the likelihood of observing pulse occurrence towards the ends of the faults (e.g., **Error! Reference source not found.** depicting pulse occurrence probability contours of SHB11 for different fault-site locations). CHS13, on the other hand, relies on  $\Delta PP$  that is based on the wave propagation theory while addressing the directivity for different fault-site patterns. Figure 3.9 further discusses this specific issue (pulse occurrence conditioned on fault-site geometry) to highlight the overall picture of modeling perspectives between SHB11 and CHS13. Another important observation from Figure 3.6 is the different spectral amplification trends between CHS13 and SHB11. Spectral amplifications by CHS13 tend to increase for periods up to  $T \sim 4$ sec displaying a more stable pattern after this spectral period. SHB11 becomes maximum in the vicinity of the same spectral period and then decreases for longer periods.  $T \sim 4$ sec is close to the median pulse period ( $T_p$ ) for a characteristic earthquake of  $M_{ch} 7.2$  according to the empirical magnitude vs. pulse period expressions by Shahi (2013) or Shahi and Baker (2011).  $T_p$  is considered as log-normally distributed in the PSHA runs (Figure 3.2) per recommendations in

Shahi (2013) and  $T_{max} \approx T_p$  for the given case study suggests that median  $T_p$  can grossly describe the locus of maximum spectral amplification due to directivity for return periods about 2475-year. Although CHS13 does not explicitly predict the pulse occurrence, the isochrones theory employed by this model is consistent with pulse period scaling with magnitude. That's why spectral amplifications by CHS13 show an increasing trend at periods close to  $T_p$ . They maintain a more stable trend for  $T > T_p$  as the model is not devised for the sole amplification of spectral ordinates in the vicinity of  $T_p$ . To distinguish the different theoretical backgrounds employed by CHS13 and SHB11 in this aspect, the spectral period at which the directivity-dominant spectral amplification is maximized is called as  $T_{corner}$  in CHS13.

Figure 3.9 compares the 475-year return period spectral amplification contours of SHB11 and CHS13 to illustrate an overall picture about how the directivity effects are interpreted by these models in the probabilistic seismic hazard context. The illustrations are particularly useful to understand the consideration of fault-site geometry by SHB11 and CHS13 while addressing the directivity influence on spectral amplitudes. The spectral amplifications are computed for  $T = 4$ sec. The fictitious fault segment is a  $90^\circ$  dipping strike-slip fault of  $L = 100$ km with a slip rate ( $\dot{s}$ ) equal to 2cm/year. The spectral amplification contours of SHB11 (Figure 3.9a) are larger than those of CHS13 (Figure 3.9b) because  $\alpha = 90^\circ$  is used in SHB11 to estimate FN spectral amplitudes as discussed in the previous paragraphs. Both models tend to estimate the largest directivity amplifications close to the ends of the fault whereas no amplification is computed by the two models at the center of the fault. This is consistent with the Somerville et al. (1997) model. The directivity amplifications of CHS13 are exclusively concentrated at the ends of the fault and they extend beyond the fault edges. This is inherited from the isochrone theory as explained while discussing the case study in Figure 3.6 as well as the theoretical background of this model. The directivity amplifications by SHB11 are shaped by the consideration of pulse occurrence probability that systematically increases towards the ends of the fault (e.g., **Error! Reference source not found.**). Otherwise, SHB11 would not change the spectral amplifications at equidistant sites from the fault strike. Note that SHB11 directivity amplifications significantly decrease for  $R_x/L > 0.6$ , which is, again, due to the decreased probability of observing pulse occurrence at sites

located slightly remote from the far ends of the fault segment. Such modeling constraints do not exist in CHS13.

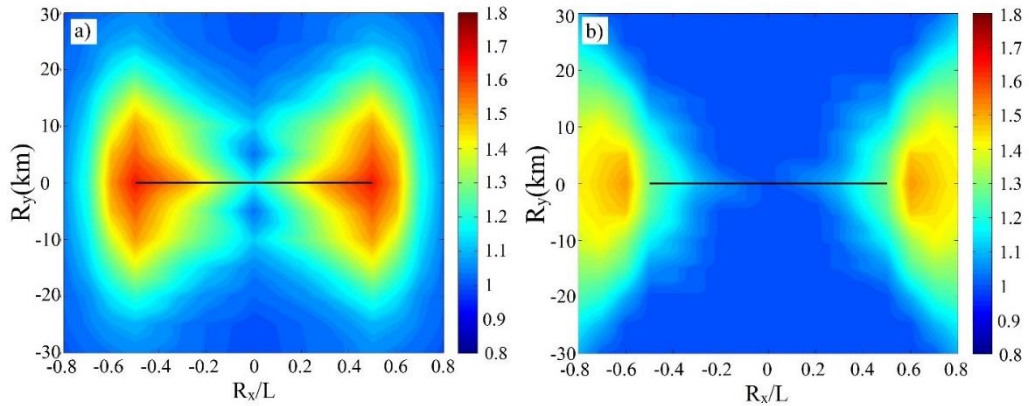


Figure 3.9 475-year probabilistic spectral amplifications for forward-directivity computed by (a) SHB11 and (b) CHS13 (via CY14) for a fault length of  $L = 100\text{km}$  and  $\dot{s} = 2\text{cm/year}$

Discussions on the probabilistic scenarios in Figure 3.6 and Figure 3.9 indicate that different narrow-band models impose different trends to describe directivity effects on spectral amplitudes because their theoretical backgrounds differ. SHB11 opts to modify traditional GMPMs for directivity effects in the vicinity of pulse period and they consider pulse occurrence probability to emphasize the fault-site geometry in directivity-dominant spectral amplifications. CHS13 applies isochrone theory to measure the directivity-induced amplification of an S-wave to model forward-directivity effects. Thus, CHS13 combines source kinematics as well as the rupture dynamics together with the empirical data to explain forward-directivity spectral amplitudes whereas the models by Shahi and Baker structure the directivity effects using a probabilistic platform from empirical observations. The next section discusses the overall roles of some important seismological and geometrical parameters in directivity dominated spectral ordinates through the modeling perspectives of SHB11 and CHS13.

### 3.3 Significance of Major Seismological Parameters in NFFD Spectral Amplitudes

The site configuration for the probabilistic scenarios are already given in Figure 3.5. Five different fault lengths ( $L = 20\text{km}, 50\text{km}, 100\text{km}, 150\text{km}$  and  $300\text{km}$ ) are utilized that are capable of generating characteristic earthquakes with characteristic

magnitudes ( $M_{ch}$ ) of  $M_w$  6.25, 6.7, 7.0, 7.2 and 7.5, respectively under full rupture conditions according to Wells and Coppersmith (1994)  $M_w$  vs. rupture area ( $A_{rup}$ ) relations. The seismogenic fault width is assumed 10km in all cases. Three different slip rates of  $\dot{s}_{total} = 0.5\text{cm/year}$ ,  $1.0\text{cm/year}$  and  $2.0\text{ cm/year}$  are assumed to account for different seismic activities. These slip rates represent average seismic activities for the considered fictitious faults and can be referred to as the long-term slip rates. The characteristic earthquake recurrence model proposed in Youngs and Coppersmith (1985) is used (Figure 3.7) for stochastic earthquake recurrence (see relevant discussions in Section 3.2.3). Table 3.1 lists the slip rate decomposition of the exponential and characteristic earthquakes for each fictitious fault. The long-term slip rates ( $\dot{s}_{total}$ ) are entirely dominated by the characteristic slip rates ( $\dot{s}_{char}$ ) indicating that the forward-directivity related demands are mainly represented by the characteristic earthquakes.

For each fictitious fault, PSHA was run using SHB11 and CHS13 directivity models and the spectral amplifications were computed at each site by normalizing “*directivity considered*” spectra with “*no directivity*” spectra. The spectral amplification computations are the same as those described in Section 3.2.3. The “*no directivity*” spectra are computed using BA08 (counterpart of SHB11) and CY14 with  $\Delta PP = 0$  (counterpart of CHS13).

Given a set of  $R_x/L$ ,  $T/T_{max}$  (for SHB11) and  $T/T_{corner}$  (for CHS13) ratios, Figure 3.13 and Figure 3.11 show the non-exceedance probabilities of spectral amplifications (i.e.,  $P(A_f \leq amp)$ ) computed from SHB11 and CHS13, respectively. The presented non-exceedance probabilities are actually count statistics and are obtained from the discrete cumulative densities of  $A_f$  for each directivity model. Given a specific  $R_x/L$  and  $T/T_{max}$  (or  $T/T_{corner}$  in the case of CHS13) each cumulative density plot is computed from the spectral amplifications at 7 sites located between  $0\text{km} \leq R_y \leq 30\text{km}$  (Figure 3.5). Since each site contains 5 spectral amplifications resulting from the PSHA runs of 5 fictitious faults, the cumulative density plots are computed from 35 spectral amplification points. They can show the influence of the fault-site geometry (as a function of  $R_x/L$ ),  $T/T_{max}$  (or  $T/T_{corner}$ ) and the slip rate on directivity dominant spectral intensities. The cumulative densities (CDFs) in the first three rows show the 475-year return period spectral amplifications whereas the last three rows show the

same cumulative densities for 2475-year return period. Hence, the plots in Figure 3.10 and Figure 3.11 also describe the importance of mean annual exceedance rate (or return period) for directivity dominated spectral amplifications.

Table 3.1 Decomposition of average slip rates for the exponential and characteristic earthquakes represented by the stochastic earthquake recurrence model used in the fictitious fault segments

	$L = 20 \text{ km} / M_{ch} 6.25$		$L = 50 \text{ km} / M_{ch} 6.7$	
$\dot{S}_{total}$ (cm/yr)	Exponential $5.0 \leq M_w \leq 6.0$	Characteristic $6.0 < M_w \leq 6.5$	Exponential $5.0 \leq M_w \leq 6.45$	Characteristic $6.45 < M_w \leq 6.95$
	$\dot{S}_{exp}$	$\dot{S}_{char}$	$\dot{S}_{exp}$	$\dot{S}_{char}$
<b>0.5</b>	0.024	0.476	0.0278	0.4722
<b>1.0</b>	0.050	0.950	0.0556	0.9444
<b>2.0</b>	0.099	1.901	0.1112	1.8888
	$L = 100 \text{ km} / M_{ch} 7.0$		$L = 150 \text{ km} / M_{ch} 7.2$	
$\dot{S}_{total}$ (cm/yr)	Exponential $5.0 \leq M_w \leq 6.75$	Characteristic $6.75 < M_w \leq 7.25$	Exponential $5.0 \leq M_w \leq 6.95$	Characteristic $6.95 < M_w \leq 7.45$
	$\dot{S}_{exp}$	$\dot{S}_{char}$	$\dot{S}_{exp}$	$\dot{S}_{char}$
<b>0.5</b>	0.0292	0.4708	0.0298	0.4702
<b>1.0</b>	0.0584	0.9416	0.0597	0.9403
<b>2.0</b>	0.1168	1.8832	0.1194	1.8806
	$L = 300 \text{ km} / M_{ch} 7.5$			
$\dot{S}_{total}$ (cm/yr)	Exponential $5.0 \leq M_w \leq 7.25$	Characteristic $7.25 < M_w \leq 7.75$		
	$\dot{S}_{exp}$	$\dot{S}_{char}$		
<b>0.5</b>	0.0305	0.4695		
<b>1.0</b>	0.0611	0.9389		
<b>2.0</b>	0.1221	1.8779		

The 475-year CDFs in Figure 3.10 indicate the prominence of slip rate in directivity dominant spectral amplitudes by SHB11 because the non-exceedance probabilities are sensitive to the variations in slip rate for the directivity dominant sites ( $0.25 \leq R_x/L \leq 0.5$ ). The slip rate, however, becomes less important for 2475-year directivity-based spectral amplifications in SHB11. The directivity effects are minimum in SHB11 at  $R_x/L = 0.7$  (sites remotely located from the ends of the fault) for both 475-year and 2475-year return periods (more visible in 475-year CDFs). This specific feature of SHB11 is related to pulse occurrence probability that becomes fairly small at large  $R_x/L$  that is already discussed in the case studies in Section 3.2.3 (Figure 3.6 and Figure 3.9). The non-exceedance probabilities in Figure 3.10 also suggest higher spectral amplifications for  $T \geq T_{max}$  especially for directivity dominant cases according to SHB11 (i.e.,  $0.25 \leq R_x/L \leq 0.5$ ).

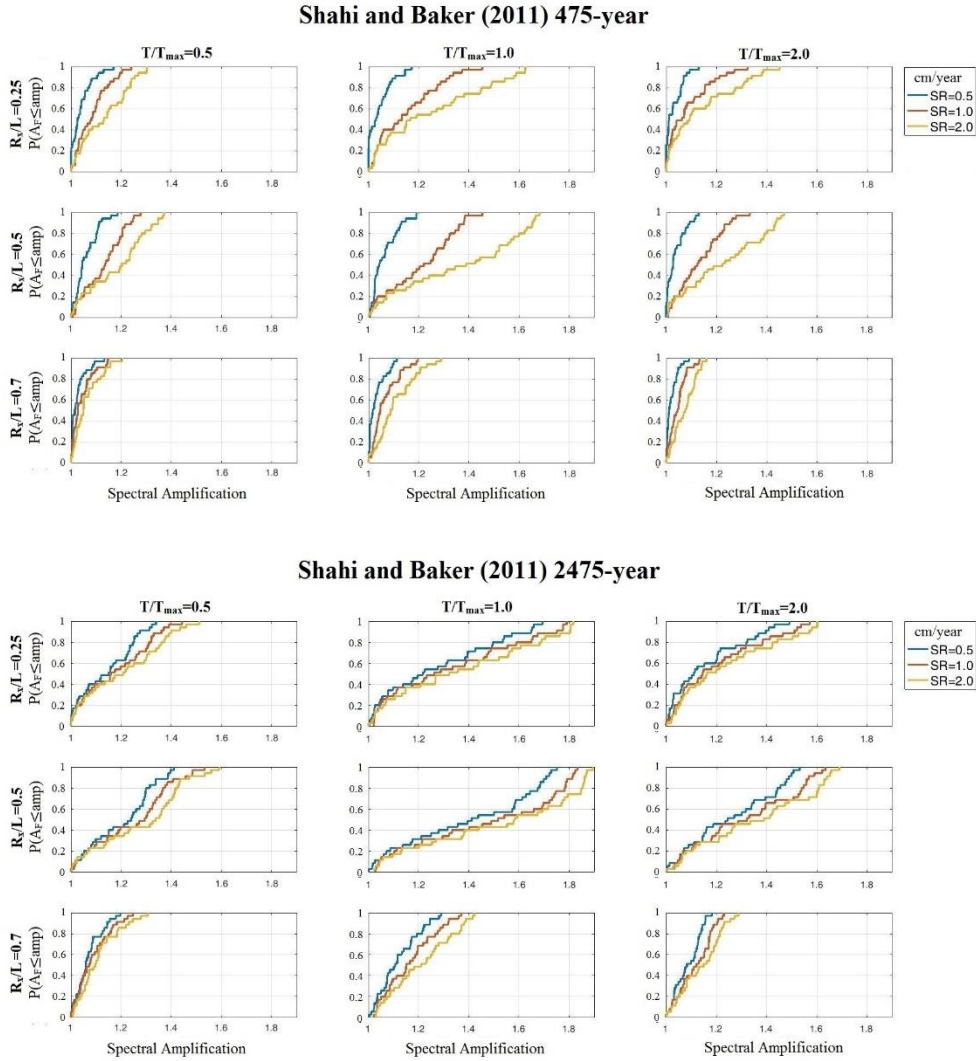


Figure 3.10 Non-exceedance probabilities (cumulative density functions) of directivity spectral amplifications according to Shahi and Baker (2011) directivity model given a range of  $R_x/L$ ,  $T/T_{max}$  and average slip rate. First three rows show the probabilities for the 475-year return period. The last three rows pertain to the 2475-year return period probabilities

Contrary to the observations in SHB11, the CDFs by CHS13 presented in Figure 3.11 suggest independency of the forward-directivity spectral amplifications on slip rate for both the 475-year and 2475-year return periods. Besides, the spectral amplifications in Figure 3.11 are significant for sites located along  $R_x/L = 0.5$  and  $R_x/L = 0.7$ . The large non-exceedance probabilities at  $R_x/L = 0.7$  by CHS13 are exactly the opposite of SHB11. This observation is not surprising because CHS13

considers the directivity related spectral amplifications only for regions extending beyond the fault ends (i.e.,  $R_x/L \geq 0.5$ ; see Figure 3.9b and relevant discussions). That's why the directivity related spectral amplifications are barely significant for  $R_x/L = 0.25$  in CHS13 (first and fourth row CDFs in Figure 3.11). As in the case of SHB11, CHS13 directivity-based spectral amplifications are larger for  $T \geq T_{corner}$ . Note that spectral amplifications by SHB11 are larger than those computed from CHS13 that can partially originate from the different horizontal component definitions by the two models. SHB11 spectral amplifications are computed by normalizing FN *directivity* spectra by GMRotI50 *no directivity* spectra. CHS13 computes spectral amplifications from *directivity* and *no directivity* spectral ratios of RotD50 horizontal component definition. The 2475-year spectral amplifications are larger than those of 475-year spectral amplifications for the SHB11 directivity model whereas CHS13 spectral amplifications are almost insensitive to return period.

The period-dependent variations of directivity spectral amplifications are presented in Figure 3.12 for different fault lengths ( $L = 100\text{km}, 150\text{km}, 300\text{km}$ ) for a slip rate of  $\dot{s}_{total} = 2.0\text{cm/year}$ . The spectral amplifications represent a hazard level of 2475-year return period. Given a fault length, the period-dependent forward-directivity spectral amplifications in each panel are plotted for the entire site distribution (i.e., 42 sites as shown in Figure 3.5) that are displayed in light gray color. In order to underline the variation of spectral amplifications for fault-site geometries along perpendicular and parallel directions to the fault strike, the median period-dependent spectral amplifications for constant  $R_x/L$  ( $R_x/L = 0, 0.25, 0.5, 0.6, 0.7, 0.8$ ) and  $R_y$  ( $R_y = 0\text{km}, 5\text{km}, 10\text{km}, 15\text{km}, 20\text{km}, 25\text{km}$  and  $30\text{km}$ ) are also shown. The spectral amplifications of 7 sites located along the same  $R_x/L$  are used to compute the median spectral amplifications for a given  $R_x/L$ . Similarly, the median spectral amplification for a specific  $R_y$  is computed from the spectral amplifications of 6 stations located along the same  $R_y$ . The first two columns in Figure 3.12 show the median spectral amplitude variations for constant  $R_y$  computed from SHB11 (first column) and CHS13 (second column) for the fault lengths of  $L = 100\text{km}$  (1<sup>st</sup> row),  $L = 150\text{km}$  (2<sup>nd</sup> row) and  $L = 300\text{km}$  (3<sup>rd</sup> row). The last two columns display the same median spectral amplitude variations for constant  $R_x/L$ . The changes in fault length (affecting the characteristic magnitude) as well as the fault-site geometry (in terms of  $R_x/L$  and  $R_y$ )

are important to understand the sensitivity of directivity-dominated spectral amplifications against these two parameters.

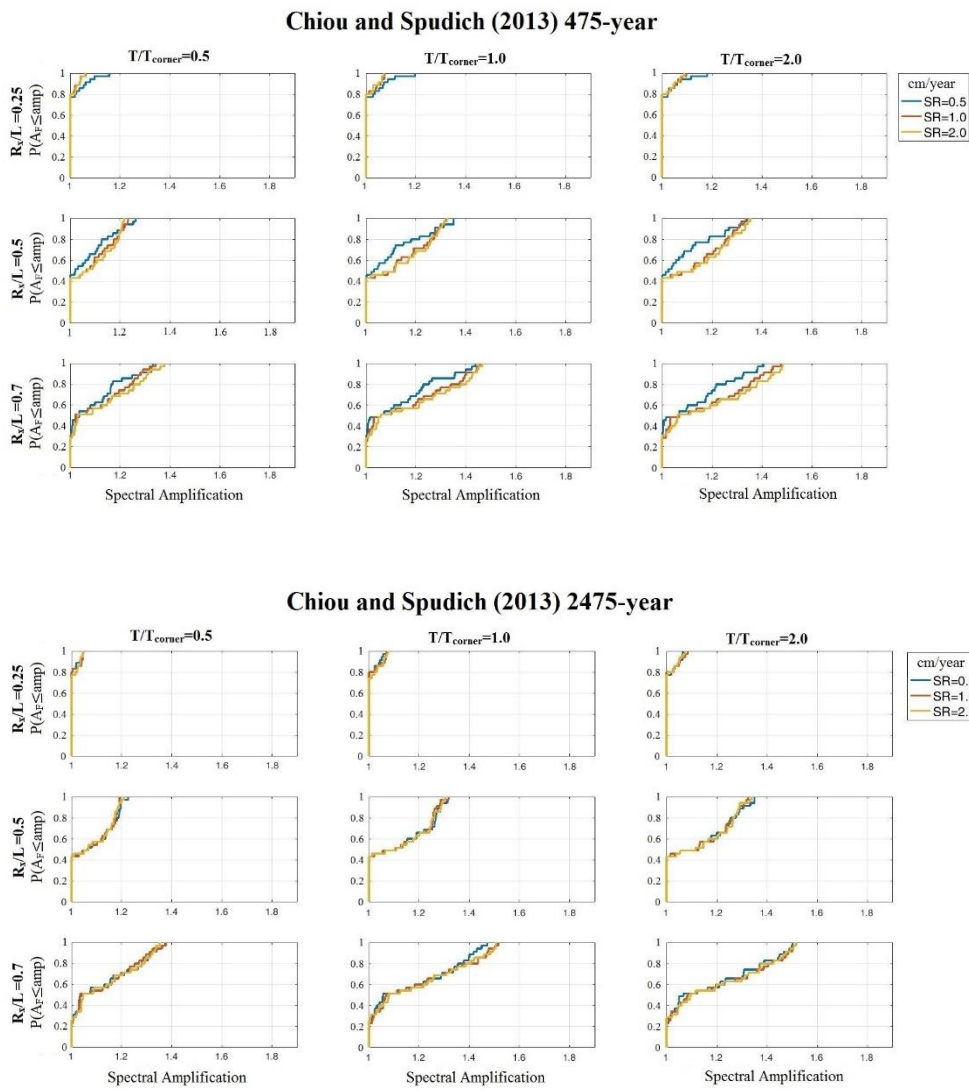


Figure 3.11 Same as Figure 3.10 but the forward-directivity model is Chiou and Spudich (2013; Chapter 6 in Spudich et al., 2013) implemented in Chiou and Youngs (2014) GMPM

One can make interesting observations from Figure 3.12. Firstly, there is a clear difference between the period-dependent spectral amplification shapes estimated from the SHB11 and CHS13 directivity models. This difference is already discussed in Section 3.2.3 under specific probabilistic scenarios. The SHB11 spectral amplifications shows a steep increase until a peak. This is followed by a decrease with a steep slope. The CHS13 spectral amplifications also increase until a maximum

but this trend is milder with respect to SHB11. The increase in spectral amplifications follows either a stable trend or a slight reduction that can even be neglected compared to the steep decreasing trends observed in SHB11.

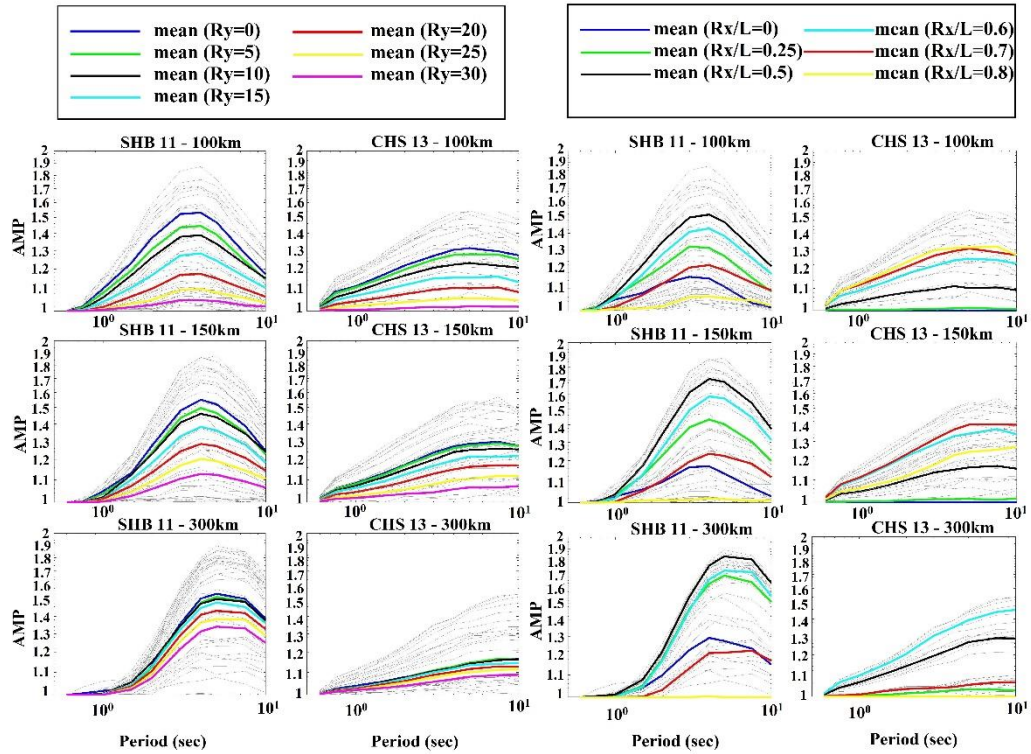


Figure 3.12 Period-dependent 2475-year forward-directivity spectral amplifications estimated by SHB11 and CHS13 for PSHA scenarios of fault lengths  $L = 100\text{km}$  (top row),  $L = 150\text{km}$  (middle row) and  $L = 300\text{km}$  (bottom row) having  $\dot{s}_{total} = 2.0\text{cm/year}$ . The first two columns show mean spectral amplifications of SHB11 (first column) and CHS13 (second column) for sites located at a constant  $R_y$  and the last two columns show mean spectral amplifications of SHB11 (third column) and CHS13 (fourth column) for sites located at a constant  $R_x/L$

The locus of maximum spectral amplifications for both directivity models shift towards longer periods as the fault length increases. The increase in fault length is associated with a larger  $M_{ch}$  (discussed in the previous paragraphs) that eventually yields longer periods ( $T_{max}$  or  $T_{corner}$ ) where directivity-dominant spectral amplifications are maximized. Since SHB11 relies on the pulse occurrence probability (Section 3.2.1 and Figure 3.2),  $T_{max}$  is inherently related to  $T_p$  due to the relation between magnitude and pulse period (Alavi and Krawinkler 2004; Shahi 2013; Somerville 2003). CHS13 does not explicitly consider pulse period occurrence

but the isochrone theory recaps the  $T_p$  effect so  $T_{corner}$  approximates  $T_{max}$ . However, the directivity-based spectral amplification trends differ between CHS13 and SHB11 for differences underlying the background theory of each model. The probabilistic case studies presented in this study suggest that  $T_{max}$  or  $T_{corner}$  can be approximated by the median  $T_p$  of empirical pulse period relationships for 475-year and 2475-year return periods.

The forward-directivity spectral amplifications are inversely proportional to  $R_y$ : the median amplifications are maximum at on-fault sites ( $R_y = 0\text{km}$ ) and they decrease as  $R_y$  increases. However, the fault length seems to be prominent on  $R_y$  dependent median spectral amplifications because increase in fault length reduces the difference between the median spectral amplifications of consecutive  $R_y$  values. This observation is more noticeable in CHS13: the differences between the median spectral amplifications of two consecutive  $R_y$  values for  $L = 300\text{km}$  fault are almost negligible with respect to the same median trends of  $L = 100\text{km}$  fault. This phenomenon may suggest that the directivity dependent spectral amplifications at some equidistant sites from the fault strike decrease drastically with the increase in fault length. In other words, sites located at identical  $R_y$  would be subject to significant variation in the directivity dependent spectral amplifications depending on the fault length.

The directivity spectral amplifications have a more intricate relationship with  $R_x/L$ . The investigated directivity models behave differently against variations in this parameter. The median spectral amplifications along  $R_x/L = 0.5$  and  $R_x/L = 0.6$  are estimated to be the maximum by SHB11. These two locations represent the fault ends where the pulse occurrence is more likely according to SHB11, which essentially promotes larger directivity spectral amplifications. SHB11 advocates  $R_x/L = 0.25$  as another potential location for large spectral amplifications and, in fact,  $R_x/L = 0.25$  becomes as critical as the fault ends for the ruptures occurring on large fault lengths (represented by  $L = 300\text{km}$  in this study). SHB11 gives almost no credit for directivity-based spectral amplification for sites remotely located from the fault ends (represented by  $R_x/L = 0.8$  in the case studies). The directivity spectral amplifications by CHS13 show a more complicated pattern. CHS13 estimates large spectral amplifications at the sites located along and beyond the fault ends (i.e.,  $R_x/L \geq 0.5$ ).

However, the increase in the fault length decreases the possibility of observing large spectral amplifications at sites remotely located from the fault ends ( $R_x/L \geq 0.7$ ). In contrast to SHB11, this directivity model does not give any credit to sites located along  $R_x/L = 0.25$  for directivity based spectral amplifications.

### 3.4 Spatial Extension of Directivity Dominated Sites (Regions) in the Fault Vicinity

The discussions in the previous sections indicate the significance of the fault length (hence the characteristic earthquake generated by the fault that also puts forward the importance of  $T_{max}$  or  $T_{corner}$ ), the slip rate as well as the return period in NFFD spectral amplifications. The fault-site geometry brings additional complexity to the directivity dominated spectral amplifications that further invokes the constraints imposed by the different directivity models. However, one can still develop some practical rules to delineate the directivity-dominated regions within the ruptured fault segment by making use of the probabilistic scenarios discussed throughout this study. These rules would be expressed in terms of the aforementioned seismological and geometrical parameters. Figure 3.13 and Figure 3.14 show the spatial distribution of directivity based spectral amplifications for SHB11 and CHS13, respectively. They are compiled from the entire set of probabilistic scenarios considered in this study. Both figures display the maximum spectral amplifications in the vicinity of  $T_{max}$  or  $T_{corner}$  (dependent of fault length thus the characteristic earthquake magnitude) for the 475-year (top 5 panels) and the 2475-year (bottom 5 panels) return periods. Each column in the figures represents a specific slip rate (first column -  $\dot{s}_{total}=0.5\text{cm/year}$ , second column -  $\dot{s}_{total}=1.0\text{cm/year}$ , third column -  $\dot{s}_{total}=2.0\text{cm/year}$ ). The five rows for each return period represent the PSHA results of the fault lengths  $L = 20\text{km}$ ,  $50\text{km}$ ,  $100\text{km}$ ,  $150\text{km}$  and  $300\text{km}$ .

The panels in Figure 3.13 and Figure 3.14 show the overall influence of the slip rate, the fault length and the return period on the directivity spectral amplifications. They also suggest the existence of a spatial distribution pattern for the spectral amplifications to delineate the directivity affected sites. The geometry of the spatial distribution pattern of the directivity affected region as well as the level of spectral amplifications enclosed by this region is directivity model dependent.

Figure 3.15 shows the proposed geometry for each directivity model to idealize the spatial distribution of the directivity-affected regions for spectral amplifications greater than 1.1. In other words, the regions enclosed by the proposed geometrical shape possess a spectral amplitude of 1.1 or above. Table 3.2 lists the proposed rules to establish the geometrical shapes for SHB11 and CHS13 in terms of the slip rate, the return period and the fault length.

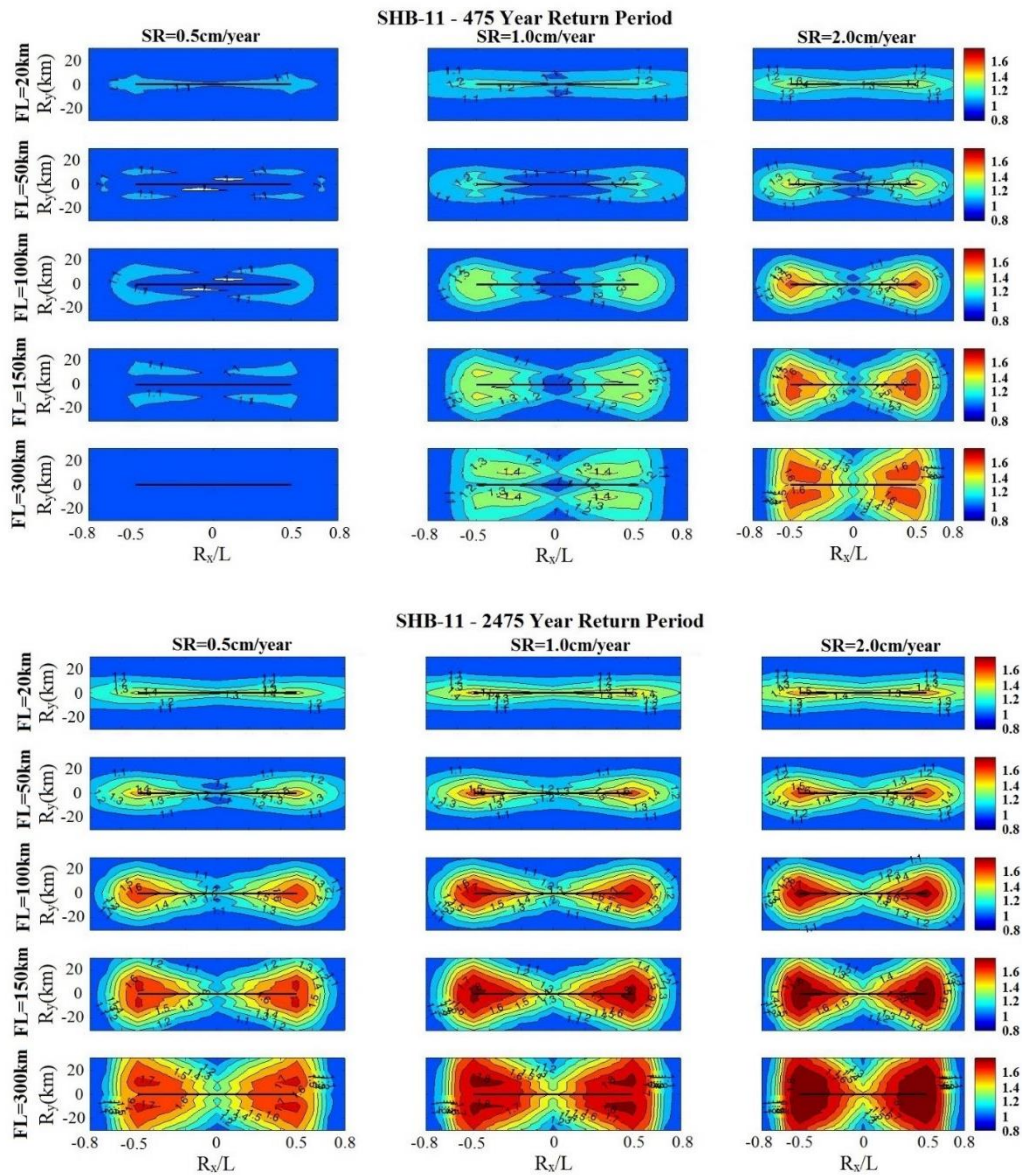


Figure 3.13 The spatial distribution of the forward-directivity spectral amplifications by SHB11 in terms of the return period, slip rate and the fault length (thus the characteristic earthquake magnitude)

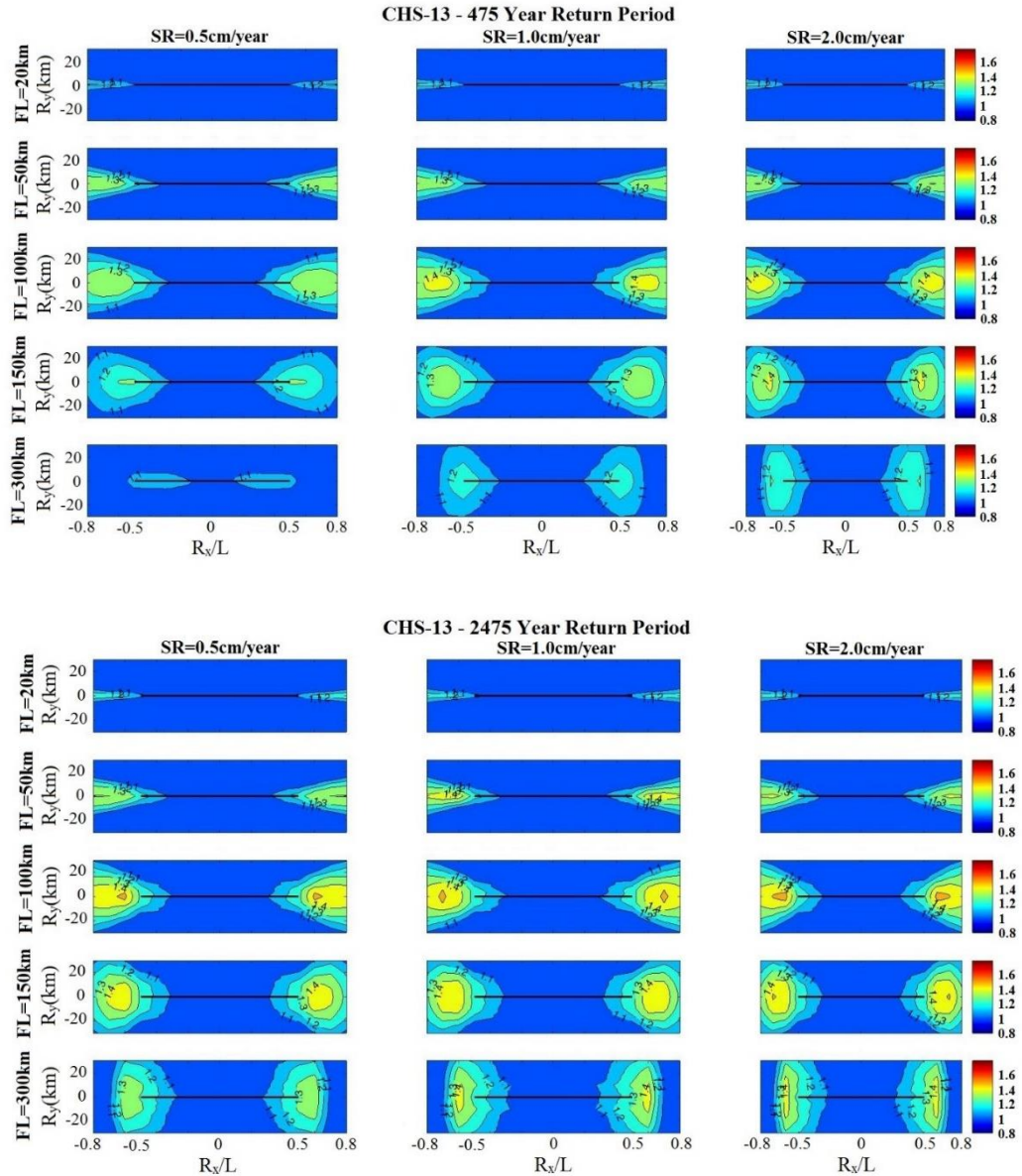


Figure 3.14 The spatial distribution of the forward-directivity spectral amplifications by CHS13 in terms of the return period, slip rate and the fault length (thus the characteristic earthquake magnitude)

The proposed geometry for SHB11 suggests perpendicular fault distances ( $D_{y1}$  and  $D_{y2}$ ) ranging between 10km to 20km for the strike-normal extension of directivity dominated regions in 475-year spectral amplifications.  $D_{y2}$  can exceed 30km for fault lengths of 150km and above for the 2475-year spectral amplifications. SHB11 imposes a wide perpendicular distance coverage from the fault strike for directivity-dominated regions that tends to increase towards the edges of the fault (Figure 3.15, left panel). SHB11 suggests the extension of directivity effects beyond the fault edges

for horizontal distances ( $D_x$ ) of 20% to 30% fault length.  $D_x$  can attain even larger values (i.e.,  $D_x > 0.3L$ ) for the relatively shorter faults ( $L \leq 50\text{km}$ ) in particular for the 2475-year spectral amplifications.

The geometry to define directivity-dominated regions draws a simpler pattern for CHS13 because this model lumps the directivity effects at the edges of the faults (Figure 3.15, right panel). The directivity effects generally commence in the last quarter length of the fault ( $D_{x1}$ ) and they extend beyond the fault edges by 30% of fault length ( $D_{x2}$ ) regardless of the slip rate and the return period. The perpendicular fault distance ( $D_y$ ) ranges from 5km to 30km (and even larger for the long faults and the 2475-year return period) from one side of the fault strike.

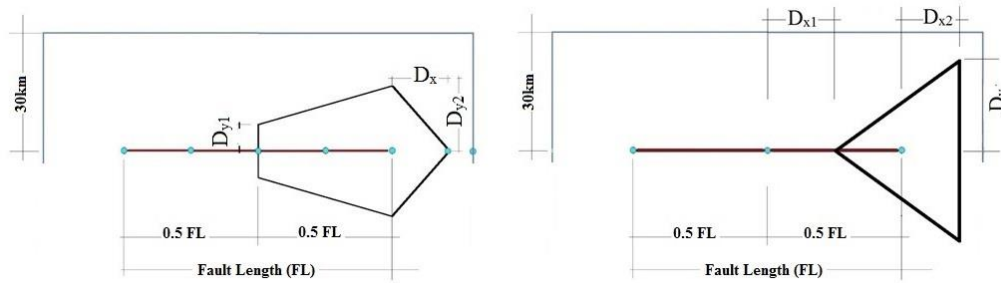


Figure 3.15 Simplified geometries to highlight the directivity affected regions in the ruptured fault vicinity for directivity spectral amplitudes greater than 1.1. Left panel: SHB11, Right panel: CHS13

Table 3.2 Proposed rules for (a) SHB11 and (b) CHS13 to define the spatial distribution of directivity affected spectral amplifications within the fault

(a) SHB11

475 year	$D_x^*$			$D_{y1}^*$			$D_{y2}^*$		
FL	SR=0.5	SR=1.0	SR=2.0	SR=0.5	SR=1.0	SR=2.0	SR=0.5	SR=1.0	SR=2.0
L = 20km	0.2L	>0.3L	>0.3L	5km	10km	10km	10km	15km	15km
L = 50km	0.2L	0.3L	>0.3L	10km	10km	10km	15km	15km	15km
L = 100km	0.2L	0.2L	0.2L	10km	10km	10km	15km	20km	20km
L = 150km	0.2L	0.2L	0.2L	10km	10km	10km	20km	30km	>30km
L = 300km	0.2L	0.2L	0.2L	20km	20km	20km	>30km	>30km	>30km
2475 year	$D_x^*$			$D_{y1}^*$			$D_{y2}^*$		
FL	SR=0.5	SR=1.0	SR=2.0	SR=0.5	SR=1.0	SR=2.0	SR=0.5	SR=1.0	SR=2.0
L = 20km	>0.3L	>0.3L	>0.3L	10km	15km	15km	15km	15km	20km
L = 50km	>0.3L	>0.3L	>0.3L	15km	15km	15km	20km	20km	20km
L = 100km	0.3L	0.3L	0.3L	15km	15km	15km	25km	30km	30km
L = 150km	0.3L	0.3L	0.3L	15km	15km	15km	>30km	>30km	>30km
L = 300km	0.2L	0.2L	0.2L	25km	25km	25km	>30km	>30km	>30km

Table 3.2 (Continued)

## (b) CHS13

475 year	Dx1*			Dx2*			Dy*		
FL	SR=0.5	SR=1.0	SR=2.0	SR=0.5	SR=1.0	SR=2.0	SR=0.5	SR=1.0	SR=2.0
L = 20km	0.50L	0.50L	0.50L	0.3FL	0.3L	0.3L	5km	5km	5km
L = 50km	0.25L	0.25L	0.25L	0.3FL	0.3L	0.3L	15km	15km	15km
L = 100km	0.25L	0.25L	0.25L	0.3FL	0.3L	0.3L	25km	25km	25km
L = 150km	0.25L	0.25L	0.25L	0.3FL	0.3L	0.3L	30km	30km	30km
L = 300km	0.25L	0.25L	0.25L	0.2FL	0.2L	0.2L	10km	30km	>30km
2475 year	Dx1*			Dx2*			Dy*		
FL	SR=0.5	SR=1.0	SR=2.0	SR=0.5	SR=1.0	SR=2.0	SR=0.5	SR=1.0	SR=2.0
L = 20km	0.50L	0.50L	0.50L	0.3L	0.3L	0.3L	5km	5km	5km
L = 50km	0.25L	0.25L	0.25L	0.3L	0.3L	0.3L	15km	15km	15km
L = 100km	0.25L	0.25L	0.25L	0.3L	0.3L	0.3L	30km	30km	30km
L = 150km	0.25L	0.25L	0.25L	0.3L	0.3L	0.3L	>30km	>30km	>30km
L = 300km	0.25L	0.25L	0.25L	0.2L	0.2L	0.2L	>30km	>30km	>30km

\* Refer to Figure 3.15 for the definition of geometrical parameters

### 3.5 Summary and Conclusion

This chapter investigated the influence of some seismological and geometrical parameters on the spatial distribution and the amplitude variation of directivity dominated elastic spectral amplitudes by using the directivity models by Shahi and Baker (2011) (SHB11) and Chiou and Spudich (CHS13;(Spudich et al. 2013; Chiou and Youngs 2014)). SHB11 and CHS13 are narrow-band directivity models utilizing different approaches to consider spectral amplitude modifications for directivity dominant waveforms at sites relatively closer to the ruptured fault segment. SHB11 uses a probabilistic framework and computes the exceedance probabilities of spectral ordinates by convolving the occurrence probabilities of pulses with the “*pulse observed*” and the “*no pulse observed*” cases. The fault-site geometry in SHB11 accounts for the orientation of the incident pulselike waveform with respect to the fault strike ( $\alpha$ ). The pulse occurrence probability is also related to fault-site geometry in SHB11. CHS13 is based on the DPP predictor that accounts for the fault-site geometry to physically explain the directivity effects. Given a site, CHS13 considers the forward-directivity effect by measuring the offset between the site-specific DPP and the average DPP computed from the equidistant sites surrounding the ruptured fault segment. It does not explicitly consider the pulse occurrence or orientation of

incident pulselike waveform with respect to the fault strike. SHB11 is calibrated by using BA08 whereas CHS13 is integrated with CY14 to address the directivity effects for elastic spectral amplitudes. Shahi and Baker (2011) state that SHB11 can equally be applicable to any other conventional GMPM whereas CY14 tailored CHS13 as part of its functional form via regression analysis.

The observations made from this study rely on the probabilistic earthquake scenarios of strike-slip faults. They can be useful for the explicit consideration of the directivity effects in the future seismic design codes. The following conclusive remarks constitute the major outcomes of this study.

- SHB11 and CHS13 estimate the largest spectral amplifications in the vicinity of spectral periods that are called as  $T_{max}$  and  $T_{corner}$ , respectively. These periods shift towards longer spectral intervals with increasing characteristic earthquake magnitude,  $M_{ch}$  (thus, longer fault length). SHB11 relies on the occurrence of pulses, hence  $T_{max}$  is eventually related to  $T_p$  that is a function of  $M_w$ . CHS13 uses isochrone theory and it does not rely on pulse occurrence but accounts for the relation between magnitude and  $T_p$ . Thus,  $T_{corner}$  is correlated to pulse period but it would be inappropriate to make a direct comparison between these concepts. For the return periods of interest (475-year and 2475-year), median  $T_p$  can fairly represent  $T_{max}$  and  $T_{corner}$ .
- Period-dependent spectral amplifications by SHB11 show a steep increase until the maximum spectral amplification is reached in the vicinity of  $T_{max}$ . This trend is followed by a decrease with a steep slope. The spectral amplifications by CHS13 also increase until a maximum in the vicinity of  $T_{corner}$ . Contrary to spectral amplifications estimated by SHB11, they almost fluctuate about the maximum for  $T > T_{corner}$ .
- Spectral amplifications of SHB11 are larger than those of CHS13 that can be partially explained by the differences in their horizontal component definitions. Fault-normal horizontal component metric is used in SHB11 while considering the forward-directivity effects. CHS13 inherently uses RotD50 horizontal component definition in the computation of directivity dominated spectral amplifications.

- SHB11 is sensitive to the variations in slip rate while estimating the directivity dominated spectral amplifications. Its influence seems to be more prominent for smaller return-period spectral amplifications (475-year return period in the case studies). The variations in the slip rate do not significantly affect the spectral amplifications of CHS13.
- Longer return periods result in larger spectral amplifications due to forward-directivity for SHB11. This observation is barely significant for CHS13.
- SHB11 estimates large spectral amplifications for sites between  $0.25 \leq R_x/L \leq 0.5$ . The effect of directivity vanishes after  $R_x/L = 0.7$ . The directivity spectral amplifications of CHS13 are concentrated between  $0.5 \leq R_x/L \leq 0.7$ . The observed differences in the spectral amplification locations along the fault strike originate from theoretical backgrounds of SHB11 and CHS13 for the consideration of fault-site geometry in directivity phenomenon. The directivity-based spectral amplifications by CHS13 are inherited from the isochrone theory that maximizes the directivity effect towards and beyond the fault edges. SHB11 uses pulse occurrence probabilities that are larger at the fault ends and amplify spectral ordinates in the vicinity of corresponding pulse period.
- Fault length ( $L$ ) is an important parameter in the observed spectral amplifications. Larger fault lengths reduce the significance of perpendicular fault distances (designated by  $R_y$  in this study) in forward-directivity spectral amplifications. In other words, the difference between the spectral amplifications of two consecutive  $R_y$  values decreases as the fault length increases.
- The spatial distribution of directivity affected sites are dependent on the slip rate, return period and the fault length. The first two parameters are particularly effective in the directivity dominated spatial distribution patterns suggested by SHB11. The directivity affected sites can exceed 30km in the fault normal direction. One can observe significant directivity dominated spectral amplifications within 60km radial distance from the fault ends for 2475-year return period and for fault lengths of  $L \geq 150$ km.



## CHAPTER 4

### A PROPOSED RELATIONSHIP BETWEEN DIRECTIVITY AND NONDIRECTIVITY SPECTRAL AMPLITUDES FOR MAXIMUM DIRECTION

#### 4.1 Introduction

The orientation of horizontal ground-motion components can affect the spectral demand level. This phenomenon is referred to as “directionality” that reflects the effect of ground-motion polarization on the spectral amplitude variation at different orientations. Since ground-motion predictive models (GMPMs) represent the spectral effects of two horizontal ground-motion components as a single component, they employ a variety of horizontal component definitions among which the geometric mean (GM), GMRot150 (Boore et al., 2006), RotD50 (Boore, 2010) (Table 4.1) are the most popular in recently developed GMPEs. Notwithstanding, many researchers tend to focus on the strike-normal component of horizontal ground-motions to address the high spectral demands in directivity dominant ground motions (Huang et al., 2008).

The horizontal component definition, in particular the directivity, becomes even more important since recent seismic design codes such as ASCE/SEI 7-10 (ASCE, 2010), the 2009 and 2015 editions of NEHRP provisions (BSSC, 2009; 2015) built their design strategies for maximum direction. This is because the earthquake spectral demands resulting from the geometrical mean of two horizontal components (geomean of horizontal components) are lesser with respect to those determined from the maximum direction (i.e., the direction corresponding to maximum of rotated horizontal components;  $S_{aRotD100}$ ). Since structures will have different levels of resistance at different orientations, their design that is based on the maximum

direction of horizontally rotated components sounds a reasonable strategy to many engineers. This strategy could be particularly relevant for structural systems having symmetry in all directions (known as azimuth-independent structures).

Many studies in the literature address the directionality issue to harmonize the horizontal component definitions. For example, Beyer and Bommer (2006) provide a suite of expressions to convert one horizontal component definition to the other. Of those definitions, they propose empirical expressions to convert GMRotI50 to maximum of horizontally rotated component (RotD100) without making any distinction between near-fault and far-fault recordings. Hong and Goda (2007) define a model to estimate the spectral demands at any desired azimuthal angle from  $S_{a_{RotD100}}$ . Huang et al. (2008) seek relationships between geomean-based (GMRotI50) and maximum direction horizontal component definitions for near-fault records. Shahi and Baker (2014) propose horizontal-component conversion expressions between RotD50 and RotD100 without making any classification about directivity and non-directivity records.

The directionality becomes even more important when directivity effect is of concern for sites close to the ruptured fault segment. As discussed in the previous chapter, directivity models such as the one proposed by Chiou and Spudich (Spudich et al., 2013) evaluates the directivity effects by considering the RotD50 horizontal component definition. In other words, Chiou and Spudich directivity model intermediates between  $S_{a_{RotD50}}$  and  $S_{a_{RotD50,directivity}}$  ( $S_{a_{RotD50}}$  component when directivity is dominant). In a similar manner, the Shahi and Baker (2011) directivity model modifies the GMPEs estimating geomean-based (i.e., GMRotI50) spectrum for arbitrary orientations relative to fault strike. This study uses the Shahi and Baker (2011) directivity model to compute the directivity spectral amplifications for strike-normal horizontal component (see discussions in Chapter 5). As there is no specific scaling model to understand the relation between directivity and no-directivity  $S_{a_{RotD100}}$  (i.e.,  $S_{a_{RotD100,directivity}}$  vs.  $S_{a_{RotD100,nodirectivity}}$  -or simply  $S_{a_{RotD100}}$ -), the directivity amplification expressions developed from Shahi and Baker (2011) directivity model cannot be assessed for its use to represent  $S_{a_{RotD100,directivity}}$  in code-based approaches. Note that a relationship between  $S_{a_{RotD100,directivity}}$  vs.  $S_{a_{RotD100,nodirectivity}}$  would also be useful to understand the level of additional

amplification to scale  $Sa_{RotD50directivity}$  to  $Sa_{RotD100directivity}$ . Currently, CALTRANS (2013) recommends a 20% increase in  $Sa_{RotD50directivity}$  to mimic  $Sa_{RotD100directivity}$ .

This chapter aims to establish a relationship between  $Sa_{RotD100directivity}$  vs.  $Sa_{RotD100nodirectivity}$  in order to respond to the discussions posed in the previous paragraph. In other words, the relationship established between  $Sa_{RotD100directivity}$  and  $Sa_{RotD100nodirectivity}$  would be useful to see if the directivity spectral amplification expressions developed for SN horizontal component from SHB11 directivity model is sufficient while addressing  $Sa_{RotD100directivity}$  for seismic guidelines. The next section describes the horizontal component metrics for establishing the terminology and then explains the database as well as the methodology while developing the relationship between  $Sa_{RotD100directivity}$  and  $Sa_{RotD100nodirectivity}$ . The expressions developed in this chapter would also be useful to assess the suggestions by CALTRAN (2013) to obtain  $Sa_{RotD100directivity}$  from  $Sa_{RotD50directivity}$ .

## 4.2 Horizontal Component Definitions

The early versions of ground-motion predictive models use the spectral ordinates of (a) both “as recorded” horizontal components (referred to as random horizontal component metric) or (b) the maximum of spectral ordinate of “as recorded” horizontal components (referred to as maximum horizontal component metric). Later, the model developers have started to use either the arithmetic mean or geometric mean of “as recorded” horizontal ground motions as the ground-motion component metric. These metric definitions, however, disregard the ground motion orientation in component definition and they depend on the orientation of the recording device (Boore et al, 2006). In recent years, there is a growing effort among the engineering seismology and earthquake engineering community to surmount these drawbacks by adopting different horizontal component metrics that can reflect the ground-motion characteristics at different orientations. This is also important for describing earthquake demands in seismic design. The importance of an efficient horizontal component definition is more evident in highly polarized records (e.g., forward-directivity records at which one of the horizontal components are under the influence of a strong pulse). Component definitions such as geometric mean would certainly fail to capture the polarization effect, as it would simply take the arithmetic average

of the two horizontal components in the logarithmic domain. An example of a highly polarized ground-motion record is given in Figure 4.1.a: Rolleston station recording from the 24 September 2010  $M_w$ 7.1 Darfield earthquake (Bradley and Baker, 2015). As depicted from this figure, the oscillator displacements of two mutually perpendicular horizontal axes at  $T= 2.0$ s show a strong polarization in the NW-SE directions ( $120^\circ$ - $300^\circ$  axis).

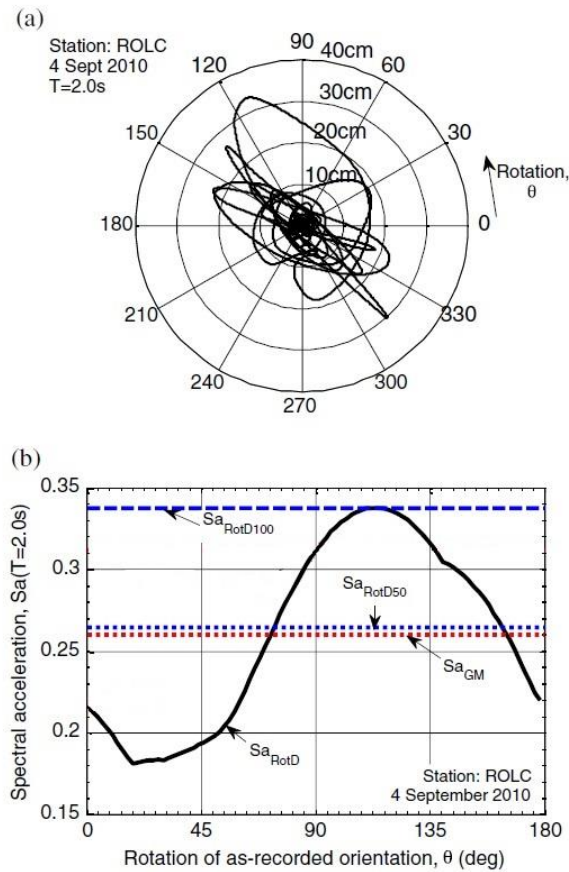


Figure 4.1 (a) Illustration of polarization by plotting the displacement response of horizontal components at  $T = 2$ s for at the Rolleston station from the 24 September 2010  $M_w$ 7.1 Darfield earthquake), (b)  $S_a$  values at  $T = 2.0$ s obtained by rotating the horizontal ground-motion components at  $0^\circ \leq \theta \leq 179^\circ$  (Bradley and Baker 2015)

Boore et al. (2006) proposed  $GMRotD_{pp}$  and  $GMRotI_{pp}$  horizontal component metrics that are independent of sensor orientations. Given a set of spectral periods, these component metrics are based on a set of geometric means at each spectral period computed from “as recorded” orthogonal horizontal motions rotated through all possible non-redundant rotation angles. Here, “GM” refers to the geometric mean of

horizontal spectral ordinates at the designated spectral periods, “RotD” or “RotI” indicate rotation-dependency or rotation-independency as a function of spectral period and “pp” describes the designated percentile from the distribution of spectral ordinates at a given period at non-redundant rotation angles. In GMRotIpp, the most common rotation angle that minimizes the spread of the rotation-dependent geometric mean is chosen from the considered period range in the spectrum calculations.

Boore (2010) introduces RotDpp and RotIpp that represent the ppth fractile of rotated horizontal ground motions at non-redundant rotation angles without computing geometric means. The computation of horizontal ground motion for RotDpp or RotIpp is given in equation (4.1).

$$OSC(t, \theta) = OSC_1(t) \cdot \cos \theta + OSC_2(t) \cdot \sin \theta \quad 4.1$$

The variable  $OSC(t, \theta)$  is the resultant horizontal ground-motion vector at angle  $\theta$  computed from the mutually perpendicular horizontal ground-motion components of  $OSC_1(t)$  and  $OSC_2(t)$ . The angle  $\theta$  is the rotation angle measured from the horizontal axis along  $OSC_1$  and  $t$  refers to time. Given a period  $T$ , one can compute the spectral ordinates for non-redundant angles  $0^\circ \leq \theta \leq 179^\circ$  and select the ppth fractile from the populated spectral ordinates at all angles. In case  $pp = 50$ , the corresponding spectral value is the median spectral amplitude (probability of exceedance is 50%) whereas if  $pp = 100$ , the corresponding spectral value is the maximum of all rotated components (and the corresponding direction is maximum direction) because the probability of exceedance is 0%. As in the case of GMRotDpp, RotDpp indicates rotation-dependent spectral ordinates in terms of period whereas RotIpp is rotation-independent spectral ordinates for the period of concern in the spectrum computations. In other words, the analyst selects the rotation angle such that the variation of rotation angles is minimum along the entire period range at the pre-selected fractile, pp for RotIpp component metric.

Figure 4.1b graphically illustrates the differences between geometric mean of “as recorded” components ( $Sa_{GM}$ ) together with  $Sa_{RotD100}$ ,  $Sa_{RotD50}$  as well as the orientation dependency ( $Sa_{Rot}$ ) of spectral ordinates at  $T = 2s$  for the recording given in Figure 4.1a. Note that  $Sa_{RotD100}$  occurs at about  $\theta = 120^\circ$  whereas  $Sa_{RotD50}$  occurs at about  $\theta = 70^\circ$ . The variation of spectral ordinates is significant in terms of rotation angle  $\theta$ .

Table 4.1 Definitions of horizontal component metrics

Horizontal Parameter	Definition
As recorded	The orientation of the recording instruments is commonly arbitrary with respect to the fault alignment (very often north–south and east–west) and is generally not correlated to the orientation of nearby faults
Geometric Mean	Geometric mean of spectra of $x$ and $y$ components $S_{a_{GMxy}}(T_i) = \sqrt{S_{a_x}(T_i) \cdot S_{a_y}(T_i)}$
FN and FP	Fault-normal and fault-parallel components with respect to fault-strike
GMRotDpp	This component definition accounts for the random orientation of the horizontal axis system by choosing, at each response period, the $p$ th percentile of the geometric mean from all possible orientations (Boore et al. 2006)
GMRotIpp	This ground-motion measure is an approximation of GMRotDpp with a constant axis orientation for all periods, which minimizes the sum of differences between GMRotIpp and GMRotDpp over all considered periods (Boore et al. 2006)
RotDpp	This component is a measure of horizontal-component seismic intensity that represent any fractile in a consistent way with GMRotDpp without computing geometric means but yet still independent of the in situ orientations of the recorded ground motions (Boore 2010)
RotIpp	This ground-motion measure is an approximation of RotDpp with a constant axis orientation which is the most representative of the SaRotDnn spectrum over all considered periods (Boore 2010)

As indicated, for this specific period ( $T = 2\text{s}$ ), the maximum direction spectral acceleration occurs when  $\theta \approx 120^\circ$  but this angle would be different for the rest of the spectral periods. In passing, it should be noted that the fault-normal and fault parallel component definitions are frequently used in the literature to emphasize some important features of the directivity-dominated ground motions. As already described in the previous chapters, fault normal is perpendicular to the azimuthal strike of the ruptured fault plane whereas fault parallel is the component along the azimuthal strike of the ruptured fault. Table 4.1 lists the definitions of horizontal component metrics discussed in this section.

### 4.3 Ground-motion Data Set

The ground-motion database used in this study is a subset of PEER (Pacific Earthquake Research Center) NGA-West2 database (<http://ngawest2.berkeley.edu>; [Ancheta et al. \(2014\)](#)). The ground motions with  $6.0 < M_w < 8.0$  and  $R_{rup} < 30\text{km}$  are selected from the PEER NGA-West2 database for pulselike and non-pulse cases. The magnitude range covers the characteristic magnitudes considered in this study. The distance range of these records is also consistent with the distance interval of interest (i.e.,  $R_y \leq 30\text{km}$ ). The basic premise about non-pulse recordings is that they mainly represent the backward directivity phenomenon whereas the pulselike ground motions in the dataset are recordings of forward-directivity. The studies by Baker (2007) and Shahi and Baker (2014) are used while determining the pulselike recordings in the NGA-West2 strong-motion database. These studies determine pulselike records near the ruptured fault segment through wavelet analysis and use a set of criteria such as pulse indicator index being greater than 0.85, occurrence of impulsive signals at the beginning of ground-velocity waveform and amplitudes of peak ground velocities greater than 30 cm/s. (Already stated in Chapter 3). A total of 58 non-pulse and 113 pulselike ground-motions are compiled for the designated magnitude and distance intervals. The pulselike records used in this study are also used by Shahi (2013) to develop the directivity model (SHB13) discussed in Chapter 3.

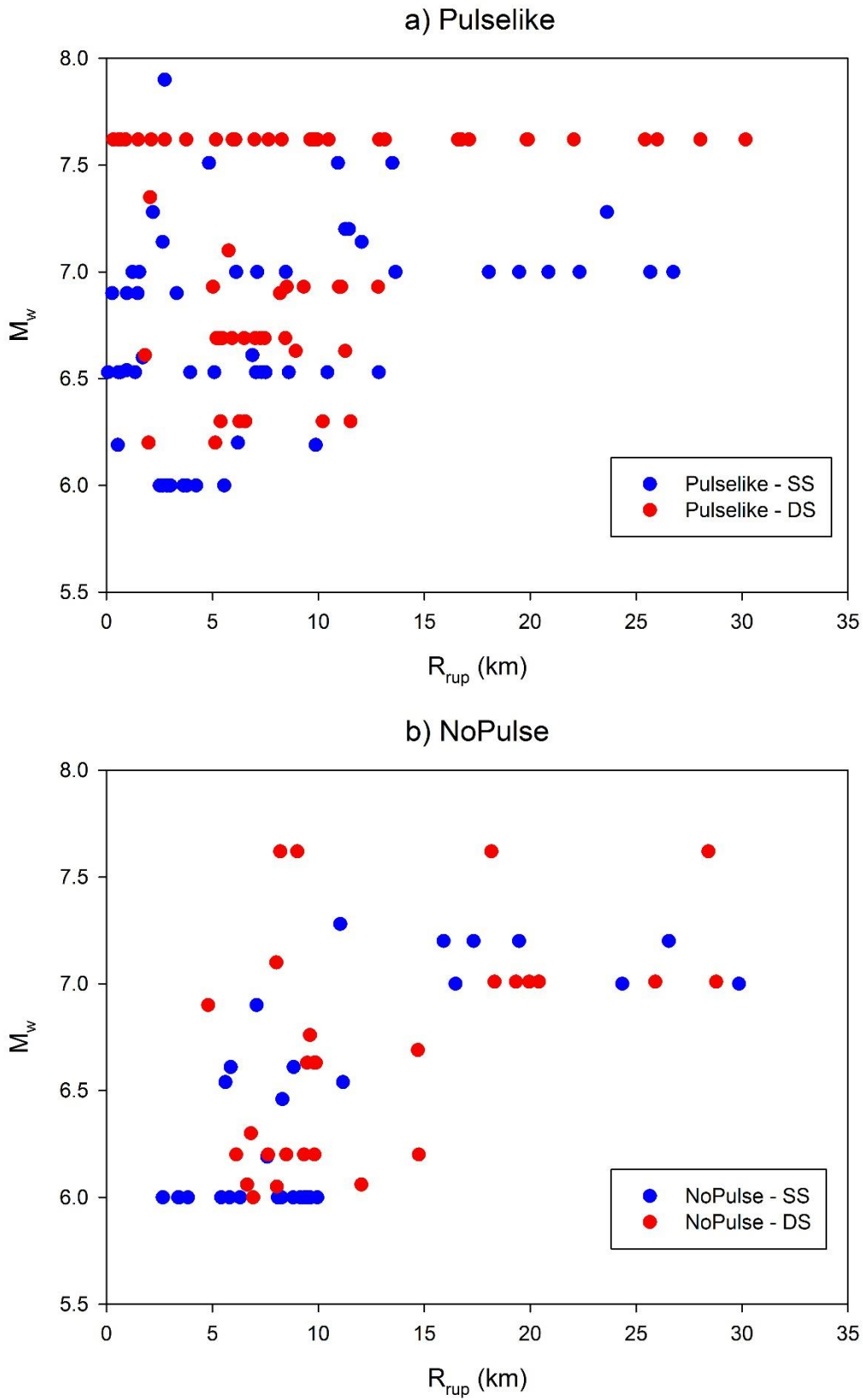


Figure 4.2 Magnitude versus distance distribution of (a) pulselike and (b) non-pulse ground motions for different styles of faults (dip-slip and strike-slip)

Strong motion recordings that exhibit unequal durations in their horizontal components or recordings from very soft soil conditions ( $V_{S30} < 140\text{m/s}$ ) as well as those having  $V_{S30} > 900\text{m/s}$  are disregarded in the database. The accelerograms with unequal durations are disregarded as  $S_{aRotD100}$  spectral computations require acceleration time series with equal lengths.  $S_{aRotD100}$  spectrum is required in the derivation of proposed spectral amplification factor between maximum direction pulselike and non-pulse horizontal ground motions. Very soft and hard rock records are also disregarded because the proposed spectral amplification factor is established from a limited number of ground-motion records and a dataset showing large  $V_{S30}$  variations may yield biased spectral amplifications in terms of soil conditions. The current  $V_{S30}$  interval ( $140\text{m/s} < V_{S30} < 800\text{m/s}$ ) of the dataset represents stiff soil conditions and the proposed amplification factor would be suitable for this  $V_{S30}$  interval. Figure 4.2 shows the magnitude vs. distance distributions of pulselike (Figure 4.2a) and non-pulse (Figure 4.2b) records. The scatters use different color codes for dip-slip (normal and reverse) and strike-slip records. The pulselike records display a fairly uniform  $M_w$  vs.  $R_{rup}$  distribution for  $R_{rup} < 15\text{km}$ . The non-pulse records are sparse and lack uniformity in terms of  $M_w$  and  $R_{rup}$ . Appendix C lists the pulselike and non-pulse ground motions with their important features.

As discussed in Chapters 2 and 3, Somerville et al. (1997) is one of the first systematic studies to distinguish the general features of directivity dominated pulselike ground motions. The Somerville et al. (1997) forward-directivity model makes use of some fault-site geometry parameters to identify the important properties of directivity-dominated ground. These parameters are length ratio for strike-slip faults,  $X$ ; a width ratio for dip-slip faults,  $Y$ ; an azimuth angle between the fault plane and ray path to site for strike-slip faults,  $\theta$ ; and a zenith angle between the fault plane and ray path to the site for dip-slip faults,  $\phi$ . (See relevant discussions in Chapter 2). These parameters are still used to identify the directivity dominated (pulselike) recordings (e.g., Huang et al., 2008). According to Somerville et al. (1997) (a)  $X\cos(\theta)$  or  $Y\cos(\phi)$  is greater than 0.5 in the forward-directivity region, and for  $M_w > 6.5$  and for  $T > 0.6\text{s}$  the geomean spectral demands of directivity dominated records are larger than those estimated from the conventional GMPEs, (b) for  $M_w > 6$  and  $T > 0.5\text{s}$ , strike-

normal (SN or fault-normal; FN) spectral demands are, on average, greater than the strike-parallel (SP or fault parallel; FP) spectral demands when  $\theta$  or  $\phi$  is less than  $45^\circ$ .

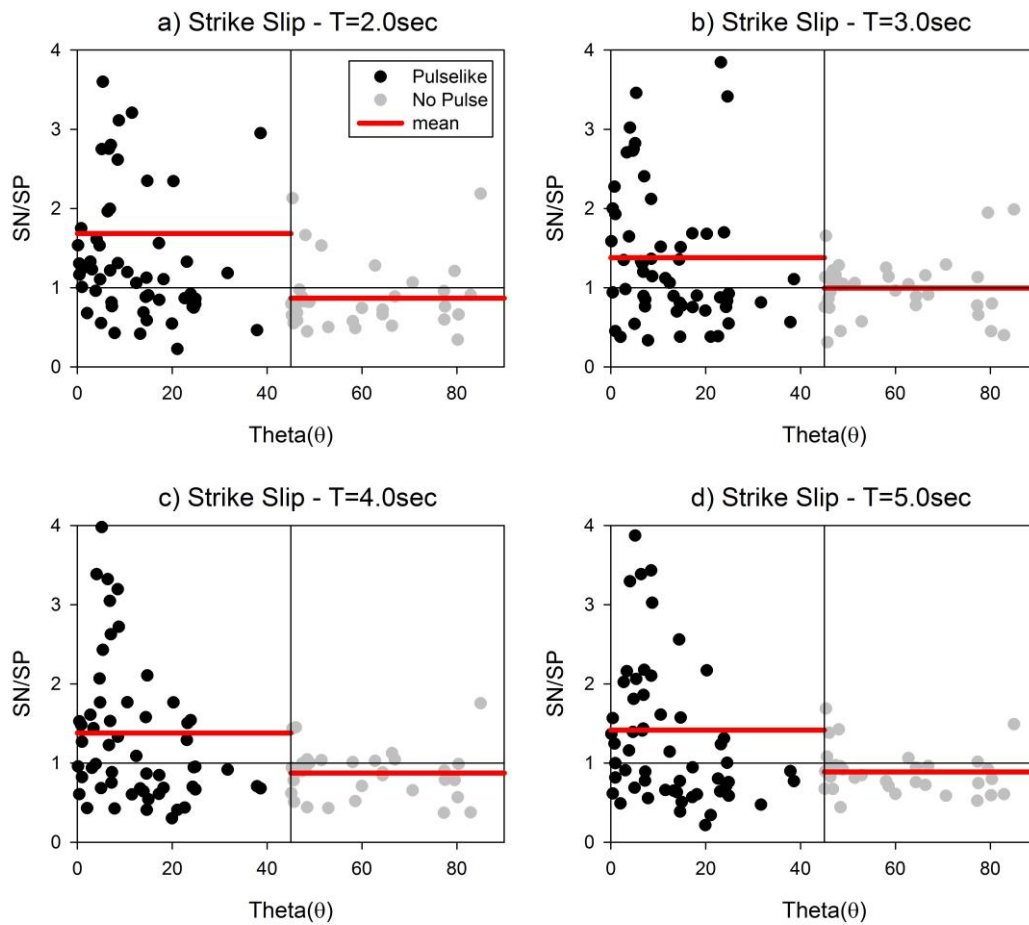


Figure 4.3 Comparisons of SN/SP spectral ratios at  $T = 2s, 3s, 4s$  and  $5s$  by considering the  $\theta = 45^\circ$  criterion as the boundary between pulselike and non-pulse strike-slip recordings. The red solid lines show the average of pulselike and non-pulse SN/SP ratios.

Figure 4.3 compares the SN-to-SP (SN/SP) spectral ratios of strike-slip pulselike and non-pulse datasets at  $T = 2s, 3s, 4s$  and  $5s$  by considering the second observation of Somerville et al. (1997). The pulselike recordings are those having  $\theta \leq 45^\circ$  and the non-pulse recordings are designated by  $\theta > 45^\circ$ . The panels in Figure 4.3 also show the average of SN/SP spectral ratios ( $\overline{SN/SP}$ ) for pulselike and non-pulse records. The SN/SP pulselike records attain larger values that is also certified by their larger mean (i.e.,  $\overline{SN/SP}$ ) with respect to non-pulse recordings. Figure 4.4 displays the

same comparison for dip-slip (i.e., normal and reverse faults) recordings. The same observations are also valid for this case: SN/SP spectral ratios of pulselike ground motions exhibit larger values with respect to those of non-pulse records.

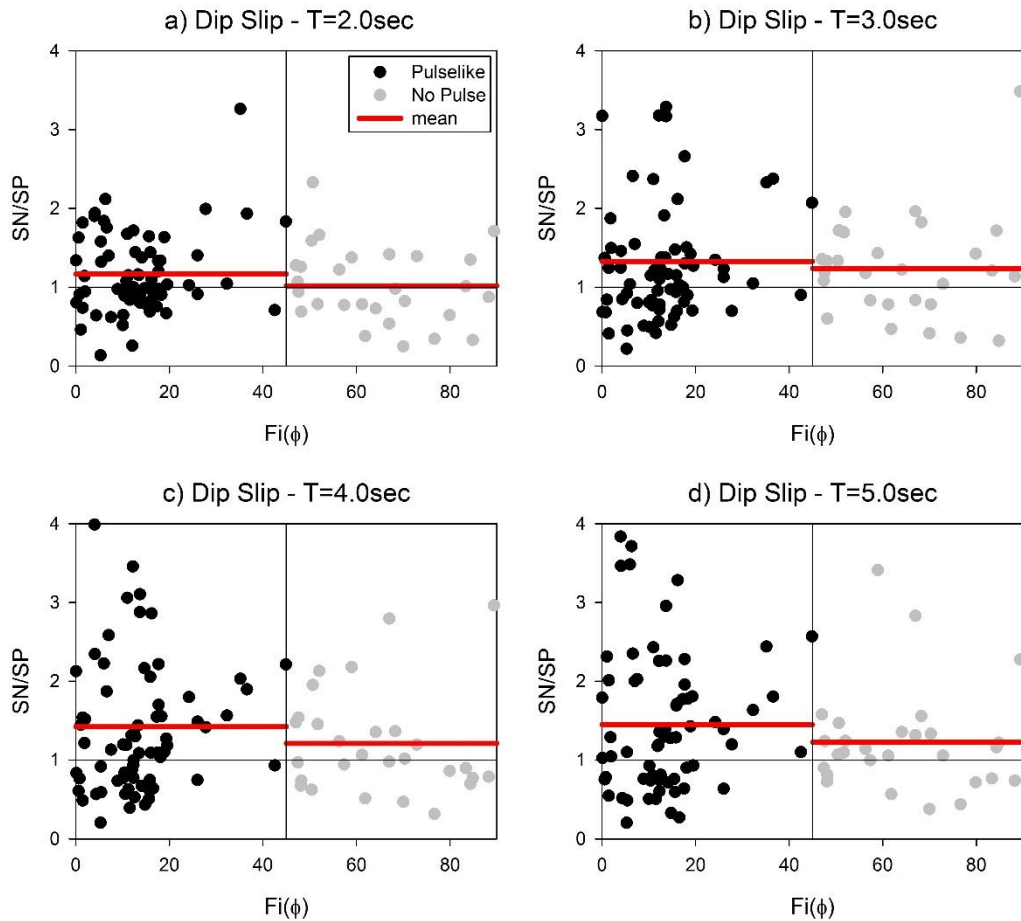


Figure 4.4 Comparisons of SN/SP spectral ratios at  $T = 2s, 3s, 4s$  and  $5s$  by considering the  $\phi = 45^\circ$  criterion as the boundary between pulselike and non-pulse dip-slip recordings. The red solid lines show the average of pulselike and non-pulse SN/SP ratios.

Figure 4.5 and Figure 4.6 further validate the above remarks by implementing the first observation of Somerville et al. (1997) to data in hand. This time the SN/SP spectral ratios at  $T = 2s, 3s, 4s$  and  $5s$  are compared between pulselike and non-pulse records by making use of  $X\cos\theta = 0.5$  (strike-slip) and  $Y\cos\phi = 0.5$  border (dip-slip). The pulselike SN/SP spectral ratios are populated in the  $X\cos\theta \geq 0.5$  (strike-slip events; Figure 4.5) or  $Y\cos\phi \geq 0.5$  regions (dip-slip events; Figure 4.6). As expected, these figures also depict larger SN/SP ratios for pulselike recordings.

The discussions in this section suggest that the compiled pulselike and non-pulse recordings follow the observations made by Somerville et al. (1997) that is a one of the renown studies in the literature to identify the distinctive features of directivity-dominated ground motions. Thus, these recordings can be used in confidence to develop the empirical modification factors to estimate the maximum rotated horizontal component for directivity effects ( $RotD100_{directivity}$ ). The following sections describe the methodology followed to reach this objective.

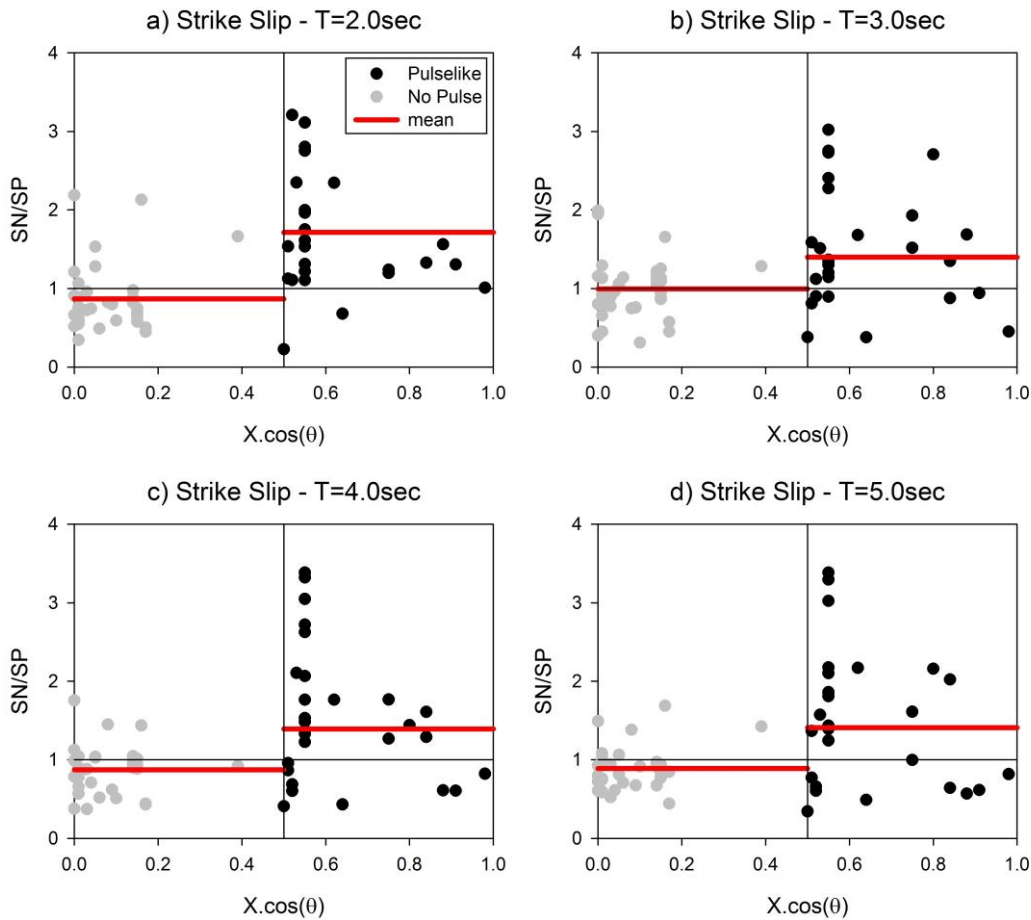


Figure 4.5 Comparisons of SN/SP spectral ratios at  $T = 2s, 3s, 4s$  and  $5s$  by considering the  $X\cos(\theta) = 0.5$  criterion as the boundary between pulselike and non-pulse strike-slip recordings. The red solid lines show the average of pulselike and non-pulse SN/SP ratios.

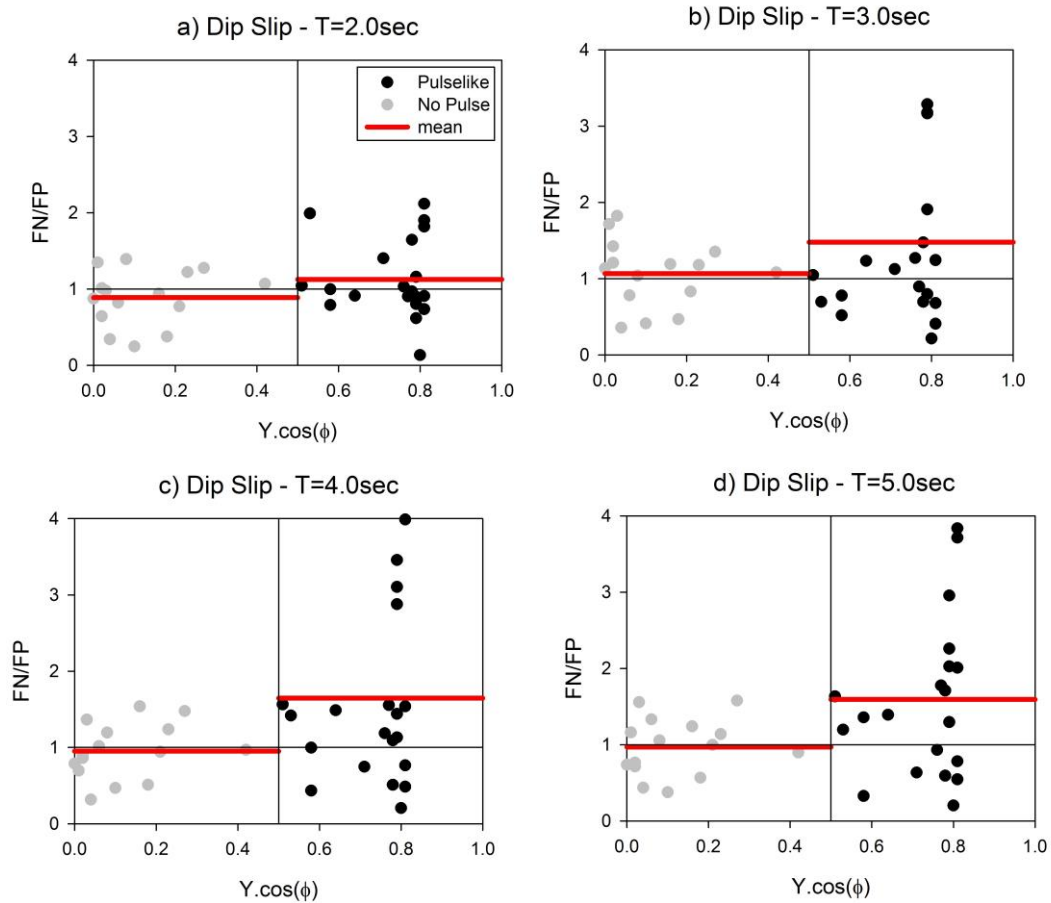


Figure 4.6 Comparisons of SN/SP spectral ratios at  $T = 2s, 3s, 4s$  and  $5s$  by considering the  $Y\cos(\phi) = 0.5$  criterion as the boundary between pulselike and non-pulse dip-slip recordings. The red solid lines show the average of pulselike and non-pulse SN/SP ratios.

#### 4.4 Conceptual Discussions on $RotD100_{directivity}$

In recent years, several studies have proposed conversion factors to estimate the maximum rotated horizontal component of ground motions ( $RotD100$ ) from an arbitrary horizontal component definition. (In fact, most of the time the proposed conversion factors aim to convert geomean type horizontal components -  $GMRotI50$ ). This is because the specification of maximum direction ground motions (i.e.,  $RotD100$ ), referred to as directionality, gains popularity in seismic design codes (ASCE, 2010; BSSC 2009; 2015). The studies by Beyer and Bommer (2006), Campbell and Bozorgnia (2008) and Huang et al. (2008) proposed conversion factors to estimate maximum rotated horizontal spectral acceleration component ( $Sa_{RotD100}$ )

from GMRotI50 spectral acceleration ( $Sa_{GMRotI50}$ ). These studies use the  $Sa_{RotD100}$  to  $Sa_{GMRotI50}$  ratios from observed ground-motion data to propose their empirical conversion factors. The 2009 NEHRP provisions (FEMA P-750; BSSC, 2009) also propose similar conversion factors that are based on the studies of Huang et al. (2008). Shahi and Baker (2014) propose a conversion factor that scales  $Sa_{RotD50}$  component for the maximum rotated component ( $Sa_{RotD100}$ ). Shahi and Baker (2014) use the scaling factors provided by Boore (2010) to modify their conversion expression (i.e.,  $Sa_{RotD100}/Sa_{RotD50}$ ) to ( $Sa_{RotD100}/Sa_{GMRotI50}$ ). The later study investigates the relation between  $Sa_{RotD50}$  and  $Sa_{GMRotI50}$  indicating that, on average, there are slight differences between the spectral amplitudes of these two horizontal component definitions and the differences are insignificant for many engineering studies. Hence, these two conversion factors (i.e.,  $Sa_{RotD100}/Sa_{RotD50}$  and  $Sa_{RotD100}/Sa_{GMRotI50}$ ) can be assumed the same without losing significant accuracy. Figure 4.7 compares different conversion models proposed for  $Sa_{RotD100}/Sa_{GMRotI50}$  ratio. Note that the 2015 NEHRP provisions (FEMA P-1050; BSSC, 2015) still use the same scaling factors of the 2009 edition of NEHRP provisions to convert geomean horizontal component definitions for maximum rotated component.

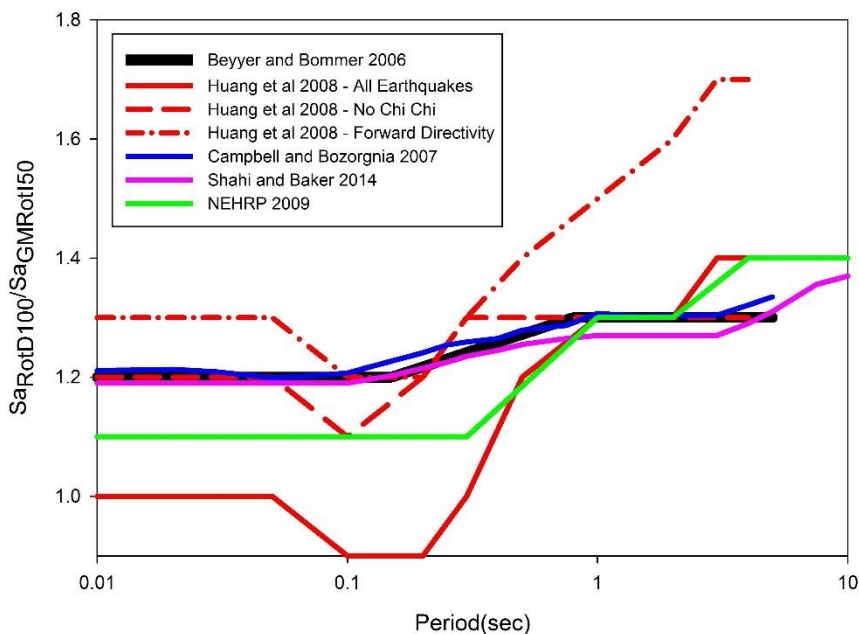


Figure 4.7 Comparison of different scaling (conversion) models proposed for  $Sa_{RotD100}/Sa_{GMRotI50}$  ratio

The curves by Campbell and Bozorgnia (2007), Beyer and Bommer (2006), and Shahi and Baker (2014) follow very similar trends as given in Figure 4.7 because these conversion models blend the near-fault and far-fault records in the same ground-motion dataset. The 2009 edition of NEHRP curve is a compromise between Huang et al. (2008) “all earthquakes” and “no Chi-Chi” cases. Note that the Huang et al. (2008) curves are developed from near-fault recordings but they are classified into different bins including (a) those of forward-directivity dominant ground motions, (b) all near-fault recordings in the database, and (c) near-fault ground motions excluding those of the 1999 Chi-Chi, Taiwan earthquake. That’s why the curves by Huang et al. (2008) follow a different path with respect to other conversion models. As a matter of fact, the Huang et al. (2008) “forward-directivity” conversion factor imposes significantly larger values with respect to the other models since it combines the directivity as well as directionality effects in a single curve. In other words, the “forward-directivity” conversion factors by Huang et al. (2008) establish a relationship between the geomean horizontal component and the maximum direction horizontal component including forward-directivity. It should be noted that the curves presented in Figure 4.7 display median conversion values whereas the compared models also provide the 84<sup>th</sup> percentile curves to account for ground-motion variability.

The comparative plots in Figure 4.7 indicate the lack of an intermediate relationship between  $S_{a_{RotD100}}$  and directivity-dominated maximum-direction spectral amplitudes ( $S_{a_{RotD100directivity}}$ ). The significance of directivity-dominated spectral demands for maximum rotated component is emphasized by Bradley and Baker (2015) by studying the directivity-dominated ground motions of the 2010 Canterbury earthquake. Huang et al. (2008) estimate the maximum rotated component for forward-directivity effects ( $RotD100_{directivity}$ ) from a geomean horizontal component definition ( $GMRotI50$ ). The same study indicates the similarity between SN horizontal component spectral demands ( $S_{a_{FN}}$ ) and  $S_{a_{RotD100}}$  (maximum rotated component spectral demands) at sites very close to the ruptured fault segment ( $R_{rup} < 3\text{km}$ ) when forward-directivity conditions are met. However, this assertion loses its validity as rupture distance increases even if the directivity effects are still

prominent. Thus, a conversion factor between the spectral demands of maximum rotated component ( $Sa_{RotD100}$ ) and maximum rotated component dominated by directivity ( $Sa_{RotD100,directivity}$ ) would have practical implications for code-based spectrum development. In essence, this chapter provides this model by taking the ratios of spectral demands of RotD100 horizontal component between pulselike and non-pulse recordings. This is given in Equation 4.2.

$$AF_{directivity} = \frac{Sa_{RotD100,directivity,observed}}{Sa_{RotD100,nodirectivity,observed}} \quad 4.2$$

Note that the spectral demands of maximum rotated component dominated by directivity can be computed from Equation 4.3.

$$Sa_{RotD100,Directivity} = Sa_{RotD50} \cdot AF_{RotD100} \cdot AF_{directivity} \quad 4.3$$

where  $AF_{RotD100}$  can be the directionality conversion factor proposed by Shahi and Baker (2014) or it could be the conversion factor by Beyer and Bommer (2006) if RotD50 spectral demands are assumed to be the same as GMRotI50 spectral demands. In fact, the next chapter presents directivity amplification expressions for strike-normal spectral demands from the Shahi and Baker (2011) narrow-band directivity model by modifying the GMRotI50 elastic spectrum. Thus, comparisons of  $AF_{RotD100} \cdot AF_{directivity}$  with the proposed model in the next chapter would lead to useful observations about (a) directivity models presented in this chapter and the next chapter as well as their implications on code spectrum for directivity effects, and (b) the similarity (as well as validity) between SN and maximum rotated component spectral demands under directivity dominant cases. The next chapter also develops an alternative directivity amplification equation for  $Sa_{RotD50,directivity}$  by considering the Chiou and Spudich (2013) directivity model. Thus, the developed  $AF_{directivity}$  expression can be useful to understand the level of difference between  $Sa_{RotD50,directivity}$  and  $Sa_{RotD100,directivity}$ . This is again a topic considered in the next chapter.

#### 4.5 Proposed Model for Calculation of $RotD100_{directivity}$

The database presented in Section 4.3 is used for the computation  $AF_{directivity}$ . The dataset is divided into different bins considering different magnitude and distance intervals. The bins are generated whenever the number of data (either in pulselike or non-pulse ground-motion groups) are greater than 4. This limitation is necessary

since the ratio expression given in Equation (4.2) is developed from the median spectrum computed from each bin. Average statistics determined from a small number of data would be dubious for computing reasonable spectral amplifications. Table 4.2 lists the ground-motion bins, the number of data in each bin as well as their magnitude and distance intervals. In brief, the ground-motion bins are classified into two broad magnitude bins ( $6.0 < M_w < 7.0$  and  $7.0 < M_w < 8.0$ ). The bins having close distance ( $R_{rup} < 15\text{km}$ ) recordings are the majority. There is one pulslike and non-pulse ground-motion bin pair from the larger magnitude interval ( $7.0 < M_w < 8.0$ ) representing recordings of distances between  $15\text{km} < R_{rup} < 30\text{km}$ . The sparse data do not allow a rupture-mechanism (dip slip vs. strike-slip) type classification in the computation of  $AF_{\text{directivity}}$ .

Table 4.2 Classification of the records for different magnitude, distance and site class ranges and the related subgroups

<b>Moment Magnitude</b>	<b><math>R_{rup}</math> (km)</b>	<b>Number of pulslike records</b>	<b>Number of non-pulse records</b>
$6.0 < M_w < 7.0$	$0 < R_{rup} < 5$	23	6
$6.0 < M_w < 7.0$	$5 < R_{rup} < 10$	29	36
$6.0 < M_w < 7.0$	$10 < R_{rup} < 15$	8	5
$7.0 < M_w < 8.0$	$0 < R_{rup} < 15$	37	4
$7.0 < M_w < 8.0$	$15 < R_{rup} < 30$	16	7

The median spectral amplitudes (log mean of spectral amplitudes) as well as  $Sa_{\text{RotD100directivity}}$  and  $Sa_{\text{RotD100nondirectivity}}$  spectra of individual ground motions in the ground-motion bins listed in Table 4.2 are given in Figure 4.8 and Figure 4.9, respectively. Note that no attempt is made to eliminate some of the outlier spectral variations since data is quite limited. These outlier spectral shapes are considered as the cases showing intricate nature of the ground motions and in a way depict record-to-record variability.

The median ratio curves (medians of  $Sa_{\text{RotD100directivity}}$  to  $Sa_{\text{RotD100nondirectivity}}$  from pulslike and non-pulse bin pairs) are displayed in Figure 4.10. Larger spectral amplifications due to directivity are observed at closer sites independent of magnitude (i.e.,  $AF_{\text{directivity}}$  values of  $6 < M_w < 7$ ,  $0\text{km} < R_{rup} < 5\text{km}$  are the largest with respect to all

other amplification values). Although vague, in general, the  $AF_{\text{directivity}}$  variations show an increasing trend up to a certain spectral period that is followed by a more stable trend towards longer periods. This trend is similar to the one observed from Chiou and Youngs (2013) narrow-band directivity model. (See discussions on CHS13 directivity model held in Chapter 3 as well as Chapter 5).

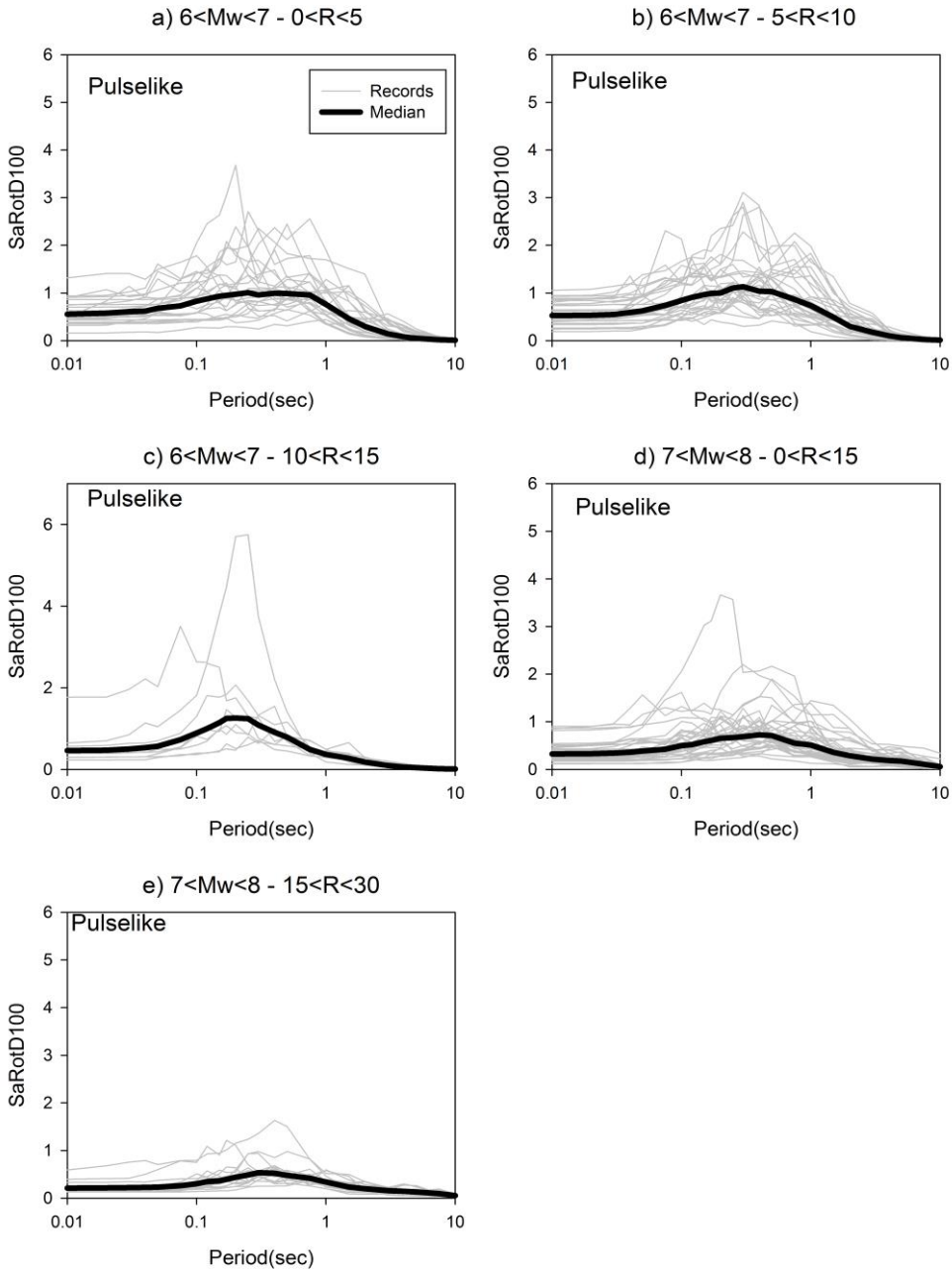


Figure 4.8  $Sa_{\text{RotD100directivity}}$  (from pulselike records) spectral amplitudes of individual ground motions of the bins given in Table 4.2

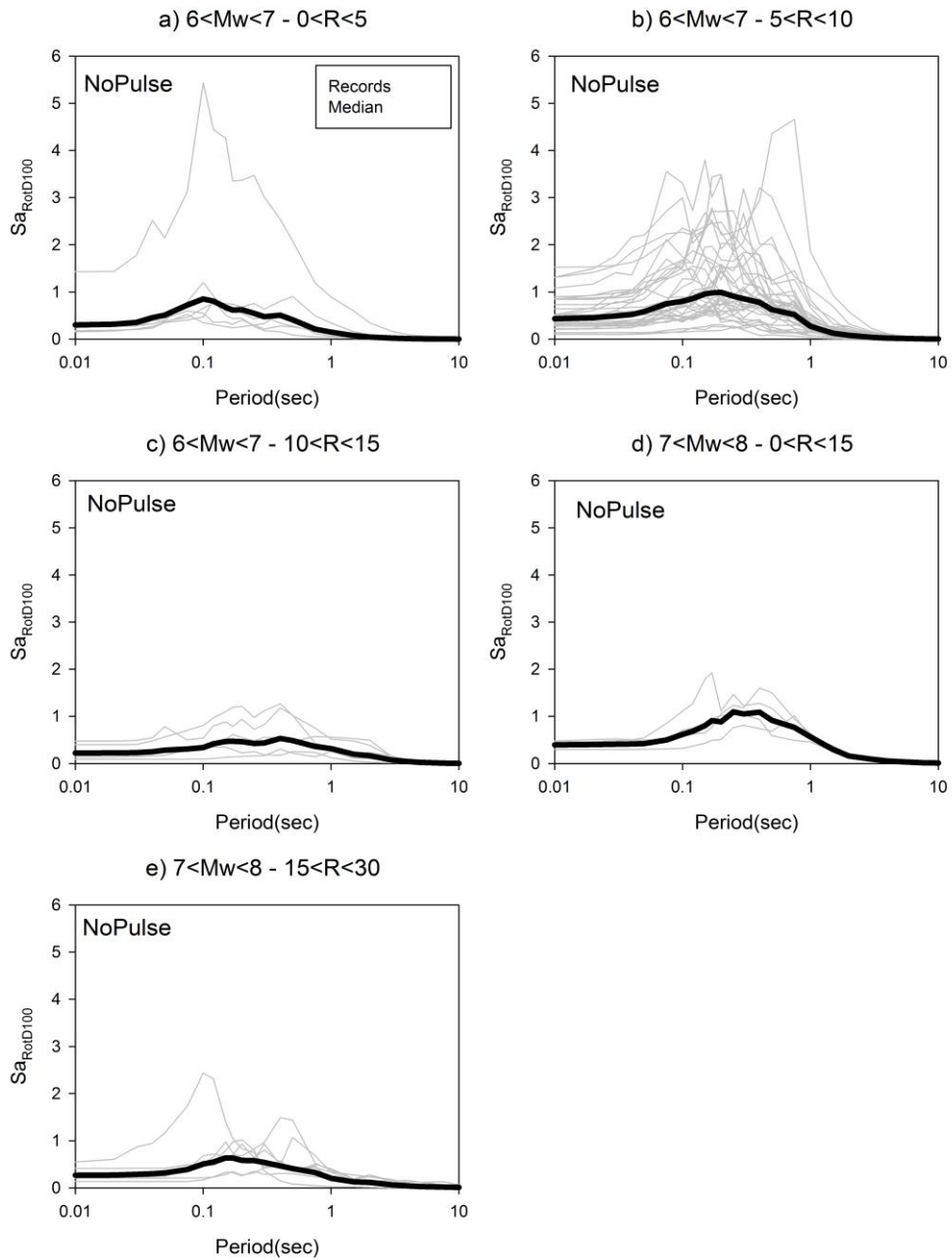


Figure 4.9  $Sa_{RotD100nodirectivity}$  (from non-pulse records) spectral amplitudes of individual ground motions of the bins given in Table 4.2

The aforementioned observation is violated only by the  $AF_{directivity}$  curve of  $7 < M_w < 8$  and  $0 \text{ km} < R_{rup} < 15 \text{ km}$  bin that follows a spectral amplification trend similar to SHB11 narrow-band directivity model. (See discussions on CHS13 directivity model held in Chapter 3 as well as Chapter 5). However, this analogy can be considered as weak and it would be difficult to justify because it is the only  $AF_{directivity}$  curve showing a trend comparable to SHB11 narrow-band directivity model and, yet, the gradient of

descending branch (after  $T \approx 7s$ ) is very slow with respect to those of SHB11 model presented in Chapters 3 and 5. Given the sparse data in the considered database, the shape-wise similarity in SHB11 and  $AF_{\text{directivity}}$  curve for the  $7 < M_w < 8$  and  $0\text{km} < R_{\text{rup}} < 15\text{km}$  bin is coincidental.

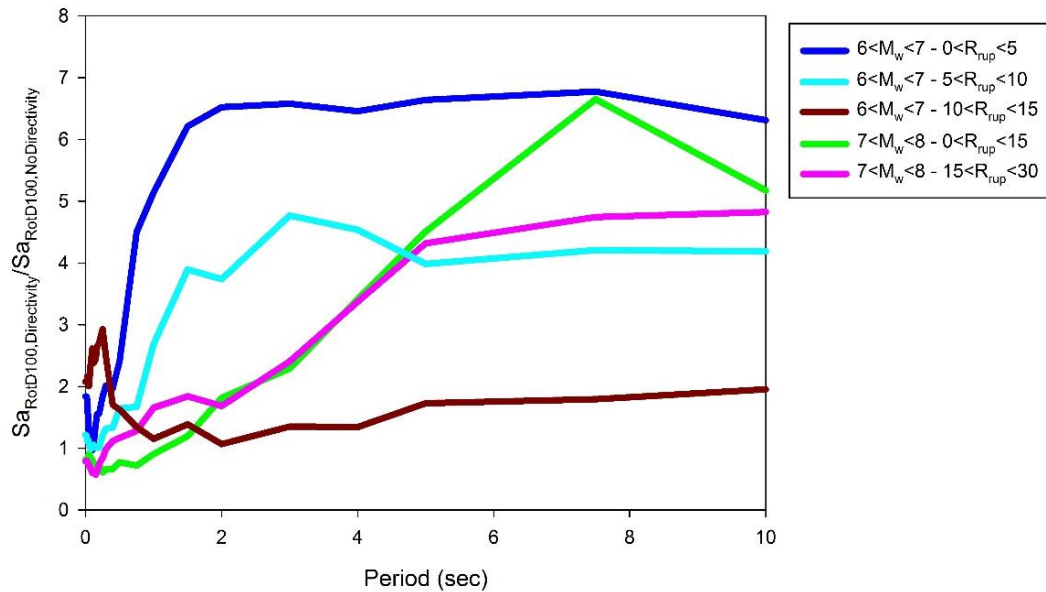


Figure 4.10  $AF_{\text{directivity}}$  curves computed from median  $Sa_{\text{RotD100directivity}}$  to  $Sa_{\text{RotD100nodirectivity}}$  ratios of the ground-motion bins presented in Table 4.2

For comparison purposes, the same exercise is repeated for  $Sa_{\text{RotD50directivity}}/Sa_{\text{RotD50nodirectivity}}$  using the same ground-motion bins presented in Table 4.2. The RotD50 spectra for directivity and nodirectivity bins are given in Figure 4.11 and Figure 4.12, respectively. These plots also display the mean logarithmic spectrum of each ground-motion bin as well. The log-mean  $Sa_{\text{RotD50directivity}}/Sa_{\text{RotD50nodirectivity}}$  ratios are presented in Figure 4.13. Note the significant similarity between these spectral ratios and those presented in Figure 4.10 (log-mean  $Sa_{\text{RotD100directivity}}/Sa_{\text{RotD100nodirectivity}}$  ratios). The observed similarity between the spectral ratios for different horizontal component definitions requires further investigation and may suggest that the pulselike and non-pulse ground-motion databases as well as the ratio computations have some specific implications. This topic would be discussed later in the last section of Chapter 5.

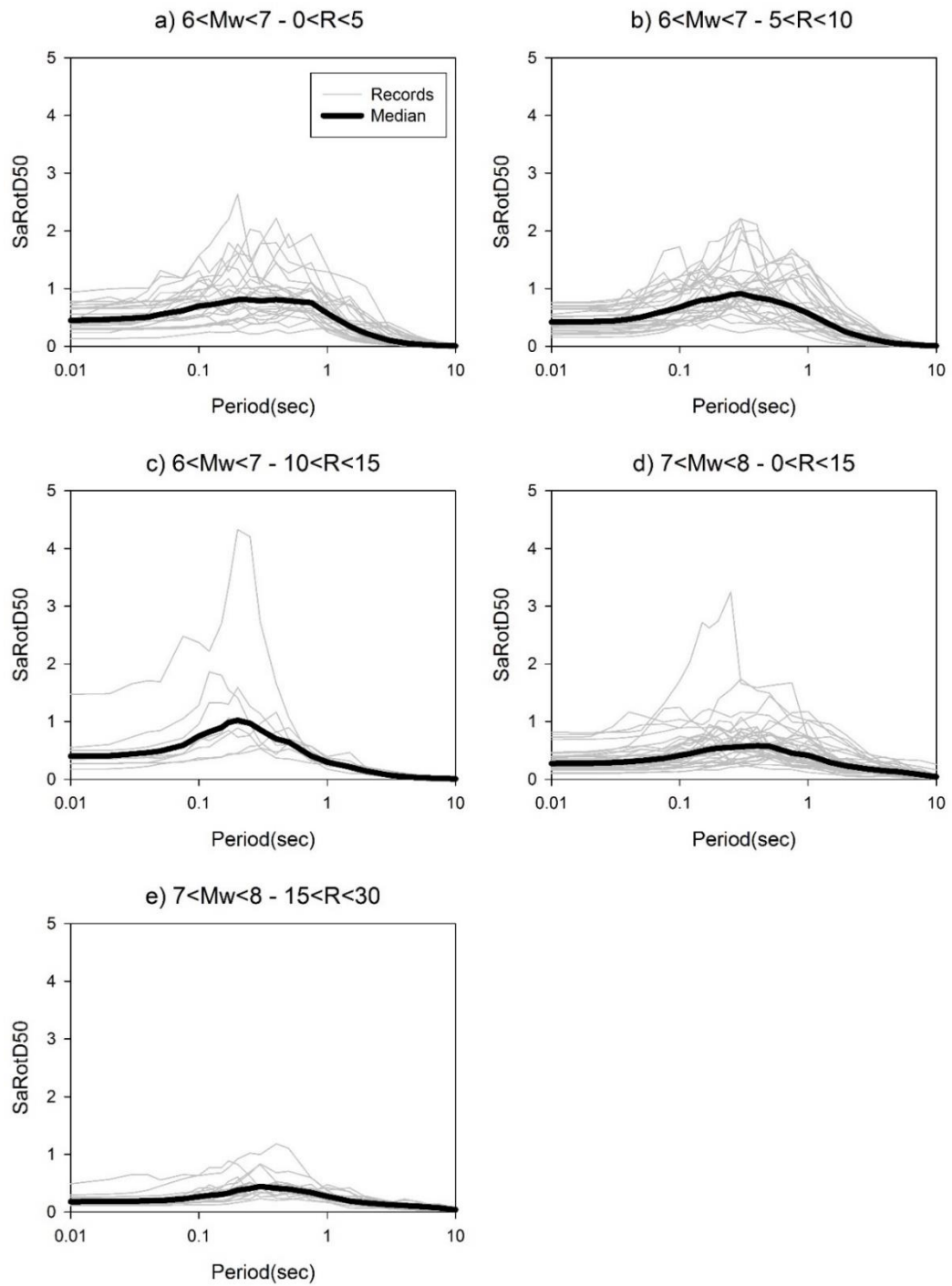


Figure 4.11  $Sa_{RotD50}^{directivity}$  (from pulselike records) spectral amplitudes of individual ground motions of the bins given in Table 4.2. The solid black lines are the log-mean (median) spectral curves of each bin.

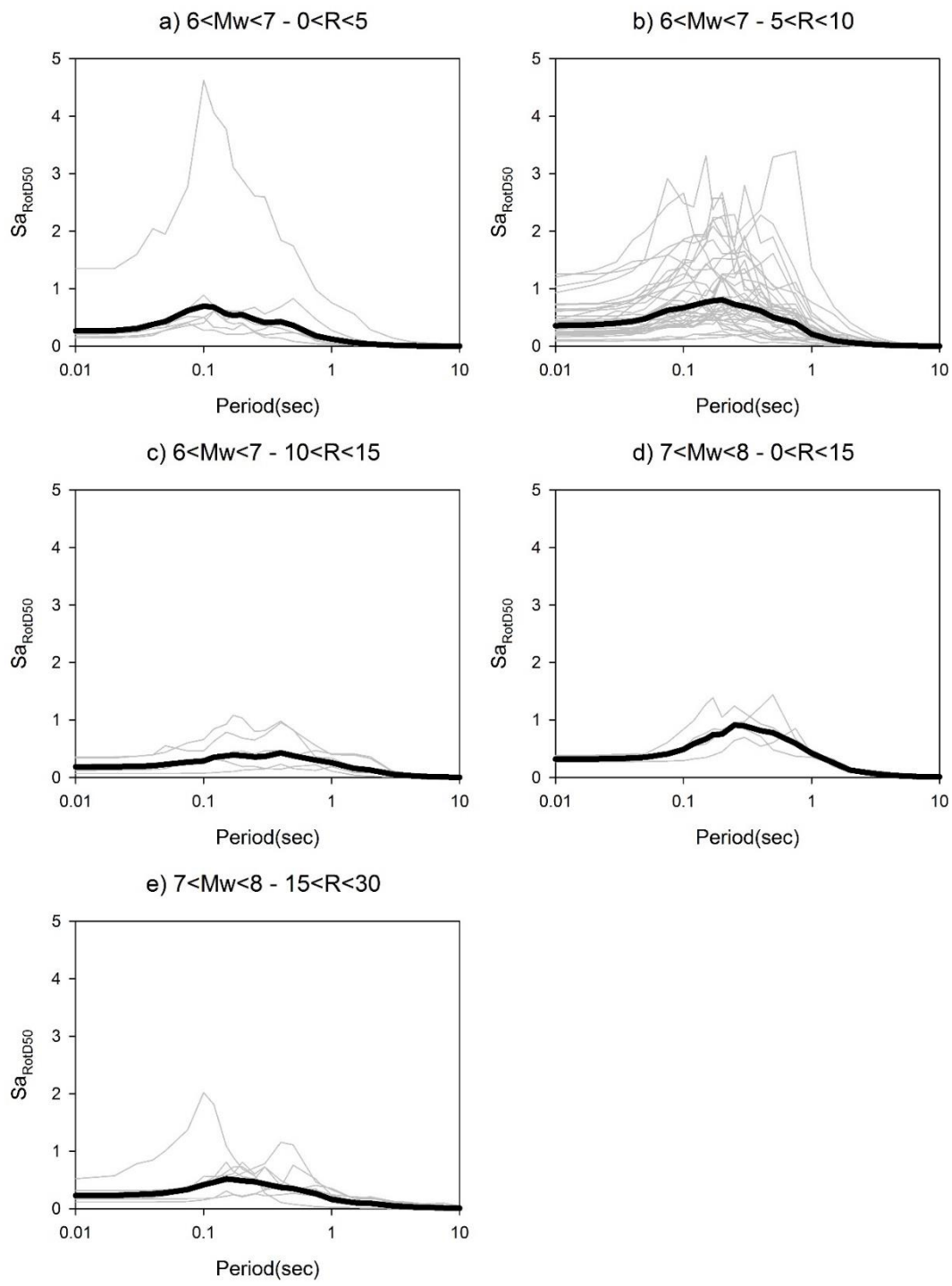


Figure 4.12  $Sa_{RotD50_{non-directional}}$  (from non-pulse records) spectral amplitudes of individual ground motions of the bins given in Table 4.2. The solid black lines are the log-mean (median) spectral curves of each bin

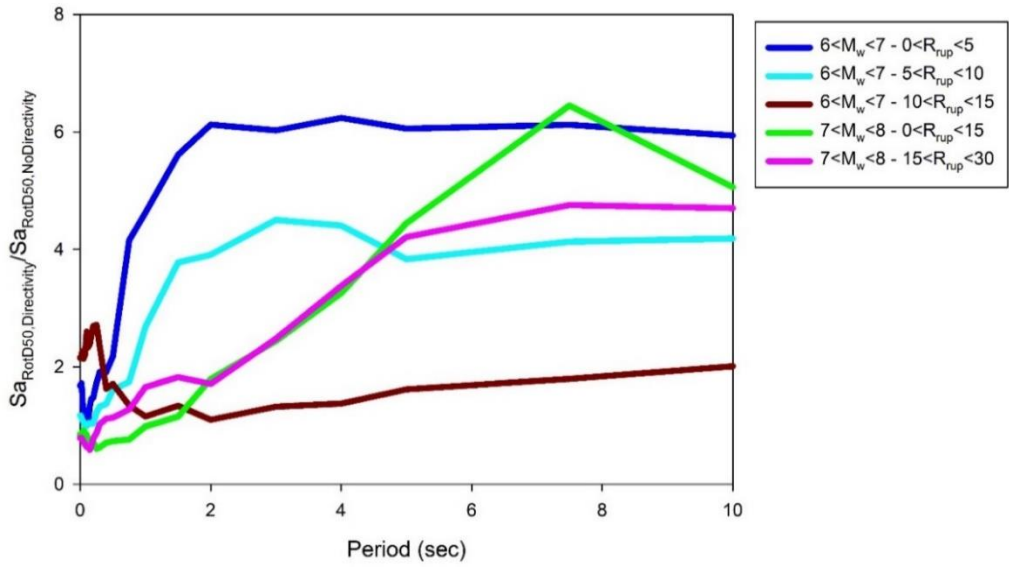


Figure 4.13 Median  $Sa_{RotD50directivity}$  to  $Sa_{RotD50nodirectivity}$  ratios computed by normalizing the median  $Sa_{RotD50directivity}$  spectrum of each pulse-like ground-motion bin in Table 4.2 with the corresponding median  $Sa_{RotD50nodirectivity}$  spectrum of non-pulse ground-motion bin

#### 4.6 Summary and Conclusion

This chapter emphasizes the significance of directionality in response spectrum computations and investigates the relationship between directivity and nondirectivity spectral amplifications for maximum direction (RotD100) (i.e.,  $AF_{directivity} = Sa_{RotD100directivity}/Sa_{RotD100nodirectivity}$ ). A specific dataset is compiled from pulselike and non-pulse ground motions having magnitudes between  $6 < M_w < 8$  and rupture distances up to  $R_{rup} = 30$  km. The rupture mechanisms of the compiled ground motions are either dip-slip or strike-slip whereas  $V_{S30}$  values used as an indicator for site conditions range between  $140 \text{ m/s} < V_{S30} < 900 \text{ m/s}$ . The non-pulse data resemble backward directivity phenomenon and pulselike data represent directivity-dominated earthquake scenarios. To this end, RotD100 spectral ratios of pulselike and non-pulse records populated under different magnitude and distance intervals would yield a first-order approximation on spectral amplitude variations along maximum direction between directivity-dominated and nondirectivity near-source recordings. The  $AF_{directivity}$  ratios computed under these conditions for earthquake scenarios (or magnitude and distance intervals) given in Table 4.2 are presented in Figure 4.10. Note that for very close distances to the ruptured fault segment ( $R_{rup} < 5$  km), the

$AF_{\text{directivity}}$  ratios exhibit significantly large values ( $AF_{\text{directivity}} \approx 6.5$  for  $T > 2\text{s}$  even if the magnitude range is between  $6 < M_w < 7$ ).

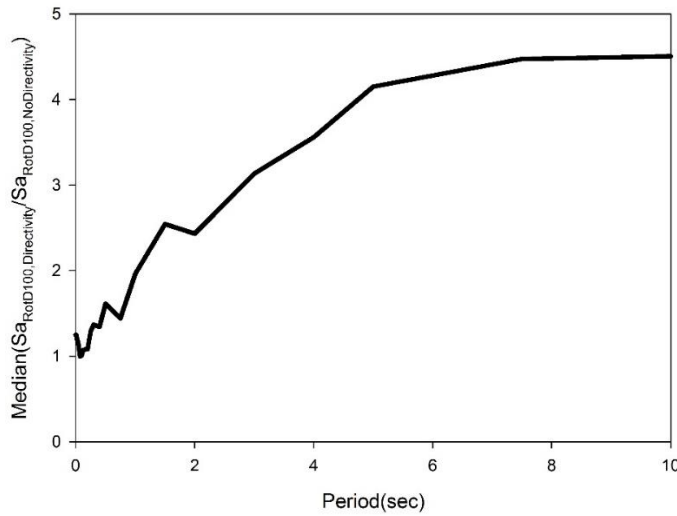


Figure 4.14 Median of  $Sa_{\text{RotD100directivity}}$  to  $Sa_{\text{RotD100nodirectivity}}$  ratios presented in Figure 4.10

In fact, Figure 4.14 shows the period-dependent median variation of  $AF_{\text{directivity}}$  curves given in Figure 4.10 for an overall idea about the directivity-dominated spectral amplification along maximum direction. Table 4.3 lists the period dependent variation of this median curve.

As indicated above, the proposed relationships are developed from a limited number of data that may pose questions about the reliability of the presented results. They do not reveal any explicit information about fault-site geometry as discussed in Chapter 3. Besides the magnitude and distance intervals are quite large. Moreover, the median  $Sa_{\text{RotD50directivity}}/Sa_{\text{RotD50nodirectivity}}$  ratios (Figure 4.13) that are computed for the same ground-motion bins are very similar to those of  $Sa_{\text{RotD100directivity}}/Sa_{\text{RotD100nodirectivity}}$ . The observed similarity can be an indicator of some specific features in the compiled pulseline and non-pulse ground-motion bins that are reflected on the the ratio statistics. This topic will be discussed in the last section of Chapter 5.

Nevertheless, to the best knowledge of the author, this type of relationship ( $Sa_{\text{RotD100directivity}}/Sa_{\text{RotD100nodirectivity}}$ ) is presented for the first time in the literature. Essentially, this first-order relationship can serve to understand the level of spectral amplification for compound effects of directionality (along maximum direction) and directivity. The discussions in this section are also useful to see the limits of

directivity amplifications that are developed from SHB11 describing the relation between directivity-dominated fault normal to nondirectivity geomean type horizontal spectra. (See details in Chapter 5).

Table 4.3 Period-dependent variation of  $S_{\text{RotD100directivity}}$  to  $S_{\text{RotD100nondirectivity}}$  ratios presented in Figure 4.14

<b>Period (s)</b>	<b>Median of <math>S_{\text{RotD100}}</math> ratio</b>
0	1.25
0.01	1.25
0.02	1.22
0.03	1.16
0.04	1.17
0.05	1.11
0.075	1.00
0.1	1.01
0.12	1.07
0.15	1.08
0.17	1.08
0.2	1.08
0.25	1.29
0.3	1.37
0.4	1.34
0.5	1.61
0.75	1.44
1	1.96
1.5	2.55
2	2.43
3	3.14
4	3.56
5	4.15
7.5	4.47
10	4.51

Another useful relation that can be developed from the compiled pulselike and non-pulse ground-motion bins is the period-dependent RotD100/RotD50 ratios of pulselike and non-pulse records. These ratios are given in Figure 4.15 (for pulselike bins) and Figure 4.16 (for non-pulse bins). Figure 4.17 shows the median curves of the ground-motion bin specific ratios given in Figures 4.15 and 4.16. The presented median curves can be a first-order modification factor for CHS13-based directivity spectral amplifications (see Chapter 5) because, as it is already stated in Chapter 3,

CHS13 model yields spectral amplifications between  $Sa_{RotD50directivity}$  and  $Sa_{RotDnodirectivity}$  whereas the median directivity amplification presented in Figure 4.17 can rescale  $Sa_{RotD50directivity}$  for  $Sa_{RotD100directivity}$ . Table 4.4 lists the median amplification curves presented in Figure 4.17.

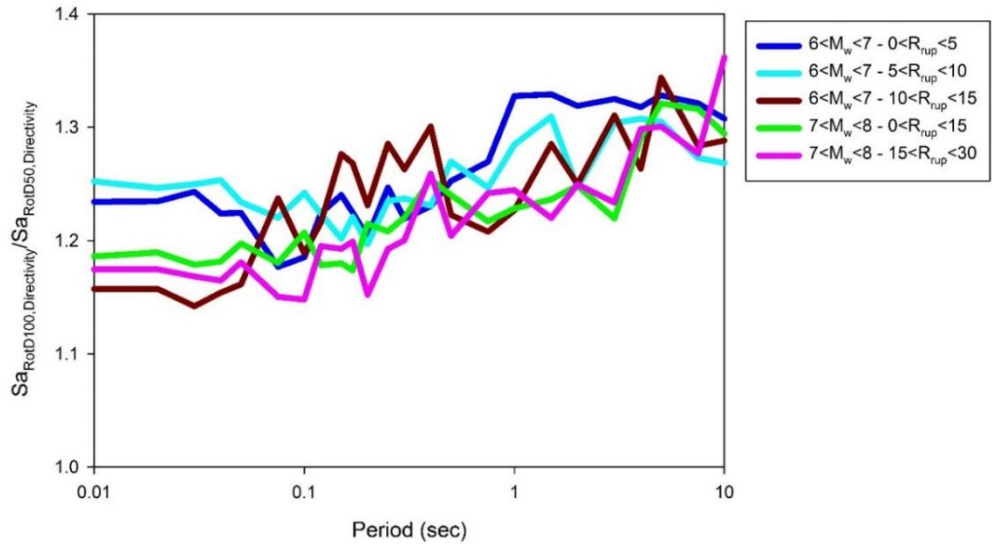


Figure 4.15 RotD100 to RotD50 spectral amplitude ratios for the pulselike bins in Table 4.2

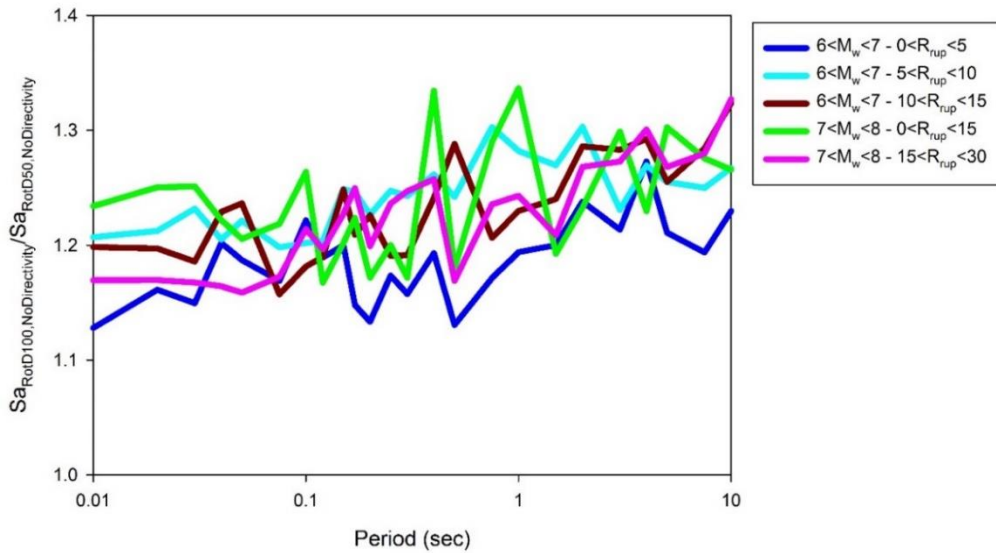


Figure 4.16 RotD100 to RotD50 spectral amplitude ratios for the nonpulse bins in Table 4.2

Table 4.4 Period-dependent variation of  $S_{a_{RotD100}}$  to  $S_{a_{RotD50}}$  ratios presented in

Figure 4.17

<b>Period (s)</b>	<b>Median of RotD100 to RotD50 for pulselike</b>	<b>Median of RotD100 to RotD50 for nonpulse</b>
0	1.1861	1.1978
0.01	1.1861	1.1985
0.02	1.1895	1.1972
0.03	1.1787	1.1859
0.04	1.1816	1.2051
0.05	1.1974	1.2056
0.075	1.1803	1.1726
0.1	1.1887	1.2142
0.12	1.2161	1.1898
0.15	1.2016	1.2272
0.17	1.2210	1.2239
0.2	1.2031	1.1992
0.25	1.2348	1.2001
0.3	1.2204	1.1913
0.4	1.2538	1.2576
0.5	1.2400	1.1796
0.75	1.2419	1.2357
1	1.2446	1.2431
1.5	1.2853	1.2088
2	1.2496	1.2683
3	1.3039	1.2728
4	1.2984	1.2730
5	1.3210	1.2552
7.5	1.2835	1.2756
10	1.2942	1.2672

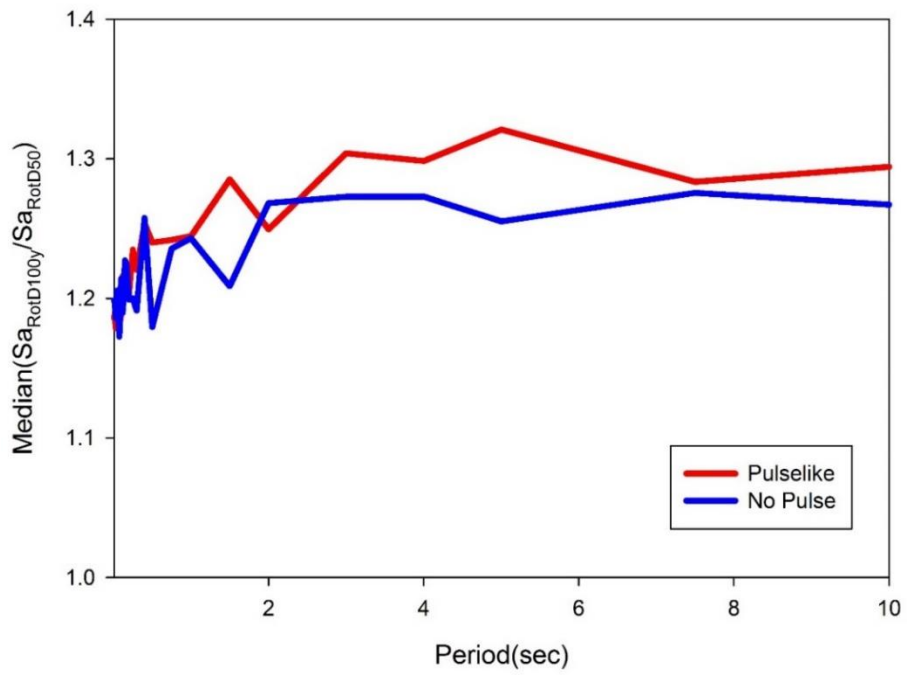


Figure 4.17 Medians of RotD100 to RotD50 spectral ratio curves computed from pulselike (Figure 4.15) and non-pulse (Figure 4.16) bins

## CHAPTER 5

### AMPLIFICATION MODELS FOR FORWARD-DIRECTIVITY

#### 5.1 Introduction

In Chapter 3 the effects of some salient seismological parameters such as slip rate and fault characteristic magnitude on directivity dominant spectral amplifications are investigated. In addition, the influence of target hazard level (mean annual exceedance rate or return period) as well as source-site geometry are studied to address the variations in spectral ordinate amplifications under directivity. The observations show that the above parameters play important roles on the directivity dominated spectral amplifications but different narrow-band models (SHB11 and CHS13 in this case) consider their affects at different levels. SHB11 is sensitive to all of the above parameters to describe the forward-directivity dominated spectral amplitudes whereas CHS13 model is influenced by the characteristic magnitude and source-site geometry while estimating spectral amplifications for directivity.

Based on the findings and observations of Chapter 3, the expressions for directivity amplification are proposed in this chapter for their direct incorporation to elastic response spectrum. The important point about the proposed expressions is their level of complexity. In other words, the expressions proposed here are kept simple enough to facilitate their implementation to seismic design codes with a balance of preserving their effectiveness and efficiency in predicting the directivity dominated spectral amplification factors.

In order to show how a model can be very complex, SHB11 narrow-band model is used to propose two alternative forward-directivity spectral amplification expressions for 475-year and 2475-year return periods. The complicated expressions developed from SHB11 also showed the approach to develop the simpler formulations. Of the two alternative SHB11 based expressions, the simpler one is compared with another

formulation developed from the CHS13 narrow-band model to comprehend how different narrow-band directivity models describe the spectral amplifications due to directivity. A similar discussion already takes place in Chapter 3 while highlighting the influence of seismological and geometrical parameters in directivity dominated spectral amplitudes. However, this time the comparisons are focused on the implications of different narrow-band directivity models on the design spectrum.

## 5.2 Complex Nature of Forward-directivity Spectral Amplification

The forward-directivity spectral amplification is affected by a set of geometrical and seismological parameters as discussed in Chapter 3. The major objective in this chapter is to propose spectral amplification expressions for directivity that can represent the variations in elastic spectral ordinates under different directivity scenarios. However, the contribution of several seismological and geometrical factors (used as estimator parameters in the proposed expressions) to describe the directivity-dominated spectral amplifications makes it difficult to propose a simple amplification model. Besides, the interaction (correlation) between these parameters may complicate the nature of proposed expressions. As an example, the fault characteristic magnitude not only changes the spectral amplification amplitudes due to directivity but also affects the period range where spectral amplifications become maximum (discussed in Section 3.3). In order to address and illustrate the complexity of the directivity-dominated spectral amplifications a set of equations is developed from SHB11 narrow-band model by considering all the contributing seismological and geometrical parameters. The expressions for estimating the spectral amplifications due to directivity are developed from the normalized spectral ordinates: given a specific return period directivity dominated spectral ordinates ( $S_{a_{\text{directivity}}}$ ) are normalized with their counterparts that disregard the directivity ( $S_{a_{\text{no-directivity}}}$ ). In other words, the developed expressions in this section as well as in the rest of this chapter estimate  $S_{a_{\text{directivity}}}/S_{a_{\text{no-directivity}}}$  ratio. Although the earthquake scenarios used in the calculations of  $S_{a_{\text{directivity}}}/S_{a_{\text{no-directivity}}}$  are already given in Table 3.1, they are repeated here for convenience. Five different fault lengths (FL = 20km, 50km, 100km, 150km and 300km) with a constant fault width (FW=10km) to represent five different characteristic magnitude ( $M_{\text{ch}}$  6.25, 6.7, 7.0, 7.2 and 7.5) together with three

slip rates ( $\dot{s}=0.5\text{cm/year}$ ,  $1.0\text{cm/year}$  and  $2.0\text{cm/year}$ ) corresponding to different levels of seismic activity are used to establish the aforementioned earthquake scenarios. The probabilistic seismic hazard computations are run over 42 sites that are spatially distributed around the fault to address the influence of source-site geometry on  $Sa_{\text{directivity}}/Sa_{\text{no-directivity}}$ . The proposed spectral amplification expressions in this section consider the variation of all of the above estimator parameters as explained in the following.

**5.2.1 A Comprehensive 475-year Return Period Spectral Amplification Expression from the SHB11 Narrow-band Model**

As stated in Chapter 3 the directivity-dominated spectral amplifications become maximum at sites located close to the edges of the faults in SHB11 model. This behavior results in a bilinear trend for the spectral amplification curves along the fault strike direction (designated by  $R_x/L$  in Chapter 3). The spatial distribution of the sites around the fault used in this study is illustrated here once again (Figure 5.1) for convenience together with the boundary regions highlighted with red boxes. These boundary regions are used in the development of spectral amplification expressions for 475-year return period.

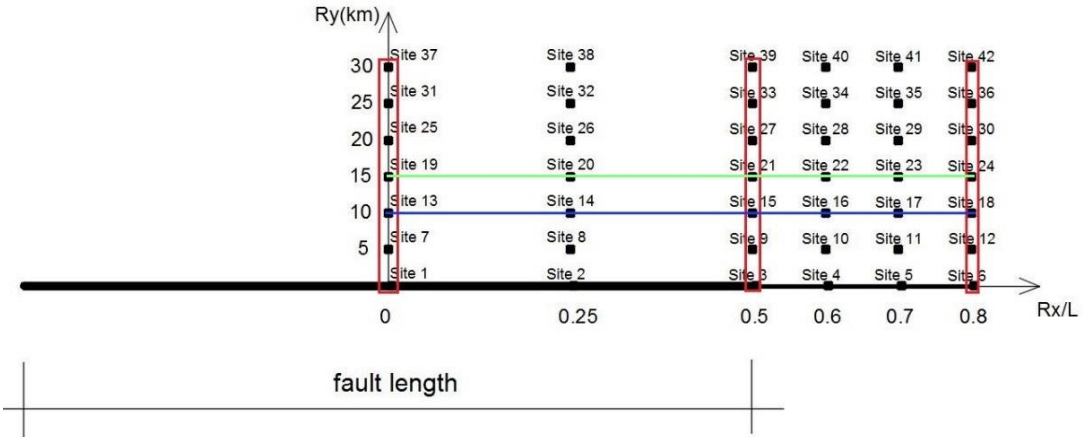


Figure 5.1 Spatial distribution of sites around the fictitious fault and the sites located in the boundary region enclosed by red rectangles

As an example to directivity-dominated bilinear spectral amplification trends along  $R_x/L$ , Figure 5.2 shows the amplification curves ( $Sa_{\text{directivity}}/Sa_{\text{no-directivity}}$ ) at different spectral periods for sites located 15km away from the fault in  $R_y$  direction (the sites

along the green line as shown in Figure 5.1). The depicted amplification curves correspond to an earthquake scenario of  $FL = 100\text{km}$  and  $\dot{s} = 1\text{cm/year}$ .

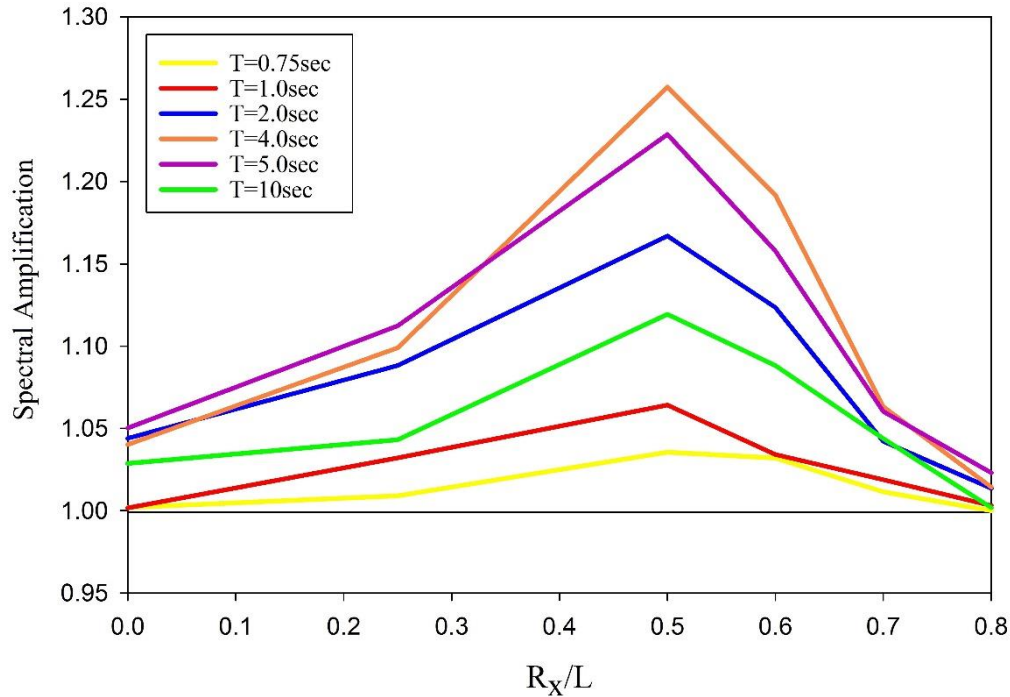


Figure 5.2 Bilinear trend for directivity-dominated spectral amplifications along fault strike,  $R_x/L$ , direction for a suit of spectral periods ( $FL = 100\text{km}$ ,  $\dot{s} = 1.0\text{cm/year}$ ,  $R_y=15\text{km}$ )

As it can be seen in Figure 5.2, the maximum spectral amplifications due to forward-directivity are observed at sites located along  $R_x/L = 0.5$  and the amplification curves follow a bilinear trend between the sites located in the boundary regions. The level of spectral amplifications is sensitive to spectral period that is proportional to pulse period,  $T_p$ , in SHB11 (see relevant discussions in Chapter 3). For example, in this specific earthquake scenario, the characteristic magnitude is  $M_{ch} 7$  since  $FL=100\text{km}$  that corresponds to a pulse period of ( $T_p$ )  $\sim 4\text{sec}$ . Eventually directivity originated spectral amplifications are mostly maximized at  $T = 4\text{sec}$  in Figure 5.2. This observation is common in most of the earthquake scenarios studied in this thesis under SHB11 narrow-band directivity model. In fact, Figure 5.3 shows the 475-year return period maximum  $S_{a\text{directivity}}/S_{a\text{no-directivity}}$  spectral amplification values that are populated from all earthquake scenarios generated under different combinations of fault length and slip rate at sites located 10km from the fault strike in  $R_y$  direction (the sites along the blue line as shown in Figure 5.1). (Side note: maximum spectral

amplification corresponds to the spectral period at which  $S_{a_{\text{directivity}}}/S_{a_{\text{no-directivity}}}$  is maximum for a specific earthquake scenario that is dictated by fault length, slip rate, etc). As it can be seen in this figure the majority of maximum spectral amplifications due to directivity occur at sites located on  $R_x/L = 0.5$ . These observations justify the use of a bilinear functional form to express the directivity-dominated spectral amplifications for SHB11 narrow-band model.

The bilinear trends discussed in the previous paragraphs require two functional forms to describe the spectral amplifications at two regions:  $0 < R_x/L < 0.5$  and  $0.5 < R_x/L < 0.8$ . The maximum spectral amplifications at the sites located inside the boundary regions (i.e., shown with red boxes in Figure 5.1 and they are located on  $R_x/L = 0$  and  $R_x/L = 0.5$ ) are used to develop the maximum spectral amplification equations for sites enclosed by these regions (Equations 5.1 and 5.2). For sites located between these boundary regions ( $0 < R_x/L < 0.5$  or  $0.5 < R_x/L < 0.8$ ), the maximum spectral amplifications are calculated from linear interpolation as given in Equation 5.3.

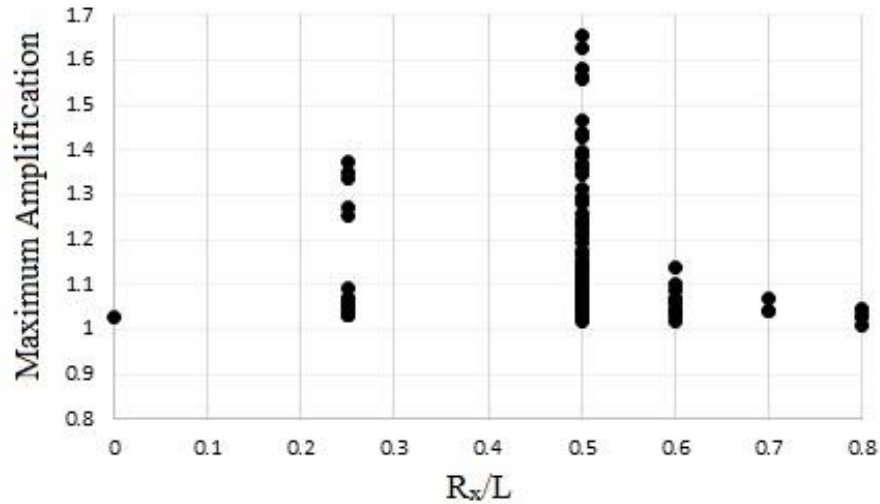


Figure 5.3 Maximum amplification values and location of the sites which experience the maximum value

$$AMP_{\left(\frac{R_x}{L}=0, R_y, T\right)} = a_{01} + a_{11} \cdot R_y + a_{21} \cdot T + a_{31} \cdot T^2 + a_{41} \cdot R_y \cdot T \quad 5.1$$

$$AMP_{\left(\frac{R_x}{L}=0.5, R_y, T\right)} = a_{02} + a_{12} \cdot R_y + a_{22} \cdot T + a_{32} \cdot R_y^2 + a_{42} \cdot T^2 + a_{52} \cdot R_y \cdot T + a_{62} \cdot R_y^2 \cdot T + a_{72} \cdot R_y \cdot T^2 + a_{82} \cdot R_y^2 \cdot T^2 \quad 5.2$$

$$AMP_{\left(\frac{R_x}{L}, R_y, T\right)} = 2 \times \left(\frac{R_x}{L}\right) \times \left[ AMP_{\left(\frac{R_x}{L}=0.5, R_y, T\right)} - AMP_{\left(\frac{R_x}{L}=0, R_y, T\right)} \right] + AMP_{\left(\frac{R_x}{L}=0, R_y, T\right)} \quad 0 < \frac{R_x}{L} < 0.5 \quad 5.3a$$

$$AMP_{\left(\frac{R_x}{L}, R_y, T\right)} = \frac{\left(\frac{R_x}{L}\right) - 0.5}{0.3} \times \left[ 1 - AMP_{\left(\frac{R_x}{L}=0.5, R_y, T\right)} \right] + AMP_{\left(\frac{R_x}{L}=0.5, R_y, T\right)} \quad 0.5 < \frac{R_x}{L} < 0.8 \quad 5.3b$$

As discussed throughout the text as well as in Sections 3.3 and 3.4, the directivity dominated spectral amplifications are functions of the spectral period (T),  $R_y$ ,  $R_x/L$  and the slip rate values. The characteristic magnitude (that is proportional to fault length) also determines the period range that maximum spectral amplifications occur. (Characteristic magnitude,  $M_{ch}$ , is closely related to pulse period,  $T_p$ , for SHB11 as discussed in Chapter 3). Therefore, the developed amplification equations (Equations 5.1 to 5.3) are dependent on these parameters (spectral period (T),  $R_y$ ,  $R_x/L$  and slip rate and  $M_{ch}$ ) for the sites located along the first and second boundary regions (i.e., along  $R_x/L=0$  and  $R_x/L=0.5$ ). Regarding the discussions in Section 3.4 (Figure 3.13 and Table 3.2) the directivity-dominated spectral amplifications at sites located along  $R_x/L = 0.8$  can be taken as unity. Limited to the case studies in this study, directivity amplifications are either insignificant or they do not exist at or beyond  $R_x/L = 0.8$ . The coefficients of Equation 5.1 ( $R_x/L = 0$ ) and Equation 5.2 ( $R_x/L = 0.5$ ) are computed from the regression analysis on the maximum spectral amplifications that are extracted from the entire set of earthquake scenarios generated within the context of this thesis (discussed and presented in Section 3.3). These coefficients are given in Table 5.1 and Table 5.2. The general form of the spectral amplification expression that can be used for all sites located around the fault is shown in Equation 5.3. The first part of this expression (Equation 5.3a) gives the directivity-dominant spectral amplifications for sites located between  $0 < R_x/L \leq 0.5$  and the second part (Equation 5.3b) gives the directivity-dominant spectral amplifications for sites located between  $0.5 < R_x/L \leq 0.8$ .

The residuals that show the differences between the spectral amplifications calculated from PSHA (observed) and Equations 5.1 to 5.3 (estimated) are shown in Figure 5.4. This basic statistical measure reveals information about the existence of bias in the estimated spectral amplifications. Any apparent trend in the mean residuals indicate

the existence of bias in the estimated spectral amplifications against a specific estimator parameter. The residual trends are shown for  $R_x/L$ ,  $R_y$  and the spectral periods respectively. Mean and mean  $\pm$  standard deviation of the residuals are also given in these figures (as error bars) to envisage the possibility of bias in the estimated spectral amplifications for directivity. The plots show that the mean values of the residuals are either zero or they are close to zero. This is consistent with the theoretical expectations because residuals are expected to be normally distributed zero mean varieties. The standard deviations of residuals show a dependency on the selected estimator parameters (i.e.,  $R_x/L$ ,  $R_y$  and  $T$ ).

Table 5.1 Coefficients of the directivity dominant spectral amplifications of Equation (5.1) for sites located along  $R_x/L = 0$

<b>Characteristic Magnitude</b>	<b>Slip Rate (cm/year)</b>	<b>a<sub>01</sub></b>	<b>a<sub>11</sub></b>	<b>a<sub>21</sub></b>	<b>a<sub>31</sub></b>	<b>a<sub>41</sub></b>
<b>M<sub>ch</sub>=6.25</b>	<b><math>\dot{s} = 0.5</math></b>	1.12642	-0.00397	-0.02851	0.00146	0.00054
	<b><math>\dot{s} = 1.0</math></b>	1.16436	-0.00534	-0.03444	0.00161	0.00072
	<b><math>\dot{s} = 2.0</math></b>	1.22046	-0.00771	-0.04034	0.00148	0.00103
<b>M<sub>ch</sub>=6.75</b>	<b><math>\dot{s} = 0.5</math></b>	1.06475	-0.00209	-0.01058	0.00039	0.00029
	<b><math>\dot{s} = 1.0</math></b>	1.07242	-0.00245	-0.01152	0.00043	0.00040
	<b><math>\dot{s} = 2.0</math></b>	1.12303	-0.00487	-0.01290	-0.0001	0.00058
<b>M<sub>ch</sub>=7.0</b>	<b><math>\dot{s} = 0.5</math></b>	1.05341	-0.00177	-0.00659	0.00025	0.00025
	<b><math>\dot{s} = 1.0</math></b>	1.05150	-0.00179	-0.00317	-0.00015	0.00021
	<b><math>\dot{s} = 2.0</math></b>	1.07892	-0.00363	0.00641	-0.00135	0.00031
<b>M<sub>ch</sub>=7.25</b>	<b><math>\dot{s} = 0.5</math></b>	1.05752	-0.00177	-0.00671	0.00017	0.00023
	<b><math>\dot{s} = 1.0</math></b>	1.04008	-0.00125	0.00165	-0.00045	0.00015
	<b><math>\dot{s} = 2.0</math></b>	1.03573	-0.00252	0.02337	-0.00243	0.00015
<b>M<sub>ch</sub>=7.5</b>	<b><math>\dot{s} = 0.5</math></b>	1.07911	-0.00222	-0.01194	0.00049	0.00034
	<b><math>\dot{s} = 1.0</math></b>	1.02404	-0.00147	0.02584	-0.00237	0.00019
	<b><math>\dot{s} = 2.0</math></b>	0.96960	-0.00160	0.08205	-0.00628	-0.00042

Table 5.2 Coefficients of the directivity dominant spectral amplifications of Equation (5.1) for sites located along  $R_v/L = 0.5$

Characteristic Magnitude	Slip Rate (cm/year)	a <sub>02</sub>	a <sub>12</sub>	a <sub>22</sub>	a <sub>32</sub>	a <sub>42</sub>	a <sub>52</sub>	a <sub>62</sub>	a <sub>72</sub>	a <sub>82</sub>
M <sub>ch</sub> =6.25	$\dot{s} = 0.5$	1.311211	-0.02717	-0.11684	0.000575	0.007401	0.012174	-0.00029	-0.0008	1.91E-05
	$\dot{s} = 1$	1.381247	-0.03163	-0.10923	0.000657	0.005861	0.010781	-0.00025	-0.00061	1.47E-05
	$\dot{s} = 2$	1.449586	-0.0372	-0.09475	0.000754	0.003481	0.009674	-0.00022	-0.00043	1.04E-05
M <sub>ch</sub> =6.75	$\dot{s} = 0.5$	1.197158	-0.01586	-0.06284	0.000323	0.003477	0.009076	-0.00024	-0.00063	1.79E-05
	$\dot{s} = 1$	1.20928	-0.01583	0.018009	0.000303	-0.00478	0.001853	-8.4E-05	0.000109	1.88E-06
	$\dot{s} = 2$	1.213298	-0.01644	0.089514	0.000318	-0.01176	-0.0036	1.81E-05	0.000625	-7.8E-06
M <sub>ch</sub> =7.0	$\dot{s} = 0.5$	1.157175	-0.01228	-0.03054	0.000246	0.001371	0.008594	-0.00026	-0.00063	2E-05
	$\dot{s} = 1$	1.063276	-0.00674	0.11367	0.000151	-0.01142	0.001413	-0.00017	1.02E-06	1.27E-05
	$\dot{s} = 2$	0.951488	-0.00085	0.250529	7.26E-05	-0.02354	-0.00549	-8.5E-05	0.000613	4.82E-06
M <sub>ch</sub> =7.25	$\dot{s} = 0.5$	1.12122	-0.00782	-0.02248	0.000139	0.001237	0.005842	-0.00016	-0.00042	1.21E-05
	$\dot{s} = 1$	1.02716	-0.0109	0.102985	0.00033	-0.0095	0.008903	-0.00038	-0.00065	2.98E-05
	$\dot{s} = 2$	0.87108	-0.00523	0.261686	0.000263	-0.02273	0.00418	-0.00035	-0.00028	2.77E-05
M <sub>ch</sub> =7.5	$\dot{s} = 0.5$	1.098747	-0.00564	-0.02116	0.000101	0.001151	0.001613	-3E-05	-8.1E-05	1.42E-06
	$\dot{s} = 1$	1.099142	-0.01505	0.0216	0.000361	-0.0019	0.010893	-0.0003	-0.00082	2.29E-05
	$\dot{s} = 2$	0.913597	-0.01433	0.178919	0.0004	-0.01351	0.011557	-0.00037	-0.00088	2.86E-05

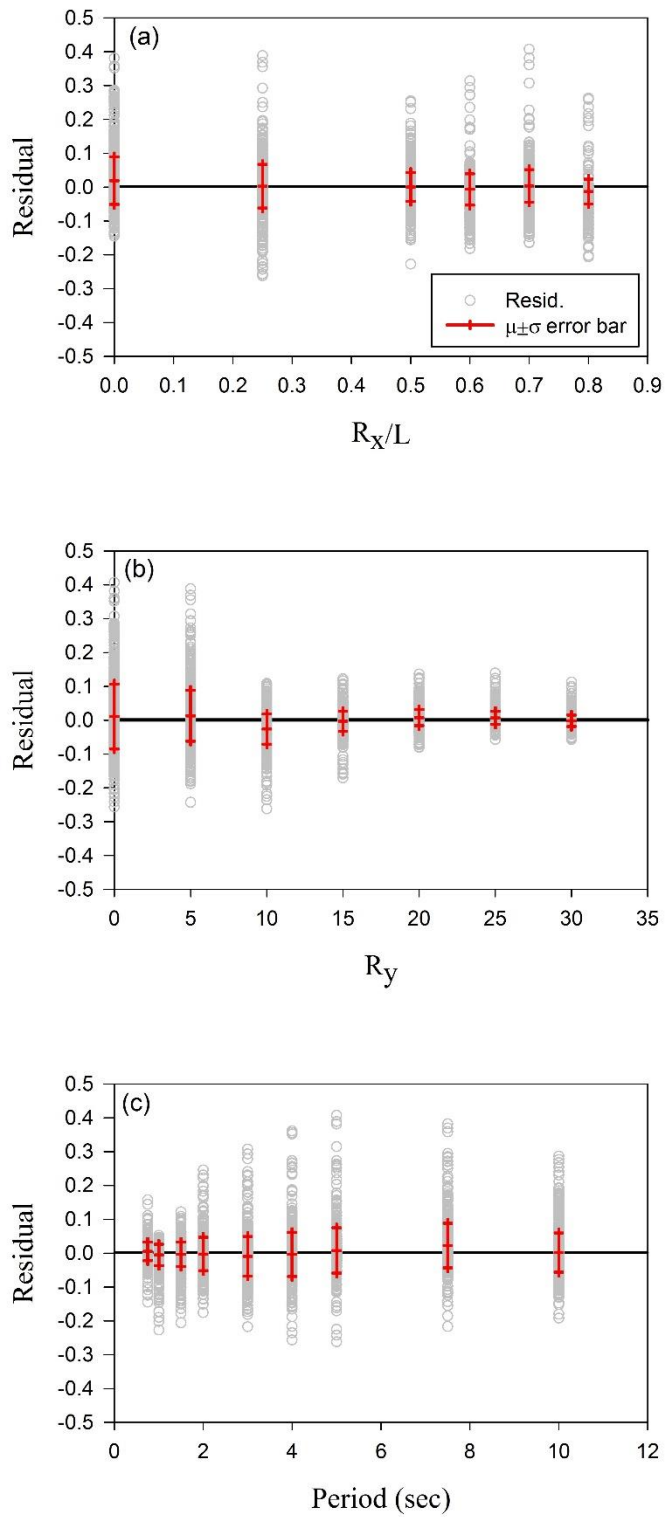


Figure 5.4 Residuals between PSHA (observed) and the estimated directivity amplifications for 475-year return period

**5.2.2 Estimating the 2475-year Return Period Spectral Amplifications from the Complicated Formulations Developed from SHB11 Narrow-band Directivity Model**

The directivity-dominant spectral amplitudes for 2475-year return period (referred to as Maximum Considerable Earthquake, MCE, in seismic design codes) are developed by modifying the corresponding expressions (Equations 5.1 to 5.3) that are valid for 475-year return period spectral amplifications. This approach is explained in the following paragraphs.

The  $Sa_{\text{directivity}}/Sa_{\text{no-directivity}}$  ratios are extracted for 2475-year return period from the PSHA runs of all earthquake scenarios. This step is similar to the one described in the development of directivity-dominant spectral amplification expressions for the 475-year return period. Let this ratio be called as  $amp_{2475}(T)$  that is given in Equation 5.4. Figure 5.5 presents a typical case of two spectra corresponding to  $Sa_{\text{directivity}}$  and  $Sa_{\text{no-directivity}}$ , and  $amp_{2475}(T)$  is essentially the ratio between these spectra.

$$amp_{2475}(T) = \frac{Sa_{\text{directivity}}(T)}{Sa_{\text{nodirectivity}}(T)} \quad 5.4$$

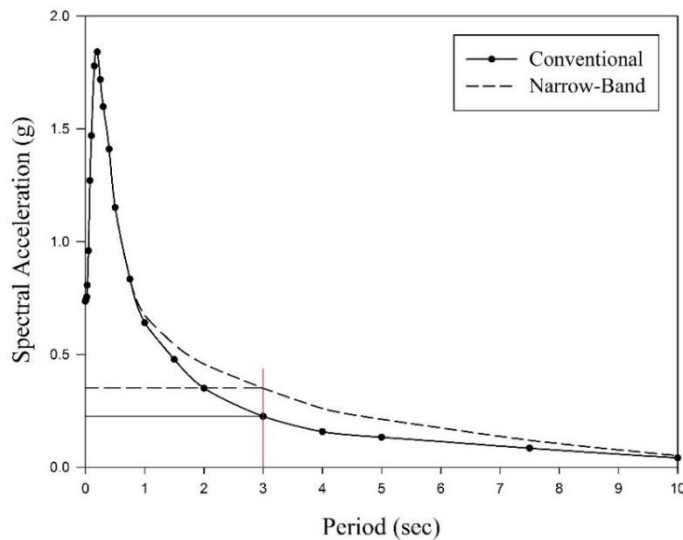


Figure 5.5 Normalization of 2475-year return period narrow-band spectrum to conventional spectrum

The similar amplification factors for 475-year return period can be called as  $amp_{475}(T)$  that are, in fact, already computed for the entire earthquake scenarios and for all sites for the derivation of Equations 5.1 to 5.3 as explained in the previous section. In essence, the ratio between these amplification factors (i.e.,  $amp_{2475}(T)/amp_{475}(T)$ ) that is given in Equation 5.5 would describe the spectral amplification difference for the two return periods of concern when the directivity effects are prevalent.

$$NRM_{amp}(T) = \frac{amp_{2475}(T)}{amp_{475}(T)} \quad 0.6\text{sec} \leq T < 10\text{sec} \quad 5.5$$

The normalized spectral amplification factor ( $NRM_{amp}(T)$ ) is unity for periods less than 0.6s as SHB11 narrow-band directivity model inherently accounts for the forward-directivity effects for  $T \geq 0.6\text{s}$ . This is partially observed in Figure 5.5 for the 2475-year return period sample. Figure 5.6 shows  $NRM_{amp}(T)$  variations of 42 sites for two specific earthquake scenarios having different fault lengths ( $FL = 50\text{km}$  and  $FL = 100\text{km}$ ), thus exposed to different  $M_{ch}$ , and  $\dot{s} = 1\text{cm/year}$ . The plots in Figure 5.6 include the logarithmic mean ( $\mu$ ) and three different fractiles of  $NRM_{amp}(T)$  ( $\mu \pm \sigma$  and  $\mu + 2\sigma$ ) assuming that  $NRM_{amp}(T)$  is lognormally distributed. Note that  $NRM_{amp}(T)$  is above unity almost for the entire spectral period range. The exception is the relatively shorter periods ( $T < 1\text{s}$ ) where the directivity-dominant spectral amplifications are almost equal to 1.0 and directivity spectral amplifications of 475-year return period ( $amp_{475}(T)$ ) are slightly larger than those of 2475-year return period directivity spectral amplifications ( $amp_{2475}(T)$ ). This is an inherent feature of the SHB11 narrow-band directivity model.

An approach similar to directivity dominant area concept that is discussed at the end of Chapter 3 is used for utilizing  $NRM_{amp}(T)$  distributions to modify the 475-year return period directivity spectral amplifications for the 2475-year return period. The region around the fault is divided into 4 regions by combining the fault-site geometry and  $NRM_{amp}(T)$  distribution. For each region the  $NRM_{amp}(T)$  distribution is represented by a specific value:  $\mu_{\ln(NRM_{amp})}$ ,  $\mu_{\ln(NRM_{amp})} \pm \sigma_{\ln(NRM_{amp})}$  or  $\mu_{\ln(NRM_{amp})} + 2\sigma_{\ln(NRM_{amp})}$ . As already explained,  $\mu_{\ln(NRM_{amp})}$  and  $\sigma_{\ln(NRM_{amp})}$  denote the logarithmic mean and logarithmic standard deviation of  $NRM_{amp}(T)$  calculated from 42 sites

given a specific earthquake scenario. The next paragraphs discuss how the directivity dominated fault vicinity is divided into four regions.

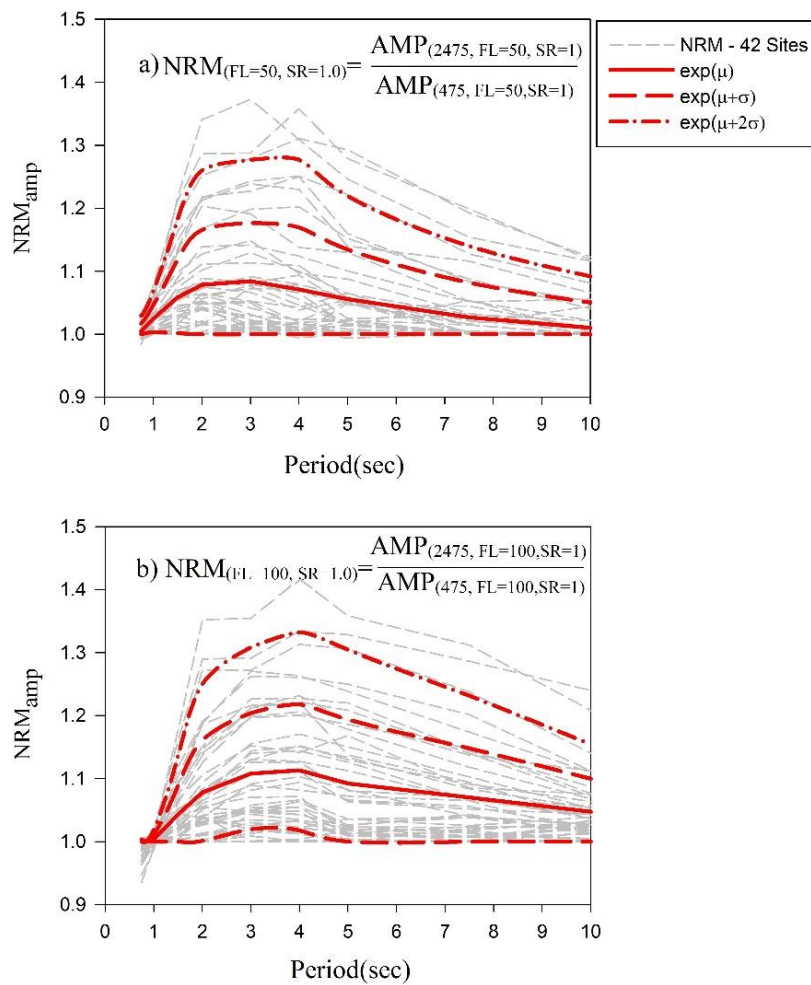


Figure 5.6 Normalized period-dependent 2475-year to 475-year directivity dominant spectral amplification ratios of 42 sites (grey curves) and corresponding logarithmic mean,  $\pm\sigma$  as well as  $2\sigma$  over logarithmic mean a) fictitious fault with 50km length and  $\dot{s} = 1\text{cm/year}$  b) fictitious fault with 100km length and  $\dot{s} = 1\text{cm/year}$

Figure 5.7 shows the  $\text{NRM}_{\text{amp}}(T)$  contour maps at  $T = 2\text{sec}$  (top row) and  $T = 4\text{sec}$  (bottom row) for faults having 20km and 100km lengths with 1 cm/year slip rate. Next to each contour map, the corresponding  $\text{NRM}_{\text{amp}}(T)$  curves for 42 sites are plotted for  $T$  up to 10s. These curves indicate that at  $T = 2\text{sec}$  and  $T = 4\text{sec}$ , the  $\text{NRM}_{\text{amp}}(T)$  values are maximized for 20km and 100km fault length earthquake scenarios, respectively. The contour maps of corresponding earthquake scenarios deliberately

display the distribution of  $NRM_{amp}(T)$  at these periods to show the extent of difference between the 475-year and 2475-year directivity dominant spectral amplitudes. The  $NRM_{amp}(T)$  curves also include  $\mu$ ,  $\mu \pm \sigma$  and  $\mu + 2\sigma$  fractiles that are given as red lines. (Note that  $\mu_{\ln(NRM_{amp})}$  and  $\sigma_{\ln(NRM_{amp})}$  are abbreviated as  $\mu$  and  $\sigma$ , respectively to increase the readability of the text). The comparisons between the contour maps and maximum  $NRM_{amp}(T)$  at  $\mu$ ,  $\mu \pm \sigma$  and  $\mu + 2\sigma$  suggest that the directivity dominated region can be represented by four sub regions and each region can attain one of the  $NRM_{amp}(T)$  fractile values:  $\mu$ ,  $\mu \pm \sigma$  or  $\mu + 2\sigma$ .

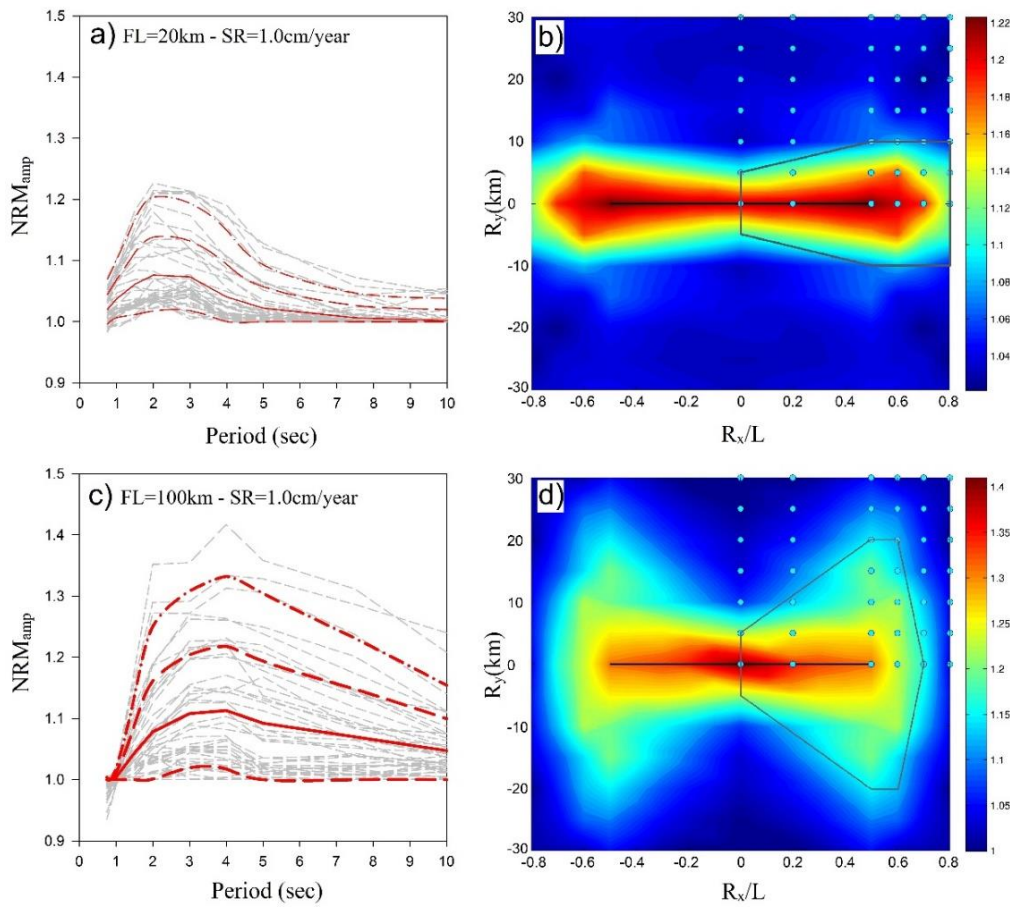


Figure 5.7 Comparison of  $NRM_{amp}$  and the related contour maps for classification of the sites a)  $NRM_{amp}$  vs  $T(sec)$  for  $FL=20km$ ,  $\dot{S}=1cm/year$  b) contour map of  $NRM_{amp}$  for  $T=2.0sec$   $FL=20km$ ,  $\dot{S}=1cm/year$  c)  $NRM_{amp}$  vs  $T(sec)$  for  $FL=100km$ ,  $\dot{S}=1cm/year$  d) contour map of  $NRM_{amp}$  for  $T=4.0sec$   $FL=100km$ ,  $\dot{S}=1cm/year$

Inherently, the sites located on the fault have the largest  $NRM_{amp}(T)$  (Figure 5.7). These on-fault sites are classified as Group 1 and  $\mu+2\sigma^3$  value of  $NRM_{amp}(T)$  can represent the amplification at these sites fairly well. The gradual decrease in  $NRM_{amp}(T)$  values as depicted by the contour maps in Figure 5.7 suggest that one can create three additional regions (Group 2, Group 3 and Group 4) and the sites within the boundaries of these regions can be idealistically represented by  $\mu+\sigma$ ,  $\mu$  and  $\mu-\sigma$   $NRM_{amp}(T)$  values, respectively.

Table 5.3 Geometric parameters for determination of four region boundaries defined for the calculation of amplifications

Characteristic Magnitude	Slip Rate (cm/year)	Rx1 (km)	Rx2 (km)	Dy (km)
<b>M<sub>w</sub> 6.25</b>	<b><math>\dot{s}=0.5</math></b>	$0.3 \times FL$	0	10
	<b><math>\dot{s}=1.0</math></b>	$0.3 \times FL$	0	10
	<b><math>\dot{s}=2.0</math></b>	$0.3 \times FL$	0	10
<b>M<sub>w</sub> 6.75</b>	<b><math>\dot{s}=0.5</math></b>	$0.3 \times FL$	0	10
	<b><math>\dot{s}=1.0</math></b>	$0.3 \times FL$	0	15
	<b><math>\dot{s}=2.0</math></b>	$0.3 \times FL$	0	20
<b>M<sub>w</sub> 7.0</b>	<b><math>\dot{s}=0.5</math></b>	$0.1 \times FL$	$0.1 \times FL$	15
	<b><math>\dot{s}=1.0</math></b>	$0.1 \times FL$	$0.1 \times FL$	20
	<b><math>\dot{s}=2.0</math></b>	$0.1 \times FL$	$0.1 \times FL$	25
<b>M<sub>w</sub> 7.25</b>	<b><math>\dot{s}=0.5</math></b>	$0.1 \times FL$	$0.1 \times FL$	25
	<b><math>\dot{s}=1.0</math></b>	$0.1 \times FL$	$0.1 \times FL$	30
	<b><math>\dot{s}=2.0</math></b>	$0.1 \times FL$	$0.1 \times FL$	30
<b>M<sub>w</sub> 7.5</b>	<b><math>\dot{s}=0.5</math></b>	$0.1 \times FL$	$0.1 \times FL$	30
	<b><math>\dot{s}=1.0</math></b>	$0.1 \times FL$	$0.1 \times FL$	30
	<b><math>\dot{s}=2.0</math></b>	$0.1 \times FL$	$0.1 \times FL$	30

<sup>3</sup> There is one exception to this rule: for on-fault sites that are exposed to  $M_{ch}>7.25$  (or  $FL>150km$ ), one should use  $\mu+\sigma$   $NRM_{amp}(T)$  value. This is due to the saturation of amplification factors for such long faults.

The idealized four regions are shown in Figure 5.8. The suggested pattern in Figure 5.8 is very similar to the one in Figure 3.15. However, the subregions in Figure 5.8 represent the overall variation of  $NRM_{amp}(T)$  (2475-year to 475-year directivity spectral amplification) whereas Figure 3.15 reveals information about the spatial extent of directivity in the vicinity of the ruptured fault. In essence,  $NRM_{amp}(T)$  values of  $\mu+2\sigma$ ,  $\mu+\sigma$ ,  $\mu$  and  $\mu-\sigma$  can be used by the sites enclosed with red (Group 1), green (Group 2), yellow (Group 3) and blue (Group 4) colors, respectively. The boundaries in Figure 5.8 are given in Table 5.3 for different earthquake scenarios considered in this study.

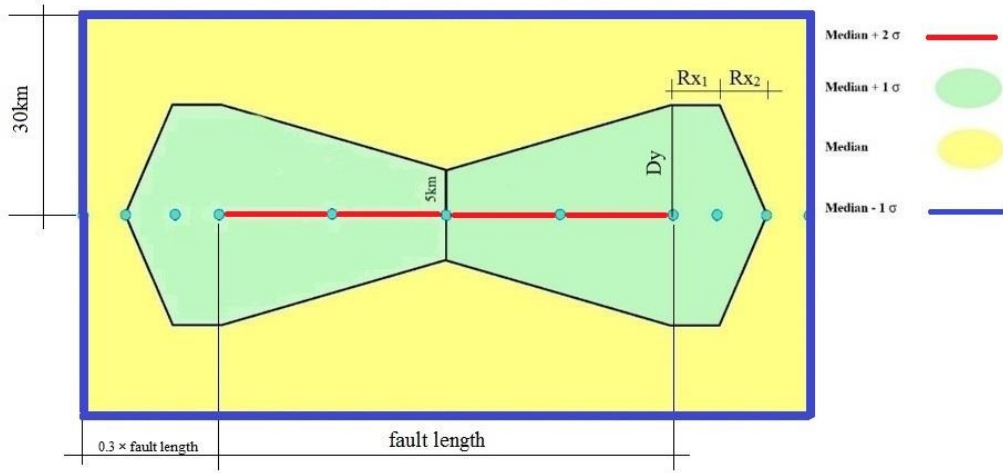


Figure 5.8 Classification of the area around the fault into four regions with respect to  $NRM_{amp}(T)$  intensities

Polynomial curves are fit by using the discrete logarithmic mean and standard deviation values of  $NRM_{amp}(T)$  at  $T = 0.75s, 1.0s, 1.5s, 2.0s, 3.0s, 4.0s, 5.0s, 7.5s$  and  $10s$ . These expressions are given in Equations 5.6 and 5.7 for  $\mu_{\ln(NRM_{amp})}$  and  $\sigma_{\ln(NRM_{amp})}$ , respectively. Table 5.4 lists the regression coefficients for different combinations of  $M_{ch}$  and  $\dot{s}$  representing the entire set of earthquake scenarios considered in this study.

$$\mu_{\ln NRM_{amp}(T)} = \ln(b_4 \cdot T^4 + b_3 \cdot T^3 + b_2 \cdot T^2 + b_1 \cdot T + b_0) \quad 5.6$$

$$\sigma_{\ln NRM_{amp}(T)} = \ln(c_3 \cdot T^3 + c_2 \cdot T^2 + c_1 \cdot T + c_0) \quad 5.7$$

Table 5.4 Coefficient for fitted median and standard deviation curves of  $NRM_{amp}(T)$

Characteristic Magnitude	Slip Rate (cm/year)	b <sub>4</sub>	b <sub>3</sub>	b <sub>2</sub>	b <sub>1</sub>	b <sub>0</sub>	c <sub>3</sub>	c <sub>2</sub>	c <sub>1</sub>	c <sub>0</sub>
$M_{ch}=6.25$	$\dot{s}=0.5$	-0.0003	0.006945	-0.054	0.150055	0.932436	0.000802	-0.01377	0.06023	0.992911
	$\dot{s}=1$	-0.0003	0.007132	-0.05681	0.161982	0.92629	0.000523	-0.00908	0.040222	1.002405
	$\dot{s}=2$	-0.00029	0.00673	-0.05142	0.138731	0.945988	0.000358	-0.00656	0.03101	1.003432
$M_{ch}=6.75$	$\dot{s}=0.5$	-0.00022	0.005817	-0.05297	0.18398	0.884975	0.001281	-0.02402	0.123468	0.930142
	$\dot{s}=1$	-0.00022	0.005521	-0.04832	0.159788	0.909522	0.000792	-0.01518	0.080499	0.962303
	$\dot{s}=2$	-0.00012	0.003095	-0.02817	0.099284	0.952269	0.000385	-0.00755	0.041244	0.992939
$M_{ch}=7.0$	$\dot{s}=0.5$	0	0.001308	-0.02622	0.148656	0.882809	0.001047	-0.02186	0.129	0.914879
	$\dot{s}=1$	0	0.001029	-0.02045	0.115271	0.913128	0.000575	-0.01227	0.074354	0.959389
	$\dot{s}=2$	0	0.000761	-0.01521	0.085494	0.941592	0.000427	-0.00834	0.046031	0.982642
$M_{ch}=7.25$	$\dot{s}=0.5$	0	0.001085	-0.02491	0.164805	0.855247	0.00063	-0.01645	0.118793	0.914569
	$\dot{s}=1$	0	0.000965	-0.02127	0.136224	0.877662	0.000513	-0.01173	0.077368	0.953259
	$\dot{s}=2$	0	0.000744	-0.01584	0.097596	0.918322	0.000348	-0.00741	0.046564	0.980096
$M_{ch}=7.5$	$\dot{s}=0.5$	0	0.000115	-0.01147	0.136935	0.864001	0	-0.00597	0.080798	0.94132
	$\dot{s}=1$	0	0.000291	-0.0124	0.124418	0.860227	0	-0.00415	0.057114	0.961728
	$\dot{s}=2$	0	0.000572	-0.01381	0.102278	0.88871	0	-0.00162	0.02307	0.999135

The estimation of directivity spectral amplifications for the 2475-year return period is done by following the below expressions:

$$\text{Group 1 Sites: } amp_{2475}(T) = amp_{475}(T) \cdot e^{\mu+2\sigma}$$

$$\text{Group 2 Sites: } amp_{2475}(T) = amp_{475}(T) \cdot e^{\mu+\sigma}$$

$$\text{Group 3 Sites: } amp_{2475}(T) = amp_{475}(T) \cdot e^{\mu}$$

$$\text{Group 4 Sites: } amp_{2475}(T) = amp_{475}(T) \cdot e^{\mu-\sigma}$$

In the above expressions  $amp_{475}(T)$  is determined from Equations 5.1 to 5.3 by considering source-site geometry whereas Equations 5.6 and 5.7 are used in the exponential terms to modify 475-year directivity amplifications for 2475-year. Note that the resulting 2475-year directivity-dominated spectral amplifications are not fully sensitive to the source-site geometry because a simplified regional classification is used to reflect the proximity of the site to the fault. Thus, although the complicated formulations given in this section tend to acknowledge the influence of all prominent directivity parameters, they are not fully capable of capturing the entire physical model for a precise description of directivity dominated spectral amplification. This last statement is at least valid for the 2475-year return period directivity spectral amplifications. Notwithstanding, the expressions presented in this section are far too complex to be considered in the seismic design codes since an expert needs to use many tabulated coefficients to obtain the directivity amplifications for a specific scenario. The next sections provide alternative approaches to address the directivity dominated spectral amplifications in a simplified manner.

### **5.3 Simplified Directivity Amplification Equations for SHB11 and CHS13**

Spectral amplification equations proposed in the previous sections for SHB11 are developed by considering the effect of slip rate, fault characteristic magnitude and fault-site geometry as well as the interaction between these parameters. The consideration of all these parameters adds significant complexity to the proposed equations (significant number of coefficients to be considered to address the directivity effects on spectral ordinates). The proposed equations suggest a good

agreement with the results of PSHA (observed cases) for the 475-year return period amplifications (Figure 5.4) but the 2475-year amplifications that are obtained by modifying the corresponding estimations of 475-year values are not fully sensitive to the fault-site geometry for a simplified regionalization approach as explained in the previous section. Besides estimation of the 2475-year spectral amplifications over the 475-year spectral amplification predictions may not be very practical.

In this section, simpler expressions are proposed for the directivity amplifications using the observed PSHA results of SHB11 and CHS13 models. The proposed expressions prevail a compromise between accuracy and simplicity. To this end, a different approach is used to incorporate the effect of fault-site geometry in the directivity-based amplification equations: first amplification expressions are developed for sites where the highest directivity spectral amplifications are observed. This step is followed by defining source-site geometry scaling factors to estimate the directivity spectral amplifications at the other locations around the fault. As it is discussed at different parts of the text (e.g., Section 3.4), the largest directivity spectral amplifications occur at the sites located along  $R_x/L=0.5$  in SHB11 (the sites inside the red box in Figure 5.9). The maximum directivity spectral amplifications are observed at the sites located along  $R_x/L=0.6$  in CHS13 (the sites inside the blue box in Figure 5.9).

The base models are developed for the sites located inside the green buffer around the fault (Figure 5.9). These sites are at the most 15km away from the fault strike (along y direction). The premise is that the distance-dependent variation of directivity spectral amplification beyond this buffer zone is more significant and tapers down rather fast. A similar distance capping is also implemented in Caltrans seismic design provisions (CALTRANS 2013) (Section 2.3, Figure 2.7). The proposed expressions for SHB11 narrow-band directivity model considers the effects of slip rate, fault-site geometry and hazard level. The proposed expressions that originate from CHS13 narrow-band directivity model are functions of source-site geometry and hazard level as slip rate is not a critical parameter while determining the level of directivity spectral amplification in CHS13 (refer to Figure 3.11). In order to develop the base amplification equations, the medians of directivity-dominant spectral amplifications

are calculated from the sites that experience the largest amplification (sites inside the red box for SHB11 and the sites inside the blue box for CHS13 in Figure 5.9).

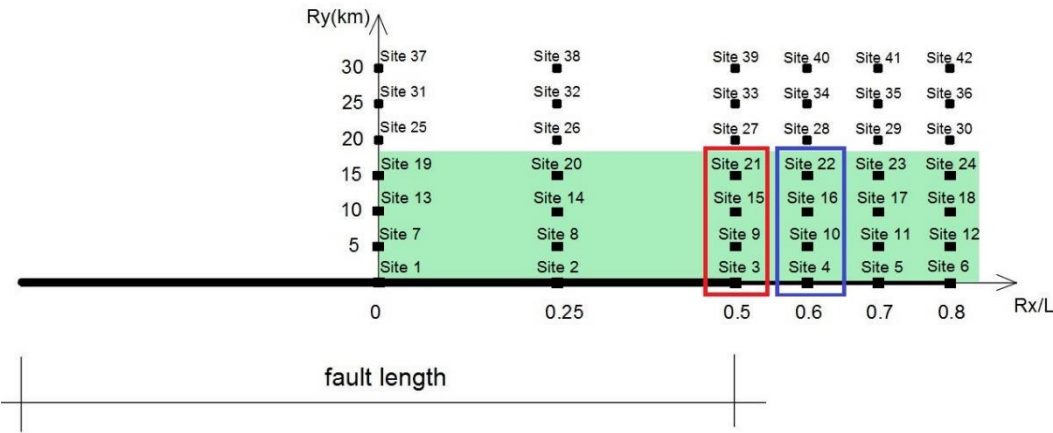


Figure 5.9 Spatial distribution of the sites around the fault and the sites located in the boundary region

The median amplifications are calculated at the spectral period where maximum amplification occurs ( $AMP_{(T_{max})}$  in SHB11 and  $AMP_{(T_{corner})}$  in CHS13) as well as at  $T = 10s$  for SHB11-based model. For spectral periods less than  $T_{max}$  (or  $T_{corner}$ ) or for periods between  $T_{max}$  and  $T = 10s$ , the directivity amplifications are approximated from linear interpolation. A scaling methodology is used to estimate the directivity amplifications at locations other than the sites where directivity amplifications are maximum. The details of entire process are discussed in the next sections.

**5.3.1 Relationship between the Characteristic Magnitude and Amplification Period Range**

In Section 3.3 it is shown that the fault characteristic magnitude affects the amplitude of directivity spectral amplification as well as the period interval where the maximum amplification occurs. SHB11 and CHS13 narrow-band directivity models reflect this effect on to spectral amplifications in different ways. To start developing the simplified expressions, the relationship between the characteristic magnitude and the period interval where the maximum directivity spectral amplification occurs is investigated in this subsection. The directivity spectral amplification patterns for both SHB11 and CHS13 are also highlighted while studying the above relationship.

As it is depicted in Section 3.3 both SHB11 and CHS13 models show a bilinear trend for period-dependent directivity amplifications. The spectral period where the directivity amplification becomes maximum is called as  $T_{\max}$  and  $T_{\text{corner}}$  in SHB11 and CHS13, respectively. The PSHA results indicate that given a specific fault characteristic magnitude (or a specific fault length)  $T_{\max}$  and  $T_{\text{corner}}$  attain similar values. This observation is shown in Figure 5.10 that illustrates the 2475-year return period directivity amplifications for a fault of 150km length ( $M_{\text{ch}} = 7.25$ ) at  $\dot{s}=0.5, 1.0$  and  $2.0\text{cm/year}$ . The period-dependent directivity amplifications are plotted for sites located within the 15km distance from the fault strike in y-direction. The upper and lower panels display the results of SHB11 and CHS13, respectively and both panels display the median directivity amplifications as well. The  $T_{\max}$  and  $T_{\text{corner}}$  values can be approximated as 4.0s for both SHB11 and CHS13 although the trends in the directivity amplifications between the SHB11 and CHS13 are quite different. SHB11 amplifications increase up to  $T_{\max}$ , decrease after  $T_{\max}$  whereas CHS13 amplifications increase up to  $T_{\text{corner}}$ , and keep almost a constant value after  $T_{\text{corner}}$ . Note that the amplification values are quite different between SHB11 and CHS13: SHB11-based amplification values are larger than those of CHS13 because SHB11 estimates the directivity amplifications for fault-normal horizontal component whereas the directivity amplifications by CHS13 are for RotD50 (Boore, 2010).

The period values at which the directivity amplifications are maximized increase with the characteristic magnitude of the fault. Larger the characteristic magnitude, greater is the period where that directivity amplification reaches its maximum ( $T_{\max}$  or  $T_{\text{corner}}$  in SHB11 and CHS13, respectively). Figure 5.11 shows the median directivity amplifications to describe the change in  $T_{\max}$  (SHB11) and  $T_{\text{corner}}$  (CHS13) as  $M_{\text{ch}}$  shifts towards larger values. Each median directivity amplification curve is computed from the directivity amplification curves of sites within the first 15km from the strike of the fault that generates the designated  $M_{\text{ch}}$  earthquake. All three slip rates ( $\dot{s}=0.5, 1.0$  and  $2.0\text{cm/year}$ ) are considered in the calculations. The  $T_{\max}$  values picked from the median directivity amplification curves are plotted against  $M_{\text{ch}}$  in Figure 5.12a. The  $T_{\max}$  values are linearly related with  $M_{\text{ch}}$ . The same trend is also valid for  $T_{\text{corner}}$  since  $T_{\max} \sim T_{\text{corner}}$  as discussed in the above lines (Figure 5.12b).

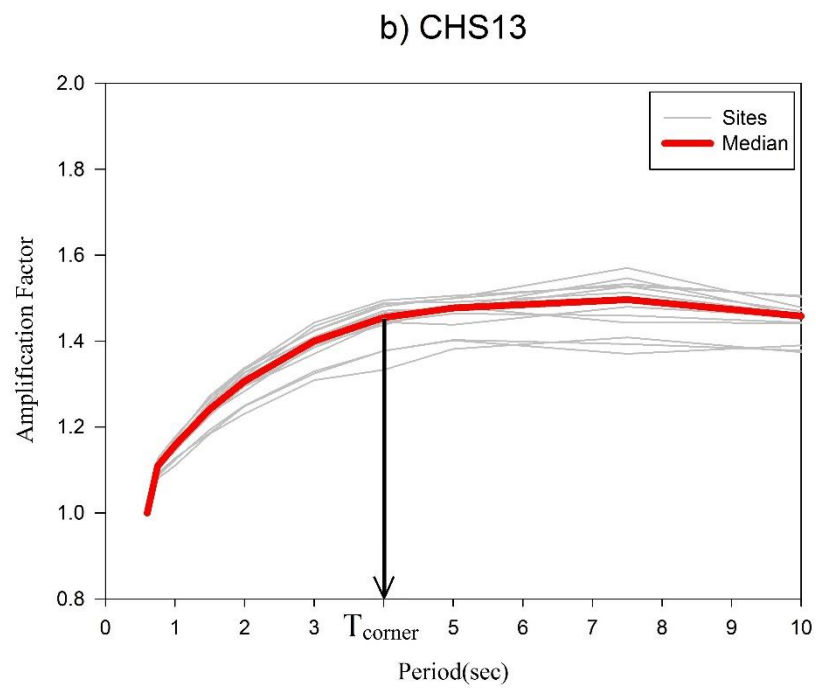
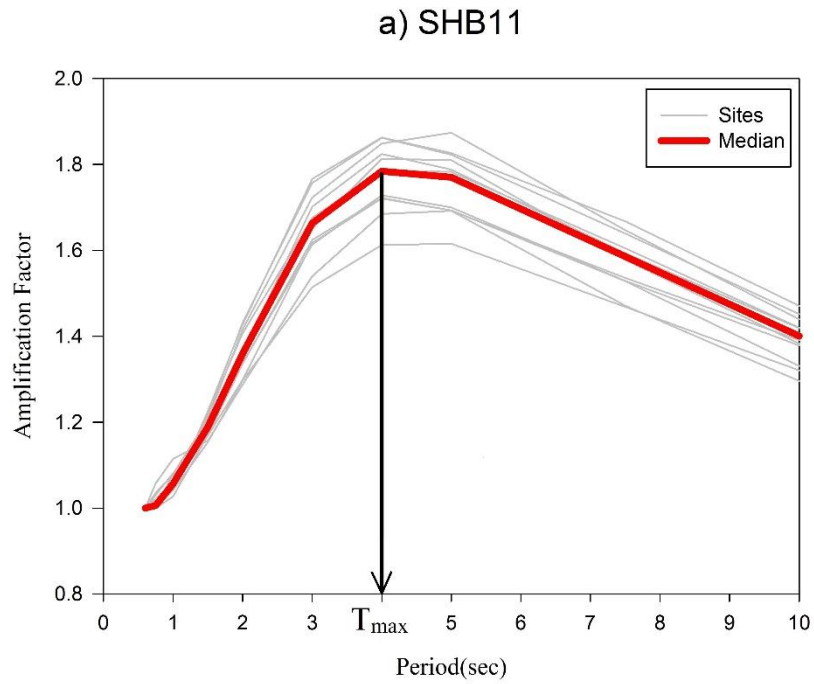


Figure 5.10  $T_{max}$  and  $T_{corner}$  values for directivity amplifications. The earthquake scenario is FL=150km ( $M_{ch}=7.25$ ),  $\dot{s} = 0.5\text{cm/year}$ ,  $1\text{cm/year}$ ,  $2\text{cm/year}$  a) SHB11 model b) CHS13 model

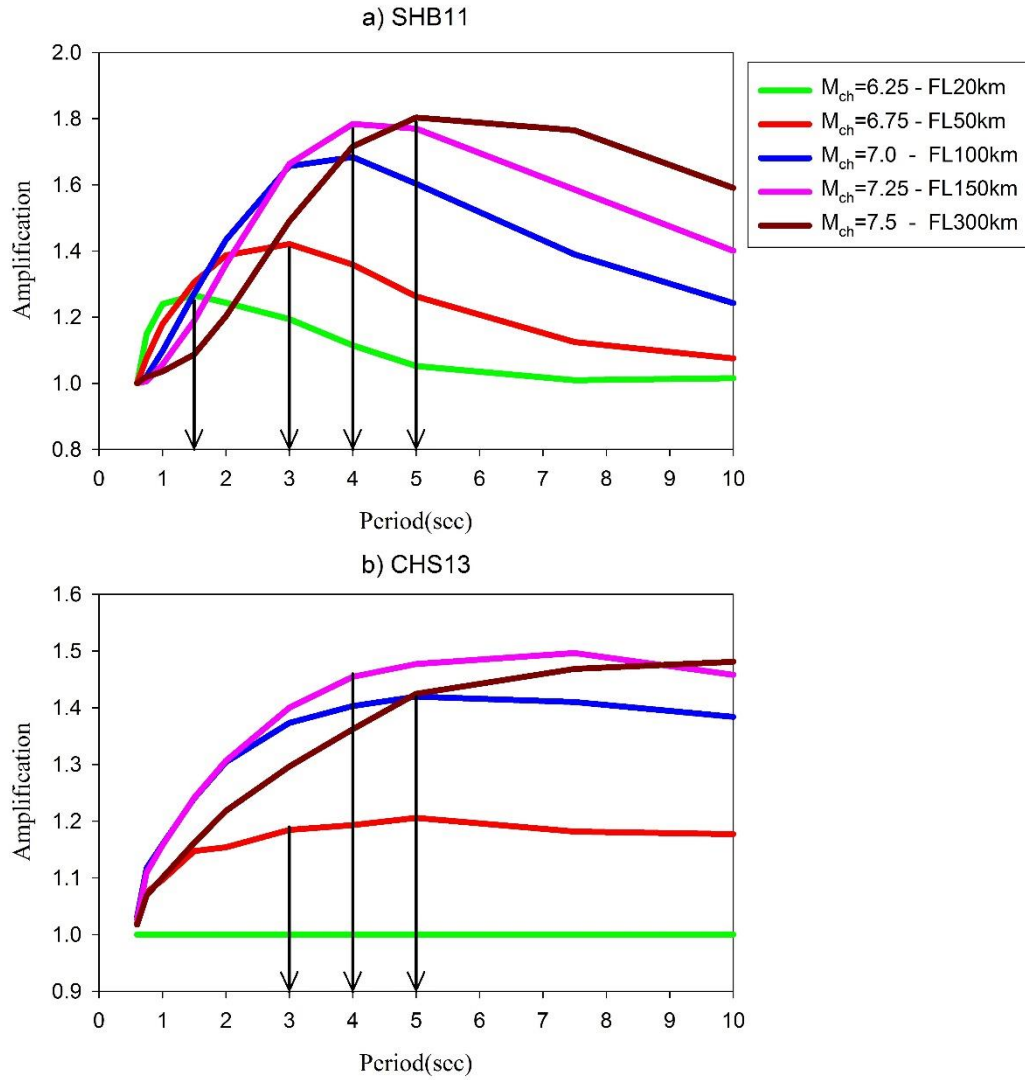


Figure 5.11 Median SHB11 and CHS13 directivity amplifications in terms of  $M_{ch}$  and the variation of  $T_{max}$  and  $T_{corner}$  with the characteristic magnitudes

The almost linearly related characteristic magnitude and  $T_{max}$  (or  $T_{corner}$ ) is represented by Equation 5.8.

$$T_{mc} = 2.72 \cdot M_{ch} - 15.37 \quad 5.8$$

where  $T_{mc}$  denotes either  $T_{max}$  (SHB11) or  $T_{corner}$  (CHS13) and  $M_{ch}$  is the characteristic magnitude of the fault. Note that the characteristic magnitude is described by  $M_{ch}$  in this study. Equation 5.8 is compared with the probability of pulse occurrence for different pulse periods versus discretized magnitude. The figures of these comparisons and related discussions are given in Appendix B.

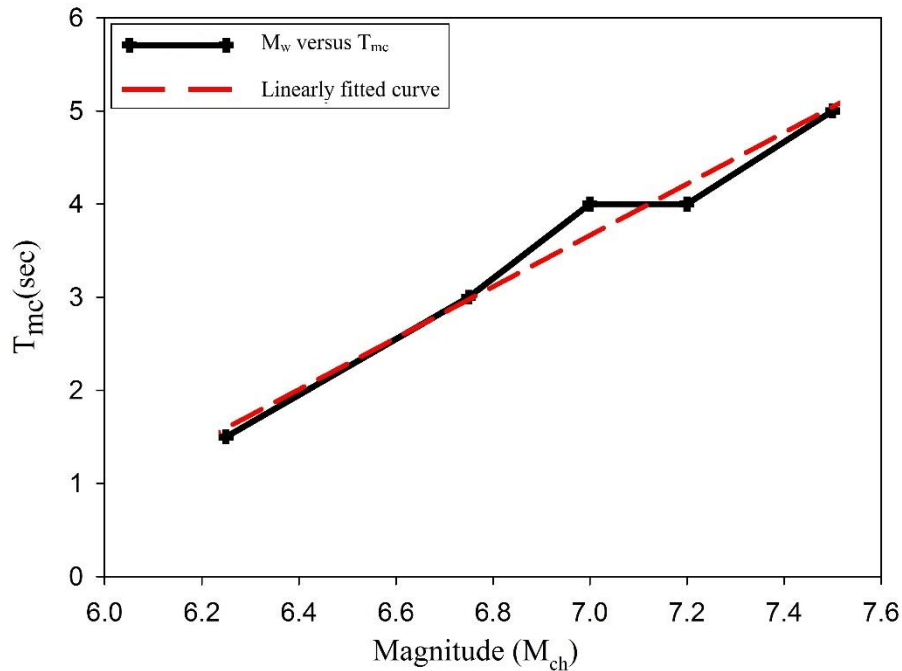


Figure 5.12 Relationship between characteristic magnitude and the spectral period ( $T_{mc}$ ) at which the maximum directivity amplification occur. Dashed red line is the fit to the actual trend given in black

### 5.3.2 Simplified Amplification Equation for SHB11 Model

Firstly, a base expression is proposed for the sites where maximum directivity amplification occurs. To this end, median directivity amplifications are computed at  $T_{max}$  for the sites located along  $R_x/L=0.5$  and  $R_y \leq 15\text{km}$  (i.e., sites 3, 9, 15 and 21 that are enclosed by the red box in Figure 5.9). The same calculations (using the same sites) are also repeated at  $T = 10\text{s}$  to compute the median directivity amplifications at the end of the period range of interest in this study.

In Figure 5.13 the median directivity amplifications of sites 3, 9, 15 and 21 are plotted as a function of  $M_{ch}$  at  $T_{max}$  for the three slip rates (i.e.,  $\dot{s} = 0.5\text{cm/year}$ ,  $1.0\text{cm/year}$  and  $2\text{cm/year}$ ) as well as for the two return periods of interest (475-year and 2475-year). The directivity amplifications have a linearly increasing trend between  $6.25 \leq M_{ch} \leq 7.25$ . They tend to flatten (or either decrease) after  $M_{ch} 7.25$  that is interpreted as amplification saturation in this study. The amplification saturation is experienced on long faults (thus, faults with large  $M_{ch}$ ) and the sites located close to

the edges of such faults are not affected from directivity when ruptures occur at remote locations with respect to the fault edges.

The relationship between  $M_{ch}$  and directivity amplification at  $T_{max}$  ( $AMP_{T_{max},base}$ ) is represented by linear curves fitted to the observed (from PSHA) data by least squares method for magnitude range between  $6.25 \leq M_{ch} \leq 7.25$ . For magnitudes beyond  $M_{ch} > 7.25$ , the directivity amplifications are assumed to follow a constant value. This relationship is given in Equation 5.9.

$$AMP_{T_{max},base} = \alpha_{T_{max}} \cdot M_{ch} + \beta_{T_{max}} \quad 6.25 < M_{ch} \leq 7.25 \quad 5.9a$$

$$AMP_{T_{max},base} = \alpha_{T_{max}} \cdot 7.25 + \beta_{T_{max}} \quad M_{ch} > 7.25 \quad 5.9b$$

$AMP_{T_{max},base}$  estimates the median directivity amplifications at the sites 3, 9, 15 and 21 (shown in Figure 5.9) and Table 5.5 lists the values for  $\alpha_{T_{max}}$  and  $\beta_{T_{max}}$  for different slip rates as well as return periods.

Figure 5.14 shows the relationship between  $M_{ch}$  and the directivity amplification at  $T=10s$  for the three slip rates ( $\dot{s} = 0.5\text{cm/year}$ ,  $1.0\text{cm/year}$  and  $2\text{cm/year}$ ) and for the two return periods (475-year and 2475-year). This figure also shows the linear curve fitted to data for each slip rate value. The relationship between  $AMP_{T10,base}$  and  $M_{ch}$  is given in Equation 5.10.

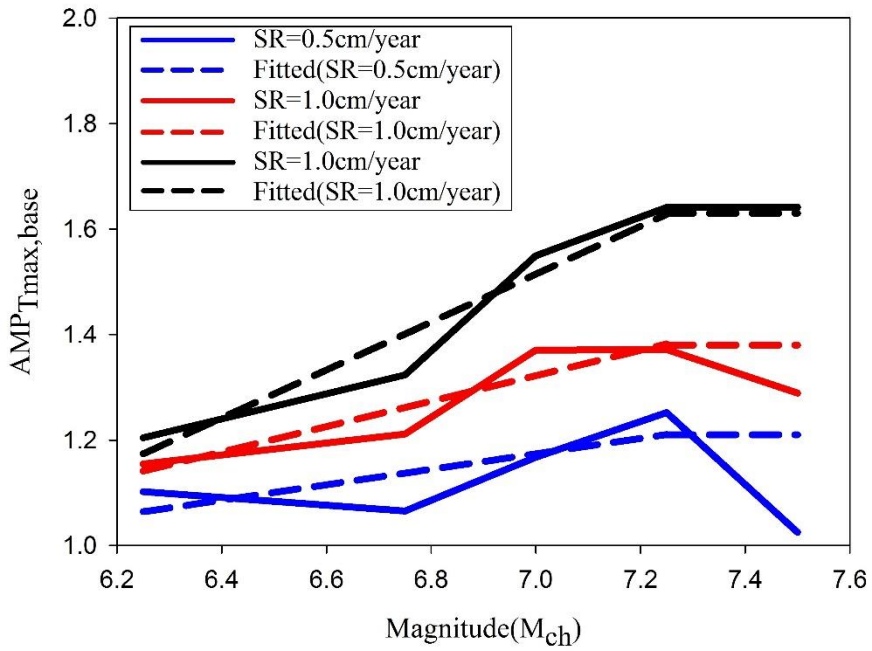
$$AMP_{T10,base} = \alpha_{T10} \cdot M_{ch} + \beta_{T10} \quad 5.10$$

where  $\alpha_{T10}$  and  $\beta_{T10}$  denote the regression coefficients of the fitted curve and are given in Table 5.6 for the slip rates and return periods considered in this study. Note again that  $AMP_{T10,base}$  estimates the median directivity amplifications of sites 3, 9, 15 and 21 at  $T=10s$ .

Alternative to Equation 5.10, a cubic relationship is also fitted to represent  $AMP_{T10,base}$ . The functional form of this expression is given in Equation 5.11 (Table 5.7 lists the coefficients) whereas Figure 5.15 compares the fitted expression with the actual data. Although  $AMP_{T10,base}$  can be calculated from either of these two equations, Equation 5.10 is preferred for its simplicity.

$$AMP_{T10,base} = \alpha_{T10} \times M_{ch}^3 + \beta_{T10} \times M_{ch}^2 + \gamma_{T10} \times M_{ch} + \zeta_{T10} \quad 5.11$$

a)  $AMP_{T_{max, base}}$  - 475-year -  $R_x/L=0.5$  -  $R_y < 15\text{km}$



b)  $AMP_{T_{max, base}}$  - 2475-year -  $R_x/L=0.5$  -  $R_y < 15\text{km}$

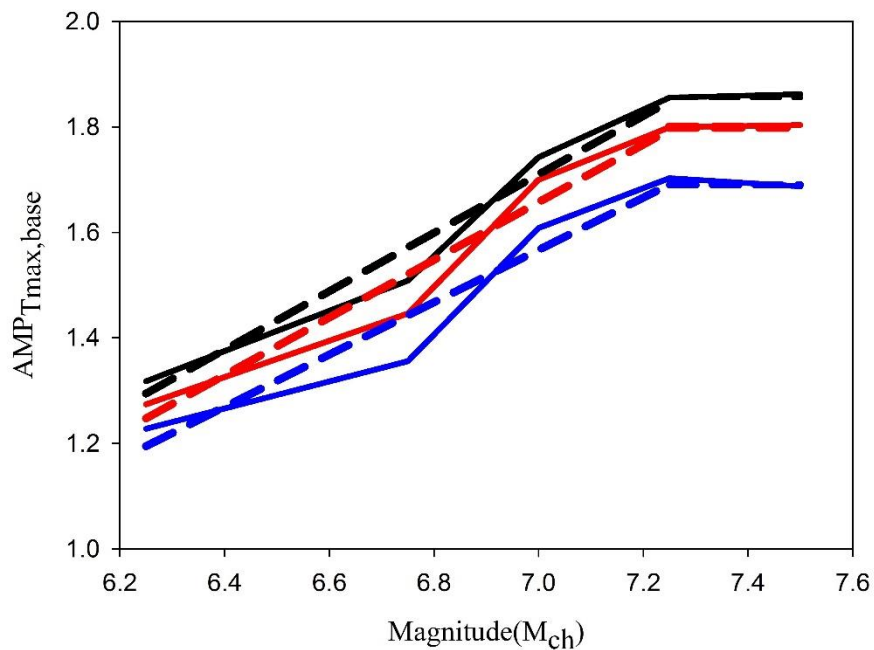
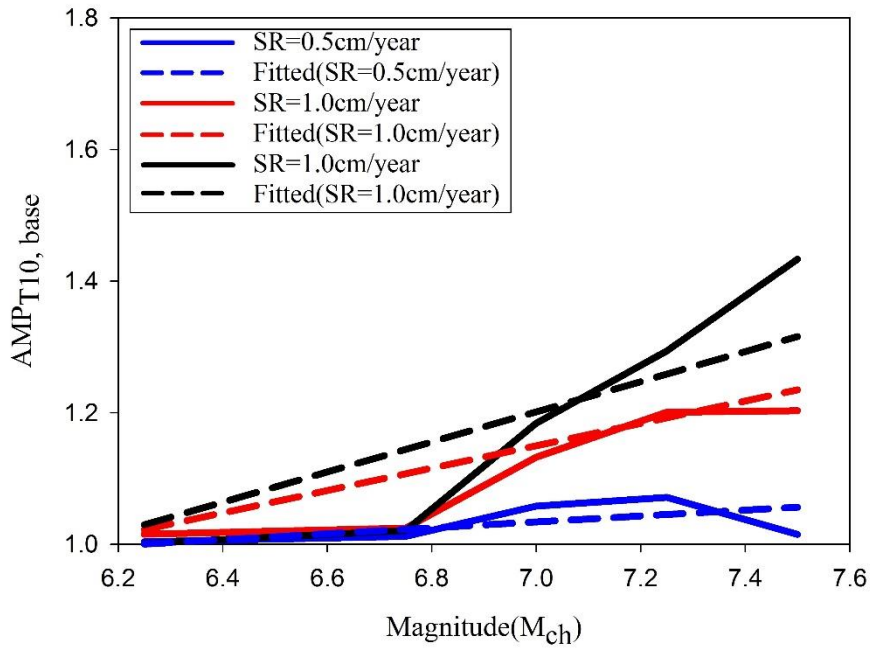


Figure 5.13 SHB11-based directivity amplification vs  $M_{ch}$  relationship together with linear fits calculated for the sites 3, 9, 15 and 21 at spectral period  $T_{max}$  a) 475-year return period b) 2475-year return period

a)  $AMP_{T=10, base}$  - 475-year -  $R_x/L=0.5$  -  $R_y < 15km$



b)  $AMP_{T=10, base}$  - 2475-year -  $R_x/L=0.5$  -  $R_y < 15km$

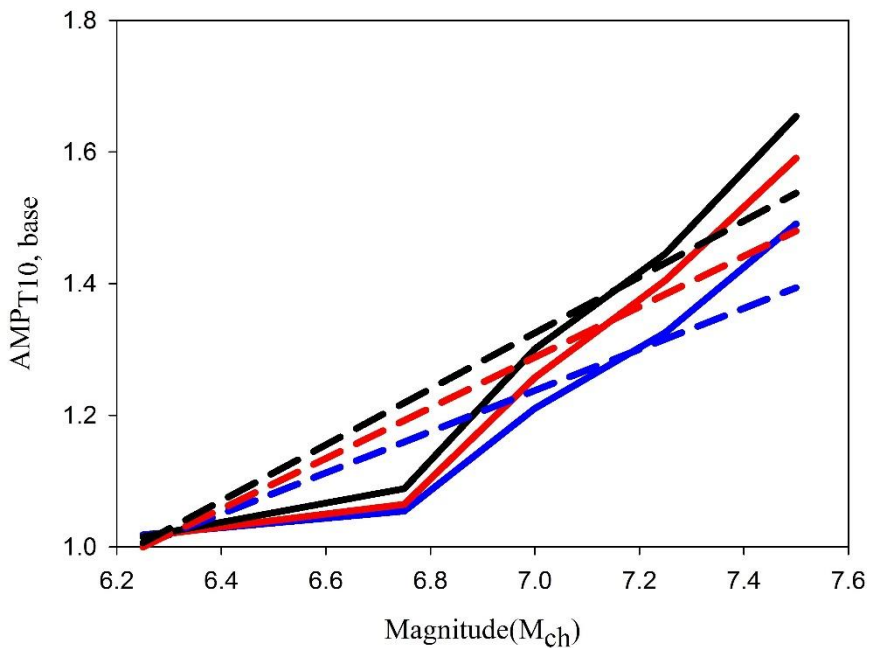
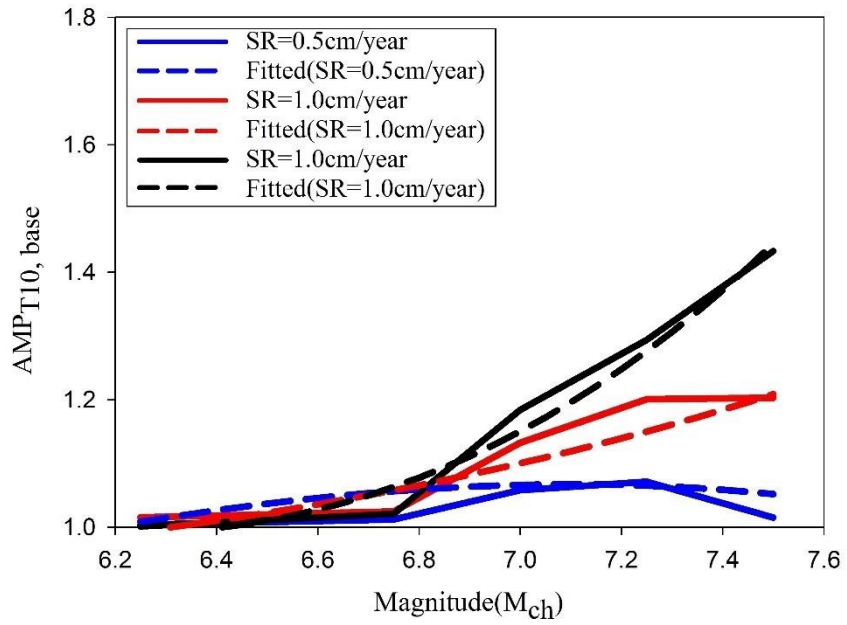


Figure 5.14 SHB11-based directivity amplification vs  $M_{ch}$  relationship together with linear fits calculated for the sites 3, 9, 15 and 21 at  $T = 10s$  a) 475-year return period b) 2475-year return period

a)  $AMP_{T=10, \text{ base}} - 475\text{-year} - R_x/L=0.5 - R_y < 15\text{km}$



b)  $AMP_{T=10, \text{ base}} - 2475\text{-year} - R_x/L=0.5 - R_y < 15\text{km}$

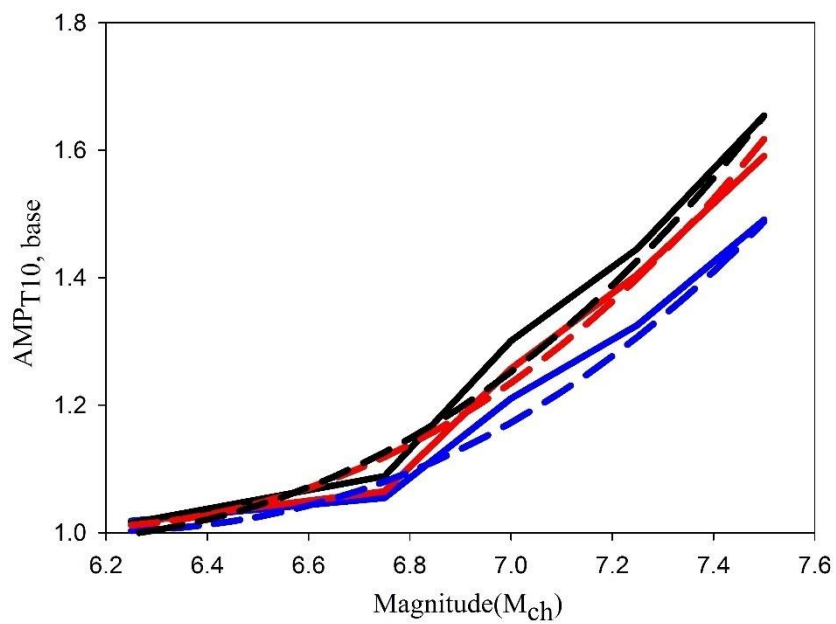


Figure 5.15 SHB11-based directivity amplification vs  $M_{ch}$  relationship together with cubic fits calculated for the sites 3, 9, 15 and 21 at  $T = 10\text{s}$  a) 475-year return period b) 2475-year return period

Table 5.5  $\alpha_{T_{\max}}$  and  $\beta_{T_{\max}}$  coefficients for  $AMP_{T_{\max},base}$  – SHB11

$AMP_{T_{\max}}$	475-year Return Period		2475-year return period	
SR(cm/year)	$\alpha_{T_{\max}}$	$\beta_{T_{\max}}$	$\alpha_{T_{\max}}$	$\beta_{T_{\max}}$
SR=0.5	0.146	0.149	0.495	-1.9
SR=1.0	0.241	-0.364	0.546	-2.168
SR=2.0	0.454	-1.664	0.554	-2.167

Table 5.6  $\alpha_{T_{10}}$  and  $\beta_{T_{10}}$  coefficients for  $AMP_{T_{10},base}$  – SHB11

$AMP_{T_{\max}}$	475-year Return Period		2475-year return period	
SR(cm/year)	$\alpha_{T_{10}}$	$\beta_{T_{10}}$	$\alpha_{T_{10}}$	$\beta_{T_{10}}$
SR=0.5	0.045	0.72	0.313	-0.95
SR=1.0	0.167	-0.04	0.384	-1.4
SR=2.0	0.229	-0.4	0.425	-1.65

Table 5.7  $\alpha_{T_{10}}$ ,  $\beta_{T_{10}}$ ,  $\gamma_{T_{10}}$  and  $\zeta_{T_{10}}$  coefficients for  $AMP_{T_{10},base}$  – SHB11

$AMP_{T_{\max}}$	475-year Return Period				2475-year return period			
SR(cm/year)	$\alpha_{T_{10}}$	$\beta_{T_{10}}$	$\gamma_{T_{10}}$	$\zeta_{T_{10}}$	$\alpha_{T_{10}}$	$\beta_{T_{10}}$	$\gamma_{T_{10}}$	$\zeta_{T_{10}}$
SR=0.5	-0.012	0.162	-0.502	0.72	0.0448	-0.606	2.35	-0.95
SR=1.0	0.008	-0.115	0.554	-0.04	0.0515	-0.695	2.718	-1.4
SR=2.0	0.04	-0.531	1.979	-0.4	0.0511	-0.689	2.735	-1.65

Equations 5.9, 5.10 and 5.11 are developed from directivity amplifications of sites located along  $R_x/L=0.5$  and  $R_y \leq 15\text{km}$ . To estimate the directivity amplifications of sites at other locations around the fault geometric scale factors ( $GSF_{T_{\max}}$  and  $GSF_{T_{10}}$ ) are used in the directivity amplification expressions. The geometric scale factors,  $GSF_{T_{\max}}$  and  $GSF_{T_{10}}$  modify  $AMP_{T_{\max},base}$  and  $AMP_{T_{10},base}$  to calculate  $AMP_{T_{\max}}$  and  $AMP_{T_{10}}$  for different locations around the fault. As in the case of  $AMP_{T_{\max},base}$  and  $AMP_{T_{10},base}$ , a linear trend is assumed between  $AMP_{T_{\max}}$  and  $AMP_{T_{10}}$  to estimate the directivity amplifications at the intermediate periods between  $0.6s \leq T \leq T_{\max}$  and  $T_{\max} < T \leq 10s$  at locations other than  $R_x/L = 0.5$ . The derivations of relevant expression are discussed in the following paragraphs.

Figure 5.16 and Figure 5.17 as well as Figure 5.18 to Figure 5.19 show the variations of 475-year and 2475-year  $GSF_{T_{\max}}$  and  $GSF_{T_{10}}$  along  $R_x/L = 0, 0.25, 0.5, 0.6, 0.7$  and  $0.8$  for  $s = 0.5\text{cm/year}, 1.0\text{cm/year}$  and  $2.0\text{cm/year}$ . The GSF computations are done with the directivity amplifications of sites within  $R_y \leq 15\text{km}$  because for relatively remote sites ( $R_y > 15\text{km}$ ) a distance taper will be considered as explained

later. Given a specific  $M_{ch}$ , GSF is the normalized directivity amplifications at  $R_x/L \neq 0.5$  by those at  $R_x/L = 0.5$ . These plots suggest that the directivity amplifications do not change dramatically at  $M_{ch} 6.25$  for different  $R_x/L$ . Thus, the directivity amplification is not affected seriously from the site location at small magnitudes. Thus, the characteristic magnitude dependent variations of  $GSF_{T_{max}}$  and  $GSF_{T_{10}}$  start with unity at  $M_{ch} 6.25$  and increases linearly up to  $M_{ch} 7.25$ . Both geometric scale factors ( $GSF_{T_{max}}$  and  $GSF_{T_{10}}$ ) attain a constant value after  $M_{ch} 7.25$  that corresponds to the geometric scale factor at  $M_{ch} 7.25$ . The expressions for the computation of  $GSF_{T_{max}}$  and  $GSF_{T_{10}}$  are given in Equations 5.12 and 5.13. The corresponding scale factors ( $SF_{T_{max}}$  and  $SF_{T_{10}}$ ) values are given in Table 5.8.

$$GSF_{T_{max}} = [1 + (SF_{T_{max}} - 1) \cdot (M_{ch} - 6.25)] \quad 6.25 < M_{ch} \leq 7.25 \quad 5.12a$$

$$GSF_{T_{max}} = SF_{T_{max}} \quad M_{ch} > 7.25 \quad 5.12b$$

$$GSF_{T_{10}} = [1 + (SF_{T_{10}} - 1) \cdot (M_{ch} - 6.25)] \quad 6.25 < M_{ch} \leq 7.25 \quad 5.13a$$

$$GSF_{T_{10}} = SF_{T_{10}} \quad M_{ch} > 7.25 \quad 5.13b$$

Table 5.8 Scale factor values for  $T_{max}$  and  $T = 10s$  for the computation of geometric scale factors at different  $R_x/L$  values (SHB11 model)

	$R_x/L=0$	$R_x/L=0.25$	$R_x/L=0.5$	$R_x/L=0.6$	$R_x/L=0.7$	$R_x/L=0.8$
<b>2475-<math>SF_{T_{max}}</math></b>	0.67	0.89	1	0.93	0.7	0.6
<b>2475- <math>SF_{T_{10}}</math></b>	0.78	0.94	1	0.93	0.83	0.78
<b>475- <math>SF_{T_{max}}</math></b>	0.83	0.85	1	0.93	0.85	0.83
<b>475- <math>SF_{T_{10}}</math></b>	0.96	0.96	1	0.98	0.96	0.96

The directivity amplifications at  $T_{max}$  and  $T = 10s$  ( $AMP_{T_{max}}$  and  $AMP_{T_{10}}$ , respectively) at locations other than  $R_x/L = 0.5$  are computed from  $AMP_{T_{max},base}$ ,  $AMP_{T=10,base}$ ,  $GSF_{T_{max}}$  and  $GSF_{T_{10}}$  per Equations 5.9, 5.10, 5.11, 5.12 and 5.13. For convenience, the relevant expressions for  $AMP_{T_{max}}$  and  $AMP_{T_{10}}$  are given in Equations 5.14 and 5.15.

$$AMP_{T_{max}} = AMP_{T_{max},base} \cdot GSF_{T_{max}} =$$

$$(\alpha_{T_{max}} \cdot M_{ch} + \beta_{T_{max}}) \cdot [1 + (SF_{T_{max}} - 1) \cdot (M_{ch} - 6.25)] \quad 6.25 < M_{ch} \leq 7.25 \quad 5.14a$$

$$AMP_{T_{max}} = AMP_{T_{max},base} \cdot GSF_{T_{max}} = \quad M_{ch} > 7.25 \quad 5.14b$$

$$(\alpha_{T_{max}} \cdot 7.25 + \beta_{T_{max}}) \cdot SF_{T_{max}}$$

$$AMP_{T_{10}} = AMP_{T_{10},base} \cdot GSF_{T_{10}} = \quad 6.25 < M_{ch} \leq 7.25 \quad 5.15a$$

$$(\alpha_{T_{10}} \cdot M_{ch} + \beta_{T_{10}}) \cdot [1 + (SF_{T_{10}} - 1) \cdot (M_{ch} - 6.25)]$$

$$AMP_{T_{10}} = AMP_{T_{10},base} \cdot GSF_{T_{10}} = \quad M_{ch} > 7.25 \quad 5.15b$$

$$(\alpha_{T_{10}} \cdot 7.25 + \beta_{T_{10}}) \cdot SF_{T_{10}}$$

As already stated the extension of directivity amplifications at periods other than  $T_{max}$  and  $T = 10s$  is done by assuming a bilinear variation of directivity amplifications between  $0.6s \leq T \leq T_{max}$  and  $T_{max} < T \leq 10s$ . The general form of directivity amplification function for this computation is given in Equation 5.16. This equation can be used to compute the directivity amplifications between  $0.6 \text{ sec} < T < 10 \text{ sec}$  for 475-year and 2475-year return periods by using the auxiliary formulations given in Equations 5.9, 5.10, 5.11, 5.12 and 5.13. The functional form accounts for the particular influence of  $M_{ch}$  and  $\dot{s}$ .

$$AMP(T) = 1 + \quad 5.16a$$

$$[(AMP_{T_{max}} - 1) \cdot \left(\frac{T-0.6}{T_{max}-0.6}\right)] \quad 0.6s < T < T_{max}$$

$$AMP(T) = AMP_{T_{max}} + \quad 5.16b$$

$$[(AMP_{T_{10}} - AMP_{T_{max}}) \cdot \left(\frac{T-T_{max}}{10-T_{max}}\right)] \quad T_{max} < T < 10s$$

The above expressions compute  $T_{max}$  by considering the directivity amplifications for distances up to 15km from the fault strike. In other words, the variation of  $T_{max}$  is assumed to be dominated by the directivity effects up to  $R_y = 15km$  (Equation 5.8). As explained in the beginning of this chapter and at different locations throughout the text, the computed directivity amplifications from above expressions are assumed to be constant for  $R_y \leq 15km$ . The directivity amplifications taper down to unity between  $15km < R_y \leq 30km$  and this is discussed in the last part of this chapter (Section 5.3.4).

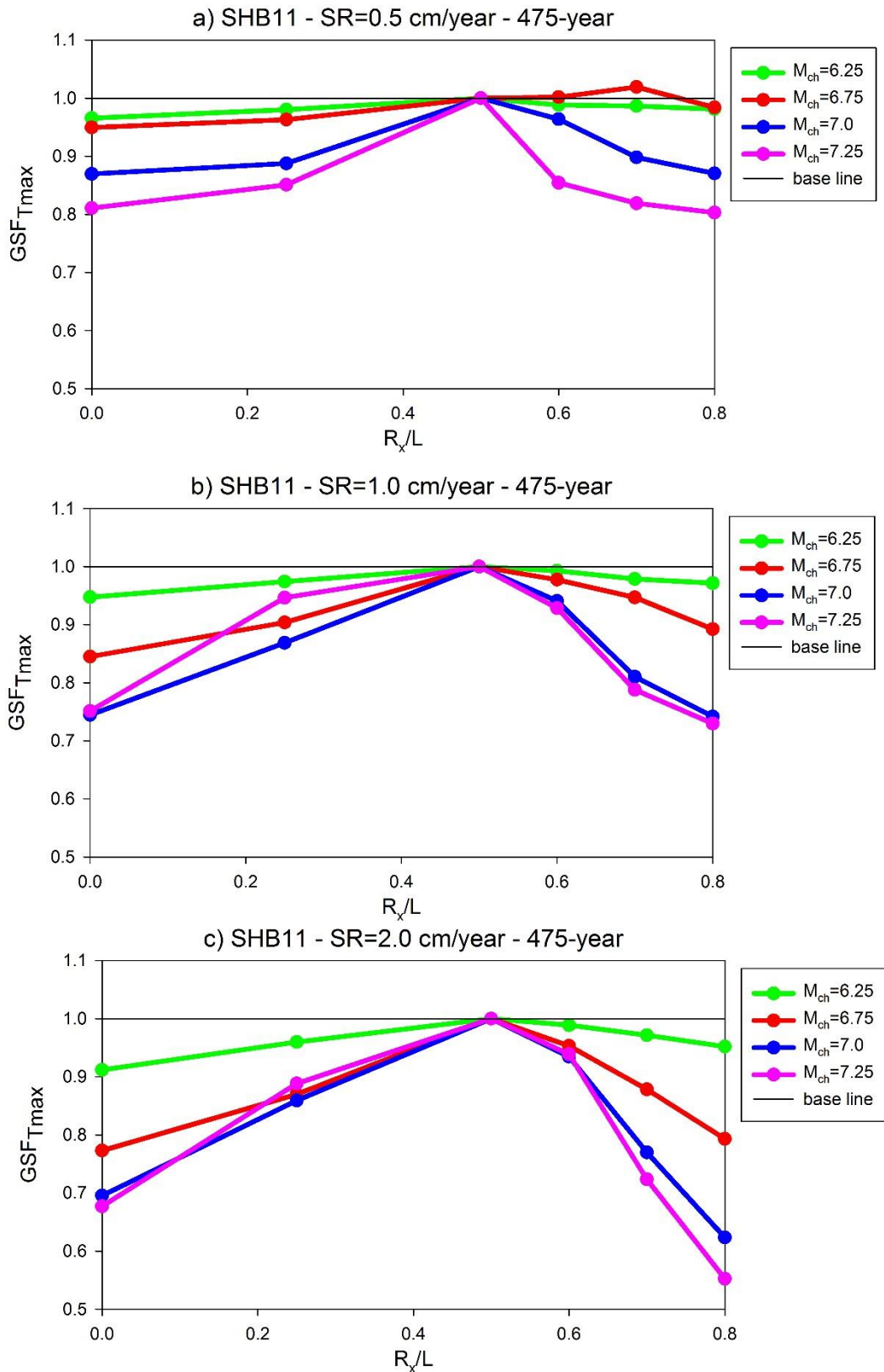


Figure 5.16 Observed geometric scale factors for  $AMP_{T_{max}}$  - 475-year return period and  $\dot{s} = 0.5\text{cm/year}$ ,  $\dot{s} = 1.0\text{cm/year}$  and  $\dot{s} = 2.0\text{cm/year}$  (SHB11)

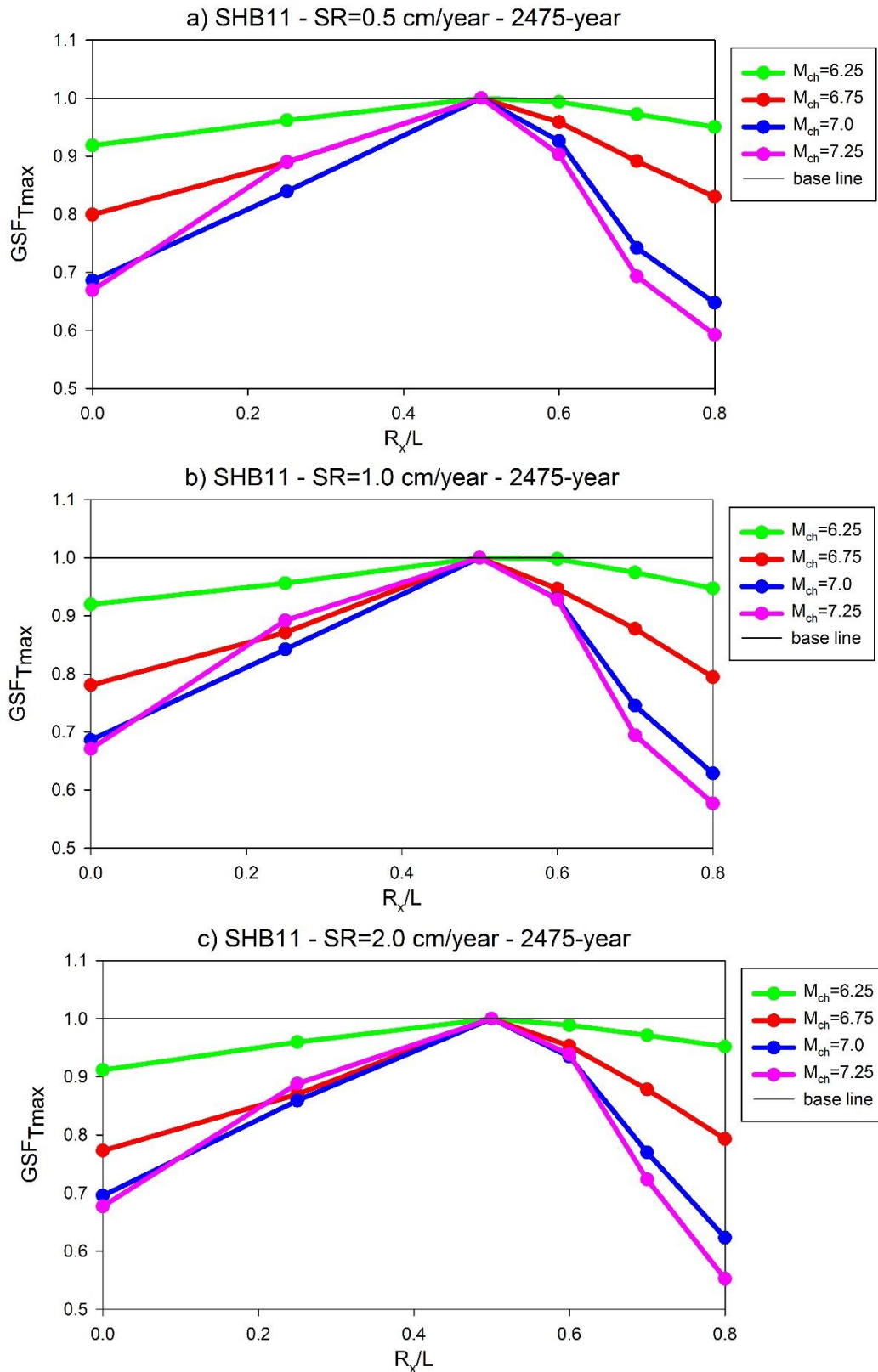


Figure 5.17 Observed geometric scale factors for  $AMP_{Tmax}$  - 2475-year return period and  $\dot{s} = 0.5\text{cm/year}$ ,  $\dot{s} = 1.0\text{cm/year}$  and  $\dot{s} = 2.0\text{cm/year}$  (SHB11)

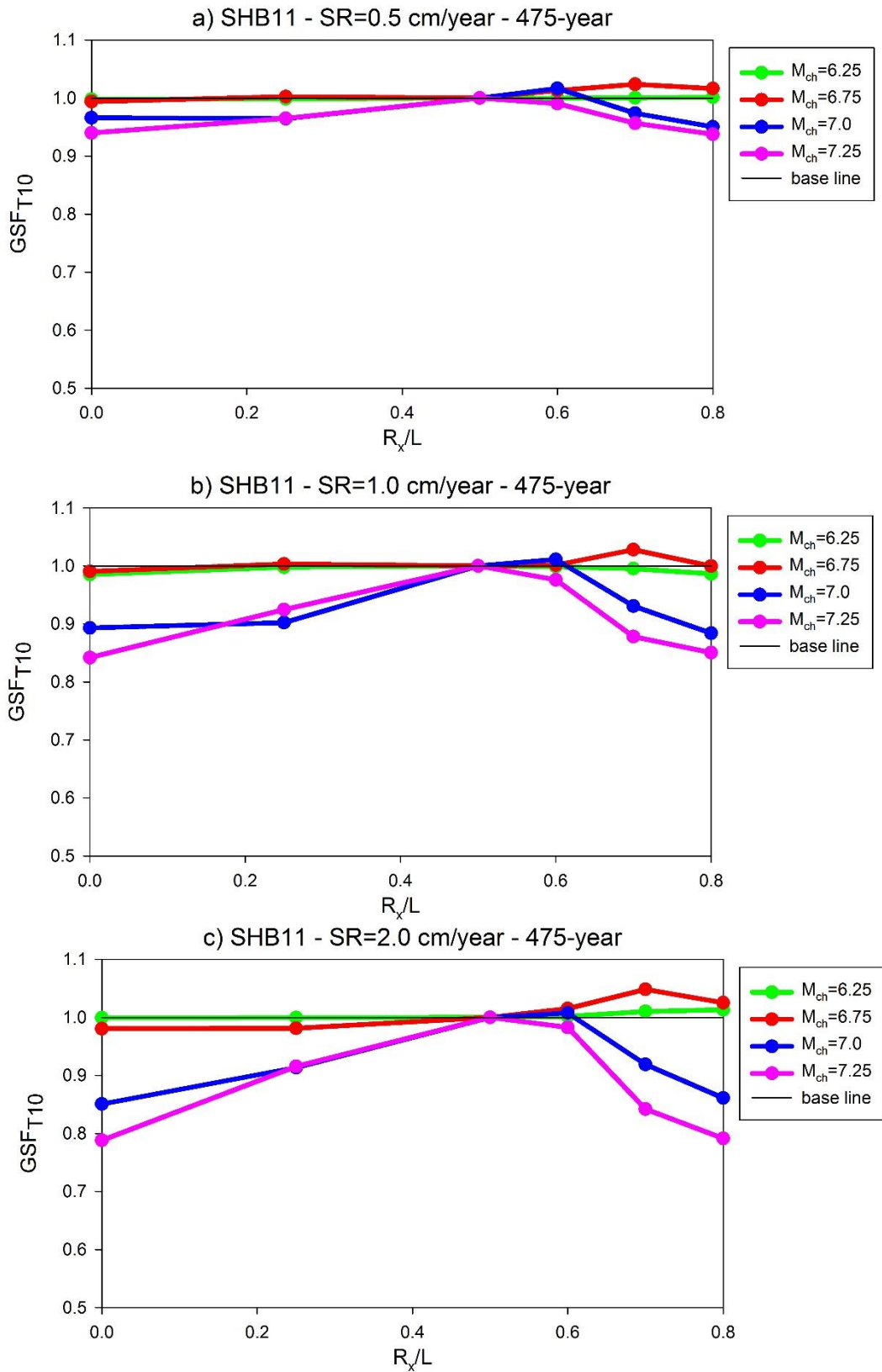


Figure 5.18 Observed geometric scale factors for  $AMP_{T10}$  - 475-year return period and  $\dot{s} = 0.5\text{cm/year}$ ,  $\dot{s} = 1.0\text{cm/year}$  and  $\dot{s} = 2.0\text{cm/year}$  (SHB11)

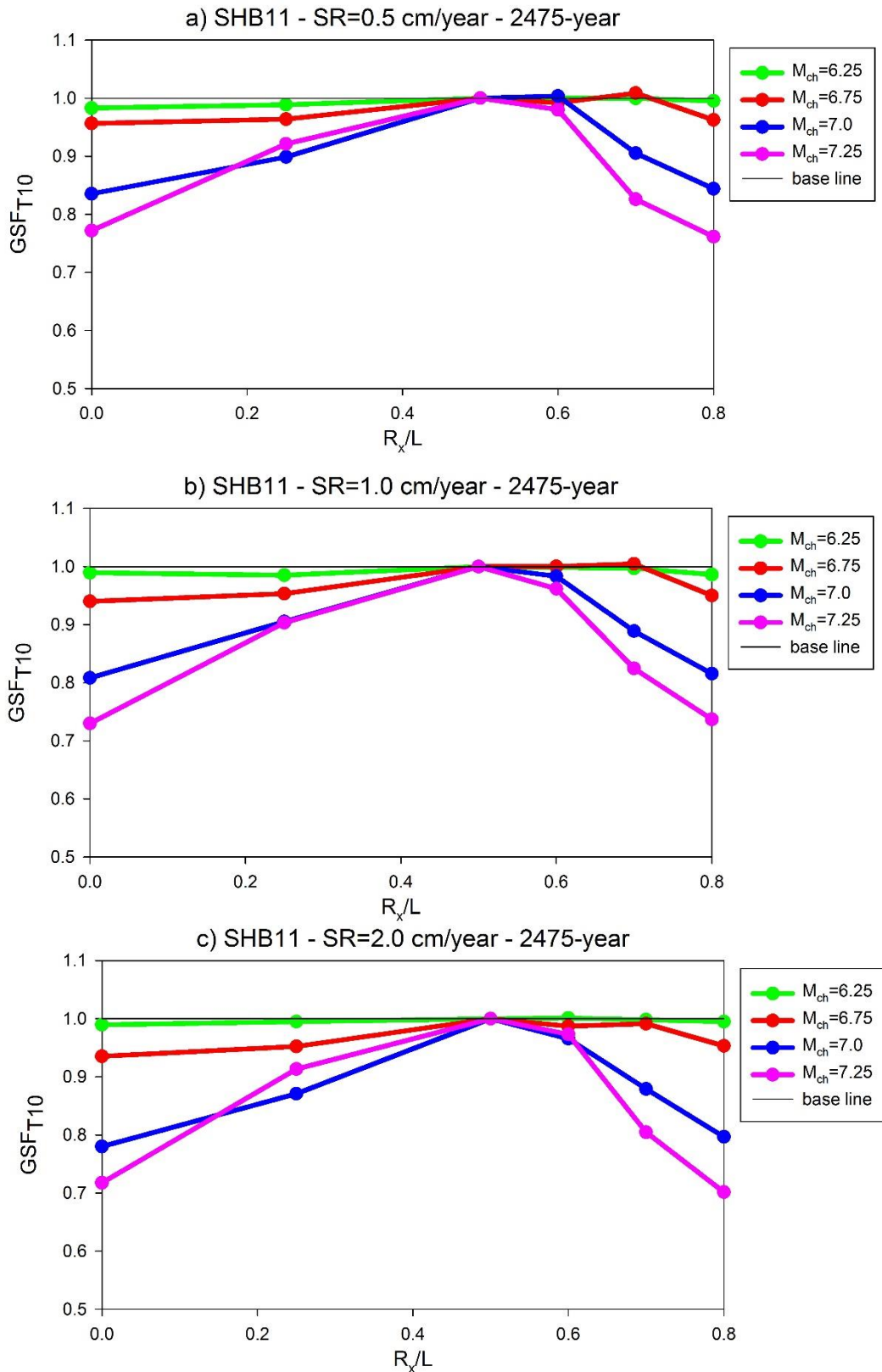


Figure 5.19 Observed geometric scale factors for  $AMP_{T10}$  - 2475-year return period and  $\dot{s} = 0.5\text{cm/year}$ ,  $\dot{s} = 1.0\text{cm/year}$  and  $\dot{s} = 2.0\text{cm/year}$  (SHB11)

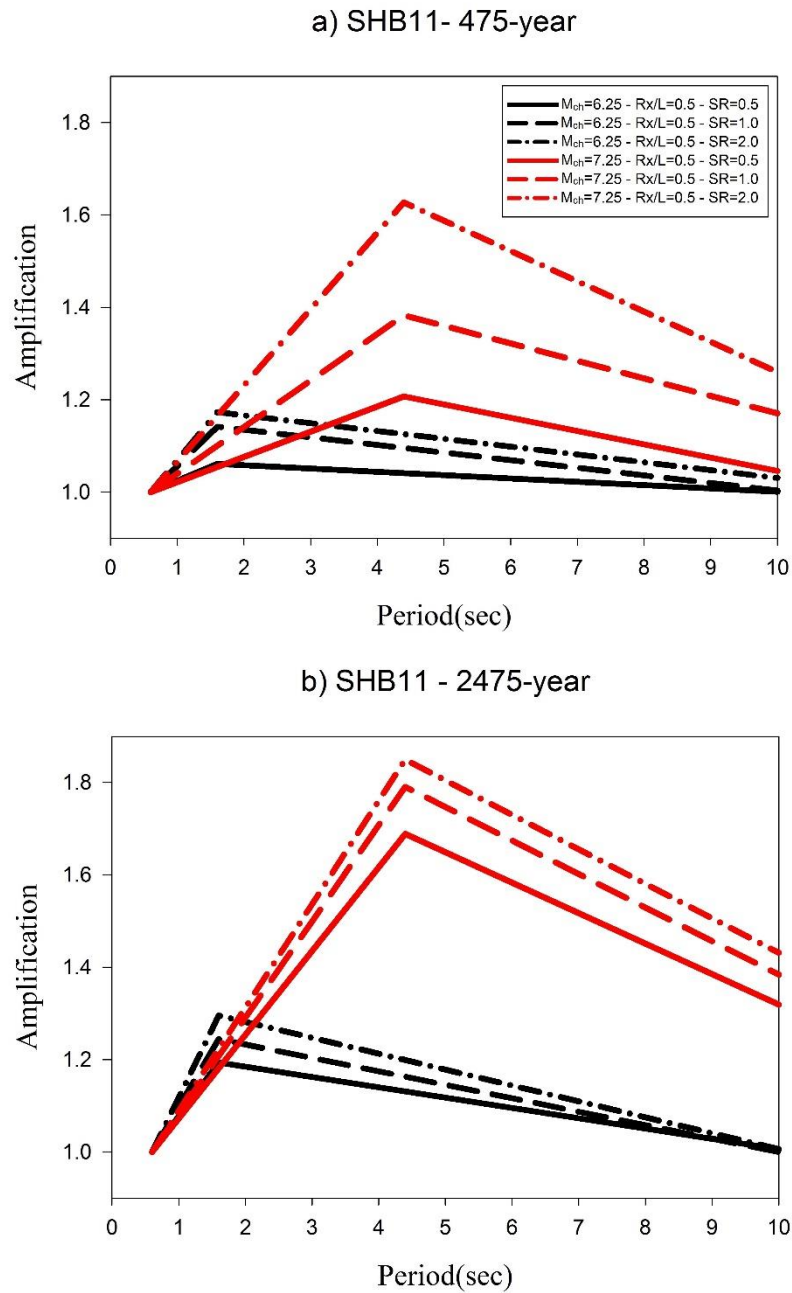


Figure 5.20 Effect of characteristic magnitude and slip rate on the directivity amplifications for SHB11 model computed from proposed simplified expressions  
a) 475-year return period b) 2475-year return period

The directivity amplification expressions developed here are employed for different earthquake scenarios to grasp the variations in directivity under different parameters. Figure 5.20 illustrates the period-dependent variation of directivity amplifications at  $R_x/L=0.5$  when faults of different lengths rupture with  $M_{ch}$  6.25 and  $M_{ch}$  7.25. The plots include the slip rate effects confined to the slip rates considered in this study.

As it is expected, the increase in slip rates as well as  $M_{ch}$  lead to larger directivity amplifications. Needless to say, the change in return periods from 475-year to 2475-year) also lead to larger directivity amplifications. Note that the maximum directivity amplifications occur at  $T_{max} = 1.6s$  and  $T_{max} = 4.4s$  for  $M_{ch} 6.25$  and  $M_{ch} 7.25$ , respectively. These values are comparable with the patterns observed from PSHA.

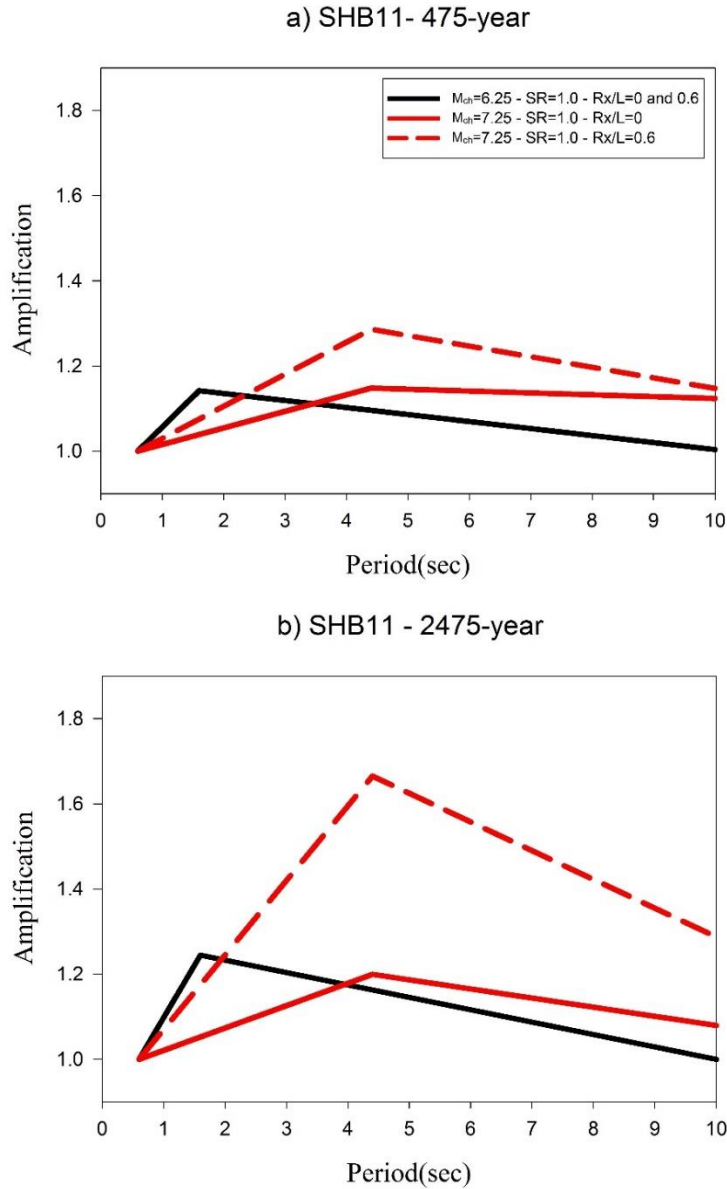


Figure 5.21 Effect of fault-site geometry ( $R_x/L$ ) on the directivity amplifications of SHB11 narrow-band model computed from the proposed simplified formulations a) 475-year return period b) 2475-year return period

Figure 5.21 compares the period-dependent variation of directivity amplifications for  $R_x/L=0$  and  $R_x/L=0.6$  at Mch 6.25 and Mch 7.25. The directivity amplifications also account for the differences due to different return periods. There is a single curve for  $M_{ch}$  6.25 as the model assumes indifferent spatial variation of directivity amplifications at small magnitude events. (Side note: the smallest characteristic magnitude considered in this study is  $M_{ch}$  6.25 that is approximately the lower bound limit of narrow-band directivity models used in this study). The amplitude of directivity amplifications are higher for  $R_x/L=0.6$  as the characteristic magnitude attains larger values. This observation is even stronger for larger return periods (2475-year in the comparative plots). These simple comparisons suggest that the important features of forward-directivity as discussed in Chapter 3 are incorporated fairly well with the proposed expressions in this section.

### ***5.3.3 Simplified Directivity Amplification Equations for CHS13 Narrow-Band Model***

The directivity amplification equations that are developed from CHS13 narrow-band directivity model follow a similar methodological pattern as in the case of SHB11-based expressions (discussions in the previous section). As discussed in Chapter 3, the directivity amplifications computed from CHS13 increase for spectral periods up to  $T_{corner}$  (between  $0.5s \leq T \leq T_{corner}$ ) that is followed by a constant plateau towards very long periods (between  $T_{corner} < T \leq 10s$ ). In addition, CHS13 modifies RotD50 horizontal component for directivity effects ( $RotD50_{Directivity}$ ) while SHB11 modifies GMRotI50 horizontal component for directivity and the modified horizontal component is along the strike normal direction (simply fault-normal component). Similar to the methodology followed in SHB11, the reference (base) expressions for CHS13 are developed from the median directivity amplifications at sites along  $R_x/L = 0.6$  and  $R_y \leq 15km$  (Sites 4, 10, 16 and 22 in Figure 5.9). These sites show the maximum directivity amplification in CHS13 and the median directivity amplification ( $AMP_{T_{corner},base}$ ) is computed for the spectral period  $T_{corner}$  in this case. The spectral period  $T_{corner}$  is also calculated from Equation 5.8 as in the case of SHB11 because PSHA results suggest  $T_{corner} \approx T_{max}$ . The relationship between  $AMP_{T_{corner},base}$  and characteristic magnitude is given in Equation 5.17.

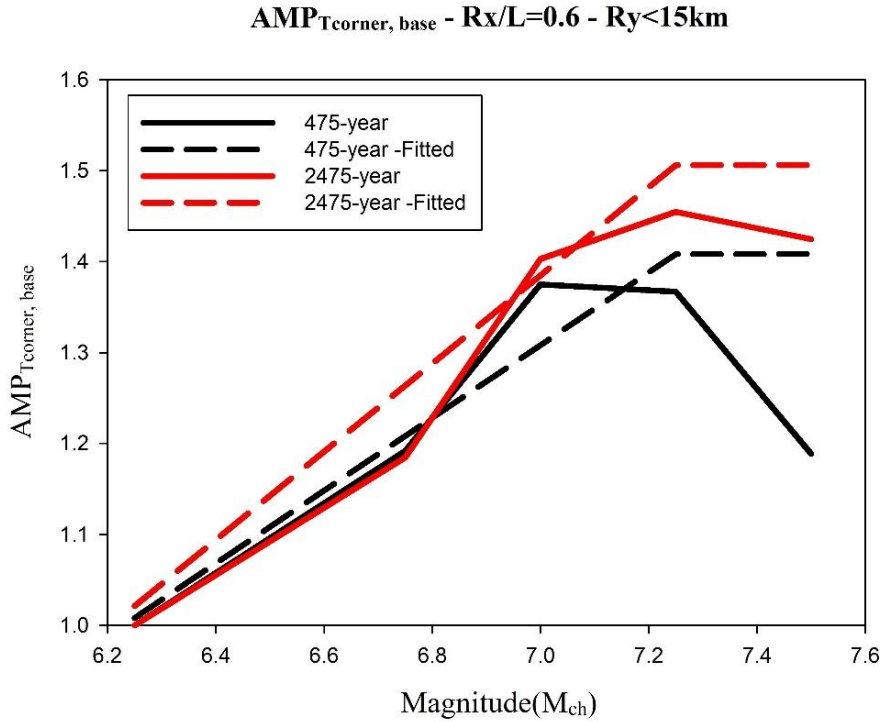


Figure 5.22 Base amplification factors and magnitude relationships together with linear line fits calculated for sites 4, 10, 16 and 22 at spectral period  $T_{corner}$  - CHS13 model, 475- and 2475-year return period

$$AMP_{T_{corner},base} = \alpha_{T_{corner}} \cdot M_{ch} + \beta_{T_{corner}} \quad 6.25 < M_{ch} \leq 7.25 \quad 5.17a$$

$$AMP_{T_{corner},base} = \alpha_{T_{corner}} \cdot 7.25 + \beta_{T_{corner}} \quad M_{ch} > 7.25 \quad 5.17b$$

where  $\alpha_{T_{corner}}$  and  $\beta_{T_{corner}}$  are the regression coefficients and are computed by fitting a straight line over the observed data (Figure 5.22). The  $\alpha_{T_{corner}}$  and  $\beta_{T_{corner}}$  coefficients of Equation 5.17 are given in Table 5.9 for the return periods of interest in this study.

Table 5.9  $\alpha_{T_{corner}}$  and  $\beta_{T_{corner}}$  coefficients for linearly fitted  $AMP(T_{corner})$  function - CHS13

<b>475-Year</b>		<b>2475-Year</b>	
$\alpha_{T_{corner}}$	$\beta_{T_{corner}}$	$\alpha_{T_{corner}}$	$\beta_{T_{corner}}$
0.4	-1.4931	0.464	-1.9

As it is depicted in Figure 5.22 the directivity amplifications are linearly related to  $M_{ch}$  between  $6.25 \leq M_{ch} \leq 7.25$ . The amplification saturation is also observed for this

case as in SHB11, thus,  $AMP_{T_{corner},base}$  value at  $M_{ch} 7.25$  is assumed to be valid for  $M_{ch}>7.25$ . Note that the slip rate does not play an important role in the directivity amplification amplitudes so  $\dot{s}$  is disregarded in the formulations developed for CHS13.

The effect of site location (spatial variation of sites around the fault) is incorporated into this model via geometric scale factor ( $GSF_{T_{corner}}$ ). The approach is again similar to the one followed in SHB11 model. The maximum scale factor ( $GSF_{T_{corner}}$ ) is unity for  $M_{ch} 6.25$  whereas it is the normalized directivity amplifications at locations  $R_x/L \neq 0.6$  with those at  $R_x/L = 0.6$ . The procedure for the computation of  $GSF_{T_{corner}}$  is given in Figure 5.23 for 475 and 2475-year return period. The related  $SF_{T_{corner}}$  values are given in Table 5.10.

The geometric scale factor ( $GSF_{T_{corner}}$ ) is assumed to vary linearly between  $6.25 \leq M_{ch} \leq 7.25$  whereas it is kept as constant between  $7.25 < M_{ch} \leq 7.5$  with the corresponding value at  $M_{ch} 7.25$ . The relevant expressions for the computation of  $GSF_{T_{corner}}$  are given in Equation 5.18.

$$GSF_{T_{corner}} = [1 + (SF_{T_{corner}} - 1) \times (M_{ch} - 6.25)] \quad 6.25 < M_{ch} \leq 7.25 \quad 5.18a$$

$$GSF_{T_{corner}} = SF_{T_{corner}} \quad M_{ch} > 7.25 \quad 5.18b$$

Table 5.10 Geometric scale factor for different  $R_x/L$  values -CHS13

	$R_x/L=0$	$R_x/L=0.25$	$R_x/L=0.5$	$R_x/L=0.6$	$R_x/L=0.7$	$R_x/L=0.8$
<b>475-<math>T_{corner}</math></b>	0.73	0.74	0.93	1	0.98	0.89
<b>2475-<math>T_{corner}</math></b>	0.69	0.70	0.86	1	0.98	0.88

After determining  $AMP_{T_{corner},base}$  and geometric scale factor ( $GSF_{T_{corner}}$ ) the directivity amplification at any location around the fault for CHS13 narrow-band directivity model can be calculated (Equation 5.19). The  $AMP_{T_{corner}}$  in Equation 5.19 is the maximum directivity amplification corresponding to spectral period  $T_{corner}$ . As noted previously, for spectral periods larger than  $T_{corner}$  the directivity amplification takes a constant value that is equal to  $AMP_{T_{corner}}$ .

$$AMP_{T_{corner}} = AMP_{T_{corner},base} \cdot GSF_{T_{corner}} =$$

$$(\alpha_{T_{corner}} \cdot M_{ch} + \beta_{corner}) \cdot \quad 6.25 < M_{ch} \leq 7.25 \quad 5.19a$$

$$[1 + (SF_{T_{cor}} - 1) \cdot (M_{ch} - 6.25)]$$

$$AMP_{T_{corner}} = AMP_{T_{corner},base} \cdot GSF_{T_{corner}} = \quad M_{ch}>7.25 \quad 5.19b$$

$$(\alpha_{T_{corner}} \cdot 7.25 + \beta_{T_{corner}}) \cdot SF_{T_{corner}}$$

The extension of directivity amplifications for periods other than  $T_{corner}$  is given in Equation 5.20 where a linear trend is assumed between  $0.5s \leq T \leq T_{corner}$  and a constant value for  $T > T_{corner}$ .

$$AMP(T) = 1 + \left[ (AMP_{T_{corner}} - 1) \times \frac{T-0.5}{T_{corner}-0.5} \right] \quad 0.5s < T \leq T_{corner} \quad 5.20a$$

$$AMP(T) = AMP_{T_{corner}} \quad T_{corner} < T < 10s \quad 5.20b$$

As already emphasized in the previous section, the corner periods ( $T_{corner}$ ) are estimated from Equation 5.8 that is developed from the observed  $T_{corner}$  (or  $T_{max}$  in case of SHB11) for  $R_y \leq 15km$ . A distance taper is implemented for sites beyond  $R_y = 15km$  to account for the decrease in directivity effects and it will be discussed in Section 5.3.4.

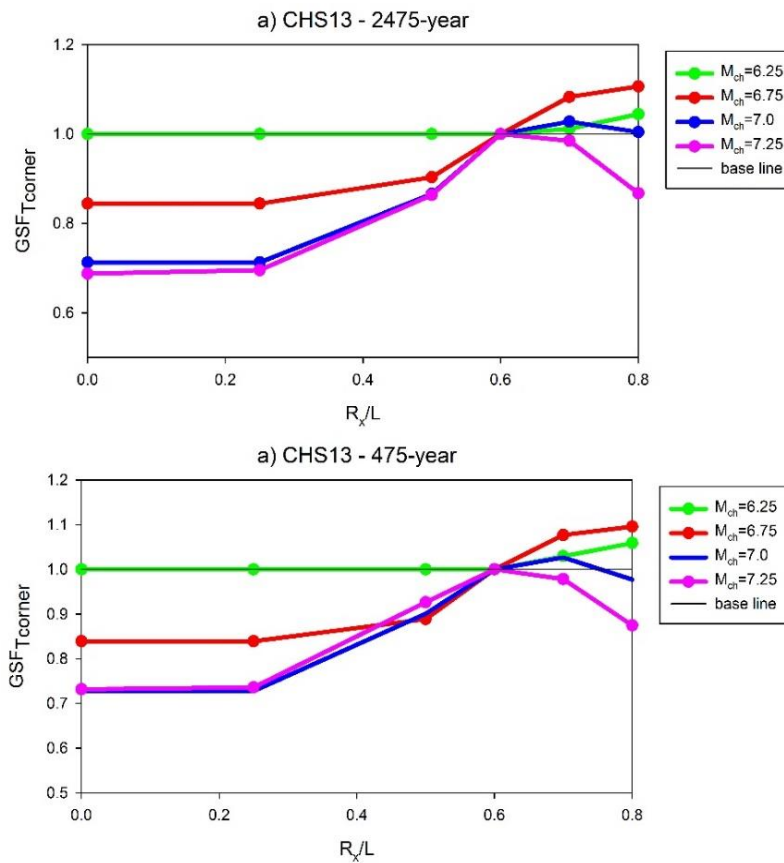


Figure 5.23 Calculation of Geometric Scale Factor for  $AMP_{T_{corner}} - 475\text{-year}$  CHS13

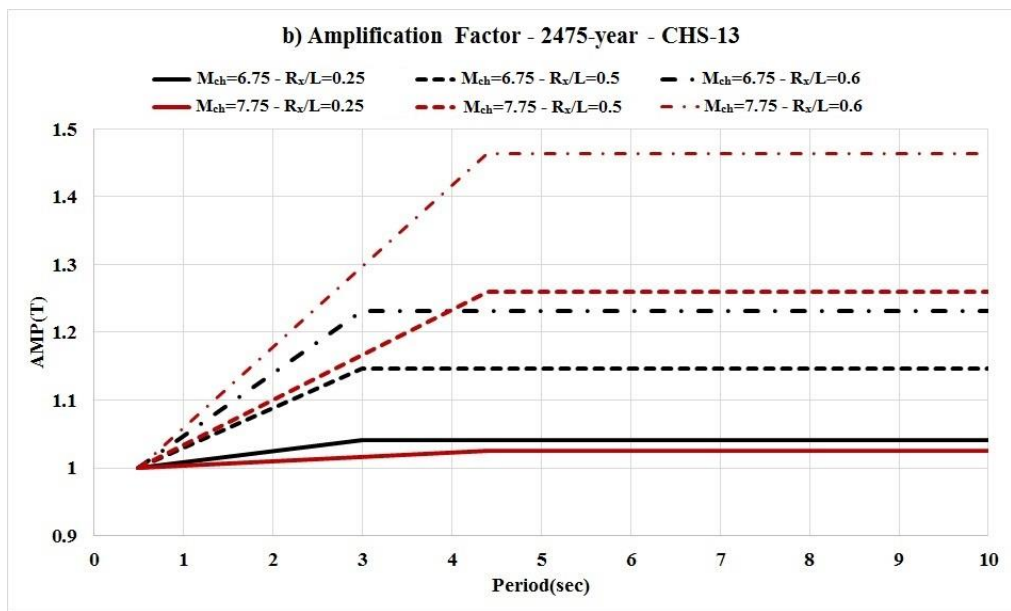
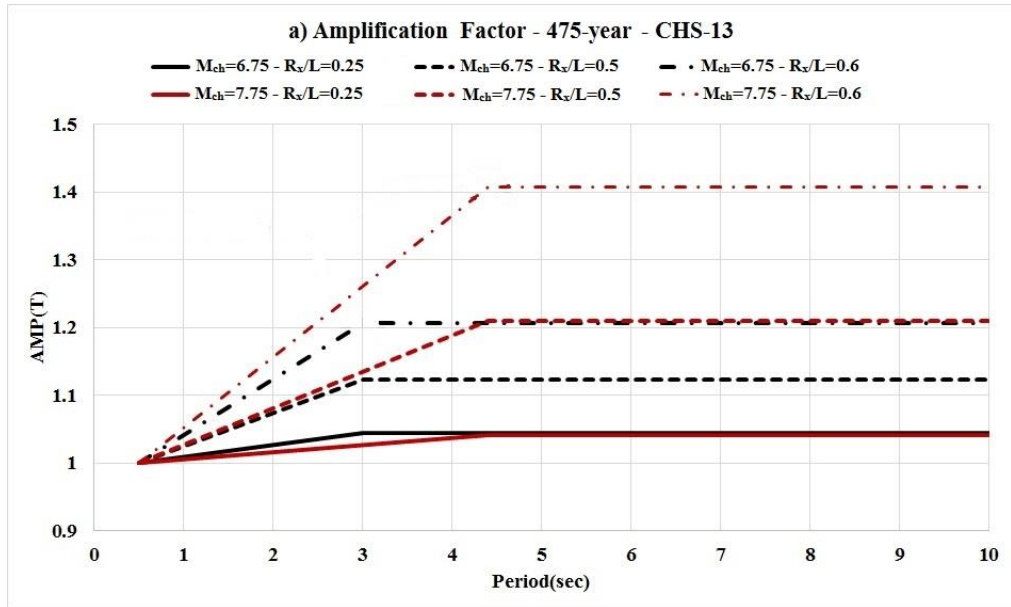


Figure 5.24 Amplification Model for RotD50 Component of CHS13

a) 475-year Return Period b) 2475-year return period

Equations 5.19 and 5.20 are used to compute directivity amplifications to observe the behavior of CHS13 narrow-band model under different combinations of  $M_{ch}$  and site location. Figure 5.24 shows the 475-year and 2475-year return period directivity amplifications plotted for  $M_{ch}$  6.75 and  $M_{ch}$  7.25 at three site locations ( $R_x/L=0.25$ ,

0.5 and 0.6). The displayed directivity amplifications are assumed to be invariant of fault-normal distance up to  $R_y = 15\text{km}$ . As it is depicted from this figure, the site location and  $M_{ch}$  can significantly affect the directivity amplifications. The corner periods shift towards longer periods with increasing  $M_{ch}$  that also results in increased directivity amplifications. As  $R_x/L$  attains values closer to 0.6, the directivity amplifications increase. Inherently, the larger return periods (2475-year vs. 475-year return periods in this case) result in larger directivity amplifications. These observations are similar to those highlighted from the simplified SHB11 narrow-band directivity model. The difference is in the period-dependent directivity amplification trend as well as the amplitudes of directivity amplifications (originates from different horizontal component definitions of the two models).

### 5.3.4 Taper function for the distance

The simplified equations proposed for SHB11 and CHS13 directivity models assume an invariant directivity amplification for distances up to  $R_y = 15\text{km}$ . The directivity amplifications taper down linearly to unity between  $15\text{km} < R_y \leq 30\text{km}$ . In essence, the simplified directivity amplification expressions given in the previous two section estimate constant directivity amplifications that are valid for  $R_y \leq 15\text{km}$  and these values should be decreased linearly to unity between  $15\text{km} < R_y \leq 30\text{km}$ . This approach is similar to the one used in the seismic design guidelines of CALTRANS (CALTRANS, 2013). Equations 5.21 show the implementation of this approach as discussed in this paragraph. The whole concept is presented in Figure 5.25.

$$AMP^{SHB11 \text{ or } CHS13}(T) = AMP_{0\text{km} \leq R_{rup} \leq 15\text{km}}^{SHB11 \text{ or } CHS13}(T) \quad R_{rup} \leq 15\text{km} \quad 5.21a$$

$$AMP^{SHB11 \text{ or } CHS13}(T) = AMP_{0\text{km} \leq R_{rup} \leq 15\text{km}}^{SHB11 \text{ or } CHS13}(T) + \left[ (1 - AMP_{0\text{km} \leq R_{rup} \leq 15\text{km}}^{SHB11 \text{ or } CHS13}(T)) \cdot \left( \frac{R_{rup} - 15}{15} \right) \right] \quad 15\text{km} < R_{rup} \leq 30\text{km} \quad 5.21b$$

$$AMP^{SHB11 \text{ or } CHS13}(T) = 1 \quad R_{rup} > 30\text{km} \quad 5.21c$$

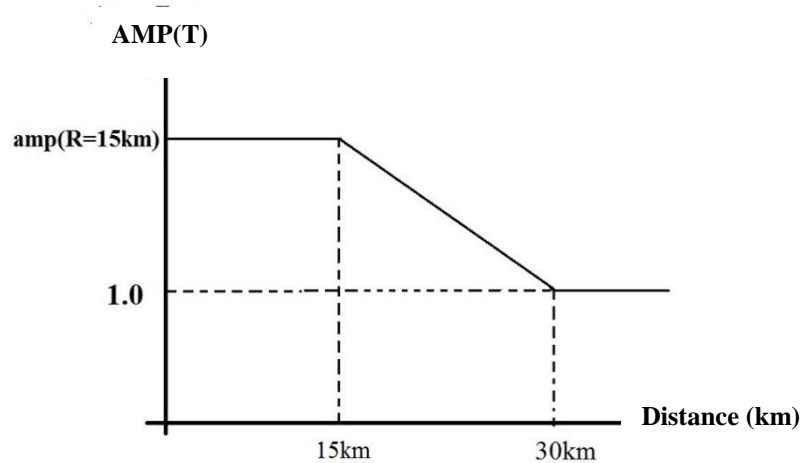


Figure 5.25 Distance Tapering of Directivity Amplification Factor

The parameter  $AMP^{SHB11 \text{ or } CHS13}(T)$  is the directivity amplification estimated either from SHB11 or CHS13 directivity models.  $AMP_{0km \leq R_{rup} \leq 15km}^{SHB11 \text{ or } CHS13}(T)$  is the directivity amplification computed either from SHB11 or CHS13 directivity models by considering the simplified expressions given in the previous two sections. Note that Equation 5.21b is a linear taper  $15km \leq R_{rup} \leq 30km$  that goes down to unity with increasing distance.

The distance tapering presented above is verified by using the observed trends from PSHA. Figure 5.26 shows the variation of observed SHB11-based directivity amplifications at  $T_{max}$  as a function of  $R_y$  ( $0km \leq R_y \leq 30km$ ). Figure 5.27 displays the same information for CHS13 directivity model but this time directivity amplifications are given at  $T_{corner}$ . Both figures consider the target return periods of this study: 475-year and 2475-year return periods. The red circles display the aforementioned observed directivity amplifications whereas dark red diamonds along each stripe is the median of observed directivity amplifications. The stripes at each discrete  $R_y$  (i.e.,  $R_y = 0km$  to  $R_y = 30km$ ) display the directivity amplifications at all  $R_x/L$  values ( $R_x/L = 0$  to  $R_x/L = 0.8$ ). This way, the reader gets an overall picture on the distance tapering at a discrete period ( $T_{max}$  or  $T_{corner}$  in these comparisons but the period can be any other specific value as well). The corresponding estimated directivity amplifications are given as grey circles and their median at each stripe is given in black.

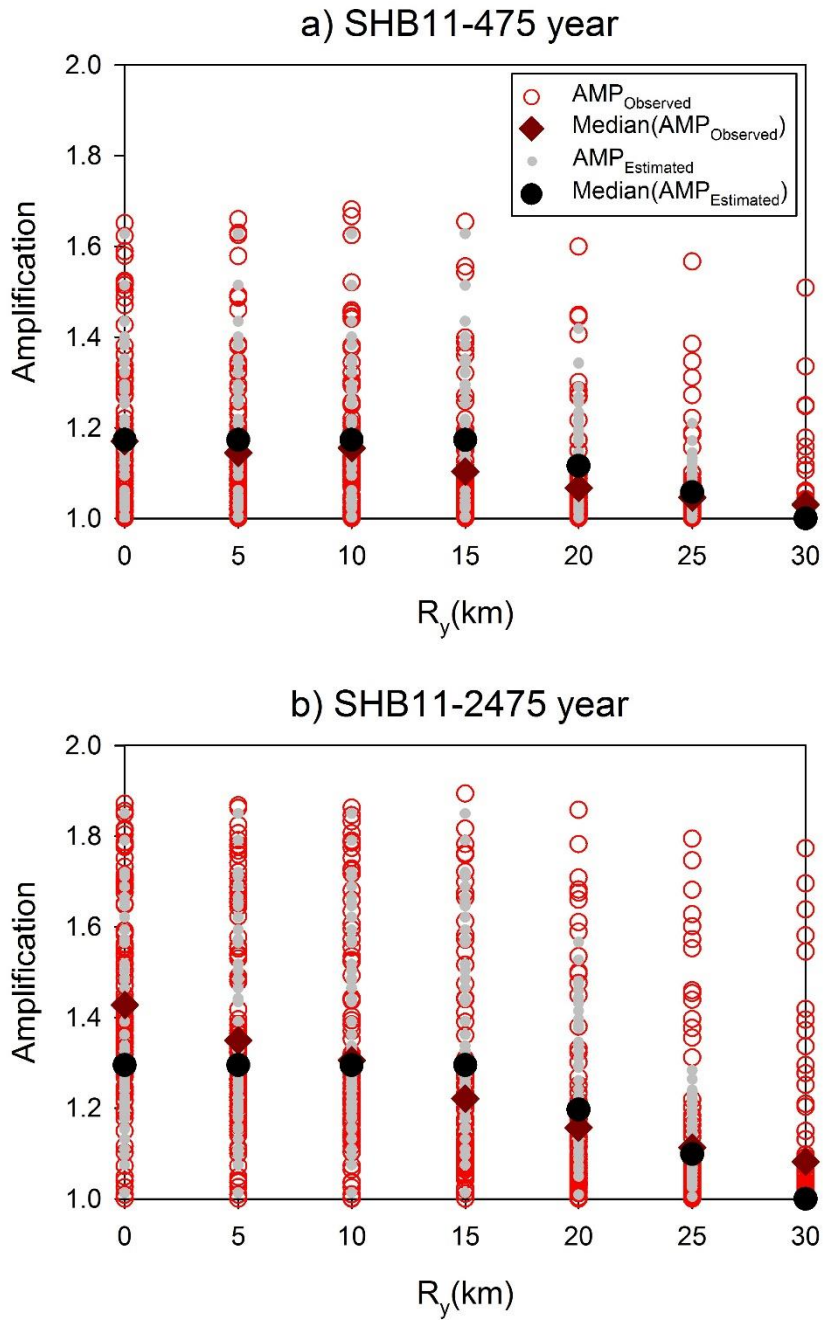


Figure 5.26 Observed and estimated directivity amplifications as a function of  $R_y$  for simplified SHB11 model

The estimated and observed medians compare fairly well for SHB11 (in particular for 475-year return period) whereas the estimated directivity amplifications for CHS13 show some level of discrepancy with respect to the PSHA results. The simplified expressions for CHS13 are conservative with respect to the observed

trends for  $10\text{km} \leq R_y \leq 25\text{km}$ . As indicated above such discrepancies are not significant in the simplified SHB11 directivity amplification model.

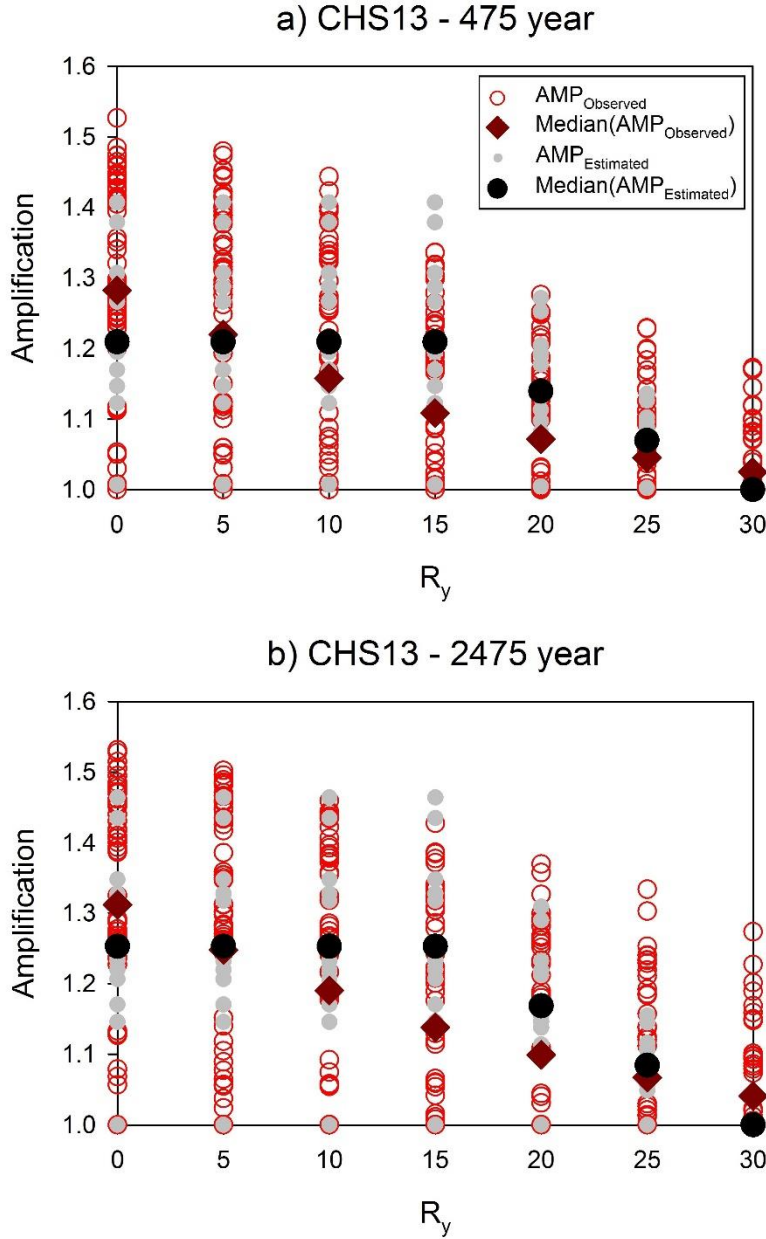


Figure 5.27 Observed and estimated directivity amplifications as a function of  $R_y$  for CHS13 model

Note that the problem tackled in this chapter (development of simplified expressions for directivity amplification) is not straightforward as the proposed expressions are tailored for their use in seismic design codes. Handful approximations and

simplifications are done to achieve this objective. The results should be evaluated under this perspective. The next section displays the residual analyses for both simplified expressions to assess their performance in a wider perspective.

### 5.3.5 *Residual Analyses*

The unbiased directivity amplification estimations of the proposed expressions are verified by classical residual (difference between observed and estimated quantities) analysis. Figure 5.28 and Figure 5.29 display the residual scatters for simplified SHB11-based expressions together with distance tapering approach as discussed in Section 5.3.4. The observations are the resulting directivity amplifications from PSHA. The residuals are plotted in terms of  $R_x/L$ ,  $R_y$  and spectral period for the 475-year (Figure 5.28) and 2475-year (Figure 5.29) return periods. Each residual plot also shows the mean as well as  $\pm$  standard deviation of residuals at discrete  $R_x/L$ ,  $R_y$  and spectral periods. Residual scatters without showing any specific trend about zero line suggest the unbiased directivity amplification estimates of the proposed expressions. The residual trends for the considered parameters suggest a fairly unbiased directivity amplification estimations by the proposed simplified equations for SHB11. The 2475-year on fault directivity estimations are slightly smaller than the observed directivity amplifications. This observation is consistent with Figure 5.26 since the distance tapering comparisons also suggest smaller estimations of the simplified SHB11 model for  $R_y = 0\text{km}$ .

Similar residual analyses are also run for the simplified CHS13 directivity amplification expressions. The results are given in Figure 5.30 and Figure 5.31 for 475-year and 2475-year return periods, respectively. The residual trends depicted from mean  $\pm$  standard deviation values suggest smaller directivity estimations with respect to the observed values. This observation is generally valid for all the independent parameters considered in the analysis:  $R_x/L$ ,  $R_y$  and period. The smaller estimations of the CHS13-based expressions are partly due to distance tapering approach and are consistent with the overall distance tapering picture given in Figure 5.27. Nonetheless the smaller directivity estimations do not endanger the accuracy of the proposed model because the mean residual values are very close to zero.

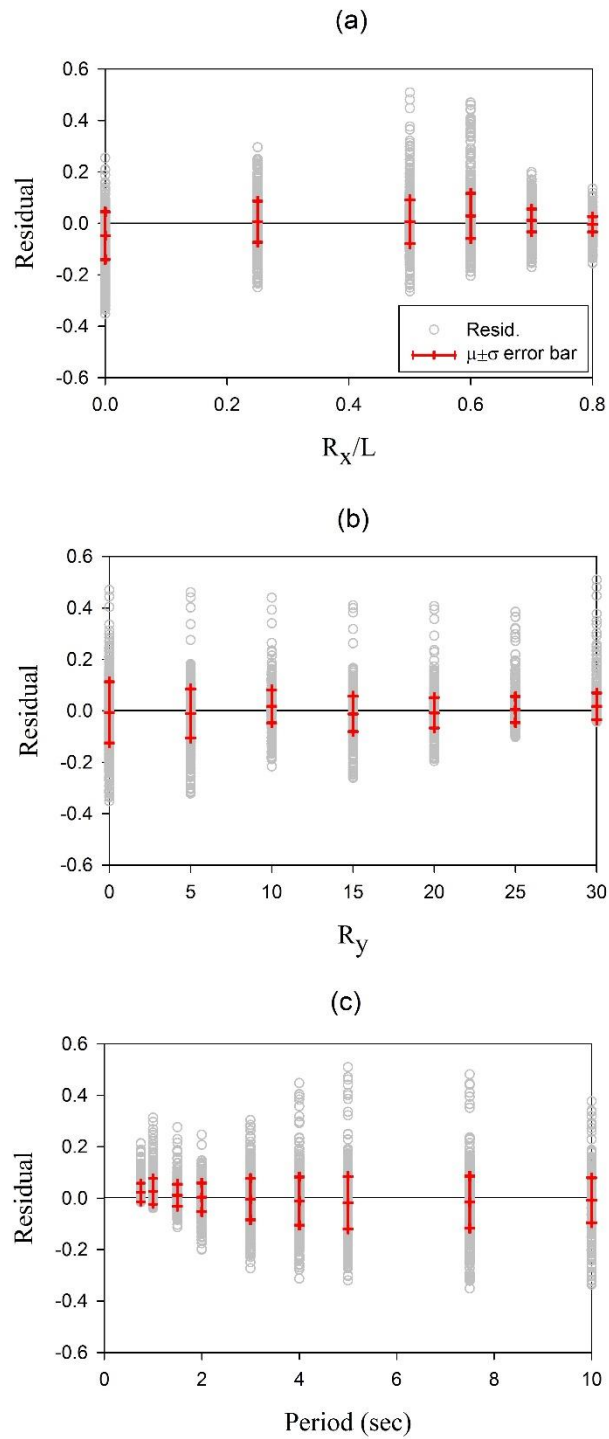


Figure 5.28 Residuals computed from PSHA (observed) and estimated directivity amplifications for SHB11 narrow-band directivity model, for the 475-year return period

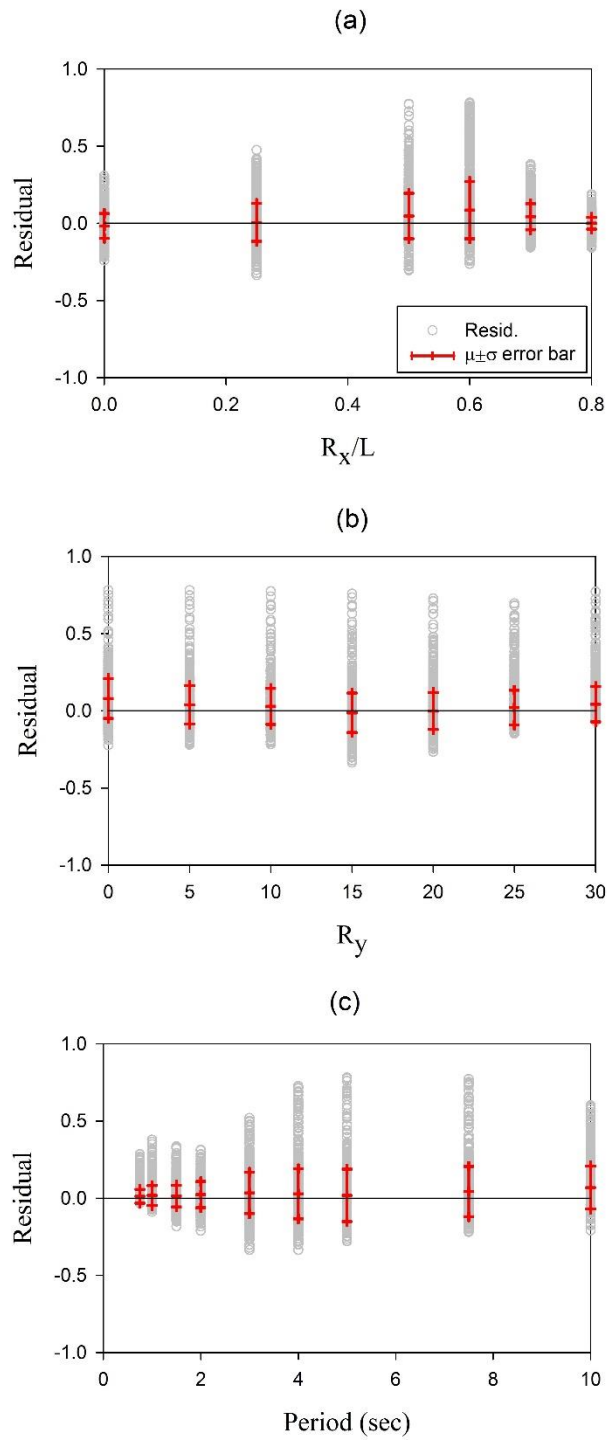


Figure 5.29 Residuals computed from PSHA (observed) and estimated directivity amplifications for SHB11 narrow-band directivity model for the 2475-year return period

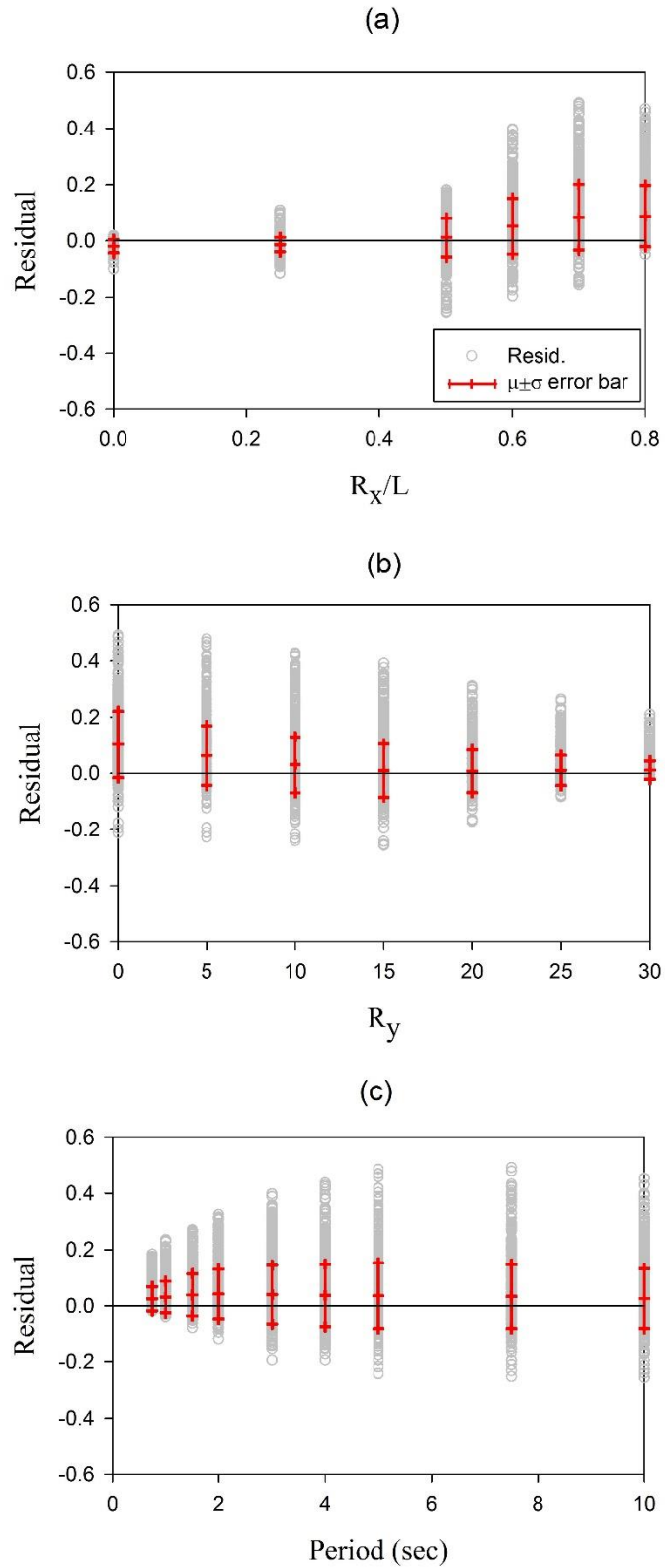


Figure 5.30 Residuals of PSHA and estimated amplification factors for CHS13 model, for the 475-year return period

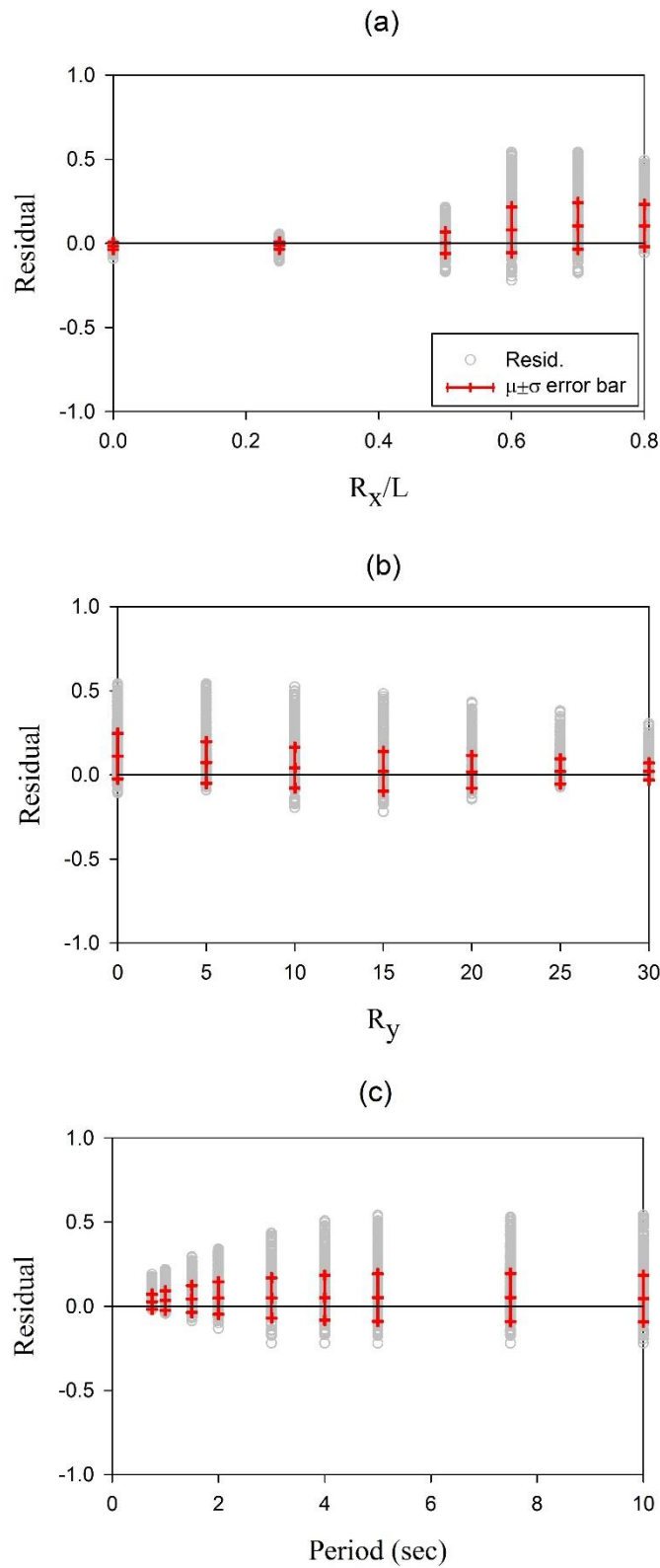


Figure 5.31 Residuals of PSHA and estimated amplification factors for CHS13 model, for the 475-year return period

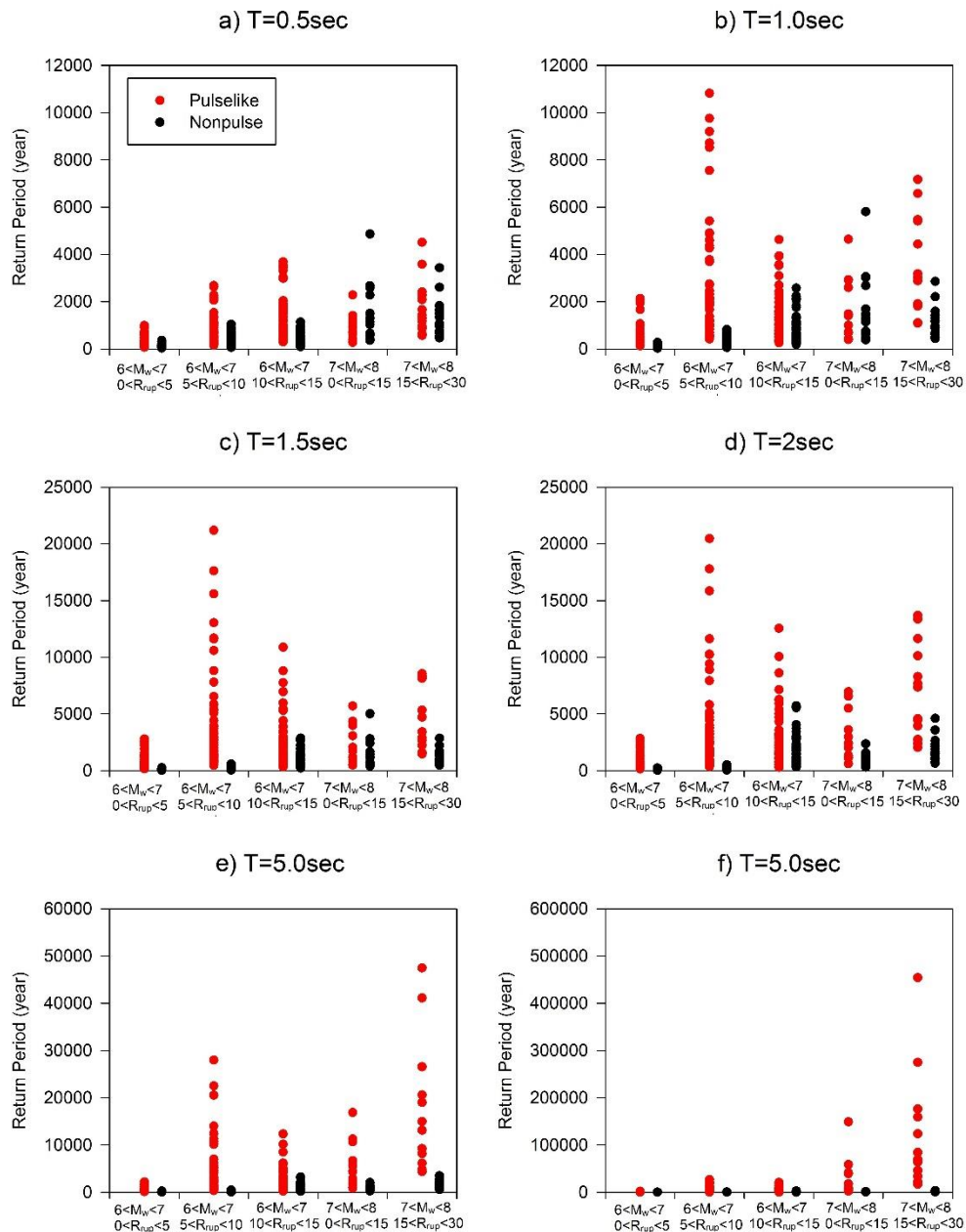


Figure 5.32 Return periods related to the spectral amplitudes of pulse-like and nonpulse recordings

#### 5.4 Consideration of Proposed Directivity Amplification Models for Directivity Dominant Maximum Direction Spectrum

The two directivity models utilized in this study (SHB11 and CHS13) estimate different horizontal components of ground motions. SHB11 is used for determining directivity amplifications to convert no-directivity GMRotI50 (can be referred to as geometric mean; Beyer and Bommer, 2006) component to directivity dominated fault

normal (FN) component. The amplification factors by CHS13 modify nondirectivity RotD50 component for directivity dominated ground motions (RotD50<sub>Directivity</sub>). In brief, SHB11 amplification factors estimate  $Sa_{FNDirectivity}/Sa_{Geomean}$  whereas CHS13 amplification factors compute  $Sa_{RotD50directivity}/Sa_{RotD50nondirectivity}$ . Equation 5.22 shows the relationship for the directivity-dominated spectral estimations for SHB11 model whereas Equation 5.23 gives the same relationship for CHS13.

$$Sa_{FNDirectivity} = AMP_{SHB11} \cdot Sa_{Geomean} \quad 5.22$$

$$Sa_{RotD50Directivity} = AMP_{CHS13} \cdot Sa_{RotD50nondirectivity} \quad 5.23$$

If  $Sa_{RotD100directivity}$  is defined as in Equation 4.3, the ratio between  $Sa_{FNDirectivity}$  and  $Sa_{RotD100directivity}$  is given in Equation (5.24) provided that  $Sa_{Geomean} \approx Sa_{RotD50}$

$$\frac{Sa_{FNDirectivity}}{Sa_{RotD100directivity}} = \frac{AMP_{SHB11}(T)}{AF_{RotD100} \cdot AF_{Directivity}} \quad 5.24$$

The directivity spectral amplification by SHB11 ( $AMP_{SHB11}(T)$ ) is already defined in Section 5.3.2 whereas  $AF_{RotD100}$  and  $AF_{Directivity}$  can be described through Shahi and Baker (2014) the  $Sa_{RotD100directivity}/Sa_{RotD100nondirectivity}$  ratio statistics described in Chapter 4. In a similar way, combination of  $Sa_{RotD100directivity}/Sa_{RotD50nondirectivity}$  ratio statistics in Chapter 4 with Equation 5.24 would give an approximate estimation for  $Sa_{RotD100directivity}$  for CHS13 directivity model.

The latter approach would lead to an average spectral amplitude increase of 25% to 30% when  $Sa_{RotD100directivity}$  is estimated from  $Sa_{RotD50directivity}$  by CHS13. However, the conversion of  $Sa_{FNDirectivity}$  to  $Sa_{RotD100directivity}$  (when  $Sa_{FNDirectivity}$  is determined from SHB11 directivity model) requires significantly large multiplicants (greater than 3 in many cases) since  $AF_{Directivity}$  factors computed in Chapter 4 (depicted in Figure 4.10 and Figure 4.14) may attain very large values confined to the coarse magnitude and distance intervals given in Table 4.2. The large difference between  $Sa_{RotD100directivity}$  between these two different approaches may stem from the specific features of the compiled pulse-like and non-pulse strong-motion database used in Chapter 4.

As indicated in Chapter 4, the directivity to nondirectivity ratio statistics presented in Sections 4.5 and 4.6 can only be a first-order approximation because the source-site geometry (or other factors affecting the directivity spectral amplitudes that are important in diertivity spectral amplitudes) is not well constrained in the absence of abundant pulse-like and non-pulse records. Besides, when the spectral amplitudes of pulse-like and nonpulse strong-motions are compared with the hazard curves determined from the PSHA results of this study, one can infer a significant difference between these two data classes in terms of annual exceedance rates (return periods). The observations are such that the spectral amplitudes of pulse-like recordings would represent very large return periods with respect to those of nonpulse recordings. This observation is presented in Figure 5.32 which suggests significantly conservative  $Sa_{RotD100directivity}/Sa_{RotD100nondirectivity}$  ( $AF_{Directivity}$ ) spectral ratios.



## CHAPTER 6

### CONCLUSION AND DISCUSSIONS

#### 6.1 Summary and Conclusions

This study investigates the effect of ground motion polarization on the amplification of response spectrum. In essence, the study concentrates on the forward-directivity ground motions since they are known to have highly polarized characteristics. It should be noted that the aim of this study is not to develop directivity models. This study utilizes the developed directivity models to capture the amplifying effects of directivity for different seismological and geometrical situations with PSHA. Two directivity models (SHB11 and CHS13) were utilized in order to simulate the directivity effect on PSHA for different earthquake scenarios. The significance of different seismological and geometrical parameters on the forward-directivity amplification are investigated for each utilized directivity model. Simple amplification models are then proposed to incorporate the directivity effects on the design spectrum.

The study also investigates the effect of directionality in determination of maximum rotated component for near fault forward-directivity ground motions. To this end, near fault ground motions with  $6.0 < M_w < 8.0$  and  $R_{rup} < 30\text{km}$  are selected from NGA-WEST2 database (<http://ngawest2.berkeley.edu>; Ancheta et al. (2014)). The ground motions are classified as pulselike and non-pulselike. The geometrical parameters defined by Somerville et. al. (1997) ( $\theta$ ,  $\varphi$ ,  $X \cdot \cos \theta$  and  $Y \cdot \cos \varphi$ ) are utilized to classify the ground motions as pulselike and non-pulselike. The ratio of maximum rotated component for pulselike and non-pulselike ground motions ( $\text{RotD100}_{\text{Directivity}} / \text{RotD100}_{\text{NoDirectivity}}$ ) is calculated and a conversion model is proposed for the

estimation of maximum rotated horizontal component for forward-directivity ground motions.

The most important observations and achieved results are as follows:

- SHB11 (the first directivity model utilized in this study) modifies GMRotI50 component of its counterpart GMPE (Boore and Atkinson 2008) to estimate the response spectrum in a desired orientation with respect to fault strike. The model considers pulse period and probability of pulse occurrence in its probabilistic framework for estimation of response spectrum. The fault normal component is selected in this study in order to extract forward-amplifications for SHB11 model. This is because the impulsive signals stemming from forward-directivity are mostly seen in this direction.
- CHS13 (the second directivity model utilized in this study) modifies the RotD50 component of its counterpart GMPE (Chiou and Young 2014) to estimate the same component for forward directivity ground motions (RotD50<sub>Directivity</sub>).
- PSHA is calculated with and without considering directivity effect and the response spectrum is extracted for different fault-site geometries, seismological parameters and two hazard levels.
- The amplification factors are extracted from normalization of directivity response spectrum ( $Sa_{\text{Directivity}}$ ) to conventional response spectrum ( $Sa_{\text{NoDirectivity}}$ ) for different earthquake scenarios.
- The extracted amplification model for SHB11 has an increasing trend up to the maximum amplification period (referred to as  $T_{\text{max}}$ ) which is followed by a descending trend for larger period ranges. Amplification model of CHS13 also shows an increasing trend up to its maximum amplification period (referred to as  $T_{\text{corner}}$ ). However, the amplification factor takes almost a constant value for larger periods in this model.
- For the case of SHB11 directivity model the results of analysis show that, slip rate, fault length (or characteristic magnitude of the fault), hazard level and source-to-site geometry play important role in the determination of amplification amplitude. On the other hand, characteristic magnitude and source-to-site geometry are determining parameters in CHS13 model,

whereas slip rate and hazard level do not change the amplification amplitude considerably.

- The amplification amplitude shows greater values for larger return periods (2475-year) and slip rate values in SHB11. The effect of slip rate on amplification amplitude is more prominent in smaller return periods (475-year).
- In both SHB11 and CHS13 models the larger amplification amplitudes are observed for the faults with greater characteristic magnitudes. However, this increment trend is saturated for the faults with characteristic magnitude greater than 7.25 in both SHB11 and CHS13 models.
- The characteristic magnitude also changes the spectral period in which the maximum amplification occurs ( $T_{\max}$  in SHB11 and  $T_{\text{corner}}$  in CHS13). It is shown that the period values at which the directivity amplifications are maximized ( $T_{\max}$  and  $T_{\text{corner}}$ ) are the same for both SHB11 and CHS13 models. It is also shown that there is a linear relationship between characteristic magnitude and maximum amplification period ( $T_{\max}$  or  $T_{\text{corner}}$ ).
- In terms of spatial distribution of directivity amplification, SHB11 and CHS13 exhibit different patterns. In SHB11 model the directivity dominant regions are located near the fault edges while in CHS13, they extend to the sites located beyond the fault edges in strike parallel direction.
- In strike normal direction the directivity dominant regions can exceed 30km in both SHB11 and CHS13 models for the fault lengths greater than 150km.
- These observations are utilized in order to set simple rules for forward-directivity amplifications. These amplification models consider the effect of all aforementioned seismological and geometrical parameters in their functional forms. They preserve, at the same time, a compromise between accuracy and simplicity because these models are proposed to be implemented on seismic design codes.
- The amplification factor of SHB11 model which estimates fault normal component reaches up to 1.8 in its maximum case while the largest amplification factor calculated from CHS13 which modifies RotD50 component forward directivity is equal to 1.5. However if this amplification

factor is integrated with conversion factor of Shahi and Baker (2013) for the estimation of maximum rotated component ( $Sa_{RotD100_{Directivity}}$ ) the generic amplification factor will be equal to 1.87 which is slightly larger than that of SHB11.

- It should be noted that the seismological aspects of directivity effect are not still verified very clearly due to lack of data in this field. Therefore, the proposed directivity models illustrate different results for directivity amplification in terms of amplitude and spatial distribution around the fault.
- A conversion factor is proposed for the estimation of maximum rotated component for forward-directivity ground motions in Chapter four. To this end, RotD100 spectral ratios of pulselike and non-pulse records (i.e.,  $AF_{directivity} = Sa_{RotD100_{directivity}}/Sa_{RotD100_{nodirectivity}}$ ) are calculated for different magnitude and distance intervals.
- The  $AF_{directivity}$  ratios exhibit significantly large values ( $AF_{directivity} \approx 6.5$  for  $T > 2s$ ) which seems to be too conservative. This is supposed to be due to the scarce number of near fault ground motions utilized in development of the conversion model. Besides, there is an inconsistency between the return periods of pulselike and non-pulselike spectral amplitudes which can be another reason of overestimation for  $AF_{directivity}$  ratios. The return periods are determined from the hazard curves of PSHA results. However, this type of relationship ( $Sa_{RotD100_{directivity}}/Sa_{RotD100_{nodirectivity}}$ ) is presented for the first time in the literature and it emphasizes on the importance of compound effects of directionality (along maximum direction) and directivity.

## 6.2 Recommendations for further research

- Directivity models are consistently updated. The new models try to propose a better description of the relationship between directivity amplification in one hand and the seismological and geometrical parameters in the other hand. These new directivity models which are capable of taking more complicated geometrical characteristics of the faults can be utilized in PSHA to catch the amplifying characteristics of forward directivity effects for near fault ground motions.

- Real case studies with application of these new directivity models can be carried out for multi-segment faults with more complicated geometries.
- The national seismic hazard maps should be updated considering the directivity and near-fault effects in a long-term plan.
- Further studies are required to determine the best horizontal component definition that should be utilized in seismic design codes.
- The adequacy of existing limit-state acceptance criteria for both global and local structural demands under pulselike ground motions should be further investigated. The structural performance should be evaluated in terms of energy dissipation capacity for different hazard levels and drift demand limit-state for forward-directivity ground motions.



## REFERENCES

- Abrahamson, N. et al., 2008. Comparisons of the NGA ground-motion relations. *Earthquake Spectra*, 24(1), pp.45–66.
- Abrahamson, N.A., 2000. Effects of rupture directivity on probabilistic seismic hazard analysis. In *Proceedings of the Sixth International Conference on Seismic Zonation: Managing Earthquake Risk in the 21st Century, Palm Springs, CA, 12-15 November 2000*. Available at: <http://nisee.berkeley.edu/elibrary/Text/200803124>.
- Abrahamson, N.A. & Silva, W.J., 1997. Empirical response spectral attenuation relationships for shallow crustal earthquakes. *Seismological Research Letters*, 68(1), pp.94–127.
- Akkan, S. & Gulkan, P., 2001. Near-field earthquakes and their implications on seismic design codes. *Report No. METU/EERC 01-01, Earthquake Engineering Research Center, Middle East Technical University, Ankara, Turkey*.
- Akkan, S.D., Yazgan, U. & Gulkan, P., 2004. Deformation Limits for simple Non-Degrading Systems subjected to Near-Fault Ground Motions. In *Proceedings 13th World Conference on Earthquake Engineering*. pp. 1–14.
- Alavi, B. & Krawinkler, H., 2004. Behavior of moment-resisting frame structures subjected to near-fault ground motions. *Earthquake Engineering and Structural Dynamics*, 33(6), pp.687–706.
- Alavi, B. & Krawinkler, H., 2001. *Effects of Near Fault Ground Motions on Frame Structures*, Available at: [Blume/TRLList.htm](http://blume.trl.com/TRLList.htm) [accessed 31 May 2006].
- Almufti, I. et al., 2015. Incorporation of velocity pulses in design ground motions for response history analysis using a probabilistic framework. *Earthquake Spectra*, 31(3), pp.1647–1666.
- Ambraseys, N. & Douglas, J., 2003. Near-field horizontal and vertical earthquake ground motions. *Soil Dynamics and Earthquake Engineering*, 23(1), pp.1–18.
- Anderson, J.C. & Bertero, V. V., 1987. Uncertainties in Establishing Design Earthquakes. *Journal of Structural Engineering*, 113(8), pp.1709–1724.
- Anderson, J.C. & Naeim, F., 1984. Design criteria and ground motion effects in the seismic response of multi-story buildings. *Proc. Applied Technology Council, ATC 10-1, Seminar on Earthquake Ground Motion and Building Damage Potential, San Francisco*.
- Anderson, N. et al., 2003. Vertical shear-wave velocity profiles generated from spectral analysis of surface waves: field examples. *Prepared for Missouri Department of Transportation Final Report, RDT 03-006*.
- ASCE7-10, 2010. Minimum Design Loads for Buildings and Other Structures. *SEI 7-10*.
- Baker, J.W., 2007. Quantitative classification of near-fault ground motions using wavelet analysis. *Bulletin of the Seismological Society of America*, 97(5), pp.1486–1501.
- Baltzopoulos, G., Chioccarelli, E. & Iervolino, I., 2015. The displacement coefficient method in near-source conditions. *Earthquake Engineering and*

- Structural Dynamics*, 44(7), pp.1015–1033.
- Baltzopoulos, G., Vamvatsikos, D. & Iervolino, I., 2016. Analytical modelling of near-source pulse-like seismic demand for multi-linear backbone oscillators. *Earthquake Engineering & Structural Dynamics*, 45(11), pp.1797–1815. Available at: <http://doi.wiley.com/10.1002/eqe.2729> [Accessed February 27, 2017].
- Bertero, V., Mahn, S. & Herrera, R., 1978. Aseismic design implications of near-fault San Fernando earthquake records. *Earthquake Engineering & Structural Dynamics*, 6(July 1976), pp.31–42. Available at: <http://onlinelibrary.wiley.com/doi/10.1002/eqe.4290060105/abstract>.
- Beyer, K. & Bommer, J.J., 2006. Relationships between median values and between aleatory variabilities for different definitions of the horizontal component of motion. *Bulletin of the Seismological Society of America*, 96(4 A), pp.1512–1522.
- Boore, D.M., 2010. Orientation-Independent, Nongeometric-Mean Measures of Seismic Intensity from Two Horizontal Components of Motion. *Bulletin of the Seismological Society of America*, 100(4), pp.1830–1835.
- Boore, D.M., 2006. Orientation-Independent Measures of Ground Motion. *Bulletin of the Seismological Society of America*, 96(4A), pp.1502–1511. Available at: <http://www.bssaonline.org/cgi/doi/10.1785/0120050209>.
- Boore, D.M., Watson-Lamprey, J. & Abrahamson, N.A., 2006. Orientation-Independent Measures of Ground Motion. *Bulletin of the Seismological Society of America*, 96(4A), pp.1502–1511.
- Boore, D.M. & Zoback, M.D., 1974. Two-dimensional kinematic fault modeling of the Pacoima Dam strong-motion recordings of the February 9, 1971, San Fernando earthquake. *Bulletin of the Seismological Society of America*, 64(3–1), pp.555–570. Available at: [http://bssa.geoscienceworld.org/content/64/3-1/555%5Cnfiles/772/Boore\\_Zoback\\_1974\\_Two-dimensional kinematic fault modeling of the Pacoima Dam strong-motion.pdf%5Cnfiles/808/555.html](http://bssa.geoscienceworld.org/content/64/3-1/555%5Cnfiles/772/Boore_Zoback_1974_Two-dimensional%20kinematic%20fault%20modeling%20of%20the%20Pacoima%20Dam%20strong-motion.pdf%5Cnfiles/808/555.html).
- Bozorgnia, Y. et al., 2014. NGA-West2 research project. *Earthquake Spectra*, 30(3), pp.973–987.
- Bradley, B.A. & Baker, J.W., 2015. Ground motion directionality in the 2010-2011 Canterbury earthquakes. *Earthquake Engineering and Structural Dynamics*, 44(3), pp.371–384.
- Bradley, B.A. & Cubrinovski, M., 2011. Near-source strong ground motions observed in the 22 February 2011 Christchurch earthquake. *Bulletin of the New Zealand Society for Earthquake Engineering*, 44(4), pp.181–194.
- Bray, J.D. & Rodriguez-Marek, A., 2004. Characterization of forward-directivity ground motions in the near-fault region. *Soil Dynamics and Earthquake Engineering*, 24(11), pp.815–828.
- BSSC., 2009. NEHRP Recommended Seismic Provisions for New Buildings and Other Structures. Washington, D.C.: Federal Emergency Management Agency.
- CALTRANS, 2013. Seismic design criteria. California Department of Transportation: Sacramento, CA, U.S. Version 1.7.
- Campbell, K. & Bozorgnia, Y., 1994. Empirical analysis of strong ground motion from the 1992 Landers, California, earthquake. *Bulletin of the Seismological Society of America*, 84(3), p.573.
- Campbell, K.W. & Bozorgnia, Y., 2008. NGA ground motion model for the

- geometric mean horizontal component of PGA, PGV, PGD and 5% damped linear elastic response spectra for periods ranging from 0.01 to 10 s. *Earthquake Spectra*, 24(1), pp.139–171.
- Chai, J.F., Loh, C.H. & Chen, C.Y., 2000. Consideration of the near fault effect on seismic design code for sites near the Chelungpu fault. *Journal of the Chinese Institute of Engineers*, 23(4), pp.447–454.
- Chai, J.F. & Teng, J., 2012. Seismic design force for buildings in Taiwan. *National Center for Research on Earthquake Engineering. Taiwan 15WCEE*.
- Chai, J.F., Teng, J. & Loh, H., 2001. Current Development of Seismic Design Code to Consider the Near-fault Effect in Taiwan. *Earthquake Engineering and Engineering Seismology*, 3(2), pp.47–56.
- Champion, C. & Liel, A., 2012. The effect of near-fault directivity on building seismic collapse risk. *Earthquake Engineering and Structural Dynamics*, 41(10), pp.1391–1409.
- Chen, K.-C. et al., 2001. An Observation of Rupture Pulses of the 20 September 1999 Chi-Chi, Taiwan, Earthquake from Near-Field Seismograms. *Bulletin of the Seismological Society of America*, 91(5), pp.1247–1254. Available at: <http://www.bssaonline.org/content/91/5/1247.abstract>.
- Chioccarelli, E. & Iervolino, I., 2010. Near-source seismic demand and pulse-like records: A discussion for L'Aquila earthquake. *Earthquake Engineering and Structural Dynamics*, 39(9), pp.1039–1062.
- Chioccarelli, E. & Iervolino, I., 2013. Near-source seismic hazard and design scenarios. *Earthquake Engineering and Structural Dynamics*, 42(4), pp.603–622.
- Chiou, B.S.J. & Youngs, R.R., 2014. Update of the Chiou and Youngs NGA model for the average horizontal component of peak ground motion and response spectra. *Earthquake Spectra*, 30(3), pp.1117–1153.
- Dalguer, L.A. & Day, S.M., 2007. Staggered-grid split-node method for spontaneous rupture simulation. *Journal of Geophysical Research: Solid Earth*, 112(2).
- Dunham, E.M. & Archuleta, R.J., 2005. Near-source ground motion from steady state dynamic rupture pulses. *Geophysical Research Letters*, 32(3), pp.1–4.
- Fukushima, Y. et al., 2000. Characteristics of observed peak amplitude for strong ground motion from the 1995 Hyogoken Nanbu (Kobe) earthquake. *Bulletin of the Seismological Society of America*, 90(3), pp.545–565.
- Gregor, N. et al., 2014. Comparison of NGA-West2 GMPEs. *Earthquake Spectra*, 30(3), pp.1179–1197.
- Gupta, A. & Krawinkler, H., 1999. Seismic demands for performance evaluation of steel moment resisting frame structures. *Report No. 132, Stanford University, Stanford, CA*, (132).
- Hall, J.F. et al., 1995. Near Source Ground Motion and its Effects on Flexible Buildings. *Earthquake Spectra*, 11, pp.569–605.
- Heaton, T.H. et al., 1995. Response of high-rise and base-isolated buildings to a hypothetical mw 7.0 blind thrust earthquake. *Science (New York, N.Y.)*, 267(5195), pp.206–211.
- Hong, H.P. & Goda, K., 2007. Orientation-Dependent Ground-Motion Measure for Seismic-Hazard Assessment. *Bulletin of the Seismological Society of America*, 97(5), pp.1525–1538. Available at:

- <http://www.bssaonline.org/content/97/5/1525.abstract>.
- Housner, G.W. & Hudson, D.E., 1958. The Port Hueneme earthquake of March 18, 1957. *Bulletin of the Seismological Society of America*, 48(2), pp.163–168. Available at: <http://www.bssaonline.org/content/48/2/163.short>.
- Housner, G.W. & Trifunac, M.D., 1967. Analysis of accelerograms--Parkfield earthquake. *Bulletin of the Seismological Society of America*, 57(6), pp.1193–1220. Available at: <http://www.bssaonline.org/cgi/content/abstract/57/6/1193>.
- Huang, Y. et al., 2008. Relocation of the M8.0 Wenchuan earthquake and its aftershock sequence. *Science in China Series D: Earth Sciences*, 51(12), pp.1703–1711. Available at: <http://dx.doi.org/10.1007/s11430-008-0135-z>.
- Iervolino, I., Chioccarelli, E. & Baltzopoulos, G., 2012. Inelastic displacement ratio of near-source pulse-like ground motions. *Earthquake Engineering and Structural Dynamics*, 41(15), pp.2351–2357.
- Iervolino, I. & Cornell, C.A., 2008. Probability of occurrence of velocity pulses in near-source ground motions. *Bulletin of the Seismological Society of America*, 98(5), pp.2262–2277.
- Kalkan, E., Adalier, K. & Pamuk, A., 2004. Near source effects and engineering implications of recent earthquakes in Turkey. In *Proceedings of the 5th International Conference on Case Histories in Geotechnical Engineering*. pp. 1–6. Available at: [http://nsmg.wr.usgs.gov/ekalkan/PDFs/Conferences/C8\\_Kalkan\\_et\\_al.pdf](http://nsmg.wr.usgs.gov/ekalkan/PDFs/Conferences/C8_Kalkan_et_al.pdf).
- Kalkan, E. & Kunnath, S.K., 2006. Effects of fling step and forward directivity on seismic response of buildings. *Earthquake Spectra*, 22(2), pp.367–390.
- Li, X. Le et al., 2007. Response spectrum of seismic design code for zones lack of near-fault strong earthquake records. *Acta Seismologica Sinica English Edition*, 20(4), pp.447–453.
- Mai, P.M., Spudich, P. & Boatwright, J., 2005. Hypocenter locations in finite-source rupture models. *Bulletin of the Seismological Society of America*, 95(3), pp.965–980.
- Malhotra, P.K., 1999. Response of buildings to near-field pulse-like ground motions. *Earthquake Engineering and Structural Dynamics*, 28(2), pp.1309–1326.
- Mavroeidis, G.P., Dong, G. & Papageorgiou, A.S., 2004. Near-fault ground motions, and the response of elastic and inelastic single-degree-of-freedom (SDOF) systems. *Earthquake Engineering and Structural Dynamics*, 33(9), pp.1023–1049.
- Mavroeidis, G.P. & Papageorgiou, A.S., 2003. A mathematical representation of near-fault ground motions. *Bulletin of the Seismological Society of America*, 93(3), pp.1099–1131.
- Menun, C. & Fu, Q., 2002. An analytical model for near-fault ground motions and the response of SDOF systems. In *Proc. of the 7th U.S. National Conf. on Earthquake Engineering, Boston, MA*. Available at: [http://peer.berkeley.edu/research/peertestbeds/Cct/Menun and Fu 2002.pdf](http://peer.berkeley.edu/research/peertestbeds/Cct/Menun%20and%20Fu%202002.pdf).
- New Zealand Standard, NZS, 1170.5:2004, 2004. Structural design actions part 5: earthquake actions. *New Zealand – Commentary*.
- Niazy, A., 1975. An exact solution for a finite, two-dimensional moving dislocation in an elastic half-space with application to the San Fernando earthquake of 1971. *Bulletin of the Seismological Society of America*, 65(6), pp.1797–1826.

- Oglesby, D.D., Archuleta, R.J. & Nielsen, S.B., 2000. The three-dimensional dynamics of dipping faults. *Bulletin of the Seismological Society of America*, 90(3), pp.616–628.
- Power, M. et al., 2008. An overview of the NGA project. *Earthquake Spectra*, 24(1), pp.3–21.
- Rowshandel, B., 2010. Directivity correction for the next generation attenuation (NGA) relations. *Earthquake Spectra*, 26(2), pp.525–559.
- Rupakhety, R. et al., 2011. Quantification of ground-motion parameters and response spectra in the near-fault region. *Bulletin of Earthquake Engineering*, 9(4), pp.893–930.
- Sasani, M. & Bertero, V.V., 2000. Importance of Severe Pulse-Type Ground Motions in Performance-Based Engineering: Historical and Critical. In *Proceedings of the 12th World Conference on Earthquake Engineering, New Zealand Society for Earthquake Engineering, Upper Hutt, New Zealand, 2000*.
- Schmedes, J. & Archuleta, R.J., 2008. Near-surface ground motion along strike-slip faults: Insights into magnitude saturation of PGV and PGA. *Bulletin of the Seismological Society of America*, 98(5), pp.2278–2290.
- Seekins, L.C. & Boatwright, J., 2010. Rupture Directivity of Moderate Earthquakes in Northern California. *Bulletin of the Seismological Society of America*, 100(3), pp.1107–1119. Available at: <http://www.bssaonline.org/content/100/3/1107.abstract>.
- Shahi, S.K., 2013. A probabilistic framework to include the effects of near-fault directivity in seismic hazard assessment. *PhD Thesis, Dept. of Civil and Environmental Engineering, Stanford University, Stanford, CA*.
- Shahi, S.K. & Baker, J.W., 2011. An empirically calibrated framework for including the effects of near-fault directivity in probabilistic seismic hazard analysis. *Bulletin of the Seismological Society of America*, 101(2), pp.742–755.
- Somerville, P. et al., 1999. Characterizing Crustal Earthquake Slip Models for the Prediction of Strong Ground Motion. *Seismological Research Letters*, 70(1), pp.59–80.
- Somerville, P. et al., 1996. Implications of the Northridge earthquake for strong ground motions from thrust faults. *Bulletin of the Seismological Society of America*, 86(1B), pp.S115–S125. Available at: <http://www.bssaonline.org/content/86/1B/S115.abstract>.
- Somerville, P.G., 2002. Characterizing Near Fault Ground Motion For The Design And Evaluation Of Bridges. In *Proceedings 3rd National Seismic Conference & Work shop on Bridges & Highways, Portland, Oregon*. pp. 137–148.
- Somerville, P.G. et al., 1997. Empirical strong ground motion attenuation relations to include the amplitude and duration effects of rupture directivity. *Seismological Research Letters*, 68(1), pp.199–222.
- Somerville, P.G., 2003. Magnitude scaling of the near fault rupture directivity pulse. *Physics of the Earth and Planetary Interiors*, 137(1–4), pp.201–212.
- Spudich, B.P. et al., 2004. A formulation of directivity for earthquake sources using Isochrone Theory. *U.S. Geol. Surv. Open-File Rept. 2004-1268*, p.54.
- Spudich, P. et al., 2014. Comparison of NGA-West2 directivity models. *Earthquake Spectra*, 30(3), pp.1199–1221.
- Spudich, P. et al., 2013. *Final Report of the NGA-West2 Directivity Working Group*, Spudich, P. & Chiou, B.S.J., 2008. Directivity in NGA earthquake ground motions:

- Analysis using isochrone theory. *Earthquake Spectra*, 24(1), pp.279–298.
- TEC, 2007. “Specification for Buildings to be Built in Seismic Zones, (in Turkish) Ministry of Public Works and Settlement, Ankara.”
- Tothong, P. & Cornell, C.A., 2006. An empirical ground-motion attenuation relation for inelastic spectral displacement. *Bulletin of the Seismological Society of America*, 96(6), pp.2146–2164.
- Tothong, P. & Cornell, C.A., 2008. Structural performance assessment under near-source pulse-like ground motions using advanced ground motion intensity measures. *Earthquake Engineering and Structural Dynamics*, 37(7), pp.1013–1037.
- Tothong, P., Cornell, C.A. & Baker, J.W., 2007. Explicit directivity-pulse inclusion in probabilistic seismic hazard analysis. *Earthquake Spectra*, 23(4), pp.867–891.
- Tothong, P. & Cornell, C.A., 2007. Probabilistic Seismic Demand Analysis Using Advanced Ground Motion Intensity Measures, Attenuation Relationships, and Near-Fault Effects. *Pacific Earthquake Engineering Research Center*, (March), pp.185–195.
- UBC, 1994. “Uniform Building Code.” *International Conference of Building Officials, Whittier, California*,
- UBC, 1997. “Uniform Building Code.” *International Conference of Building Officials, Whittier, California*,
- Watson-Lamprey, J.A. & Boore, D.M., 2007. Beyond SaGMRotI: Conversion to SaArb, SaSN, and SaMaxRot. *Bulletin of the Seismological Society of America*, 97(5), pp.1511–1524.
- Wells, D.L. & Coppersmith, K.J., 1994. New Empirical Relationships among Magnitude, Rupture Length, Rupture Width, Rupture Area, and Surface Displacement. *Bulletin of the Seismological Society of America*, 84(4), pp.974–1002.
- Yaghmaei-Sabegh, S. & Mohammad-Alizadeh, H., 2012. Improvement of Iranian Seismic Design Code Considering the Near-Fault Effects. *International Journal of Engineering*, 25(2 (C)), pp.147–158. Available at: <http://www.ije.ir/Vol25/No2/C/8.pdf>.
- Youngs, R.R. & Coppersmith, K.J., 1985. Implications of fault slip rates and earthquake recurrence models to probabilistic seismic hazard estimates. *Bulletin of the Seismological Society of America*, 75(4), pp.939–964.

## APPENDIX A

### GEOMETRICAL CALCULATIONS FOR SEISMIC HAZARD ANALYSIS WITH THE DIRECTIVITY MODELS

#### A.1 Geometrical Calculations for Chiou and Spudich (2013) model

The normal vector to the fault plane is calculated from Equation A1:

$$\text{norm}_{\text{vect}} = \frac{\text{vect}_1 \times \text{vect}_2}{|\text{vect}_1 \times \text{vect}_2|} \quad \text{A1}$$

In which vect1 and vect2 are the vectors in the direction of fault sides (Figure A1).

Three components of normal vector is shown by:

$$\text{norm}_{\text{vect}} = (n_1, n_2, n_3)$$

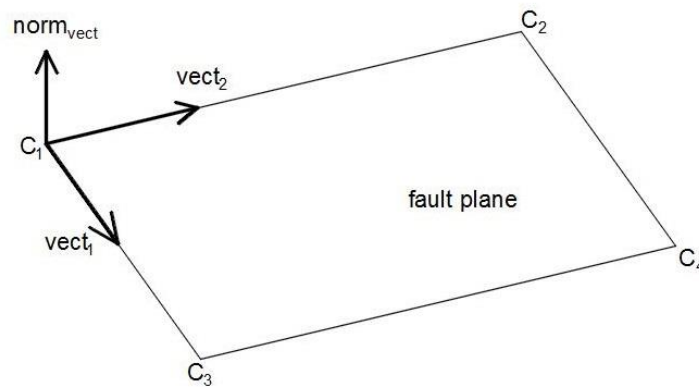


Figure A.1 Fault normal vector

The equation of the fault plane is given by:

$$ax + by + cz - d = 0 \quad \text{A2}$$

Coordinates of the point normal to the fault plane from the site is calculated from the Equation A3:

$$\begin{aligned}
x_p &= n_1 \cdot t + x_{\text{site}} \\
y_p &= n_2 \cdot t + y_{\text{site}} \\
z_p &= n_3 \cdot t + z_{\text{site}}
\end{aligned}
\tag{A3}$$

In which

$$t = \frac{n_1 \cdot x_{\text{SC1}} + n_2 \cdot y_{\text{SC1}} + n_3 \cdot z_{\text{SC1}}}{\sqrt{n_1^2 + n_2^2 + n_3^2}}
\tag{A4}$$

$SC_1$  is the line that connects the site to the first corner of the fault (Figure A2).  $SC_1$  is calculated from Equation A5:

$$SC_1 = (x_{\text{site}}, y_{\text{site}}, z_{\text{site}}) - (x_{C1}, y_{C1}, z_{C1})
\tag{A5}$$

The point normal to the fault plane is the closest point of the fault plane to the site and is shown by  $V_p$ :

$$V_p = (x_p, y_p, z_p)$$

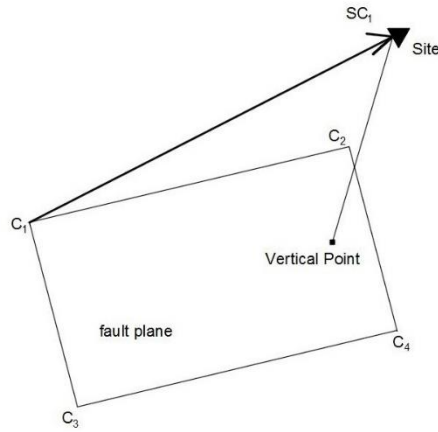


Figure A.2 Closest point of the site to the fault plane

**- Calculation of  $P_D$  (Direct Point):**

In order to find the direct point it is needed to know that the vertical point from the site to the fault plane is either inside the rupture area or not.

$$\text{area}_{V_p} = \text{area}_1 + \text{area}_2 + \text{area}_3 + \text{area}_4
\tag{A6}$$

If  $\text{area}_{V_p}$  is equal to rupture area  $P_D$  (Direct Point) is the same as  $V_p$  (Vertical Point) (Figure A3). If the  $\text{area}_{V_p}$  is greater than rupture area it means that  $V_p$  is out of the rupture segment. If the  $V_p$ -hyp line intersects the rupture area on the 2-4 side of the

rupture segment (Figure A4) then the  $P_D$  will be calculated from the equations shown below:

$$P_D = (x_D, y_D, z_D)$$

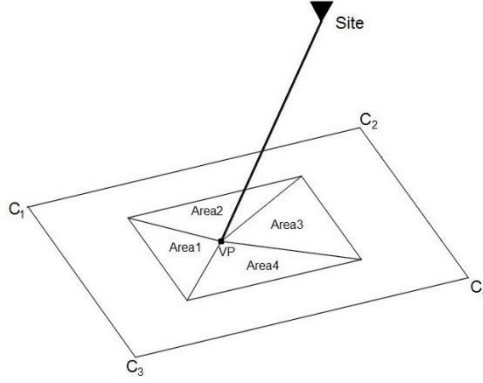


Figure A.3 Calculation of direct point for the case that closest point is located inside the rupture area

$$\begin{aligned} x_D &= x_{m_{24}} \cdot t_{24} + x_{P_{2seg}} \\ y_D &= y_{m_{24}} \cdot t_{24} + y_{P_{2seg}} \\ z_D &= z_{m_{24}} \cdot t_{24} + z_{P_{2seg}} \end{aligned} \quad A7$$

In which  $P_{2seg}$  is the coordinates of rupture corner in point 2,  $m_{24}$  is the unit vector of the line between points 2 and 4 on the rupture segment and  $t_{24}$  is calculated with Equations A8 to A11:

$$t_{24xy} = \frac{y_{m_{hv}} \cdot x_{m_{hr2}} - x_{m_{hv}} \cdot y_{m_{hr2}}}{x_{m_{24}} \cdot y_{m_{hv}} - y_{m_{24}} \cdot x_{m_{hv}}} \quad A8$$

$$t_{24xz} = \frac{z_{m_{hv}} \cdot x_{m_{hr2}} - x_{m_{hv}} \cdot z_{m_{hr2}}}{x_{m_{24}} \cdot z_{m_{hv}} - z_{m_{24}} \cdot x_{m_{hv}}} \quad A9$$

$$t_{24yz} = \frac{z_{m_{hv}} \cdot y_{m_{hr2}} - y_{m_{hv}} \cdot z_{m_{hr2}}}{y_{m_{24}} \cdot z_{m_{hv}} - z_{m_{24}} \cdot y_{m_{hv}}} \quad A10$$

here  $m_{hv}$  is the unit vector between the hypocenter and vertical point, and  $m_{hr2}$  is the unit vector between the hypocenter and point 2 on the corner of the rupture area.

$$t_{24} = \max(t_{24xy}, t_{24xz}, t_{24yz}) \quad A11$$

For some cases the projection of  $m_{hv}$  and  $m_{hr2}$  vectors on the  $xy$ ,  $xz$  and  $yz$  planes may lie on each other. In this case one of the  $t_{24xy}$ ,  $t_{24xz}$  or  $t_{24yz}$  will be equal to zero which is not the correct answer. In order to avoid the error from these cases the maximum value of  $t_{24xy}$ ,  $t_{24xz}$  and  $t_{24yz}$  for  $t_{24}$  is used.

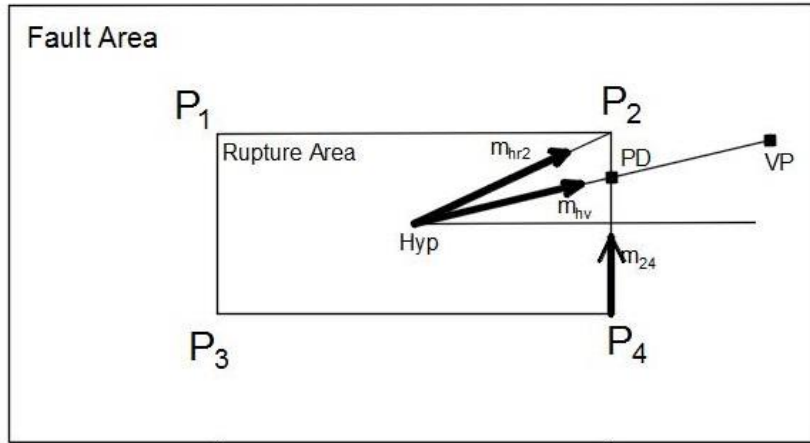


Figure A.4 Calculation of direct point for the case that closest point is located outside the rupture area

- **Calculation of the average scalar radiation pattern  $\overline{FS}$ :**

In order to find  $(\overline{FS})$  value first  $I_x$ ,  $I_n$  and  $I_\varphi$  parameters should be calculated. For the calculation of  $I_x$ ,  $I_n$  and  $I_\varphi$  the following information is needed (Figure A5):

$\vec{u}$  is the unit vector of slip direction,

$\vec{n}$  is the unit vector of fault normal direction,

$\vec{x}$  is the unit vector projected direct ray ( $\overline{P_H P_P}$ ).

$\vec{u}$  is calculated from the direction of fault top edge which is the same as the direction of fault slip.

Vector  $\vec{n}$  has already been calculated from Equation 1 and  $\vec{x}$  is calculated from Equation 12:

$$\vec{n} = \frac{V_P - hyp}{|V_P - hyp|} \quad A12$$

$$\varphi = \arctan \frac{|\vec{u} \times \vec{x}|}{|\vec{u} \cdot \vec{x}|} \quad A13$$

$$z_s = \sqrt{(x_{vp} - x_{site})^2 + (y_{vp} - y_{site})^2 + (z_{vp} - z_{site})^2} \quad A14$$

$z_s$  is the signed distance between  $P_s$  (site) and  $P_p$  (vertical point).

$$l_2 = |V_P - \text{hyp}| \quad \text{A15}$$

$l_2$  is the fixed distance between  $P_H$  and  $P_P$ .

$$R_{\text{hyp}} = |(x_{\text{site}}, y_{\text{site}}, z_{\text{site}}) - (x_{\text{hyp}}, y_{\text{hyp}}, z_{\text{hyp}})| \quad \text{A16}$$

$R_{\text{hyp}}$  is the distance between hypocenter and the site.

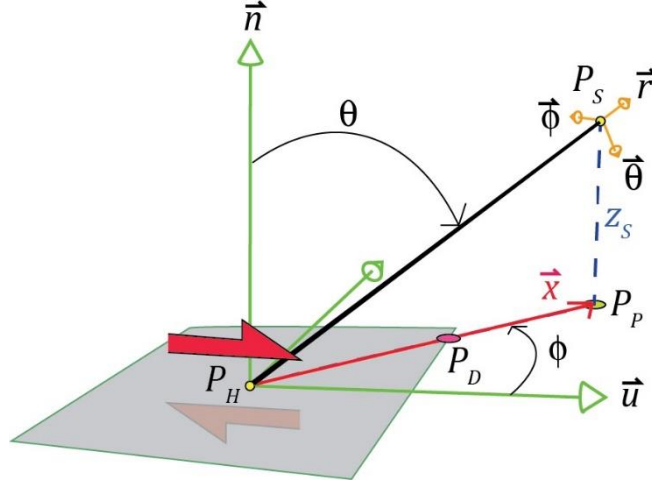


Figure A.5 Geometrical information for the calculation of average scalar radiation pattern ( $\overline{\mathbf{FS}}$ ) parameter (Spudich et al. 2013)

$$R_D = |(x_{\text{site}}, y_{\text{site}}, z_{\text{site}}) - (x_D, y_D, z_D)| \quad \text{A17}$$

$R_D$  is the distance between site and the direct point.

$$R_E = |(x_D, y_D, z_D) - (x_{\text{hyp}}, y_{\text{hyp}}, z_{\text{hyp}})| \quad \text{A18}$$

$R_E$  is the distance between hypocenter and direct point.

$$I_x = \cos \varphi \cdot \left\{ 2z_s \cdot \left( \frac{l_2}{R_{\text{hyp}}} - \frac{l_2 - R_E}{R_D} \right) - z_s \cdot \ln \frac{l_2 + R_{\text{hyp}}}{l_2 - R_E + R_D} \right\} \quad \text{A19}$$

$$I_n = \cos \varphi \cdot \left\{ -2z_s^2 \cdot \left( \frac{1}{R_{\text{hyp}}} - \frac{1}{R_D} \right) - (R_{\text{hyp}} - R_D) \right\} \quad \text{A20}$$

$$I_\varphi = \sin \varphi \cdot \left\{ z_s \cdot \ln \frac{l_2 + R_{\text{hyp}}}{l_2 - R_E + R_D} \right\} \quad \text{A21}$$

After the  $I_x$ ,  $I_n$  and  $I_\varphi$  are calculated the average scalar radiation pattern  $\overline{\mathbf{FS}}$  is calculated from Equation 22:

$$\overline{\mathbf{FS}} = \frac{\sqrt{I_x^2 + I_n^2 + I_\varphi^2}}{E} \quad \text{A22}$$

## A.2 Geometrical Calculations for Shahi and Baker (2011) Model (r and s)

In order to calculate the closest distance of the site to the fault first the direction of the rupture should be calculated. Rupture corners are shown by  $P_1$ ,  $P_2$ ,  $P_3$  and  $P_4$ .

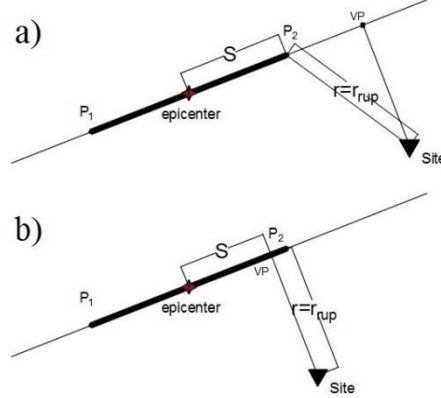


Figure A.6 Geometrical calculations for Shahi and Baker (2011) model

Calculation of direction of line  $P_1P_2$ :

$$a_{p_1p_2} = x_{P_2\text{seg}} - x_{P_1\text{seg}} \quad \text{A23}$$

$$b_{p_1p_2} = y_{P_2\text{seg}} - y_{P_1\text{seg}} \quad \text{A24}$$

After the direction of  $P_1P_2$  line is determined the location of closest distance of the site to the fault (VP) can be calculated from Equations 25, 26 and 27:

$$t_{vp} = \frac{(a_{p_1p_2} \cdot x_{\text{site}} - a_{p_1p_2} \cdot x_{P_1\text{seg}}) + (b_{p_1p_2} \cdot y_{\text{site}} - b_{p_1p_2} \cdot y_{P_1\text{seg}})}{(a_{p_1p_2}^2 + b_{p_1p_2}^2)} \quad \text{A25}$$

$$x_{vp} = a_{p_1p_2} \cdot t_{vp} + x_{P_1\text{seg}} \quad \text{A26}$$

$$y_{vp} = b_{p_1p_2} \cdot t_{vp} + y_{P_1\text{seg}} \quad \text{A27}$$

If the vertical point (closest distance of the fault to the site) is located outside the rupture length (Figure A6a) the  $s$  will be equal to the half of the rupture length and it will be calculated from the Equation 28. For this case  $r$  value is also calculated from equation 29:

$$s = \frac{|P_2\text{seg}(x, y) - P_1\text{seg}(x, y)|}{2} \quad \text{A28}$$

$$r = |P_2\text{seg}(x, y) - \text{site}(x, y)| \quad \text{A29}$$

If the vertical point (closest distance of the fault to the site) is located within the rupture length (Figure A6b) the  $s$  will be equal to the distance between epicenter

and vertical point and it will be calculated from Equation 30. For this case r value is also calculated from Equation 31:

$$s = |\text{epic}(x, y) - \text{VP}(x, y)| \quad \text{A30}$$

$$r = |\text{VP}(x, y) - \text{site}(x, y)| \quad \text{A31}$$



## APPENDIX B

### A. THE MATHEMATICAL MODEL AND THE ALGORITHM USED IN THE PSHA CALCULATIONS FOR THE SHB11 MODEL

#### B.1 Algorithm used in SHB11 PSHA

The algorithm used in PSHA are discussed in Chapter3. Here the utilized algorithm in SHB11 model is presented with more detail. The following paragraphs summarize the algorithm. In this algorithm  $i$ ,  $j$  and  $k$  parameters denote to the discretized magnitude, rupture length and the pulse period counters.

- From the seismological input data, the magnitude range, fault length, fault width, style of faulting, recurrence model, minimum rate of occurrence ( $v_{min}$ ), fault and site coordinates and shear wave velocity are prepared.
- The magnitude range is discretized into smaller intervals. For each magnitude interval ( $M_i$ ), the probability of occurrence  $P(M_i)$  is calculated from the selected recurrence model (characteristic recurrence model has been used in this study, Youngs and Coppersmith 1985).
- For each magnitude ( $M_i$ ) the rupture area is calculated from the corresponding equations (Wells and Coppersmith 1994).
- Position of rupture and hypocenter of rupture is determined on the fault surface. Uniform distribution model is used for assigning the position of this rupture area on the fault.
- Geometric parameters are calculated for each rupture area and location ( $R_{ij}$ ,  $Z_{ij}$ ). Here  $Z_{ij}$  is representative of source-to-site geometric parameters ( $r$  and  $s$ ).
- Probability of pulse occurrence is calculated for given geometric parameters (with  $M_i$ ,  $R_{ij}$  and  $Z_{ij}$  values) from the Equations B1.

$$P(pulse | r, s) = \frac{1}{1 + e^{(0.642 + 0.167 \cdot r - 0.075 \cdot s)}} \quad B1$$

- In SB-11 method, the probability of pulse occurrence can be calculated for any orientation. After the probability of pulse occurrence in a specific site is calculated from Equation B1 the probability of pulse occurrence is calculated in a desired direction ( $\alpha$ ) given that a pulse is observed at that site (Equation B2). The probability of pulse occurrence in a site in the direction of  $\alpha$  can be calculated from Equation B3.

$$P(pulse \text{ at } \alpha | pulse) = \min[0.67, 0.67 - 0.0041 \cdot (77.5 - \alpha)] \quad B2$$

$$P(pulse \text{ at } \alpha) = P(pulse \text{ at } \alpha | pulse) \cdot P(pulse) \quad B3$$

- For each magnitude ( $M_i$ ), mean value of logarithm of pulse period ( $\mu_{\ln T_p}$ ) is calculated from Equation B4. The log standard deviation for pulse period is constant for all magnitude ranges ( $\sigma_{\ln T_p} = 0.56$ ).

$$\mu_{\ln T_p i} = -5.73 + 0.99 M_i \quad B4$$

- For each magnitude ( $M_i$ ), lognormal distribution of pulse period is calculated with  $\mu_{\ln T_p i}$  and  $\sigma_{\ln T_p}$ . Pulse period range is discretized into small intervals ( $T_{p,ik}$ ) and the probability of pulse period  $P(T_{p,ik})$  is calculated for each interval.
- For each pulse period ( $T_{p,ik}$ ) the mean value of logarithm of the amplification is determined. The amplification is a function of spectral period to pulse period ratio ( $T/T_p$ ) (Equation 17 in Shahi and Baker 2011).
- Mean value of natural logarithm of spectral acceleration ( $\mu_{\ln Sa, pulse}$ ) for pulse-type cases will be calculated from Equation B5.

$$\mu_{\ln Sa, Pulse} = \mu_{Af} + \mu_{\ln Sa, gmm} \quad B5$$

- For non-pulse-type cases, deamplification factor is calculated. Deamplification factor is a function of magnitude ( $M_i$ ) and source-to-site distance ( $R_{ij}$ ) parameters (Equation 22 in Shahi and Baker 2011).
- Mean value of natural logarithm of spectral acceleration ( $\mu_{\ln Sa, no pulse}$ ) for non-pulse-type cases is calculated from Equation B6.

$$\mu_{\ln Sa, No Pulse} = \mu_{Df} + \mu_{\ln Sa, gmm} \quad B6$$

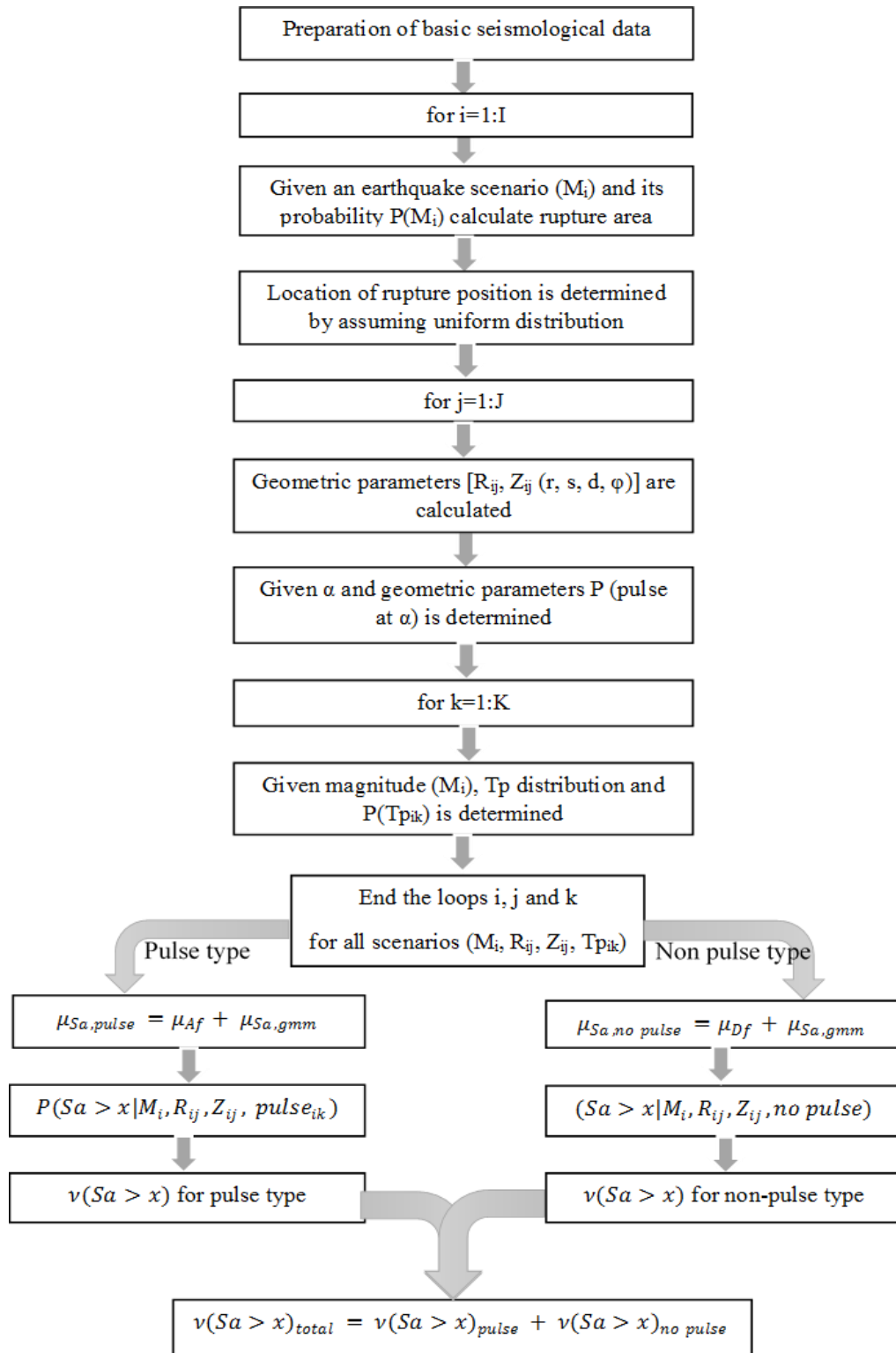


Figure B.1 Algorithm for SHB11 PSHA narrow-band model

- The algorithm is repeated from step 2 and mean logarithm of  $S_a$  ( $\mu_{\ln S_a}$ ) is calculated for all magnitude ranges ( $M_i$ ), rupture locations ( $R_{ij}$  and  $Z_{ij}$ ) and pulse period range ( $T_{p_{ik}}$ ) and both pulse-type and non-pulse-type cases.
- For pulse-type cases, the probability of exceedance is calculated from Equation B7 for each intensity level ( $x$ ).

$$P(S_a > x | m, r, z, pulse) = 1 - \Phi\left(\frac{\ln(x) - \mu_{\ln S_a, pulse}}{\sigma_{\ln S_a, pulse}}\right) \quad B7$$

- For non-pulse-type cases the probability of exceedance is calculated from Equation B8 for each intensity level ( $x$ ).

$$P(S_a > x | m, r, no pulse) = 1 - \Phi\left(\frac{\ln(x) - \mu_{\ln S_a, no pulse}}{\sigma_{\ln S_a, no pulse}}\right) \quad B8$$

The total hazard curve is calculated Equations 3.1 and 3.2. As can be seen from Equation 3.1 the total hazard curve is calculated from the summation of pulse-type and non-pulse-type cases. The flowchart of the algorithm for SHB11 model is shown in Figure B1.

## B.2 The Numerical eEvaluation of Integral in PSHA

The discretized values of random variables are used in PSHA. Proper distribution is considered for each random variable with sufficient discretization values. The discretized values and considered distributions are given below.

- Magnitude is discretized in 0.1 ranges.
- For each discretized magnitude range, mean rupture area is calculated from the Wells and Coppersmith (1994).
- The rupture area is uniformly distributed within the fault area. The epicenter of rupture area is shifted every 5km in the fault strike direction and every 3km in the fault dip direction.
- Lognormal distribution is considered for  $T_p$  and  $T_p$  is discretized in 0.2sec ranges.

The probability of magnitude and rupture location is the same as conventional PSHA procedure. The distribution considered for the pulse period and the process for calculation of its probability are explained with more detail in the next paragraphs.

For each discretized magnitude the mean pulse period is calculated from Equation B4. A lognormal distribution is considered for each discretized magnitude-pulse period as shown in Figure B2.

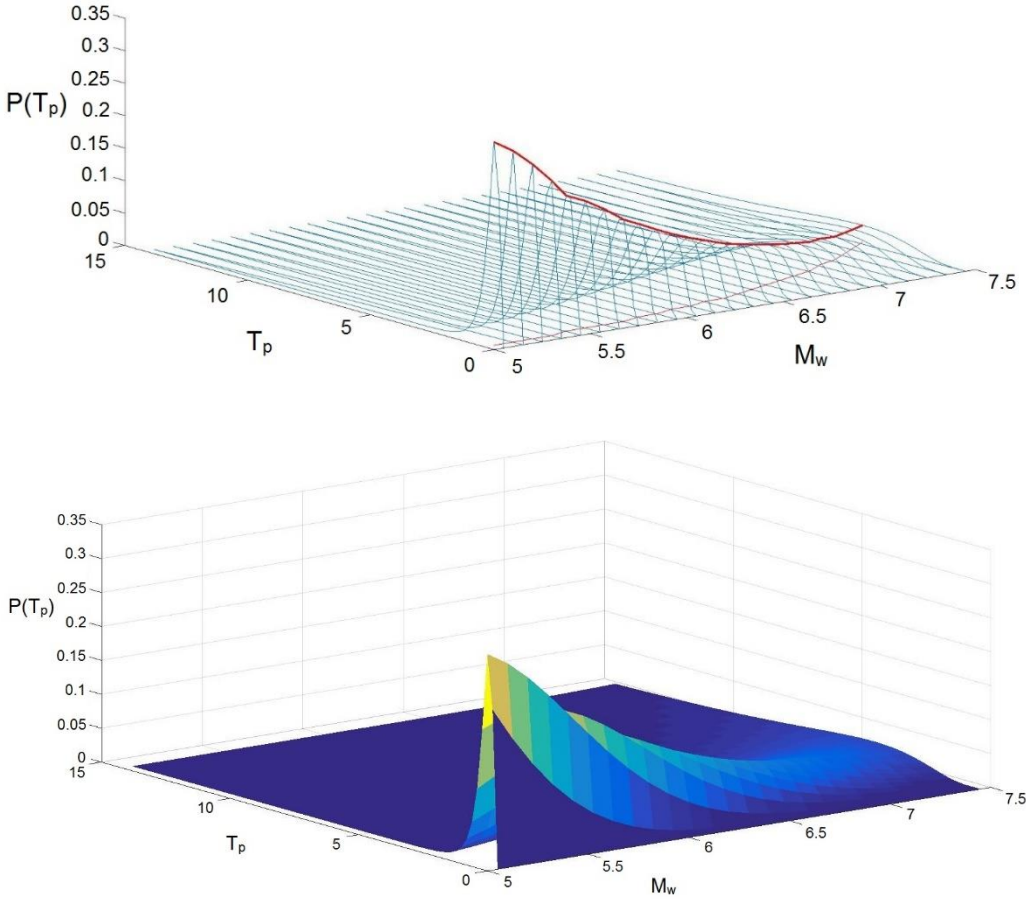


Figure B.2 Illustration of lognormal distribution for magnitude-pulse period and related probability of pulse period

The red line in this figure are the points that maximums of  $P(T_p)$  occur for different discretized magnitudes. The red line is plotted again in  $M_w$ - $T_p$  plane (illustrated with scatter red points in Figure B3). An exponential line is also fitted to the red line (The blue line). The black line is the equation proposed for the maximum amplification points ( $T_{mc}$ - $M_w$  relationship) in this study (Equation 5.8). As can be seen from this figure, the  $T_{mc}$ - $M_w$  relationship (Equation 5.8) and the maximum probability of pulse occurrence curve have a very similar trend. This is because the probability of pulse occurrence is the determining parameter in determination of directivity amplification range in PSHA. Figure B3 is again plotted in  $M_w$ - $\ln(T_p)$  coordinate. As can be seen the relationship between  $M_w$  and  $\ln(T_p)$  is linear as stated in Shahi and Baker (2011).

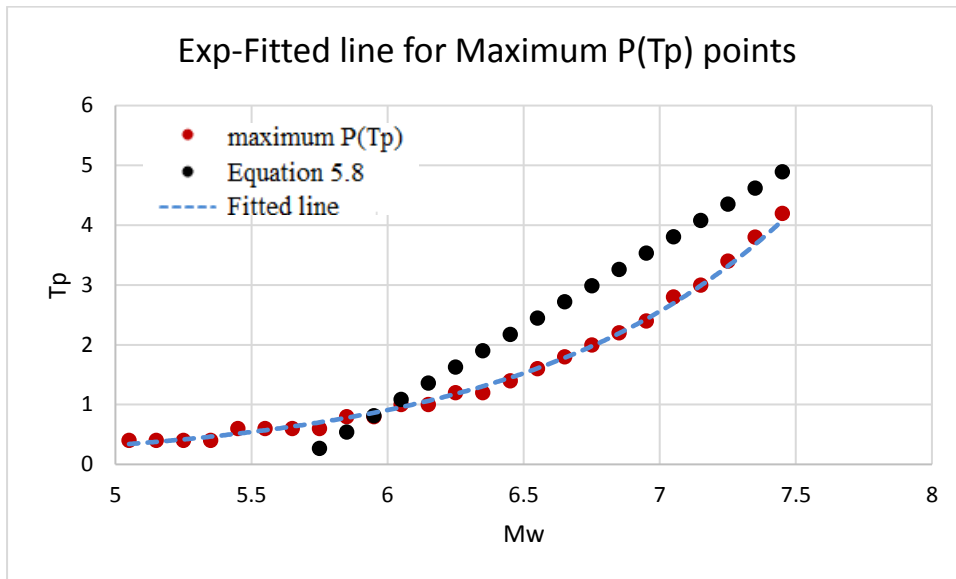


Figure B.3 Relation between magnitude and pulse period with maximum probability

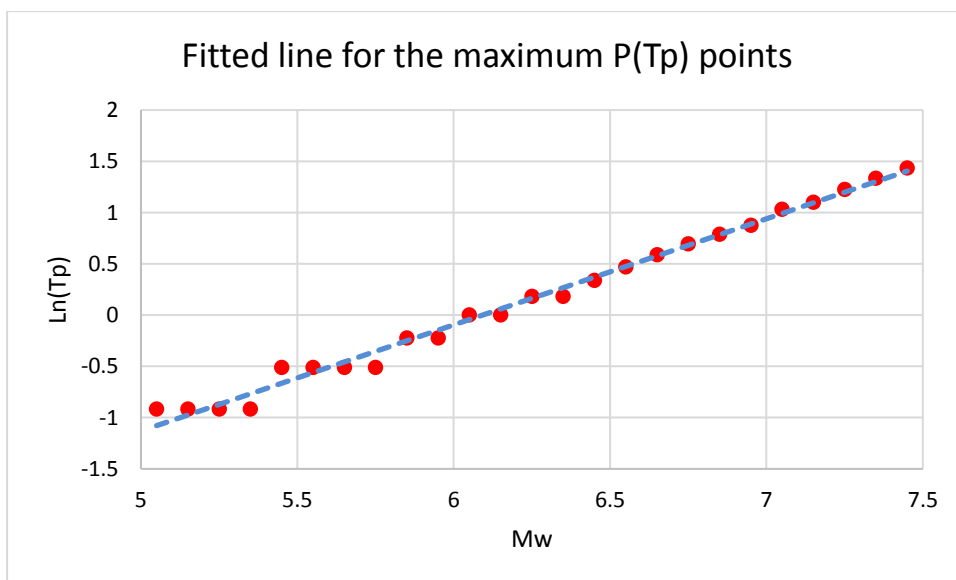
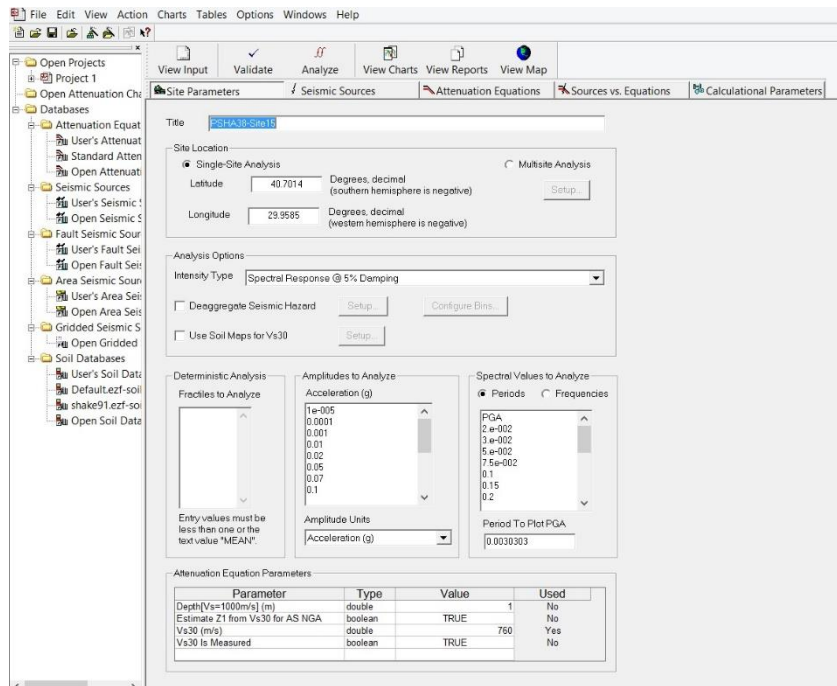


Figure B.4 Relation between magnitude and pulse period with maximum probability

The PSHA results were compared with EZ-FRISK software for the simple line source model used in this study. The comparisons were made to test the sufficiency of magnitude, rupture length and epicenter location discretization. Figure B5 shows the

site definition and discretized values applied in EZ-FRISK for PSHA for FL=20km and  $\dot{S}=1.0$ com/year and site located 15km away from the fault.

a)



b)

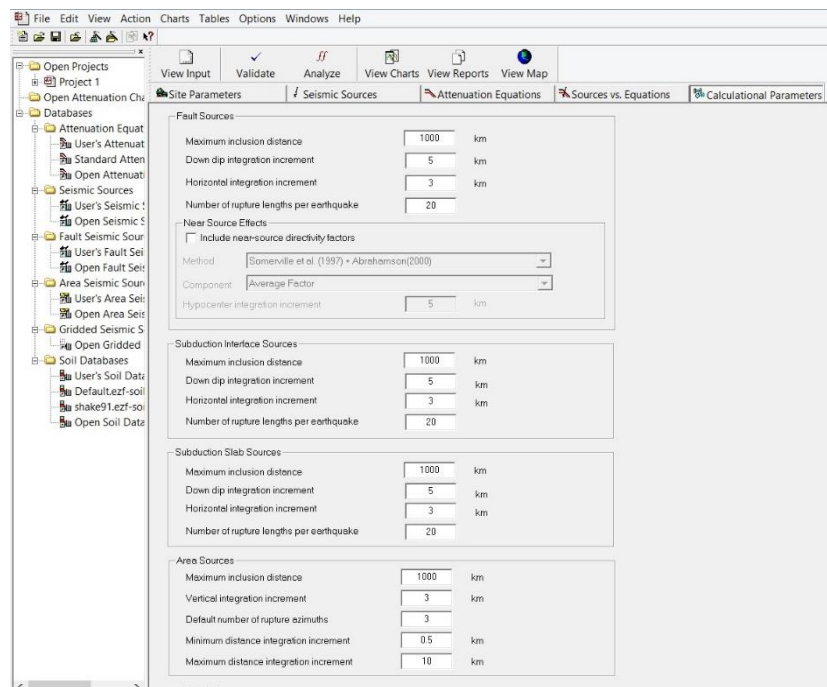


Figure B.5 a) Site definition b) Discretized values applied in EZ-FRISK

The results of PSHA code are consistent with the results of EZ-FRISK. The comparisons are done for “no directivity” case with Boore and Atkinson (2008)

GMPM. Figure B6 shows the response spectrum calculated from EZ-FRISK and the code. The comparisons indicate the sufficiency of magnitude, distance and epicenter discretization.

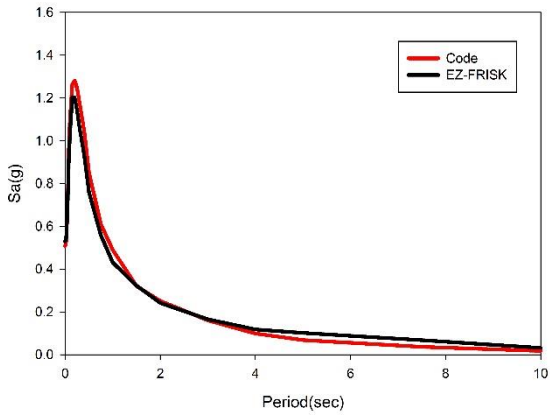
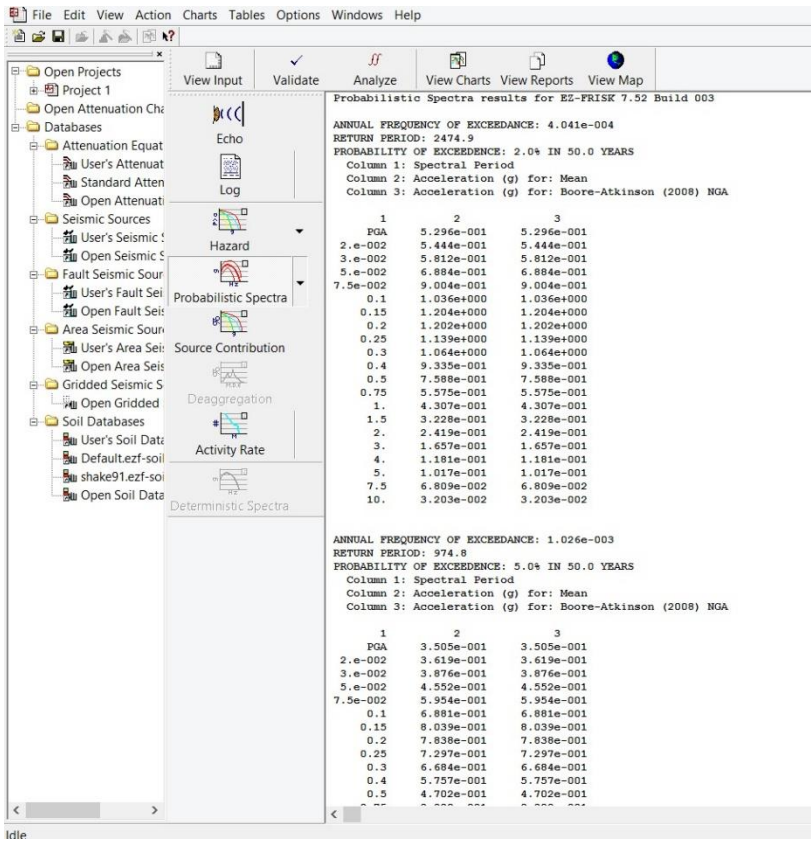


Figure B.6 Response spectrum calculated for FL=20km,  $\dot{S}=1.0\text{com/year}$  for site 15 with EZ-FRISK and the Matlab code (2475-year return period)

## B.3 The Matlab Code developed for PSHA

### - Input File Format

	B	C	D	E	F	G	H	I	J	K	L	M
1	1	Fault 1						Num. of Sites	42			
2		Fault Coordinates	1st corner	1st corner	2nd corner	3rd corner	4th corner	Site 1	Site 2	Site 3	Site 4	Site 5
3		coordinate-x(km)	0	0	100	-2.1E-28	100	50	75	100	110	120
4		coordinate-y(km)	0	0	0	-4.6E-14	-4.6246E-14	0	0	0	0	0
5		coordinate-z(km)	0	0	0	-10	-10	0	0	0	0	0
6		fault_length(km)	100	M. max	0.01829							
7		fault_width(km)	10	M. max	7.23							
8		slip rate(cm/year)	1									
9		Mu(dyne/cm <sup>2</sup> )	3.00E+11									
10		fault_pdf_type	2									
11		strike(deg)	-90									
12		dip(deg)	90									
13		Fn	0									
14		Fr	0									
15		sigma (or M_min)	5									
16		nsigma_max(or b value or M_max)	0.9									
17		Fault Mechanism	2									
18		Vs30	760									
19		F_as	0									
20		F_mes	1									
21												
22												
23												
24												
25												
26												
27												
28												

	A	B	C	D
1	Number	GMPE	Weight	
2	1	Fukushima et al. (2003)	0	
3	2	Kalkan and Gulkan (2004)	0	
4	3	Ozbey et al. (2004)	0	
5	4	Ambraseys et al. (2005)	0	
6	5	Zhao et al. (2006)	0	
7	6	Cauzzi and Faccioli (2008)	0	
8	7	Abrahamson and Silva (2008)	0	
9	8	Boore and Atkinson (2008)	1	
10	9	Campbell and Bozorgnia (2008)	0	
11	10	Chiou and Youngs (2008)	0	
12	11	Ghasemi et al. (2009)	0	
13	12	Bindi et al. (2010)	0	
14	13	Akkar and Cagnan (2010)	0	
15	14	Akkar and Bommer (2010)	0	
16	15	Saffari et al. (2012)	0	
17	16	Akkar et al. (2014)	0	
18	17	Kale and Akkar (2013)	0	
19	18	Bindi et al. (2014)	0	
20	21	Abrahamson, Silva and Kamai (2014)	0	
21	22	Boore, Stewart, Seyhan and Atkinson (2014)	0	
22	23	Campbell and Bozorgnia (2014)	0	
23	24	Chiou and Youngs (2014)	0	
24				
25		Sum of Weight (Should be equal to 1)	1	
26				
27				
28				
29				
30				

Figure B.7 Input file format for PSHA

- **PSHA File:**

```
function PSHA(inputname)
ex_input_data=strcat('outputs\',inputname,'.xlsx');
Input_Data=xlsread(ex_input_data,'Input_Data');
GMPE_Data=xlsread(ex_input_data,'GMPEs');
if GMPE_Data(24,4)~=1
    disp('Weights should sum up to 1')
    return
end
[gmpe_id]=find(GMPE_Data(:,3)>0);
GMPE_ID(:,1) =GMPE_Data(gmpe_id,1);
weigth(:,1)=GMPE_Data(gmpe_id,3);
GMPE=[GMPE_ID weigth];

Period_p=[0 0.01 0.02 0.03 0.05 0.075 0.1 0.15 0.2 0.25 0.3 0.4 0.5 0.75 1
1.5 2 3 4 5 7.5 10];

F_AS=0;
F_RV=0;
F_NM=0;
F_HW=0;
rake=-999;
Ry0=0;

format long
%%% General declarations
pi=3.14159265358979;
M_stepsize=0.1;
epsilon_step_size=0.1;
max_dis_btw_segcen=2;

%%% fault source assignments
nof_h_max_segments=20;
nof_v_max_segments=5;
nof_max_bg_segments=10;

%% Modified Rupture Distribution
ver_incrmnt=3;
hor_incrmnt=5;

%% Start reading input data
nof_stations=Input_Data(1,9);
for scon=1:nof_stations
    coords(1,scon)=Input_Data(3,7+scon);
    coords(2,scon)=Input_Data(4,7+scon);
    coords(3,scon)=Input_Data(5,7+scon);
end
nof_fault_sources=Input_Data(1,1);
con=2;
for sco=1:nof_fault_sources
    fault_data(1,sco)=Input_Data(1+con,3);
    fault_data(2,sco)=Input_Data(2+con,3);
    fault_data(3,sco)=Input_Data(3+con,3);
    fault_data(4,sco)=Input_Data(4+con,3);
    fault_data(5,sco)=Input_Data(5+con,3);
    fault_data(6,sco)=Input_Data(6+con,3);
    fault_data(7,sco)=Input_Data(7+con,3);
    fault_data(8,sco)=Input_Data(8+con,3);
    fault_data(9,sco)=Input_Data(9+con,3);
    fault_data(10,sco)=Input_Data(10+con,3);
    fault_data(11,sco)=Input_Data(11+con,3);
    fault_data(12,sco)=Input_Data(12+con,3);
    fault_data(13,sco)=Input_Data(13+con,3);
    fault_data(14,sco)=Input_Data(14+con,3);
    fault_data(15,sco)=Input_Data(15+con,3);
```

```

    fault_data(16,sco)=Input_Data(16+con,3);
    fault_data(17,sco)=Input_Data(17+con,3);
    fault_data(18,sco)=Input_Data(18+con,3);
    con=con+20;
end

%% End input data reading
if nof_fault_sources>0
    % input('Do you want to include the line source/s in hazard curve
calculations ? Y/N ', 's');
    anss='Y';
    if anss=='N' | anss=='n';
        nof_fault_sources=0;
        disp('Skip fault sources');
        single_fault_flag=0;
    else
        single_fault_flag=1;
    end
end

for kl=1:nof_stations
    j=stations(kl)
    cas_count=1;
    station(j,1)=coords(1,j);
    station(j,2)=coords(2,j);
    station(j,3)=coords(3,j);
    if single_fault_flag==1, run fault_sources; end
    if exist('outputs','dir')==7
    else
        mkdir 'outputs';
    end
    run eps_calc

    %% Pulse Type Hazard Calculation
    for sp=1:length(Period_p)
        Per=Period_p(sp);
        for sal=1:2
            if sal==1
                alfa=0;
            elseif sal==2
                alfa=90;
            end
            for k=1:cas_count-1
                l=1;
                HT_dummy1=['epsilon_',num2str(TS(k,13))];
                HT_dummy2=eval(HT_dummy1);
                nof_epsilon=length(HT_dummy2);
                HT_dummy3=['pepsilon_',num2str(TS(k,13))];
                HT_dummy4=eval(HT_dummy3);
                HT_P=zeros(length(HT_dummy2)*(nof_Tp_steps),17);
                P_alpha_dir=TS_P_alpha(k,sal);

                % GMPE calculation
                cd('.\GMPEs_02.03.2014')

                InpMag=[TS(k,1),TS(k,2),TS(k,3),Vs_30,Fault_Mech,abs(TS(k,20)),TS(k,17),TS(k,19),rake,TS(k,6),abs(TS(k,18)),TS(k,16),TS(k,21),Per];
                [IM_median,sig_total,logIM,IM_median_NP,sig_total_NP] =
                GMPE_Trellis_Plots_Mag(InpMag,GMPE);
                cd('..\')

                IM_median_M(k,1)=IM_median;
                sig_total_M(k,1)=sig_total;
                IM_median_NP_M(k,1)=IM_median_NP;
            end
        end
    end
end

```

```

sig_total_NP_M(k,1)=sig_total_NP;

for sk=1:nof_Tp_steps
    cass=1;
    Tp=TS_Tp(sk);
    P_Tp=TS_P_Tp(k,sk);
    if Tp<0.6
        Mean_ln_Af=0;
        Rf=1;
    else
        if Per<=0.88*Tp
            Mean_ln_Af=1.131*exp(-
3.11*(log(Per/Tp)+0.127)^2)+0.058;
        elseif Per>0.88*Tp
            Mean_ln_Af=0.924*exp(-
2.11*(log(Per/Tp)+0.127)^2)+0.255;
        end
        if Per<=0.21*Tp
            Rf=1-0.2*exp(-0.96*(log(Per/Tp)+1.56)^2);
        elseif Per>0.21*Tp
            Rf=1-0.21*exp(-0.24*(log(Per/Tp)+1.56)^2);
        end
    end
    %Amplification Due to Presence of Pulse
    logIM_P=logIM+Mean_ln_Af;
    IM_median_P=exp(logIM_P);

    %Reduction of Standard Deviation for Pulse Type Because
of Modified Ground-Motion Model
    sig_total_P=Rf*sig_total;
    IM_sigma_P=sig_total_P;

    for
dummy_counter=min(HT_dummy2):epsilon_step_size:max(HT_dummy2);%(nof_epsilon
)*(k-1)+1:(nof_epsilon)*k
        HT_P(1,1)=TS(k,1);
        HT_P(1,2)=TS(k,2);
        HT_P(1,3)=TS(k,9);
        HT_P(1,4)=TS(k,12);
        HT_P(1,5)=TS(k,11);
        HT_P(1,6)=TS(k,5);
        HT_P(1,7)=TS(k,7);
        HT_P(1,8)=TS(k,10);
        HT_P(1,9)=HT_dummy2(cass);
        HT_P(1,10)=HT_dummy4(cass);
        HT_P(1,11)=IM_median_P;
        HT_P(1,12)=IM_sigma_P;
        HT_P(1,13)=exp(log(HT_P(1,11)) +
            HT_P(1,9)*IM_sigma_P);
        HT_P(1,14)= HT_P(1,4)*HT_P(1,5) *HT_P(1,6)
            *HT_P(1,7) * HT_P(1,8) *
            HT_P(1,10)*P_Tp*P_alpha_dir;
        HT_P(1,15)=Tp;
        HT_P(1,16)=P_Tp;
        HT_P(1,17)=P_alpha_dir;
        cass=cass+1;
        l=l+1;
    end
    clear nof_epsilon
end
[sm,sn]=size(HT_P);
Hazard_Table_P((k-1)*(sm)+1:k*(sm),1:sn)=HT_P;
end

Sorted_Hazard_Table_P=sortrows(Hazard_Table_P,-13);

```

```

Sorted_Hazard_Table_P(1,18)=Sorted_Hazard_Table_P(1,14);
for m=2:length(Sorted_Hazard_Table_P(:,13));
    Sorted_Hazard_Table_P(m,18)=Sorted_Hazard_Table_P(m,14)+
Sorted_Hazard_Table_P(m-1,18);
end

Hazard_PT=[Sorted_Hazard_Table_P(:,13),Sorted_Hazard_Table_P(:,18)];

%% Non Pulse Hazard Calculation
l=1;
for k=1:cas_count-1
    cass=1;
    P_no_alpha_dir=1-(TS_P_alpha(k, sal));
    HT_dummy1=['epsilon_', num2str(TS(k,13))];
    HT_dummy2=eval(HT_dummy1);
    nof_epsilon=length(HT_dummy2);
    HT_dummy3=['pepsilon_', num2str(TS(k,13))];
    HT_dummy4=eval(HT_dummy3);

    for
dummy_counter=min(HT_dummy2):epsilon_step_size:max(HT_dummy2);%(nof_epsilon
)*(k-1)+1:(nof_epsilon)*k
        Hazard_Table_NP(1,1)=TS(k,1);
        Hazard_Table_NP(1,2)=TS(k,2);
        Hazard_Table_NP(1,3)=TS(k,9);
        Hazard_Table_NP(1,4)=TS(k,12);
        Hazard_Table_NP(1,5)=TS(k,11);
        Hazard_Table_NP(1,6)=TS(k,5);
        Hazard_Table_NP(1,7)=TS(k,7);
        Hazard_Table_NP(1,8)=TS(k,10);
        Hazard_Table_NP(1,9)=HT_dummy2(cass);
        Hazard_Table_NP(1,10)=HT_dummy4(cass);
        Hazard_Table_NP(1,11)=IM_median_NP_M(k,1);
        Hazard_Table_NP(1,12)=sig_total_NP_M(k,1);
        Hazard_Table_NP(1,13)=exp(log(Hazard_Table_NP(1,11)) +
Hazard_Table_NP(1,9)*sig_total_NP_M(k,1));    %%% 999 This line can be
changed according to the PE
        Hazard_Table_NP(1,14)=
Hazard_Table_NP(1,4)*Hazard_Table_NP(1,5) *Hazard_Table_NP(1,6)
*Hazard_Table_NP(1,7) * Hazard_Table_NP(1,8) *
Hazard_Table_NP(1,10)*P_no_alpha_dir;
        cass=cass+1;
        l=l+1;
    end
    clear nof_epsilon
end

Sorted_Hazard_Table_NP=sortrows(Hazard_Table_NP,-13);
Sorted_Hazard_Table_NP(1,15)=Sorted_Hazard_Table_NP(1,14);
for m=2:length(Sorted_Hazard_Table_NP(:,13));
    Sorted_Hazard_Table_NP(m,15)=Sorted_Hazard_Table_NP(m,14)+
Sorted_Hazard_Table_NP(m-1,15);
end

Hazard_NPT=[Sorted_Hazard_Table_NP(:,13),Sorted_Hazard_Table_NP(:,15)];

%% Conventional Method
l=1;
for k=1:cas_count-1
    cass=1;
    HT_dummy1=['epsilon_', num2str(TS(k,13))];
    HT_dummy2=eval(HT_dummy1);
    nof_epsilon=length(HT_dummy2);
    HT_dummy3=['pepsilon_', num2str(TS(k,13))];

```

```

HT_dummy4=eval (HT_dummy3);

for
dummy_counter=min(HT_dummy2):epsilon_step_size:max(HT_dummy2);
    Hazard_Table(1,1)=TS(k,1);
    Hazard_Table(1,2)=TS(k,2);
    Hazard_Table(1,3)=TS(k,9);
    Hazard_Table(1,4)=TS(k,12);
    Hazard_Table(1,5)=TS(k,11);
    Hazard_Table(1,6)=TS(k,5);
    Hazard_Table(1,7)=TS(k,7);
    Hazard_Table(1,8)=TS(k,10);
    Hazard_Table(1,9)=HT_dummy2(cass);
    Hazard_Table(1,10)=HT_dummy4(cass);
    Hazard_Table(1,11)=IM_median_M(k,1);
    Hazard_Table(1,12)=sig_total_M(k,1);
    Hazard_Table(1,13)=exp(log(Hazard_Table(1,11)) +
    Hazard_Table(1,9)*sig_total_M(k,1));
    Hazard_Table(1,14)= Hazard_Table(1,4)*Hazard_Table(1,5)
        *Hazard_Table(1,6) *Hazard_Table(1,7) *
        Hazard_Table(1,8) * Hazard_Table(1,10);
    cass=cass+1;
    l=l+1;
end
end
Sorted_Hazard_Table=sortrows(Hazard_Table,-13);
Sorted_Hazard_Table(1,15)=Sorted_Hazard_Table(1,14);
for m=2:length(Sorted_Hazard_Table(:,13));
    Sorted_Hazard_Table(m,15)=Sorted_Hazard_Table(m,14)+
Sorted_Hazard_Table(m-1,15);
end
Hazard_T=[Sorted_Hazard_Table(:,13),Sorted_Hazard_Table(:,15)];

%% Calculation of Total Hazard of Non-Pulse and Pulse Like
Results (Hazard Total=Hazard_P+Hazard_NP
% Elimination of Repeated Data
differ=diff(Hazard_PT,1);
Hazard_P(:,1)=Hazard_PT(find(differ(:,1)),1);
Hazard_P(:,2)=Hazard_PT(find(differ(:,1)),2);
slk=length(Hazard_P)+1;
ii=length(Hazard_PT);
Hazard_P(slk,:)=Hazard_PT(ii,:);
clear differ

differ=diff(Hazard_NPT,1);
Hazard_NP(:,1)=Hazard_NPT(find(differ(:,1)),1);
Hazard_NP(:,2)=Hazard_NPT(find(differ(:,1)),2);
slk=length(Hazard_NP)+1;
ii=length(Hazard_NPT);
Hazard_NP(slk,:)=Hazard_NPT(ii,:);
clear differ

differ=diff(Hazard_T,1);
Hazard(:,1)=Hazard_T(find(differ(:,1)),1);
Hazard(:,2)=Hazard_T(find(differ(:,1)),2);
slk=length(Hazard)+1;
ii=length(Hazard_T);
Hazard(slk,:)=Hazard_T(ii,:);

%Intrapolation to Make the Hazard Results Consistent for Non-
Pulse Like, Pulse Like and Conventional Methods
Hazard_P_M(:,1)=Hazard_NP(:,1);
Hazard_P_M(:,2) =
interp1(Hazard_P(:,1),Hazard_P(:,2),Hazard_NP(:,1));
Hazard_tot(:,1)=Hazard_P_M(:,1);

```

```

Hazard_tot(:,2)= Hazard_P_M(:,2)+Hazard_NP(:,2);

Hazard_M(:,1)=Hazard_NP(:,1);
Hazard_M(:,2) =
interp1(Hazard(:,1),Hazard(:,2),Hazard_NP(:,1));

%% Probability of Exceedance for Return Period of 50 Years
Hazard_P_50(:,2)=1-exp(-Hazard_tot(:,2)*50);
Hazard_P_50(:,1)=Hazard_tot(:,1);
Hazard_50(:,2)=1-exp(-Hazard_M(:,2)*50);
Hazard_50(:,1)=Hazard_M(:,1);

%% Calculation of 2% and 10% in 50 Years Spectra(just for Alpha
= 0 or 90 Degree)
if sal==1
for sf=1:length (Hazard_P_50)
if Hazard_P_50(sf,2)==0.1
spec_0_10P(sp,1)=Per;
spec_0_10P(sp,2)=Hazard_P_50(sf,1);
end
if Hazard_P_50(sf,2)==0.02
spec_0_2P(sp,1)=Per;
spec_0_2P(sp,2)=Hazard_P_50(sf,1);
end
end
for sf=1:length (Hazard_P_50)-1
if Hazard_P_50(sf,2)<0.1 && Hazard_P_50(sf+1,2)>0.1
spec_0_10P(sp,1)=Per;

spec_0_10P(sp,2)=Hazard_P_50(sf,1)+((Hazard_P_50(sf+1,1)-
Hazard_P_50(sf,1))/(Hazard_P_50(sf+1,2)-Hazard_P_50(sf,2)))*(0.1-
Hazard_P_50(sf,2));
end
if Hazard_P_50(sf,2)<0.02 && Hazard_P_50(sf+1,2)>0.02
spec_0_2P(sp,1)=Per;

spec_0_2P(sp,2)=Hazard_P_50(sf,1)+((Hazard_P_50(sf+1,1)-
Hazard_P_50(sf,1))/(Hazard_P_50(sf+1,2)-Hazard_P_50(sf,2)))*(0.02-
Hazard_P_50(sf,2));
end
end
if sal==2
for sf=1:length (Hazard_P_50)
if Hazard_P_50(sf,2)==0.1
spec_15_10P(sp,1)=Per;
spec_15_10P(sp,2)=Hazard_P_50(sf,1);
end
if Hazard_P_50(sf,2)==0.02
spec_15_2P(sp,1)=Per;
spec_15_2P(sp,2)=Hazard_P_50(sf,1);
end
end
for sf=1:length (Hazard_P_50)-1
if Hazard_P_50(sf,2)<0.1 && Hazard_P_50(sf+1,2)>0.1
spec_15_10P(sp,1)=Per;

spec_15_10P(sp,2)=Hazard_P_50(sf,1)+((Hazard_P_50(sf+1,1)-
Hazard_P_50(sf,1))/(Hazard_P_50(sf+1,2)-Hazard_P_50(sf,2)))*(0.1-
Hazard_P_50(sf,2));
end
if Hazard_P_50(sf,2)<0.02 && Hazard_P_50(sf+1,2)>0.02
spec_15_2P(sp,1)=Per;

spec_15_2P(sp,2)=Hazard_P_50(sf,1)+((Hazard_P_50(sf+1,1)-

```

```

Hazard_P_50(sf,1))/(Hazard_P_50(sf+1,2)-Hazard_P_50(sf,2)))*(0.02-
Hazard_P_50(sf,2));
    end
    end
end
if sal==3
    for sf=1:length (Hazard_P_50)
        if Hazard_P_50(sf,2)==0.1
            spec_30_10P(sp,1)=Per;
            spec_30_10P(sp,2)=Hazard_P_50(sf,1);
        end
        if Hazard_P_50(sf,2)==0.02
            spec_30_2P(sp,1)=Per;
            spec_30_2P(sp,2)=Hazard_P_50(sf,1);
        end
    end
    for sf=1:length (Hazard_P_50)-1
        if Hazard_P_50(sf,2)<0.1 && Hazard_P_50(sf+1,2)>0.1
            spec_30_10P(sp,1)=Per;

spec_30_10P(sp,2)=Hazard_P_50(sf,1)+((Hazard_P_50(sf+1,1)-
Hazard_P_50(sf,1))/(Hazard_P_50(sf+1,2)-Hazard_P_50(sf,2)))*(0.1-
Hazard_P_50(sf,2));
            end
            if Hazard_P_50(sf,2)<0.02 && Hazard_P_50(sf+1,2)>0.02
                spec_30_2P(sp,1)=Per;

spec_30_2P(sp,2)=Hazard_P_50(sf,1)+((Hazard_P_50(sf+1,1)-
Hazard_P_50(sf,1))/(Hazard_P_50(sf+1,2)-Hazard_P_50(sf,2)))*(0.02-
Hazard_P_50(sf,2));
            end
        end
    end
if sal==4
    for sf=1:length (Hazard_P_50)
        if Hazard_P_50(sf,2)==0.1
            spec_45_10P(sp,1)=Per;
            spec_45_10P(sp,2)=Hazard_P_50(sf,1);
        end
        if Hazard_P_50(sf,2)==0.02
            spec_45_2P(sp,1)=Per;
            spec_45_2P(sp,2)=Hazard_P_50(sf,1);
        end
    end
    for sf=1:length (Hazard_P_50)-1
        if Hazard_P_50(sf,2)<0.1 && Hazard_P_50(sf+1,2)>0.1
            spec_45_10P(sp,1)=Per;

spec_45_10P(sp,2)=Hazard_P_50(sf,1)+((Hazard_P_50(sf+1,1)-
Hazard_P_50(sf,1))/(Hazard_P_50(sf+1,2)-Hazard_P_50(sf,2)))*(0.1-
Hazard_P_50(sf,2));
            end
            if Hazard_P_50(sf,2)<0.02 && Hazard_P_50(sf+1,2)>0.02
                spec_45_2P(sp,1)=Per;

spec_45_2P(sp,2)=Hazard_P_50(sf,1)+((Hazard_P_50(sf+1,1)-
Hazard_P_50(sf,1))/(Hazard_P_50(sf+1,2)-Hazard_P_50(sf,2)))*(0.02-
Hazard_P_50(sf,2));
            end
        end
    end
if sal==5
    for sf=1:length (Hazard_P_50)
        if Hazard_P_50(sf,2)==0.1
            spec_60_10P(sp,1)=Per;

```

```

        spec_60_10P(sp,2)=Hazard_P_50(sf,1);
    end
    if Hazard_P_50(sf,2)==0.02
        spec_60_2P(sp,1)=Per;
        spec_60_2P(sp,2)=Hazard_P_50(sf,1);
    end
end
for sf=1:length (Hazard_P_50)-1
    if Hazard_P_50(sf,2)<0.1 && Hazard_P_50(sf+1,2)>0.1
        spec_60_10P(sp,1)=Per;

spec_60_10P(sp,2)=Hazard_P_50(sf,1)+((Hazard_P_50(sf+1,1)-
Hazard_P_50(sf,1))/(Hazard_P_50(sf+1,2)-Hazard_P_50(sf,2)))*(0.1-
Hazard_P_50(sf,2));
        end
        if Hazard_P_50(sf,2)<0.02 && Hazard_P_50(sf+1,2)>0.02
            spec_60_2P(sp,1)=Per;

spec_60_2P(sp,2)=Hazard_P_50(sf,1)+((Hazard_P_50(sf+1,1)-
Hazard_P_50(sf,1))/(Hazard_P_50(sf+1,2)-Hazard_P_50(sf,2)))*(0.02-
Hazard_P_50(sf,2));
        end
    end
end
if sal==6
    for sf=1:length (Hazard_P_50)
        if Hazard_P_50(sf,2)==0.1
            spec_75_10P(sp,1)=Per;
            spec_75_10P(sp,2)=Hazard_P_50(sf,1);
        end
        if Hazard_P_50(sf,2)==0.02
            spec_75_2P(sp,1)=Per;
            spec_75_2P(sp,2)=Hazard_P_50(sf,1);
        end
    end
end
for sf=1:length (Hazard_P_50)-1
    if Hazard_P_50(sf,2)<0.1 && Hazard_P_50(sf+1,2)>0.1
        spec_75_10P(sp,1)=Per;

spec_75_10P(sp,2)=Hazard_P_50(sf,1)+((Hazard_P_50(sf+1,1)-
Hazard_P_50(sf,1))/(Hazard_P_50(sf+1,2)-Hazard_P_50(sf,2)))*(0.1-
Hazard_P_50(sf,2));
        end
        if Hazard_P_50(sf,2)<0.02 && Hazard_P_50(sf+1,2)>0.02
            spec_75_2P(sp,1)=Per;

spec_75_2P(sp,2)=Hazard_P_50(sf,1)+((Hazard_P_50(sf+1,1)-
Hazard_P_50(sf,1))/(Hazard_P_50(sf+1,2)-Hazard_P_50(sf,2)))*(0.02-
Hazard_P_50(sf,2));
        end
    end
end
if sal==7
    for sf=1:length (Hazard_P_50)
        if Hazard_P_50(sf,2)==0.1
            spec_90_10P(sp,1)=Per;
            spec_90_10P(sp,2)=Hazard_P_50(sf,1);
        end
        if Hazard_P_50(sf,2)==0.02
            spec_90_2P(sp,1)=Per;
            spec_90_2P(sp,2)=Hazard_P_50(sf,1);
        end
    end
end
for sf=1:length (Hazard_P_50)-1

```

```

        if Hazard_P_50(sf,2)<0.1 && Hazard_P_50(sf+1,2)>0.1
            spec_90_10P(sp,1)=Per;
        end
spec_90_10P(sp,2)=Hazard_P_50(sf,1)+((Hazard_P_50(sf+1,1)-
Hazard_P_50(sf,1))/(Hazard_P_50(sf+1,2)-Hazard_P_50(sf,2)))*(0.1-
Hazard_P_50(sf,2));
        end
        if Hazard_P_50(sf,2)<0.02 && Hazard_P_50(sf+1,2)>0.02
            spec_90_2P(sp,1)=Per;
        end
spec_90_2P(sp,2)=Hazard_P_50(sf,1)+((Hazard_P_50(sf+1,1)-
Hazard_P_50(sf,1))/(Hazard_P_50(sf+1,2)-Hazard_P_50(sf,2)))*(0.02-
Hazard_P_50(sf,2));
        end
    end
    end
    % Spectra for Conventional Method
    for sf=1:length (Hazard_50)
        if Hazard_50(sf,2)==0.1
            spec_con_10P(sp,1)=Per;
            spec_con_10P(sp,2)=Hazard_50(sf,1);
        end
        if Hazard_50(sf,2)==0.02
            spec_con_2P(sp,1)=Per;
            spec_con_2P(sp,2)=Hazard_50(sf,1);
        end
    end
end
    for sf=1:length (Hazard_50)-1
        if Hazard_50(sf,2)<0.1 && Hazard_50(sf+1,2)>0.1
            spec_con_10P(sp,1)=Per;
            spec_con_10P(sp,2)=Hazard_50(sf,1)+((Hazard_50(sf+1,1)-
Hazard_50(sf,1))/(Hazard_50(sf+1,2)-Hazard_50(sf,2)))*(0.1-
Hazard_50(sf,2));
        end
        if Hazard_50(sf,2)<0.02 && Hazard_50(sf+1,2)>0.02
            spec_con_2P(sp,1)=Per;
            spec_con_2P(sp,2)=Hazard_50(sf,1)+((Hazard_50(sf+1,1)-
Hazard_50(sf,1))/(Hazard_50(sf+1,2)-Hazard_50(sf,2)))*(0.02-
Hazard_50(sf,2));
        end
    end
    end
    if j==1
        mkdir ('outputs',inputname);
    end
    clear Hazard_Table_P HT_P Hazard_PT Hazard_Table_NP
    Hazard_Table Sorted_Hazard_Table_P Sorted_Hazard_Table_NP
    Sorted_Hazard_Table Hazard_tot Hazard_P_M Hazard_NP Hazard_P Hazard_PT
    Hazard_NPT Hazard_T Hazard Hazard_M Hazard_P_50 Hazard_50 IM_median_M
    sig_total_M IM_median_NP_M sig_total_NP_M differ A B C
    end
end
A=zeros(length(spec_0_10P),1);

B={'Period'},{'P_sa(Alpha=0'},[],{'Period'},{'P_sa(Alpha=15'},[],{'Period'
},{'P_sa(Alpha=30'},[],{'Period'},{'P_sa(Alpha=45'},[],{'Period'},{'P_sa(Al
pha=60'},[],{'Period'},{'P_sa(Alpha=75'},[],{'Period'},{'P_sa(Alpha=90'},[],
{'Period'},{'P_sa(Conv'},[],};

C2P=[spec_0_2P,A,spec_15_2P,A,spec_30_2P,A,spec_45_2P,A,spec_60_2P,A,spec_7
5_2P,A,spec_90_2P,A,spec_con_2P];

C10P=[spec_0_10P,A,spec_15_10P,A,spec_30_10P,A,spec_45_10P,A,spec_60_10P,A,
spec_75_10P,A,spec_90_10P,A,spec_con_10P];

```

```

xlswrite(ex_name,B,'Spectra_2P',('A1'));
xlswrite(ex_name,B,'Spectra_10P',('A1'));
xlswrite(ex_name,C2P,'Spectra_2P',('A2'));
xlswrite(ex_name,C10P,'Spectra_10P',('A2'));
clear Dummy P_alpha TS TS_P_alpha TS_P_Tp sp_0 sp_90 sp_con A B C10P
C2P
end
end

```

- **fault\_sources File:**

```

for i=1:nof_fault_sources
disp('Analyzing the single line fault sources.')

x_fault(i)=fault_data(1,i);
y_fault(i)=fault_data(2,i);
z_fault(i)=fault_data(3,i);

fault_length(i)=fault_data(4,i);
fault_width(i)=fault_data(5,i);
slip_rate(i)=fault_data(6,i);
mu(i)=fault_data(7,i);
fault_cdf_type(i)=int16(fault_data(8,i));
strike_deg(i)=fault_data(9,i);
dip_deg(i)=fault_data(10,i);
Fn=fault_data(11,i);
Fr=fault_data(12,i);
Fault_Mech=fault_data(15,i);
Vs_30=fault_data(16,i);
F_as=fault_data(17,i);
F_mes=fault_data(18,i);
if Fault_Mech==0
    U=0;
    SS=0;
    NS=1;
    RS=0;
    a=2.87;
    b=0.82;
    am=3.93;
    bm=1.02;
    F_NM=1;
elseif Fault_Mech==1
    U=0;
    SS=0;
    NS=0;
    RS=1;
    a=3.99;
    b=0.98;
    am=4.33;
    bm=0.9;
    F_RV=1;
elseif Fault_Mech==2
    U=0;
    SS=1;
    NS=0;
    RS=0;
    a=3.42;
    b=0.9;
    am=3.98;
    bm=1.02;
end
%-----
fault_M_stepsize(i)=M_stepsize;
fault_area(i)=(fault_length(i)*fault_width(i));

```

```

strike_rad(i) = (strike_deg(i)+ 90) / 180 * pi;
dip_rad(i)= (dip_deg(i) + 180) / 180 * pi;

fault_corners(1,1)=x_fault(i);
fault_corners(1,2)=y_fault(i);
fault_corners(1,3)=z_fault(i);

fault_corners(2,1)= fault_corners(1,1) + fault_length(i) *
cos(strike_rad(i));
fault_corners(2,2)= fault_corners(1,2) + fault_length(i) *
sin(strike_rad(i));
fault_corners(2,3)= fault_corners(1,3);

if dip_deg(i) < 90
    fault_corners(3,1) = fault_corners(1,1) + fault_width(i) *
cos((strike_rad(i)+pi/2)) * abs(cos(dip_rad(i)));
    fault_corners(3,2) = fault_corners(1,2) + fault_width(i) *
sin((strike_rad(i)+pi/2)) * abs(cos(dip_rad(i)));
    fault_corners(4,1) = fault_corners(2,1) + fault_width(i) *
cos((strike_rad(i)+pi/2)) * abs(cos(dip_rad(i)));
    fault_corners(4,2) = fault_corners(2,2) + fault_width(i) *
sin((strike_rad(i)+pi/2)) * abs(cos(dip_rad(i)));
else
    fault_corners(3,1) = fault_corners(1,1) + fault_width(i) *
cos((strike_rad(i)+3*pi/2)) * abs(cos(dip_rad(i)));
    fault_corners(3,2) = fault_corners(1,2) + fault_width(i) *
sin((strike_rad(i)+3*pi/2)) * abs(cos(dip_rad(i)));
    fault_corners(4,1) = fault_corners(2,1) + fault_width(i) *
cos((strike_rad(i)+3*pi/2)) * abs(cos(dip_rad(i)));
    fault_corners(4,2) = fault_corners(2,2) + fault_width(i) *
sin((strike_rad(i)+3*pi/2)) * abs(cos(dip_rad(i)));
end
fault_corners(3,3) = fault_corners(1,3) + fault_width(i) *
sin(dip_rad(i));
fault_corners(4,3) = fault_corners(2,3) + fault_width(i) *
sin(dip_rad(i));

% Write Fault Corner Coordinates to Excel Input File
if i==1
    Scc=3;
end
rcc=num2str(Scc);
s_ex=strcat('E',rcc);
xlswrite(ex_input_data,fault_corners','Input_Data',s_ex);
Scc=Scc+20;
% Calculatin of Fault Normal Vector
Vectr_1=fault_corners(3,:)-fault_corners(1,:);
Vectr_2=fault_corners(2,:)-fault_corners(1,:);
norm_vectr=cross(Vectr_1,Vectr_2);
norm_vectr=norm_vectr/max(abs(norm_vectr));
%-----
fault_cline(1,1)=(fault_corners(1,1)+fault_corners(3,1))/2;
fault_cline(1,2)=(fault_corners(1,2)+fault_corners(3,2))/2;
fault_cline(1,3)=(fault_corners(1,3)+fault_corners(3,3))/2;
fault_cline(2,1)=(fault_corners(2,1)+fault_corners(4,1))/2;
fault_cline(2,2)=(fault_corners(2,2)+fault_corners(4,2))/2;
fault_cline(2,3)=(fault_corners(2,3)+fault_corners(4,3))/2;

fault_u(1,1)=(fault_cline(2,1)-fault_cline(1,1))/fault_length(i);
fault_u(1,2)=(fault_cline(2,2)-fault_cline(1,2))/fault_length(i);
fault_u(1,3)=(fault_cline(2,3)-fault_cline(1,3))/fault_length(i);

fault_u(2,1)=(fault_corners(3,1)-fault_corners(1,1))/fault_width(i);
fault_u(2,2)=(fault_corners(3,2)-fault_corners(1,2))/fault_width(i);
fault_u(2,3)=(fault_corners(3,3)-fault_corners(1,3))/fault_width(i);

```

```

fault_u(3,1)=fault_u(1,2)*fault_u(2,3)-fault_u(1,3)*fault_u(2,2);
fault_u(3,2)=-fault_u(1,1)*fault_u(2,3)+fault_u(1,3)*fault_u(2,1);
fault_u(3,3)=fault_u(1,1)*fault_u(2,2)-fault_u(1,2)*fault_u(2,1);

switch fault_cdf_type(i)
    case 1 % Truncated Normal Distribution
        fault_sigma(i)=fault_data(13,i);
        fault_nsigmax(i)=fault_data(14,i);
        fault_finsigmax(i)=normcdf(fault_nsigmax(i),0,1);
        fault_Mchar(i)=roundn(bm*log10(fault_area(i))+am,-1);
        fault_M_min(i)=fault_Mchar(i)-
roundn(fault_sigma(i)*fault_nsigmax(i),-1);

fault_M_max(i)=fault_Mchar(i)+roundn(fault_sigma(i)*fault_nsigmax(i),-1);
dumm=fault_M_min(i);
mag=roundn(dumm,-3);
dummy(1)=(1/(fault_sigma(i)*(2*pi)^0.5)*exp(-((fault_M_min(i) -
fault_Mchar(i))^2)/(2*fault_sigma(i)^2)))/(2*fault_finsigmax(i)-1))*10^(1.5*
fault_M_min(i) +16.05)*0.0005;
    for k=2:(fault_M_max(i)-fault_M_min(i))/0.001+1
        dumm=mag+0.001;
        mag=roundn(dumm,-3);
        dummy(k)=(1/(fault_sigma(i)*(2*pi)^0.5)*exp(-((mag -
fault_Mchar(i))^2)/(2*fault_sigma(i)^2)))/(2*fault_finsigmax(i)-1))*10^(1.5*
mag +16.05)*0.001;
    end
    dummy(k+1)=(1/(fault_sigma(i)*(2*pi)^0.5)*exp(-((fault_M_max(i)
- fault_Mchar(i))^2)/(2*fault_sigma(i)^2)))/(2*fault_finsigmax(i)-
1))*10^(1.5* fault_M_max(i) +16.05)*0.0005;
    dummy2=sum(dummy);

    activity_rate(i)=mu(i)*fault_area(i)*1e10*slip_rate(i)/dummy2;

    if i==1
        Scs=7;
    end
    rcc=num2str(Sc);
    rcs=num2str(Scs);
    s_ex=strcat('F',rcc);
    s_fx=strcat('F',rcs);
    xlswrite(ex_input_data,activity_rate(i),'Input_Data',s_ex);
    xlswrite(ex_input_data,fault_M_max(i),'Input_Data',s_fx);
    Sc=Sc+20;
    Scs=Scs+20;

    M_mi=fault_M_min(i);
    M_ma=fault_M_max(i);
    M_steps=fault_M_stepsize(i);
    [M_strt,M_fin]=Magnitude_threshold_TN(M_mi,M_ma,M_steps);
    fault_M_start(i)=M_strt;
    fault_M_finish(i)=M_fin;
    syms mag real
    dumm=(1/(fault_sigma(i)*(2*pi)^0.5)*exp(-((mag -
fault_Mchar(i))^2)/(2*fault_sigma(i)^2)))/(2*fault_finsigmax(i)-1));
    cdf=int(dumm);
    fault_nof_magnitudes(i)=int16((fault_M_finish(i)-
fault_M_start(i))/fault_M_stepsize(i))+1;
    for k=1:fault_nof_magnitudes(i)
        if k==1
            M_of_TS=fault_M_start(i);

PM_of_TS=double(subs(cdf,fault_M_start(i)+0.5*fault_M_stepsize(i))-
subs(cdf,fault_M_start(i)));
        elseif k<fault_nof_magnitudes(i)

```

```

M_of_TS=fault_M_start(i)+(double(k)-
1)*fault_M_stepsize(i);

PM_of_TS=double(subs(cdf,M_of_TS+0.5*fault_M_stepsize(i))-subs(cdf,M_of_TS-
0.5*fault_M_stepsize(i)));
elseif k==fault_nof_magnitudes(i)
M_of_TS=fault_M_finish(i);
PM_of_TS=double(subs(cdf,fault_M_finish(i))-
subs(cdf,fault_M_finish(i)-0.5*fault_M_stepsize(i)));
end

M_of_TS=roundn(M_of_TS,-6);
Area_of_TS=10^(b*M_of_TS-a);
PA_of_TS=1.0;
PW_of_TS=1.0;
%%
if sqrt(Area_of_TS)>fault_width(i)
W_of_TS=fault_width(i);
nof_V_segments=1;
else
W_of_TS=sqrt(Area_of_TS);
nof_V_segments=ceil(fault_width(i)/W_of_TS);
end
if nof_V_segments>nof_v_max_segments
nof_V_segments=nof_v_max_segments;
end
L_of_TS=Area_of_TS/W_of_TS;
if L_of_TS>fault_length(i)
L_of_TS=fault_length(i);
nof_H_segments=1;
else
nof_H_segments=ceil(fault_length(i)/L_of_TS);
end
if nof_H_segments>nof_h_max_segments
nof_H_segments=nof_h_max_segments;
end
nof_segments=nof_H_segments*nof_V_segments;

%%
if nof_V_segments>1
dist_v_btw_segments=(fault_width(i) - W_of_TS) /
(nof_V_segments - 1);
else
dist_v_btw_segments=0;
end

if nof_H_segments > 1
dist_H_btw_segments = (fault_length(i) - L_of_TS) /
(nof_H_segments - 1);
else
dist_H_btw_segments = 0;
end
%%

fault_cline_1(1,1)=fault_corners(1,1)+W_of_TS/2*fault_u(2,1);
fault_cline_1(1,2)=fault_corners(1,2)+W_of_TS/2*fault_u(2,2);
fault_cline_1(1,3)=fault_corners(1,3)+W_of_TS/2*fault_u(2,3);
if nof_V_segments>1
for vse=2:nof_V_segments
fault_cline_1(vse,1)=fault_cline_1(vse-
1,1)+dist_v_btw_segments*fault_u(2,1);
fault_cline_1(vse,2)=fault_cline_1(vse-
1,2)+dist_v_btw_segments*fault_u(2,2);

```

```

        fault_cline_1(vse,3)=fault_cline_1(vse-
1,3)+dist_v_btw_segments*fault_u(2,3);
        end
    end

fault_cline_2(1,1)=fault_corners(2,1)+W_of_TS/2*fault_u(2,1);
fault_cline_2(1,2)=fault_corners(2,2)+W_of_TS/2*fault_u(2,2);
fault_cline_2(1,3)=fault_corners(2,3)+W_of_TS/2*fault_u(2,3);
    if nof_V_segments>1
        for vse=2:nof_V_segments
            fault_cline_2(vse,1)=fault_cline_2(vse-
1,1)+dist_v_btw_segments*fault_u(2,1);
            fault_cline_2(vse,2)=fault_cline_2(vse-
1,2)+dist_v_btw_segments*fault_u(2,2);
            fault_cline_2(vse,3)=fault_cline_2(vse-
1,3)+dist_v_btw_segments*fault_u(2,3);
        end
    end

    %%
    for iv=1:nof_V_segments
        Cen_of_segs(iv,1)=fault_cline_1(iv,1) + (L_of_TS / 2) *
fault_u(1,1);
        Cen_of_segs(iv,2)=fault_cline_1(iv,2) + (L_of_TS / 2) *
fault_u(1,2);
        Cen_of_segs(iv,3)=fault_cline_1(iv,3) + (L_of_TS / 2) *
fault_u(1,3);
    end
    for ih=nof_V_segments+1:nof_segments
        Cen_of_segs(ih,1)=Cen_of_segs(ih-nof_V_segments,1) +
(dist_H_btw_segments) * fault_u(1,1);
        Cen_of_segs(ih,2)=Cen_of_segs(ih-nof_V_segments,2) +
(dist_H_btw_segments) * fault_u(1,2);
        Cen_of_segs(ih,3)=Cen_of_segs(ih-nof_V_segments,3) +
(dist_H_btw_segments) * fault_u(1,3);
    end
    % Calculation of Probability Distribution of Pulse Period
    Tp_min=0.2;
    Tp_max=20.2;
    tp=Tp_min;
    Tp_step_size=0.2;
    Tp_medi=exp(-5.73+0.99.*M_of_TS);
    Tp_sigma=0.56;
    syms Tp
    dumm_Tp=(1/(Tp*Tp_sigma*(2*pi)^0.5))*(exp(-((log(Tp) - log
(Tp_medi))^2)/(2*Tp_sigma^2)));
    cdf_Tp=int(dumm_Tp);
    nof_Tp_steps=int16((Tp_max-Tp_min)/Tp_step_size)+1;
    for ks=1:nof_Tp_steps
        if ks==1

Pr_of_Tp(ks)=double(subs(cdf_Tp,Tp_min+0.5*Tp_step_size)-
subs(cdf_Tp,Tp_min-0.45*Tp_step_size));
        elseif ks<nof_Tp_steps

Pr_of_Tp(ks)=double(subs(cdf_Tp,tp+0.5*Tp_step_size)-subs(cdf_Tp,tp-
0.5*Tp_step_size));
        elseif ks==nof_Tp_steps

Pr_of_Tp(ks)=double(subs(cdf_Tp,Tp_max+0.5*Tp_step_size)-
subs(cdf_Tp,Tp_max-0.5*Tp_step_size));
    end
end

```

```

        tp=tp+Tp_step_size;
    end
    sum_tp=sum(Pr_of_Tp);
    Pr_of_Tp=Pr_of_Tp/sum_tp;
    TS_Tp=[Tp_min:Tp_step_size:Tp_max];
    %%
    for m=1:nof_segments
        run single_line_fault_segments
        run Rjb_calc
        run P_pulse_calc
        TS(cas_count,1)=M_of_TS;
        TS(cas_count,2)=Rjb;
        TS(cas_count,3)=R_rup;
        TS(cas_count,4)=Area_of_TS;
        TS(cas_count,5)=PA_of_TS;
        TS(cas_count,6)=W_of_TS;
        TS(cas_count,7)=PW_of_TS;
        TS(cas_count,8)=L_of_TS;
        TS(cas_count,9)=m;
        TS(cas_count,10)=1/nof_segments;
        TS(cas_count,11)=PM_of_TS;
        TS(cas_count,12)=activity_rate(i);
        TS(cas_count,13)=100+i;
        TS(cas_count,14)=sd_dir(m);
        TS(cas_count,15)=r_dir(m);
        TS(cas_count,16)=R_x;
        TS(cas_count,17)=F_HW;
        TS(cas_count,18)=z_tor;
        TS(cas_count,19)=dip_deg(i);
        TS(cas_count,20)=Cen_of_segs(m,3);
        TS(cas_count,21)=Ry0;
        TS_P_alpha(cas_count,1:num_alp_steps)=P_pu_alpha(m,:);
        TS_P_Tp(cas_count,1:nof_Tp_steps)=Pr_of_Tp;
        cas_count=cas_count+1;
    end
    clear P1_of_segs P2_of_segs P3_of_segs P4_of_segs
    Cen_of_segs H_dist_from_station epi_of_seg fault_cline_1 fault_cline_2
    sd_dir r_dir P_pu_rs P_pu_alpha Pr_of_Tp fault_cline_1 fault_cline_2 x_h
    y_h x_hc y_hc fi
    end
    case 2 % YC Model
        fault_M_min(i)=roundn(fault_data(13,i),-1);
        fault_bvalue(i)=fault_data(14,i);
        fault_Mchar(i)=roundn(bm*log10(fault_area(i))+am,-1);
        fault_M_max(i)=fault_Mchar(i)+0.25;
        beta=fault_bvalue(i)*log(10);
        dumm=fault_M_min(i);
        mag=roundn(dumm,-3);
        c_coeff=0.5*beta*exp(-beta*(fault_Mchar(i)-fault_M_min(i)-
1.25))/(1-exp(-beta*(fault_Mchar(i)-fault_M_min(i)-0.25)));
        dummy(1)=((1/(1+c_coeff))*beta*exp(-beta*(mag-
fault_M_min(i)))/(1-exp(-beta*(fault_Mchar(i)-fault_M_min(i)-
0.25))))*10^(1.5* mag +16.05)*0.0005;
        Mw(1)=mag;
        for k=2:int16((fault_Mchar(i)-0.25-fault_M_min(i))/0.001+1)
            dumm=mag+0.001;
            mag=roundn(dumm,-3);
            Mw(k)=mag;
            if k==int16((fault_Mchar(i)-0.25-fault_M_min(i))/0.001+1);
                dummy(k)=((1/(1+c_coeff))*beta*exp(-beta*(mag-
fault_M_min(i)))/(1-exp(-beta*(fault_Mchar(i)-fault_M_min(i)-
0.25))))*10^(1.5* mag +16.05)*0.0005;
            else

```

```

dummy(k)=(1/(1+c_coeff))*beta*exp(-beta*(mag-
fault_M_min(i)))/(1-exp(-beta*(fault_Mchar(i)-fault_M_min(i)-
0.25)))*10^(1.5* mag +16.05)*0.001;
end
end
for k=int16((fault_Mchar(i)-0.25-
fault_M_min(i))/0.001+2):int16((fault_M_max(i)-fault_M_min(i))/0.001+1)
if k==int16((fault_Mchar(i)-0.25-fault_M_min(i))/0.001+2);
dummy(k)=(1/(1+c_coeff))*beta*exp(-
beta*(fault_Mchar(i)-fault_M_min(i)-1.25))/(1-exp(-beta*(fault_Mchar(i)-
fault_M_min(i)-0.25)))*10^(1.5* mag +16.05)*0.0005;
else
dumm=mag+0.001;
mag=roundn(dumm,-3);
Mw(k)=mag;
dummy(k)=(1/(1+c_coeff))*beta*exp(-
beta*(fault_Mchar(i)-fault_M_min(i)-1.25))/(1-exp(-beta*(fault_Mchar(i)-
fault_M_min(i)-0.25)))*10^(1.5* mag +16.05)*0.001;
end
end
dummy(k+1)=(1/(1+c_coeff))*beta*exp(-beta*(fault_Mchar(i)-
fault_M_min(i)-1.25))/(1-exp(-beta*(fault_Mchar(i)-fault_M_min(i)-
0.25)))*10^(1.5* fault_M_max(i)+16.05)*0.0005;
dummy2=sum(dummy);
dumm=mag+0.001;
mag=roundn(dumm,-3);
Mw(k+1)=mag;
activity_rate(i)=mu(i)*fault_area(i)*1e10*slip_rate(i)/dummy2;
if i==1
Scs=7;
end
rcc=num2str(Scs);
rcs=num2str(Scs);
s_ex=strcat('F',rcc);
s_fx=strcat('F',rcs);
xlswrite(ex_input_data,activity_rate(i),'Input_Data',s_ex);
xlswrite(ex_input_data,fault_M_max(i),'Input_Data',s_fx);
Scs=Scs+20;
Scs=Scs+20;
M_steps=fault_M_stepsize(i);
if mod(fault_Mchar(i)-0.25-
fault_M_min(i),fault_M_stepsize(i))==0;
M_strt=fault_M_min(i);
else
M_strt=mod(fault_Mchar(i)-0.25-
fault_M_min(i),fault_M_stepsize(i))+fault_M_min(i);
end
M_fin=fault_Mchar(i)+0.25;
fault_M_start(i)=M_strt;
fault_M_finish(i)=M_fin;
syms mag real
dumm1=(1/(1+c_coeff))*beta*exp(-beta*(mag-fault_M_min(i)))/(1-
exp(-beta*(fault_Mchar(i)-fault_M_min(i)-0.25)));
cdf1=int(dumm1);
dumm2=(1/(1+c_coeff))*beta*exp(-beta*(fault_Mchar(i)-
fault_M_min(i)-1.25))/(1-exp(-beta*(fault_Mchar(i)-fault_M_min(i)-0.25)));
cdf2=dumm2*mag;
fault_nof_magnitudes(i)=int16((fault_M_finish(i)-
fault_M_start(i))/fault_M_stepsize(i))+1;
for k=1:fault_nof_magnitudes(i)
if k==1
M_of_TS=fault_M_start(i);
PM_of_TS=double(subs(cdf1,fault_M_start(i)+0.5*fault_M_stepsize(i))-
subs(cdf1,fault_M_start(i)));

```

```

elseif k<fault_nof_magnitudes(i)
    M_of_TS=fault_M_start(i)+(double(k)-
1)*fault_M_stepsize(i);
    if M_of_TS<fault_Mchar(i)-0.25

PM_of_TS=double(subs(cdf1,M_of_TS+0.5*fault_M_stepsize(i))-
subs(cdf1,M_of_TS-0.5*fault_M_stepsize(i)));
    elseif M_of_TS==fault_Mchar(i)-0.25

PM_of_TS=double(subs(cdf2,M_of_TS+0.5*fault_M_stepsize(i))-
subs(cdf2,M_of_TS)+subs(cdf1,M_of_TS)-subs(cdf1,M_of_TS-
0.5*fault_M_stepsize(i)));
    elseif M_of_TS>fault_Mchar(i)-0.25

PM_of_TS=double(subs(cdf2,M_of_TS+0.5*fault_M_stepsize(i))-
subs(cdf2,M_of_TS-0.5*fault_M_stepsize(i)));
    end
elseif k==fault_nof_magnitudes(i);
    M_of_TS=fault_M_start(i)+(double(k)-
1)*fault_M_stepsize(i);
    M_of_TS=fault_M_finish(i);
    PM_of_TS=double(subs(cdf2,fault_M_finish(i))-
subs(cdf2,fault_M_finish(i)-0.5*fault_M_stepsize(i)));
    end
    M_of_TS=roundn(M_of_TS,-6);
    dummy=roundn(M_of_TS,-2);
    Area_of_TS=10^(b*M_of_TS-a);
    PA_of_TS=1.0;
    PW_of_TS=1.0;
    %%
    if sqrt(Area_of_TS)>fault_width(i)
        W_of_TS=fault_width(i);
        nof_V_segments=1;
    else
        W_of_TS=sqrt(Area_of_TS);
        nof_V_segments=ceil(fault_width(i)/W_of_TS);
    end
    if nof_V_segments>nof_v_max_segments
        nof_V_segments=nof_v_max_segments;
    end
    L_of_TS=Area_of_TS/W_of_TS;
    if L_of_TS>fault_length(i)
        L_of_TS=fault_length(i);
        nof_H_segments=1;
    else
        nof_H_segments=ceil(fault_length(i)/L_of_TS);
    end
    if nof_H_segments>nof_h_max_segments
        nof_H_segments=nof_h_max_segments;
    end
    nof_segments=nof_H_segments*nof_V_segments;
    %%
    if nof_V_segments>1
        dist_v_btw_segments=(fault_width(i) - W_of_TS) /
(nof_V_segments - 1);
    else
        dist_v_btw_segments=0;
    end

    if nof_H_segments > 1
        dist_H_btw_segments = (fault_length(i) - L_of_TS) /
(nof_H_segments - 1);
    else
        dist_H_btw_segments = 0;
    end
end

```

```

%%
fault_cline_1(1,1)=fault_corners(1,1)+W_of_TS/2*fault_u(2,1);
fault_cline_1(1,2)=fault_corners(1,2)+W_of_TS/2*fault_u(2,2);
fault_cline_1(1,3)=fault_corners(1,3)+W_of_TS/2*fault_u(2,3);
    if nof_V_segments>1
        for vse=2:nof_V_segments
            fault_cline_1(vse,1)=fault_cline_1(vse-
1,1)+dist_v_btw_segments*fault_u(2,1);
            fault_cline_1(vse,2)=fault_cline_1(vse-
1,2)+dist_v_btw_segments*fault_u(2,2);
            fault_cline_1(vse,3)=fault_cline_1(vse-
1,3)+dist_v_btw_segments*fault_u(2,3);
        end
    end

fault_cline_2(1,1)=fault_corners(2,1)+W_of_TS/2*fault_u(2,1);
fault_cline_2(1,2)=fault_corners(2,2)+W_of_TS/2*fault_u(2,2);
fault_cline_2(1,3)=fault_corners(2,3)+W_of_TS/2*fault_u(2,3);
    if nof_V_segments>1
        for vse=2:nof_V_segments
            fault_cline_2(vse,1)=fault_cline_2(vse-
1,1)+dist_v_btw_segments*fault_u(2,1);
            fault_cline_2(vse,2)=fault_cline_2(vse-
1,2)+dist_v_btw_segments*fault_u(2,2);
            fault_cline_2(vse,3)=fault_cline_2(vse-
1,3)+dist_v_btw_segments*fault_u(2,3);
        end
    end
%%
for iv=1:nof_V_segments
    Cen_of_segs(iv,1)=fault_cline_1(iv,1) + (L_of_TS / 2) *
fault_u(1,1);
    Cen_of_segs(iv,2)=fault_cline_1(iv,2) + (L_of_TS / 2) *
fault_u(1,2);
    Cen_of_segs(iv,3)=fault_cline_1(iv,3) + (L_of_TS / 2) *
fault_u(1,3);
end
for ih=nof_V_segments+1:nof_segments
    Cen_of_segs(ih,1)=Cen_of_segs(ih-nof_V_segments,1) +
(dist_H_btw_segments) * fault_u(1,1);
    Cen_of_segs(ih,2)=Cen_of_segs(ih-nof_V_segments,2) +
(dist_H_btw_segments) * fault_u(1,2);
    Cen_of_segs(ih,3)=Cen_of_segs(ih-nof_V_segments,3) +
(dist_H_btw_segments) * fault_u(1,3);
end
%% Calculation of Probability Distribution of Pulse Period
Tp_min=0.2;
Tp_max=20.2;
tp=Tp_min;
Tp_step_size=0.2;
Tp_medi=exp(-5.73+0.99.*M_of_TS);
Tp_sigma=0.56;
syms Tp
dumm_Tp=(1/(Tp*Tp_sigma*(2*pi)^0.5))*(exp(-(log(Tp) - log
(Tp_medi))^2)/(2*Tp_sigma^2)));
cdf_Tp=int(dumm_Tp);
nof_Tp_steps=int16((Tp_max-Tp_min)/Tp_step_size)+1;
for ks=1:nof_Tp_steps
    if ks==1

```

```

Pr_of_Tp(ks)=double(subs(cdf_Tp,Tp_min+0.5*Tp_step_size)-
subs(cdf_Tp,Tp_min-0.45*Tp_step_size));
    elseif ks<nof_Tp_steps

Pr_of_Tp(ks)=double(subs(cdf_Tp,tp+0.5*Tp_step_size)-subs(cdf_Tp,tp-
0.5*Tp_step_size));
    elseif ks==nof_Tp_steps

Pr_of_Tp(ks)=double(subs(cdf_Tp,Tp_max+0.5*Tp_step_size)-
subs(cdf_Tp,Tp_max-0.5*Tp_step_size));
    end
    tp=tp+Tp_step_size;
end
sum_tp=sum(Pr_of_Tp);
suml(k)=sum_tp;
Pr_of_Tp=Pr_of_Tp/sum_tp;
TS_Tp=[Tp_min:Tp_step_size:Tp_max];
%%
for m=1:nof_segments
    run single_line_fault_segments
    run Rjb_calc
    run P_pulse_calc
    TS(cas_count,1)=M_of_TS;
    TS(cas_count,2)=Rjb;
    TS(cas_count,3)=R_rup;
    TS(cas_count,4)=Area_of_TS;
    TS(cas_count,5)=PA_of_TS;
    TS(cas_count,6)=W_of_TS;
    TS(cas_count,7)=PW_of_TS;
    TS(cas_count,8)=L_of_TS;
    TS(cas_count,9)=m;
    TS(cas_count,10)=1/nof_segments;
    TS(cas_count,11)=PM_of_TS;
    TS(cas_count,12)=activity_rate(i);
    TS(cas_count,13)=100+i;
    TS(cas_count,14)=sd_dir(m);
    TS(cas_count,15)=r_dir(m);
    TS(cas_count,16)=R_x;
    TS(cas_count,17)=F_HW;
    TS(cas_count,18)=z_tor;
    TS(cas_count,19)=dip_deg(i);
    TS(cas_count,20)=Cen_of_segs(m,3);
    TS(cas_count,21)=Ry0;
    TS_P_alpha(cas_count,1:num_alp_steps)=P_pu_alpha(m,:);
    TS_P_Tp(cas_count,1:nof_Tp_steps)=Pr_of_Tp;
    cas_count=cas_count+1;
end
clear P1_of_segs P2_of_segs P3_of_segs P4_of_segs
Cen_of_segs H_dist_from_station epi_of_seg fault_cline_1 fault_cline_2
sd_dir r_dir P_pu_alpha Pr_of_Tp fault_cline_1 fault_cline_2 x_h
y_h x_hc y_hc fi
end
case 3 % Pure characteristic
    fault_M_min(i)=roundn(fault_data(13,i),-1);
    fault_M_max(i)=roundn(fault_data(14,i),-1);
    fault_Mchar(i)=roundn(bm*log10(fault_area(i))+am,-1);
    dummm=fault_M_min(i)+0.0005;
    mag=roundn(dummm,-4);
    dummy(1)=((mag+0.0005)-(mag-0.0005))*10^(1.5*mag+16.05);
    Mw(1)=mag;
    for k=2:int16((fault_M_max(i)-fault_M_min(i))/0.001)
        dummm=mag+0.001;
        mag=roundn(dummm,-4);
        Mw(k)=mag;
    end
end

```

```

dummy(k) = ((mag+0.0005) - (mag-0.0005)) * 10^(1.5 * mag
+16.05);
end
dummy2 = sum(dummy);
dumm = mag + 0.001;
mag = roundn(dumm, -4);
Mw(k+1) = mag;
activity_rate(i) = mu(i) * fault_area(i) * 1e10 * slip_rate(i) / dummy2;
if i==1
    Scs = 7;
end
rcc = num2str(Scs);
rcs = num2str(Scs);
s_ex = strcat('F', rcc);
s_fx = strcat('F', rcs);
xlswrite(ex_input_data, activity_rate(i), 'Input_Data', s_ex);
xlswrite(ex_input_data, fault_M_max(i), 'Input_Data', s_fx);
Scs = Scs + 20;
Scs = Scs + 20;
M_steps = fault_M_stepsize(i);
M_strt = fault_M_min(i);
M_fin = fault_M_max(i);
fault_M_start(i) = M_strt;
fault_M_finish(i) = M_fin;
fault_nof_magnitudes(i) = double(int16((fault_M_finish(i) -
fault_M_start(i)) / fault_M_stepsize(i)) + 1);
for k = 1 : fault_nof_magnitudes(i)
    if k==1
        M_of_TS = fault_M_start(i);
        PM_of_TS = 1 / (2 * fault_nof_magnitudes(i));
    elseif k < fault_nof_magnitudes(i)
        M_of_TS = fault_M_start(i) + (double(k) -
1) * fault_M_stepsize(i);
        PM_of_TS = (1 / fault_nof_magnitudes(i));
    elseif k == fault_nof_magnitudes(i);
        M_of_TS = fault_M_finish(i);
        PM_of_TS = 1 / (2 * fault_nof_magnitudes(i));
    end
    M_of_TS = roundn(M_of_TS, -6);
    dummy = roundn(M_of_TS, -2);
    Area_of_TS = 10^(b * M_of_TS - a);
    PA_of_TS = 1.0;
    PW_of_TS = 1.0;
    %%
    if sqrt(Area_of_TS) > fault_width(i)
        W_of_TS = fault_width(i);
        nof_V_segments = 1;
    else
        W_of_TS = sqrt(Area_of_TS);
        nof_V_segments = ceil(fault_width(i) / W_of_TS);
    end
    if nof_V_segments > nof_v_max_segments
        nof_V_segments = nof_v_max_segments;
    end
    L_of_TS = Area_of_TS / W_of_TS;
    if L_of_TS > fault_length(i)
        L_of_TS = fault_length(i);
        nof_H_segments = 1;
    else
        nof_H_segments = ceil(fault_length(i) / L_of_TS);
    end
    if nof_H_segments > nof_h_max_segments
        nof_H_segments = nof_h_max_segments;
    end
    nof_segments = nof_H_segments * nof_V_segments;

```

```

%%
if nof_V_segments>1
    dist_v_btw_segments=(fault_width(i) - W_of_TS) /
(nof_V_segments - 1);
else
    dist_v_btw_segments=0;
end

if nof_H_segments > 1
    dist_H_btw_segments = (fault_length(i) - L_of_TS) /
(nof_H_segments - 1);
else
    dist_H_btw_segments = 0;
end
%%

fault_cline_1(1,1)=fault_corners(1,1)+W_of_TS/2*fault_u(2,1);
fault_cline_1(1,2)=fault_corners(1,2)+W_of_TS/2*fault_u(2,2);
fault_cline_1(1,3)=fault_corners(1,3)+W_of_TS/2*fault_u(2,3);
if nof_V_segments>1
    for vse=2:nof_V_segments
        fault_cline_1(vse,1)=fault_cline_1(vse-
1,1)+dist_v_btw_segments*fault_u(2,1);
        fault_cline_1(vse,2)=fault_cline_1(vse-
1,2)+dist_v_btw_segments*fault_u(2,2);
        fault_cline_1(vse,3)=fault_cline_1(vse-
1,3)+dist_v_btw_segments*fault_u(2,3);
    end
end

fault_cline_2(1,1)=fault_corners(2,1)+W_of_TS/2*fault_u(2,1);
fault_cline_2(1,2)=fault_corners(2,2)+W_of_TS/2*fault_u(2,2);
fault_cline_2(1,3)=fault_corners(2,3)+W_of_TS/2*fault_u(2,3);
if nof_V_segments>1
    for vse=2:nof_V_segments
        fault_cline_2(vse,1)=fault_cline_2(vse-
1,1)+dist_v_btw_segments*fault_u(2,1);
        fault_cline_2(vse,2)=fault_cline_2(vse-
1,2)+dist_v_btw_segments*fault_u(2,2);
        fault_cline_2(vse,3)=fault_cline_2(vse-
1,3)+dist_v_btw_segments*fault_u(2,3);
    end
end
%%
for iv=1:nof_V_segments
    Cen_of_segs(iv,1)=fault_cline_1(iv,1) + (L_of_TS / 2) *
fault_u(1,1);
    Cen_of_segs(iv,2)=fault_cline_1(iv,2) + (L_of_TS / 2) *
fault_u(1,2);
    Cen_of_segs(iv,3)=fault_cline_1(iv,3) + (L_of_TS / 2) *
fault_u(1,3);
end
for ih=nof_V_segments+1:nof_segments
    Cen_of_segs(ih,1)=Cen_of_segs(ih-nof_V_segments,1) +
(dist_H_btw_segments) * fault_u(1,1);
    Cen_of_segs(ih,2)=Cen_of_segs(ih-nof_V_segments,2) +
(dist_H_btw_segments) * fault_u(1,2);
    Cen_of_segs(ih,3)=Cen_of_segs(ih-nof_V_segments,3) +
(dist_H_btw_segments) * fault_u(1,3);
end

```

```

%% Calculation of Probability Distribution of Pulse Period
Tp_min=0.2;
Tp_max=20.2;
tp=Tp_min;
Tp_step_size=0.2;
Tp_medi=exp(-5.73+0.99.*M_of_TS);
Tp_sigma=0.56;
syms Tp
dumm_Tp=(1/(Tp*Tp_sigma*(2*pi)^0.5))*(exp(-(log(Tp) - log
(Tp_medi))^2)/(2*Tp_sigma^2)));
cdf_Tp=int(dumm_Tp);
nof_Tp_steps=int16((Tp_max-Tp_min)/Tp_step_size)+1;
for ks=1:nof_Tp_steps
    if ks==1

Pr_of_Tp(ks)=double(subs(cdf_Tp,Tp_min+0.5*Tp_step_size)-
subs(cdf_Tp,Tp_min-0.45*Tp_step_size));
        elseif ks<nof_Tp_steps

Pr_of_Tp(ks)=double(subs(cdf_Tp,tp+0.5*Tp_step_size)-subs(cdf_Tp,tp-
0.5*Tp_step_size));
                elseif ks==nof_Tp_steps

Pr_of_Tp(ks)=double(subs(cdf_Tp,Tp_max+0.5*Tp_step_size)-
subs(cdf_Tp,Tp_max-0.5*Tp_step_size));
                    end
                    tp=tp+Tp_step_size;
                end
                sum_tp=sum(Pr_of_Tp);
                Pr_of_Tp=Pr_of_Tp/sum_tp;
                TS_Tp=[Tp_min:Tp_step_size:Tp_max];
                %%
                for m=1:nof_segments
                    run single_line_fault_segments
                    run Rjb_calc
                    run P_pulse_calc
                    TS(cas_count,1)=M_of_TS;
                    TS(cas_count,2)=Rjb;
                    TS(cas_count,3)=R_rup;
                    TS(cas_count,4)=Area_of_TS;
                    TS(cas_count,5)=PA_of_TS;
                    TS(cas_count,6)=W_of_TS;
                    TS(cas_count,7)=PW_of_TS;
                    TS(cas_count,8)=L_of_TS;
                    TS(cas_count,9)=m;
                    TS(cas_count,10)=1/nof_segments;
                    TS(cas_count,11)=PM_of_TS;
                    TS(cas_count,12)=activity_rate(i);
                    TS(cas_count,13)=100+i;
                    TS(cas_count,14)=sd_dir(m);
                    TS(cas_count,15)=r_dir(m);
                    TS(cas_count,16)=R_x;
                    TS(cas_count,17)=F_HW;
                    TS(cas_count,18)=z_tor;
                    TS(cas_count,19)=dip_deg(i);
                    TS(cas_count,20)=Cen_of_segs(m,3);
                    TS(cas_count,21)=Ry0;
                    TS_P_alpha(cas_count,1:num_alp_steps)=P_pu_alpha(m,:);
                    TS_P_Tp(cas_count,1:nof_Tp_steps)=Pr_of_Tp;
                    cas_count=cas_count+1;
                end
                clear P1_of_segs P2_of_segs P3_of_segs P4_of_segs
                Cen_of_segs H_dist_from_station epi_of_seg fault_cline_1 fault_cline_2
                sd_dir r_dir P_pu_rs P_pu_alpha Pr_of_Tp fault_cline_1 fault_cline_2 x_h
                y_h x_hc y_hc fi

```

```

        end

    end

    Distance_metric='Rjb';
    eps_f_min(i)=-5;
    if mod(eps_f_min(i)*10,2)==0;
        eps_f_min(i)=eps_f_min(i)-.1;
    else
        eps_f_min(i)=eps_f_min(i);
    end
    eps_f_max(i)=5;
    if mod(eps_f_max(i)*10,2)==0;
        eps_f_max(i)=eps_f_max(i)+.1;
    else
        eps_f_max(i)=eps_f_max(i);
    end
end
clear mag cdf
disp('Task Finished');

```

### - single\_line\_fault\_segments File

```

P1_of_segs(m,1)=Cen_of_segs(m,1)-(L_of_TS/2)*fault_u(1,1)-
(W_of_TS/2)*fault_u(2,1);
P1_of_segs(m,2)=Cen_of_segs(m,2)-(L_of_TS/2)*fault_u(1,2)-
(W_of_TS/2)*fault_u(2,2);
P1_of_segs(m,3)=Cen_of_segs(m,3)-(L_of_TS/2)*fault_u(1,3)-
(W_of_TS/2)*fault_u(2,3);

P2_of_segs(m,1)=Cen_of_segs(m,1)+(L_of_TS/2)*fault_u(1,1)-
(W_of_TS/2)*fault_u(2,1);
P2_of_segs(m,2)=Cen_of_segs(m,2)+(L_of_TS/2)*fault_u(1,2)-
(W_of_TS/2)*fault_u(2,2);
P2_of_segs(m,3)=Cen_of_segs(m,3)+(L_of_TS/2)*fault_u(1,3)-
(W_of_TS/2)*fault_u(2,3);

P3_of_segs(m,1)=Cen_of_segs(m,1)-
(L_of_TS/2)*fault_u(1,1)+(W_of_TS/2)*fault_u(2,1);
P3_of_segs(m,2)=Cen_of_segs(m,2)-
(L_of_TS/2)*fault_u(1,2)+(W_of_TS/2)*fault_u(2,2);
P3_of_segs(m,3)=Cen_of_segs(m,3)-
(L_of_TS/2)*fault_u(1,3)+(W_of_TS/2)*fault_u(2,3);

P4_of_segs(m,1)=Cen_of_segs(m,1)+(L_of_TS/2)*fault_u(1,1)+(W_of_TS/2)*fault
_u(2,1);
P4_of_segs(m,2)=Cen_of_segs(m,2)+(L_of_TS/2)*fault_u(1,2)+(W_of_TS/2)*fault
_u(2,2);
P4_of_segs(m,3)=Cen_of_segs(m,3)+(L_of_TS/2)*fault_u(1,3)+(W_of_TS/2)*fault
_u(2,3);

H_dist_from_station(m,1)=((station(j,1)-P1_of_segs(m,1))^2+(station(j,2)-
P1_of_segs(m,2))^2)^0.5;
H_dist_from_station(m,2)=((station(j,1)-P2_of_segs(m,1))^2+(station(j,2)-
P2_of_segs(m,2))^2)^0.5;
H_dist_from_station(m,3)=((station(j,1)-P3_of_segs(m,1))^2+(station(j,2)-
P3_of_segs(m,2))^2)^0.5;
H_dist_from_station(m,4)=((station(j,1)-P4_of_segs(m,1))^2+(station(j,2)-
P4_of_segs(m,2))^2)^0.5;

Dist_from_station(m,1)=((station(j,1)-P1_of_segs(m,1))^2+(station(j,2)-
P1_of_segs(m,2))^2+(station(j,3)-P1_of_segs(m,3))^2)^0.5;
Dist_from_station(m,2)=((station(j,1)-P2_of_segs(m,1))^2+(station(j,2)-
P2_of_segs(m,2))^2+(station(j,3)-P2_of_segs(m,3))^2)^0.5;

```

```

Dist_from_station(m,3)=(station(j,1)-P3_of_segs(m,1))^2+(station(j,2)-
P3_of_segs(m,2))^2+(station(j,3)-P3_of_segs(m,3))^2)^0.5;
Dist_from_station(m,4)=(station(j,1)-P4_of_segs(m,1))^2+(station(j,2)-
P4_of_segs(m,2))^2+(station(j,3)-P4_of_segs(m,3))^2)^0.5;

```

### - Rjb\_calc File

```

min_distance(m)=min([H_dist_from_station(m,1);H_dist_from_station(m,2);H_dist_from_station(m,3);H_dist_from_station(m,4)]);

```

```

u_btw_stat(1,1)=(station(j,1)-P1_of_segs(m,1))/H_dist_from_station(m,1);
u_btw_stat(1,2)=(station(j,2)-P1_of_segs(m,2))/H_dist_from_station(m,1);

```

```

u_btw_stat(2,1)=(station(j,1)-P2_of_segs(m,1))/H_dist_from_station(m,2);
u_btw_stat(2,2)=(station(j,2)-P2_of_segs(m,2))/H_dist_from_station(m,2);

```

```

u_btw_stat(3,1)=(station(j,1)-P3_of_segs(m,1))/H_dist_from_station(m,3);
u_btw_stat(3,2)=(station(j,2)-P3_of_segs(m,2))/H_dist_from_station(m,3);

```

```

u_btw_stat(4,1)=(station(j,1)-P4_of_segs(m,1))/H_dist_from_station(m,4);
u_btw_stat(4,2)=(station(j,2)-P4_of_segs(m,2))/H_dist_from_station(m,4);

```

```

H_width=((P1_of_segs(m,1)-P3_of_segs(m,1))^2+(P1_of_segs(m,2)-
P3_of_segs(m,2))^2)^0.5;

```

```

u_btw_1_2(1)=fault_u(1,1);
u_btw_1_2(2)=fault_u(1,2);

```

```

if H_width==0
    H_cos_angle_1=u_btw_stat(1,1)*u_btw_1_2(1)+
u_btw_stat(1,2)*u_btw_1_2(2);
    H_distance_at_1_2=H_cos_angle_1*H_dist_from_station(m,1);
    if H_distance_at_1_2 >= 0 && H_distance_at_1_2 <= L_of_TS;
        perp1_x = P1_of_segs(m,1) + H_distance_at_1_2 * u_btw_1_2(1);
        perp1_y = P1_of_segs(m,2) + H_distance_at_1_2 * u_btw_1_2(2);
        perp2_x = P3_of_segs(m,1) + H_distance_at_1_2 * u_btw_1_2(1);
        perp2_y = P3_of_segs(m,2) + H_distance_at_1_2 * u_btw_1_2(2);
        shortest1 = ((perp1_x - station(j,1)) ^ 2 + (perp1_y -
station(j,2)) ^ 2) ^ 0.5;
        shortest2 = ((perp2_x - station(j,1)) ^ 2 + (perp2_y -
station(j,2)) ^ 2) ^ 0.5;
        if shortest1 >= shortest2
            Rjb = shortest2;
        else
            Rjb = shortest1;
        end
    else
        Rjb = min_distance(m);
    end
end

```

```

else
    u_btw_1_3(1)=(P3_of_segs(m,1)-P1_of_segs(m,1))/H_width;
    u_btw_1_3(2)=(P3_of_segs(m,2)-P1_of_segs(m,2))/H_width;

```

```

H_cos_angle_1=(u_btw_stat(1,1)*u_btw_1_2(1)+u_btw_stat(1,2)*u_btw_1_2(2));

```

```

H_cos_angle_2=(u_btw_stat(1,1)*u_btw_1_3(1)+u_btw_stat(1,2)*u_btw_1_3(2));
H_distance_at_1_2=H_cos_angle_1*H_dist_from_station(m,1);
H_distance_at_1_3=H_cos_angle_2*H_dist_from_station(m,1);
if H_distance_at_1_2 >= 0 & H_distance_at_1_2 <= L_of_TS &
H_distance_at_1_3>=0 & H_distance_at_1_3<=H_width;
    Rjb=0.0;

```

```

elseif H_distance_at_1_2 >= 0 & H_distance_at_1_2 <= L_of_TS;
    perp1_x=P1_of_segs(m,1)+H_distance_at_1_2*u_btw_1_2(1);
    perp1_y=P1_of_segs(m,2)+H_distance_at_1_2*u_btw_1_2(2);
    perp2_x=P3_of_segs(m,1)+H_distance_at_1_2*u_btw_1_2(1);

```

```

        perp2_y=P3_of_segs(m,2)+H_distance_at_1_2*u_btw_1_2(2);
        shortest1 = ((perp1_x - station(j,1)) ^ 2 + (perp1_y -
station(j,2)) ^ 2) ^ 0.5;
        shortest2 = ((perp2_x - station(j,1)) ^ 2 + (perp2_y -
station(j,2)) ^ 2) ^ 0.5;
        Rjb=min([shortest1;shortest2]);
    elseif H_distance_at_1_3 >= 0 & H_distance_at_1_3 <= H_width;
        perp3_x=P1_of_segs(m,1)+H_distance_at_1_3*u_btw_1_3(1);
        perp3_y=P1_of_segs(m,2)+H_distance_at_1_3*u_btw_1_3(2);
        perp4_x=P2_of_segs(m,1)+H_distance_at_1_3*u_btw_1_3(1);
        perp4_y=P2_of_segs(m,2)+H_distance_at_1_3*u_btw_1_3(2);
        shortest3 = ((perp3_x - station(j,1)) ^ 2 + (perp3_y -
station(j,2)) ^ 2) ^ 0.5;
        shortest4 = ((perp4_x - station(j,1)) ^ 2 + (perp4_y -
station(j,2)) ^ 2) ^ 0.5;
        Rjb=min([shortest3;shortest4]);
    else
        Rjb=min_distance(m);
        if Rjb<0.001
            Rjb=0.0;
        end
    end
end
end
%% R_rup Calculation
tt=(norm_vectr(1,1)*(fault_corners(1,1)-
station(j,1))+norm_vectr(1,2)*(fault_corners(1,2)-
station(j,2))+norm_vectr(1,3)*(fault_corners(1,3)-
station(j,3)))/(norm_vectr(1,1)^2+norm_vectr(1,2)^2+norm_vectr(1,3)^2);
x_h=norm_vectr(1,1)*tt+station(j,1);
y_h=norm_vectr(1,2)*tt+station(j,2);
z_h=norm_vectr(1,3)*tt+station(j,3);
ver_p=[x_h y_h z_h];
vec1=P1_of_segs(m,:)-ver_p;
vec2=P2_of_segs(m,:)-ver_p;
vec3=P3_of_segs(m,:)-ver_p;
vec4=P4_of_segs(m,:)-ver_p;
cros1=cross(vec1,vec2);
cros2=cross(vec1,vec3);
cros3=cross(vec2,vec4);
cros4=cross(vec3,vec4);
area1=(cros1(1)^2+cros1(2)^2+cros1(3)^2)^0.5;
area2=(cros2(1)^2+cros2(2)^2+cros2(3)^2)^0.5;
area3=(cros3(1)^2+cros3(2)^2+cros3(3)^2)^0.5;
area4=(cros4(1)^2+cros4(2)^2+cros4(3)^2)^0.5;

area_vp=(area1+area2+area3+area4)/2;

vec_edge12=P2_of_segs(m,:)-P1_of_segs(m,:);
vec_edge13=P3_of_segs(m,:)-P1_of_segs(m,:);
vec_edge42=P2_of_segs(m,:)-P4_of_segs(m,:);
vec_edge43=P3_of_segs(m,:)-P4_of_segs(m,:);

cros_seg1=cross(vec_edge12,vec_edge13);
cros_seg2=cross(vec_edge42,vec_edge43);

area_seg1=(cros_seg1(1)^2+cros_seg1(2)^2+cros_seg1(3)^2)^0.5;
area_seg2=(cros_seg2(1)^2+cros_seg2(2)^2+cros_seg2(3)^2)^0.5;

area_seg=(area_seg1+area_seg2)/2;
%%%%%%%%%%%%%%%%%%%%%%%%%%%%%%%%%%%%%%%%%%%%%%%%%%%%%%%%%%%%%%%%%%%%%%%%
cof_rup_12=P2_of_segs(m,:)-P1_of_segs(m,:);
tt=(cof_rup_12(1)*ver_p(1,1)-cof_rup_12(1)*
P1_of_segs(m,1)+cof_rup_12(2)*ver_p(1,2)-cof_rup_12(2)*
P1_of_segs(m,2)+cof_rup_12(3)*ver_p(1,3)-cof_rup_12(3)*
P1_of_segs(m,3))/(cof_rup_12(1)^2+cof_rup_12(2)^2+cof_rup_12(3)^2);

```

```

x_h_12=cof_rup_12(1)*tt+P1_of_segs(m,1);
y_h_12=cof_rup_12(2)*tt+P1_of_segs(m,2);
z_h_12=cof_rup_12(3)*tt+P1_of_segs(m,3);
cord_pver_12=[x_h_12 y_h_12 z_h_12];
l_seg12=sqrt(dot(cof_rup_12,cof_rup_12));
l1_seg12=sqrt(dot((cord_pver_12-P1_of_segs(m,:)),(cord_pver_12-
P1_of_segs(m,:))));
l2_seg12=sqrt(dot((cord_pver_12-P2_of_segs(m,:)),(cord_pver_12-
P2_of_segs(m,:))));
%%%%%%%%%%%%%%%%%%%%%%%%%%%%%%%%%%%%%%%%%%%%%%%%%%%%%%%%%%%%%%%%%%%%%%%%
cof_rup_13=P3_of_segs(m,:)-P1_of_segs(m,:);
tt=(cof_rup_13(1)*ver_p(1,1)-cof_rup_13(1)*
P1_of_segs(m,1)+cof_rup_13(2)*ver_p(1,2)-cof_rup_13(2)*
P1_of_segs(m,2)+cof_rup_13(3)*ver_p(1,3)-cof_rup_13(3)*
P1_of_segs(m,3))/(cof_rup_13(1)^2+cof_rup_13(2)^2+cof_rup_13(3)^2);
x_h_13=cof_rup_13(1)*tt+P1_of_segs(m,1);
y_h_13=cof_rup_13(2)*tt+P1_of_segs(m,2);
z_h_13=cof_rup_13(3)*tt+P1_of_segs(m,3);
cord_pver_13=[x_h_13 y_h_13 z_h_13];
l_seg13=sqrt(dot(cof_rup_13,cof_rup_13));
l1_seg13=sqrt(dot((cord_pver_13-P1_of_segs(m,:)),(cord_pver_13-
P1_of_segs(m,:))));
l2_seg13=sqrt(dot((cord_pver_13-P3_of_segs(m,:)),(cord_pver_13-
P3_of_segs(m,:))));
%%%%%%%%%%%%%%%%%%%%%%%%%%%%%%%%%%%%%%%%%%%%%%%%%%%%%%%%%%%%%%%%%%%%%%%%
cof_rup_34=P4_of_segs(m,:)-P3_of_segs(m,:);
tt=(cof_rup_34(1)*ver_p(1,1)-cof_rup_34(1)*
P3_of_segs(m,1)+cof_rup_34(2)*ver_p(1,2)-cof_rup_34(2)*
P3_of_segs(m,2)+cof_rup_34(3)*ver_p(1,3)-cof_rup_34(3)*
P3_of_segs(m,3))/(cof_rup_34(1)^2+cof_rup_34(2)^2+cof_rup_34(3)^2);
x_h_34=cof_rup_34(1)*tt+P3_of_segs(m,1);
y_h_34=cof_rup_34(2)*tt+P3_of_segs(m,2);
z_h_34=cof_rup_34(3)*tt+P3_of_segs(m,3);
cord_pver_34=[x_h_34 y_h_34 z_h_34];
%%%%%%%%%%%%%%%%%%%%%%%%%%%%%%%%%%%%%%%%%%%%%%%%%%%%%%%%%%%%%%%%%%%%%%%%
cof_rup_24=P4_of_segs(m,:)-P2_of_segs(m,:);
tt=(cof_rup_24(1)*ver_p(1,1)-cof_rup_24(1)*
P2_of_segs(m,1)+cof_rup_24(2)*ver_p(1,2)-cof_rup_24(2)*
P2_of_segs(m,2)+cof_rup_24(3)*ver_p(1,3)-cof_rup_24(3)*
P2_of_segs(m,3))/(cof_rup_24(1)^2+cof_rup_24(2)^2+cof_rup_24(3)^2);
x_h_24=cof_rup_24(1)*tt+P2_of_segs(m,1);
y_h_24=cof_rup_24(2)*tt+P2_of_segs(m,2);
z_h_24=cof_rup_24(3)*tt+P2_of_segs(m,3);
cord_pver_24=[x_h_24 y_h_24 z_h_24];
%%%%%%%%%%%%%%%%%%%%%%%%%%%%%%%%%%%%%%%%%%%%%%%%%%%%%%%%%%%%%%%%%%%%%%%%
if abs(area_vp-area_seg)<=0.001
    R_rup=((station(j,1)-x_h)^2+(station(j,2)-y_h)^2+(station(j,3)-
z_h)^2)^0.5;
elseif l1_seg12<=l_seg12 && l2_seg12<=l_seg12
    R_rup12=sqrt(dot((station(j,:)-cord_pver_12),(station(j,:)-
cord_pver_12)));
    R_rup34=sqrt(dot((station(j,:)-cord_pver_34),(station(j,:)-
cord_pver_34)));
    R_rup=min(R_rup12,R_rup34);
elseif l1_seg13<=l_seg13 && l2_seg13<=l_seg13
    R_rup13=sqrt(dot((station(j,:)-cord_pver_13),(station(j,:)-
cord_pver_13)));
    R_rup24=sqrt(dot((station(j,:)-cord_pver_24),(station(j,:)-
cord_pver_24)));
    R_rup=min(R_rup13,R_rup24);
else
    R_rup1=sqrt(dot((station(j,:)-P1_of_segs(m,:)),(station(j,:)-
P1_of_segs(m,:))));
    R_rup2=sqrt(dot((station(j,:)-P2_of_segs(m,:)),(station(j,:)-
P2_of_segs(m,:))));

```

```

    R_rup3=sqrt(dot((station(j,:)-P3_of_segs(m,:)),(station(j,:)-
P3_of_segs(m,:))));
    R_rup4=sqrt(dot((station(j,:)-P4_of_segs(m,:)),(station(j,:)-
P4_of_segs(m,:))));
    R_rup_corners=[R_rup1,R_rup2,R_rup3,R_rup4];
    R_rup=min(R_rup_corners);
end

%% Calculation of Ry0
aa=P1_of_segs(m,1)-P2_of_segs(m,1);
bb=P1_of_segs(m,2)-P2_of_segs(m,2);
cc=P1_of_segs(m,3)-P2_of_segs(m,3);
tt=(aa*station(j,1)-aa* P1_of_segs(m,1)+bb*station(j,2)-bb*
P1_of_segs(m,2))/(aa^2+bb^2);
xc_h=aa*tt+P1_of_segs(m,1);
yc_h=bb*tt+P1_of_segs(m,2);

cen_of_segment=(P1_of_segs(m,:)+P2_of_segs(m,:))/2;
Ry_dummy=((xc_h-cen_of_segment(1,1))^2+(yc_h-cen_of_segment(1,2))^2)^0.5;
Ry0=Ry_dummy-L_of_TS/2;
if Ry0<0
    Ry0=0;
end

%% Calculation of Rx
cof_rup_u=P2_of_segs(m,:)-P1_of_segs(m,:);
tt=(cof_rup_u(1)*station(j,1)-cof_rup_u(1)*
P1_of_segs(m,1)+cof_rup_u(2)*station(j,2)-cof_rup_u(2)*
P1_of_segs(m,2)+cof_rup_u(3)*station(j,3)-cof_rup_u(3)*
P1_of_segs(m,3))/(cof_rup_u(1)^2+cof_rup_u(2)^2+cof_rup_u(3)^2);
x_h_rup_u=cof_rup_u(1)*tt+P1_of_segs(m,1);
y_h_rup_u=cof_rup_u(2)*tt+P1_of_segs(m,2);
z_h_rup_u=cof_rup_u(3)*tt+P1_of_segs(m,3);

cord_pver_u=[x_h_rup_u y_h_rup_u z_h_rup_u];
%%%%%%%%%%%%%%%%%%%%%%%%%%%%%%%%%%%%%%%%%%%%%%%%%%%%%%%%%%%%%%%%%%%%%%%%
cof_rup_d=P4_of_segs(m,:)-P3_of_segs(m,:);

tt=(cof_rup_d(1)*station(j,1)-cof_rup_d(1)*
P3_of_segs(m,1)+cof_rup_d(2)*station(j,2)-cof_rup_d(2)*
P3_of_segs(m,2)+cof_rup_d(3)*station(j,3)-cof_rup_d(3)*
P3_of_segs(m,3))/(cof_rup_d(1)^2+cof_rup_d(2)^2+cof_rup_d(3)^2);
x_h_rup_d=cof_rup_d(1)*tt+P3_of_segs(m,1);
y_h_rup_d=cof_rup_d(2)*tt+P3_of_segs(m,2);
z_h_rup_d=cof_rup_d(3)*tt+P3_of_segs(m,3);

cord_pver_d=[x_h_rup_d y_h_rup_d z_h_rup_d];
R_x_d=sqrt((station(j,1)-cord_pver_d(1,1))^2+(station(j,2)-
cord_pver_d(1,2))^2);
R_x_u=sqrt((station(j,1)-cord_pver_u(1,1))^2+(station(j,2)-
cord_pver_u(1,2))^2);
R_ud=sqrt((cord_pver_d(1,1)-cord_pver_u(1,1))^2+(cord_pver_d(1,2)-
cord_pver_u(1,2))^2);

R_x=R_x_u;

if dip_deg(i)~=90 && abs(R_x_d-R_x_u-R_ud)<0.001
    R_x=-1*R_x;
end
z_tor=P1_of_segs(m,3);
if R_x>=0
    F_HW=1;
else
    F_HW=0;
    Ry0=0;
end

```

## - P\_pulse\_calc File

```

%% Calculation for Directivity Parameters for Strike Slip Faults
if SS==1
    kks=m-nof_V_segments*(ceil(m/(nof_V_segments))-1);
    aa=fault_cline_2(kks,1)-fault_cline_1(kks,1);
    bb=fault_cline_2(kks,2)-fault_cline_1(kks,2);
    cc=fault_cline_2(kks,3)-fault_cline_1(kks,3);
    tt=(aa*station(j,1)-aa*fault_cline_1(kks,1)+bb*station(j,2)-bb*
    fault_cline_1(kks,2))/(aa^2+bb^2);
    x_h(m)=aa*tt+fault_cline_1(kks,1);
    y_h(m)=bb*tt+fault_cline_1(kks,2);
    epi_of_seg(m,:)=Cen_of_segs(m,:);
    epi_of_seg(m,3)=0;
    sd_dir(m)=((epi_of_seg(m,1)-x_h(m))^2+(epi_of_seg(m,2)-y_h(m))^2)^0.5;
    if sd_dir(m)>L_of_TS/2
        sd_dir(m)=L_of_TS/2;
    end
    r_dir(m)=R_rup;
    P_pu_rs(m)=1/(1+exp(0.642+0.167*r_dir(m)-0.075*sd_dir(m)));
else
    % Calculation for Directivity Parameters for Non-Strike Slip Faults
    tt=(norm_vectr(1,1)*(fault_corners(1,1)-
    station(j,1))+norm_vectr(1,2)*(fault_corners(1,2)-
    station(j,2))+norm_vectr(1,3)*(fault_corners(1,3)-
    station(j,3)))/(norm_vectr(1,1)^2+norm_vectr(1,2)^2+norm_vectr(1,3)^2);
    x_h(m)=norm_vectr(1,1)*tt+station(j,1);
    y_h(m)=norm_vectr(1,2)*tt+station(j,2);
    z_h(m)=norm_vectr(1,3)*tt+station(j,3);

    kks=m-nof_V_segments*(ceil(m/(nof_V_segments))-1);

    aa=fault_cline_2(kks,1)-fault_cline_1(kks,1);
    bb=fault_cline_2(kks,2)-fault_cline_1(kks,2);
    cc=fault_cline_2(kks,3)-fault_cline_1(kks,3);
    tt=(aa*x_h(m)-aa*fault_cline_1(kks,1)+bb*y_h(m)-bb*
    fault_cline_1(kks,2)+cc*z_h(m)-cc*fault_cline_1(kks,3))/(aa^2+bb^2+cc^2);
    x_hc(m)=aa*tt+fault_cline_1(kks,1);
    y_hc(m)=bb*tt+fault_cline_1(kks,2);
    z_hc(m)=cc*tt+fault_cline_1(kks,3);

    r_fi(m)=((x_hc(m)-station(j,1))^2+(y_hc(m)-station(j,2))^2+(z_hc(m)-
    station(j,3))^2)^0.5;
    d_fi(m)=((x_hc(m)-Cen_of_segs(m,1))^2+(y_hc(m)-
    Cen_of_segs(m,2))^2+(z_hc(m)-Cen_of_segs(m,3))^2)^0.5;

    sd_dir(m)=((x_hc(m)-x_h(m))^2+(y_hc(m)-y_h(m))^2+(z_hc(m)-
    z_h(m))^2)^0.5;
    r_dir(m)=R_rup;
    fi(m)=(atan(r_fi(m)/d_fi(m)))*180/pi;
    P_pu_rs(m)=1/(1+exp(0.128+0.055*r_dir(m)-0.061*sd_dir(m)+0.036*fi(m)));
end
alpha=[0 90];
num_alp_steps=length(alpha);
if SS==1
    P_alpha=min(0.67,0.67-0.0041*(77.5-alpha));
else
    P_alpha=min(0.53,0.53-0.0041*(70.2-alpha));
end
P_pu_alpha(m,:)= P_pu_rs(m)*P_alpha;

```



## APPENDIX C

### LIST OF PULSE-TYPE AND NON-PULSE-TYPE NEAR-FAULT GROUND MOTIONS

Table C. 1 List of near-fault pulse type ground motions (Last access 20/09/2016)

Seq_Num	Earthquake Name	Station Name	Mw	R_rup	I_Direct
143	Tabas, Iran	Tabas	7.35	2.05	1
159	Imperial Valley-06	Agrarias	6.53	0.65	1
161	Imperial Valley-06	Brawley Airport	6.53	10.42	1
170	Imperial Valley-06	EC County Center FF	6.53	7.31	1
171	Imperial Valley-06	El Centro - Meloland Geot. Array	6.53	0.07	1
173	Imperial Valley-06	El Centro Array #10	6.53	8.6	1
178	Imperial Valley-06	El Centro Array #3	6.53	12.85	1
179	Imperial Valley-06	El Centro Array #4	6.53	7.05	1
180	Imperial Valley-06	El Centro Array #5	6.53	3.95	1
181	Imperial Valley-06	El Centro Array #6	6.53	1.35	1
182	Imperial Valley-06	El Centro Array #7	6.53	0.56	1
184	Imperial Valley-06	El Centro Differential Array	6.53	5.09	1
185	Imperial Valley-06	Holtville Post Office	6.53	7.5	1
285	Irpinia, Italy-01	Bagnoli Irpinio	6.9	8.18	1
451	Morgan Hill	Coyote Lake Dam - Southwest Abutment	6.19	0.53	1
459	Morgan Hill	Gilroy Array #6	6.19	9.87	1
723	Superstition Hills-02	Parachute Test Site	6.54	0.95	1
764	Loma Prieta	Gilroy - Historic Bldg.	6.93	10.97	1
766	Loma Prieta	Gilroy Array #2	6.93	11.07	1
767	Loma Prieta	Gilroy Array #3	6.93	12.82	1
802	Loma Prieta	Saratoga - Aloha Ave	6.93	8.5	1
803	Loma Prieta	Saratoga - W Valley Coll.	6.93	9.31	1
900	Landers	Yermo Fire Station	7.28	23.62	1
982	Northridge-01	Jensen Filter Plant Administrative Building	6.69	5.43	1
983	Northridge-01	Jensen Filter Plant Generator Building	6.69	5.43	1
1004	Northridge-01	LA - Sepulveda VA Hospital	6.69	8.44	1
1013	Northridge-01	LA Dam	6.69	5.92	1
1044	Northridge-01	Newhall - Fire Sta	6.69	5.92	1
1045	Northridge-01	Newhall - W Pico Canyon Rd.	6.69	5.48	1
1052	Northridge-01	Pacoima Kagel Canyon	6.69	7.26	1

Table C.1 (Continued)

1054	Northridge-01	Pardee - SCE	6.69	7.46	1
1063	Northridge-01	Rinaldi Receiving Sta	6.69	6.5	1
1084	Northridge-01	Sylmar - Converter Sta	6.69	5.35	1
1085	Northridge-01	Sylmar - Converter Sta East	6.69	5.19	1
1086	Northridge-01	Sylmar - Olive View Med FF	6.69	5.3	1
1106	Kobe, Japan	KJMA	6.9	0.96	1
1114	Kobe, Japan	Port Island (0 m)	6.9	3.31	1
1119	Kobe, Japan	Takarazuka	6.9	0.27	1
1120	Kobe, Japan	Takatori	6.9	1.47	1
1148	Kocaeli, Turkey	Arcelik	7.51	13.49	1
1161	Kocaeli, Turkey	Gebze	7.51	10.92	1
1176	Kocaeli, Turkey	Yarimca	7.51	4.83	1
1182	Chi-Chi, Taiwan	CHY006	7.62	9.76	1
1193	Chi-Chi, Taiwan	CHY024	7.62	9.62	1
1244	Chi-Chi, Taiwan	CHY101	7.62	9.94	1
1476	Chi-Chi, Taiwan	TCU029	7.62	28.04	1
1480	Chi-Chi, Taiwan	TCU036	7.62	19.83	1
1481	Chi-Chi, Taiwan	TCU038	7.62	25.42	1
1482	Chi-Chi, Taiwan	TCU039	7.62	19.89	1
1483	Chi-Chi, Taiwan	TCU040	7.62	22.06	1
1485	Chi-Chi, Taiwan	TCU045	7.62	26	1
1486	Chi-Chi, Taiwan	TCU046	7.62	16.74	1
1489	Chi-Chi, Taiwan	TCU049	7.62	3.76	1
1491	Chi-Chi, Taiwan	TCU051	7.62	7.64	1
1492	Chi-Chi, Taiwan	TCU052	7.62	0.66	1
1493	Chi-Chi, Taiwan	TCU053	7.62	5.95	1
1496	Chi-Chi, Taiwan	TCU056	7.62	10.48	1
1498	Chi-Chi, Taiwan	TCU059	7.62	17.11	1
1501	Chi-Chi, Taiwan	TCU063	7.62	9.78	1
1502	Chi-Chi, Taiwan	TCU064	7.62	16.59	1
1503	Chi-Chi, Taiwan	TCU065	7.62	0.57	1
1505	Chi-Chi, Taiwan	TCU068	7.62	0.32	1
1510	Chi-Chi, Taiwan	TCU075	7.62	0.89	1
1511	Chi-Chi, Taiwan	TCU076	7.62	2.74	1
1515	Chi-Chi, Taiwan	TCU082	7.62	5.16	1
1519	Chi-Chi, Taiwan	TCU087	7.62	6.98	1
1528	Chi-Chi, Taiwan	TCU101	7.62	2.11	1
1529	Chi-Chi, Taiwan	TCU102	7.62	1.49	1
1530	Chi-Chi, Taiwan	TCU103	7.62	6.08	1
1531	Chi-Chi, Taiwan	TCU104	7.62	12.87	1
1548	Chi-Chi, Taiwan	TCU128	7.62	13.13	1
1550	Chi-Chi, Taiwan	TCU136	7.62	8.27	1
1602	Duzce, Turkey	Bolu	7.14	12.04	1
2114	Denali, Alaska	TAPS Pump Station #10	7.9	2.74	1

Table C.1 (Continued)

2734	Chi-Chi, Taiwan-04	CHY074	6.2	6.2	1
3473	Chi-Chi, Taiwan-06	TCU078	6.3	11.52	1
3475	Chi-Chi, Taiwan-06	TCU080	6.3	10.2	1
3965	Tottori, Japan	TTR008	6.61	6.88	1
4040	Bam, Iran	Bam	6.6	1.7	1
4065	Parkfield-02, CA	PARKFIELD - EADES	6	2.85	1
4097	Parkfield-02, CA	Slack Canyon	6	2.99	1
4098	Parkfield-02, CA	Parkfield - Cholame 1E	6	3	1
4100	Parkfield-02, CA	Parkfield - Cholame 2WA	6	3.01	1
4101	Parkfield-02, CA	Parkfield - Cholame 3E	6	5.55	1
4102	Parkfield-02, CA	Parkfield - Cholame 3W	6	3.63	1
4103	Parkfield-02, CA	Parkfield - Cholame 4W	6	4.23	1
4107	Parkfield-02, CA	Parkfield - Fault Zone 1	6	2.51	1
4113	Parkfield-02, CA	Parkfield - Fault Zone 9	6	2.85	1
4115	Parkfield-02, CA	Parkfield - Fault Zone 12	6	2.65	1
4126	Parkfield-02, CA	Parkfield - Stone Corral 1E	6	3.79	1
4211	Niigata, Japan	NIG021	6.63	11.26	1
4228	Niigata, Japan	NIGH11	6.63	8.93	1
4458	Montenegro, Yugo.	Ulcinj - Hotel Olympic	7.1	5.76	1
4480	L'Aquila, Italy	L'Aquila - V. Aterno - Centro Valle	6.3	6.27	1
4482	L'Aquila, Italy	L'Aquila - V. Aterno -F. Aterno	6.3	6.55	1
4483	L'Aquila, Italy	L'Aquila - Parking	6.3	5.38	1
6887	Darfield, New Zealand	Christchurch Botanical Gardens	7	18.05	1
6897	Darfield, New Zealand	DSLCL	7	8.46	1
6906	Darfield, New Zealand	GDLC	7	1.22	1
6927	Darfield, New Zealand	LINC	7	7.11	1
6928	Darfield, New Zealand	LPCC	7	25.67	1
6942	Darfield, New Zealand	NNBS North New Brighton School	7	26.76	1
6959	Darfield, New Zealand	Christchurch Resthaven	7	19.48	1
6960	Darfield, New Zealand	Riccarton High School	7	13.64	1
6962	Darfield, New Zealand	ROLC	7	1.54	1
6966	Darfield, New Zealand	Shirley Library	7	22.33	1
6969	Darfield, New Zealand	Styx Mill Transfer Station	7	20.86	1
6975	Darfield, New Zealand	TPLC	7	6.11	1
8119	Christchurch, New Zealand	Pages Road Pumping Station	6.2	1.98	1
8123	Christchurch, New Zealand	Christchurch Resthaven	6.2	5.13	1
8161	El Mayor-Cucapah	El Centro Array #12	7.2	11.26	1
8164	Duzce, Turkey	IRIGM 487	7.14	2.65	1
8606	El Mayor-Cucapah	Westside Elementary School	7.2	11.44	1

Table C. 2 List of near-fault nonpulse ground motions (Last access 20/09/2016)

Seq_Num	Earthquake Name	Station Name	Mw	R_rup	I_Direct
230	Mammoth Lakes-01	Convict Creek	6.06	6.63	0
297	Irpinia, Italy-02	Bisaccia	6.2	14.74	0
495	Nahanni, Canada	Site 1	6.76	9.6	0
527	N. Palm Springs	Morongo Valley Fire Station	6.06	12.03	0
558	Chalfant Valley-02	Zack Brothers Ranch	6.19	7.58	0
725	Superstition Hills-02	Poe Road (temp)	6.54	11.16	0
727	Superstition Hills-02	Superstition Mtn Camera	6.54	5.61	0
827	Cape Mendocino	Fortuna - Fortuna Blvd	7.01	19.95	0
830	Cape Mendocino	Shelter Cove Airport	7.01	28.78	0
864	Landers	Joshua Tree	7.28	11.03	0
901	Big Bear-01	Big Bear Lake - Civic Center	6.46	8.3	0
959	Northridge-01	Canoga Park - Topanga Can	6.69	14.7	0
1111	Kobe, Japan	Nishi-Akashi	6.9	7.08	0
1234	Chi-Chi, Taiwan	CHY086	7.62	28.42	0
1512	Chi-Chi, Taiwan	TCU078	7.62	8.2	0
1520	Chi-Chi, Taiwan	TCU088	7.62	18.16	0
1521	Chi-Chi, Taiwan	TCU089	7.62	9	0
1651	Northridge-02	Arleta - Nordhoff Fire Sta	6.05	8.04	0
2628	Chi-Chi, Taiwan-03	TCU078	6.2	7.62	0
2629	Chi-Chi, Taiwan-03	TCU079	6.2	8.48	0
2632	Chi-Chi, Taiwan-03	TCU084	6.2	9.32	0
2635	Chi-Chi, Taiwan-03	TCU089	6.2	9.81	0
3746	Cape Mendocino	Centerville Beach, Naval Fac	7.01	18.31	1
3748	Cape Mendocino	Ferndale Fire Station	7.01	19.32	0
3750	Cape Mendocino	Loleta Fire Station	7.01	25.91	0
3947	Tottori, Japan	SMNH01	6.61	5.86	0
3966	Tottori, Japan	TTR009	6.61	8.83	0
4067	Parkfield-02, CA	PARKFIELD - GOLD HILL	6	3.43	0
4068	Parkfield-02, CA	PARKFIELD - HOG CANYON	6	2.65	0
4116	Parkfield-02, CA	Parkfield - Fault Zone 14	6	8.81	0
4118	Parkfield-02, CA	Parkfield - Gold Hill 1W	6	2.67	0
4119	Parkfield-02, CA	Parkfield - Gold Hill 2E	6	3.84	0
4120	Parkfield-02, CA	Parkfield - Gold Hill 2W	6	3.38	0
4121	Parkfield-02, CA	Parkfield - Gold Hill 3E	6	6.3	0
4122	Parkfield-02, CA	Parkfield - Gold Hill 3W	6	5.41	0
4123	Parkfield-02, CA	Parkfield - Gold Hill 4W	6	8.27	0
4127	Parkfield-02, CA	Parkfield - Stone Corral 2E	6	5.8	0
4128	Parkfield-02, CA	Parkfield - Stone Corral 3E	6	8.08	0
4139	Parkfield-02, CA	PARKFIELD - UPSAR 02	6	9.95	0
4140	Parkfield-02, CA	PARKFIELD - UPSAR 03	6	9.95	0
4141	Parkfield-02, CA	PARKFIELD - UPSAR 05	6	9.61	0
4142	Parkfield-02, CA	PARKFIELD - UPSAR 06	6	9.61	0

Table C.2 (Continued)

4143	Parkfield-02, CA	PARKFIELD - UPSAR 07	6	9.61	0
4144	Parkfield-02, CA	PARKFIELD - UPSAR 08	6	9.41	0
4145	Parkfield-02, CA	PARKFIELD - UPSAR 09	6	9.34	0
4146	Parkfield-02, CA	PARKFIELD - UPSAR 10	6	9.14	0
4147	Parkfield-02, CA	PARKFIELD - UPSAR 11	6	9.41	0
4148	Parkfield-02, CA	PARKFIELD - UPSAR 12	6	9.47	0
4149	Parkfield-02, CA	PARKFIELD - UPSAR 13	6	9.47	0
4209	Niigata, Japan	NIG019	6.63	9.88	0
4218	Niigata, Japan	NIG028	6.63	9.79	0
4219	Niigata, Japan	NIGH01	6.63	9.46	0
4349	Umbria Marche, Italy	Colfiorito	6	6.92	0
4456	Montenegro, Yugo.	Petrovac - Hotel Olivia	7.1	8.01	0
4481	L'Aquila, Italy	L'Aquila - V. Aterno -Colle Grilli	6.3	6.81	0
5657	Iwate	IWTH25	6.9	4.8	0
5832	El Mayor-Cucapah	TAMAULIPAS	7.2	26.55	0
6961	Darfield, New Zealand	RKAC	7	16.47	0



## CIRCULUM VITAE

### PERSONAL INFORMATION

- **Family name:** Moghimi
  - **First name:** Saed
  - **Date of Birth:** 23.09.1980
  - **Marital State:** Single
  - **Tel:** 0090 554 809 5914
  - **Email:** [saaed\\_m@yahoo.com](mailto:saaed_m@yahoo.com)
- 

### EDUCATION

- **PhD.** in Civil Engineering, Earthquake Engineering, Sep. 2011 –Sep. 2017, Civil Eng. Dept., Middle East Technical University, Ankara, Turkey, GPA: 3.5/4
  - **M.Sc.** in Civil Engineering, Earthquake Engineering, Sep. 2005 – Mar.2008, Civil Eng. Dept., University of Tabriz, Iran, GPA: 80/100
  - **B.Sc.** in Civil Engineering, Sep. 1999 – Sep. 2004, University of Tabriz, Iran, GPA: 75/100
- 

### PROJECTS

- **Research Assistant.** At Bogazici University - Kandilli Observatory and Earthquake Research Institute – Earthquake Engineering Department – TUBITAK Project  
  
**Project Title:** Effect of near field earthquakes on design spectrum and its role on drift and displacement of structures (Project Number: 113M308)
- 

### PUBLICATIONS

- Moghimi S., Jalali A., Comparison of Adaptive Pushover with Nonlinear Time History and Conventional Pushover Analysis for Special Concrete Frame Structures "international Conference on Earthquake Engineering & seismology", (ICEES – 2011), Islamabad, Pakistan
- Moghimi S., Akkar S., Implications of Forward-directivity Effects on Design Ground Motions "Seismological Society of America (SSA) Annual Meeting", 20–22 April 2016, Reno, Nevada

- Moghimi S., Akkar S., Effect of Major Seismological Parameters on Directivity Dominant Spectral Amplification "6th International Conference on Computational Methods in Structural Dynamics and Earthquake Engineering, COMPDYN 2017", 15-17 June 2017, Rhodes Island, Greece
- Moghimi S., Akkar S., Mixed Effect of Directivity and Directionality for Near Fault Pulse Type Ground Motions "European Geosciences Union General Assembly 2017", 23–28 April 2017, Vienna, Austria
- Cagnan Z., Akkar S., Moghimi S., A first hazard analysis of the Harrat Ash Shamah volcanic field, Syria-Jordan Borderline "European Geosciences Union General Assembly 2017", 23–28 April 2017, Vienna, Austria
- Akkar S., Moghimi S., Arıcı Y. A study on major seismological and geometrical parameters affecting near-fault forward-directivity ground-motion demands for their possible inclusion in seismic design codes, *Soil Dynamics and Earthquake Engineering*, under review, (Submitted in March 2017)
- Moghimi, S. Akkar, S Amplification models for near fault design spectrum when directivity effect is prominent (ready for submission).

---

## WORK EXPERIENCE

- 2006-2011 Lecturer at Islamic Azad University,
- 2006-2011 Design Engineer of Iranian Construction Engineering Organization
- 2006-2011 Supervisor Engineer of Iranian Construction Engineering Organization
- 2006-2007 Supervisor Engineer of Bonyade Maskan, Urumiye, Iran
- 2009-2010 Head of technical office in Urum Arme Saghf construction engineering company
- 2014-2016 Research Assistant, Kandilli Observatory And Earthquake Research Institute – Bogazici University

---

## COMPUTER SKILLS

- **Programming** MATLAB
- **CRISIS2007** (a computer program for seismic hazard estimation)
- **EZ FRISK** (a computer program for seismic hazard estimation)
- **Perform3D** (Nonlinear Analysis And Performance Assesment for 3-D Structures)
- **Seismosignal** (a computer program for processing strong-motion data)

- **Seismostruct** (a computer program for static and nonlinear dynamic analysis of framed structures)
- **Structural Analysis and Designing Package**—SAP, ETABS, SAFE
- **PERFORM 3D** (Performance-Based Design Software )